Spring 5-15-2015

Neural Processing in the Three Layer Turtle Visual Cortex

Jeffrey Steven Pobst
Washington University in St. Louis

WASHINGTON UNIVERSITY IN ST. LOUIS

Department of Physics

Dissertation Examination Committee:
Ralf Wessel, Chair
James Buckley
Anders Carlsson
Erik Henriksen
Woodrow Shew

Neural Processing in the Three Layer Turtle Visual Cortex

by

Jeffrey Pobst

A dissertation presented to the
Graduate School of Arts & Sciences
of Washington University in
partial fulfillment of the
requirements for the degree
of Doctor of Philosophy

May 2015
St. Louis, Missouri

Table of Contents

List of Figures

List of Tables

Acknowledgments

I'd like to thank my advisor Ralf Wessel for putting up with me for the last five and a half years. Beyond supporting and advising me with the research, he's always been amazingly supportive of his students' best interests and their goals beyond graduate school. I've seen this in my own experience, but also with other students in the lab, and I'm grateful to have had him as an advisor.

I'd like to thank Anders Carlsson. Throughout my years of graduate school, as peoples' availability has changed, my committee has changed, but Anders Carlsson has always been a member. In addition to being there reliably, he also tended to have stricter requirements regarding how explicitly and clearly my research goals were presented during our committee meetings. This was a nuisance at times (as many productive tasks are), but it was always useful in helping me see the big picture, refocus, and prioritize.

I'd like to thank David Morton for serving as a programming mentor. During the time I spent coding with him, I learned to write clean, organized, and modular code. I'm absolutely certain that as a result of this, the tens of thousands of lines of analysis code that I've written leading up to this thesis have been much more productive and efficient, and have led me to discoveries that I wouldn't have reached without powerful effective code. This is also a skill that will stick with me and have limitless use beyond grad school.

I'd like to thank all members of the lab. Some were instrumental in teaching me experimental techniques (our collaborator Michael Ariel belongs with this group), and all have provided useful feedback and insights through discussions.

I'd like to thank my collaborators Woodrow Shew and Wesley Clawson. While I'm obviously grateful for the multitude of data and wealth of new ideas that have come of our collaboration, I'm also thankful that I found collaborators I enjoyed spending time with. The all day, every day experiments we would do for two to three weeks at a time would have miserable if they had been done with people that weren't great to be around.

Lastly, I'd like to thank my parents and family, who are always looking out for me. I'm very happy with where I am and the person I've become, but I didn't magically appear here. Any successes I've had and the person I've become are the product of my upbringing and the love and support I received along the way.

Jeffrey Pobst

Washington University in St. Louis

February 2015

ABSTRACT OF THE DISSERTATION

Neural Processing in the Three Layer Turtle Visual Cortex
by
Jeffrey Pobst
Doctor of Philosophy in Physics
Washington University in St. Louis, 2015
Professor Ralf Wessel, Chair

In this thesis we investigate neural processing in turtle visual cortex. To this end, we characterize the nature of both spontaneous, ongoing neural activity as well as activity evoked by visual stimulation. Data are collected from whole brain eye-attached preparations, recording with extracellular and intracellular electrodes. We investigate the activity of action potentials as well as the slower local field potential activity.

To investigate response properties, we explore spatial properties of receptive fields, temporal properties of spontaneous and evoked activity, response adaptation, and correlations between different types of activity as well as between activity recorded in different regions.

To study the roles of rhythmic oscillations in the local field potential, we examine temporal and spectral properties of oscillations. We look at the distributions of durations of oscillatory bursts as well as the distributions of the dominant frequencies within those oscillations. We also investigate the variability of these features and produce similar results in a model simulation.

Lastly, we investigate criticality and the statistics of neural activity over a range of scales in the turtle visual cortex. We use neuronal avalanches to reveal scale-free cortical dynamics and power-law statistics, which have been hypothesized to optimize information processing.

Preface

Chapter 3 is being prepared for publication. The experiments were done by Wesley Clawson, Woodrow Shew, Ralf Wessel, Nathaniel Wright, and me. The simulations were done by Mahmood Hoseini. I analyzed the data. Mahmood Hoseini, Ralf Wessel, and I wrote the paper.

Chapter 4 is being prepared for publication. Woodrow Shew and Ralf Wessel conceived the study and designed the experiments. I designed the visual stimuli. The experiments were performed by Woodrow Shew, Wesley Clawson, Nathaniel Wright, Ralf Wessel, and me. Woodrow Shew and Wesley Clawson analyzed the data. Woodrow Shew and Yahya Karimipanah performed the model simulations. Woodrow Shew and Ralf Wessel wrote the paper.

The Spikepy project (Chapter 5) was led by David Morton, and is reproduced from his dissertation. The overall framework for the program was his vision, but he and I worked on this every day for a summer, writing code and discussing how to implement ideas, to produce the first version. While he continued to work on the project beyond the summer, I moved on to other projects and my further contributions were only minor changes and suggestions.

Additionally, I have presented the following posters at conferences:

Oscillations Comprised of Multiple Narrow Frequency Bands During Cortical Visual Processing. Jeffrey Pobst et al., At Society for Neuroscience. November 2013. San Diego, CA.

Structure of Ongoing and Evoked Activity in a Three-Layer Primary Visual Cortex. Jeffrey Pobst et al., At Society for Neuroscience. October 2012. New Orleans, LA.

Direction Selectivity within Large Receptive Fields in a Three-Layer Visual Cortex. Jeffrey Pobst et al., At Computational and Systems Neuroscience. February 2012. Salt Lake City, UT.

Visual Responses in Turtle Isthmotectal System and Primary Visual Cortex. Jeffrey Pobst et al., At Society for Neuroscience. November 2011. Washington DC.

Along with coauthoring additional posters at conferences:

Dynamics of Cortical Noise Correlations During Vision. Nathaniel Wright et al., At Society for Neuroscience. November 2014. Washington DC.

Characterization and Proposed Mechanisms of Intermittent Oscillations in Cerebral Cortex. Mahmood Hoseini et al., At Society for Neuroscience. November 2014. Washington DC.

Cortical Visual Processing at Criticality. Woodrow Shew et al., At Society for Neuroscience. November 2013. San Diego, CA.

Spikepy: A Plugin Based Spike Sorting Framework. David Morton et al., At Computational and Systems Neuroscience. February 2011. Salt Lake City, UT.

Chapter 1: Introduction

I not only use all the brains that I have, but all that I can borrow.

-Woodrow Wilson

1.1 General Introduction

Our perception of the world is the product of signals sent from our various sensory organs to our cortex, which processes these signals to identify salient features useful for us to interact with the world. In addition to processing sensory input, the cortex also controls motor skills and complex thought processes like speech. Though the human cortex makes up roughly 80% of the brain and plays a role in nearly all types of sensory processing (Shepherd, 2011), we are still far from understanding how most of that processing is actually done.

The projects covered in this thesis are an effort to bring us closer to understanding cortical processing, by revealing neural representations of visual stimuli and the nature of a range of activities within the three layer cortex of turtles.

1.2 Comparative Neuroscience

Much of our understanding of the nervous system is built on foundational neural circuit research done in lampreys, lobsters, sea slugs, zebra finches, and a wide array of other taxa (Hale, 2014). In general, when two species have a traceable evolutionary history stemming from a common ancestor, we can expect to find similarities that are greater than chance (Northcutt, 1981). Time and time again, we have discovered mechanisms, neural representations, structures, and patterns of activity in nonhuman animals that inform our understanding of mammals and the search for homologies in the brain and mind (Carlson, 2012; Hildebrand & Shepherd, 1997; Platt & Spelke, 2009). With this in mind, there is much that we can learn about the human brain by studying species with a common ancestry. The promise of comparative neuroscience to provide insights into understanding the structure, functions, ontogeny, and evolution of nervous systems requires research on a broad range of species with deliberate attention given to both the differences and similarities between species (Bullock, 1984).

1.3 Reptiles and Mammals

1.3.1 Phylogeny

Though turtles and mammals aren't immediate neighbors on the phylogenic tree, the turtle has promise to be a valuable model preparation because features of its geniculo-cortical organization likely emerged early in the evolution of amniotes (Figure 1.1) and therefore should closely resemble those of the Triassic cotylosaurs (stem amniotes) from which they and all modern mammals evolved (Romer, 1977).

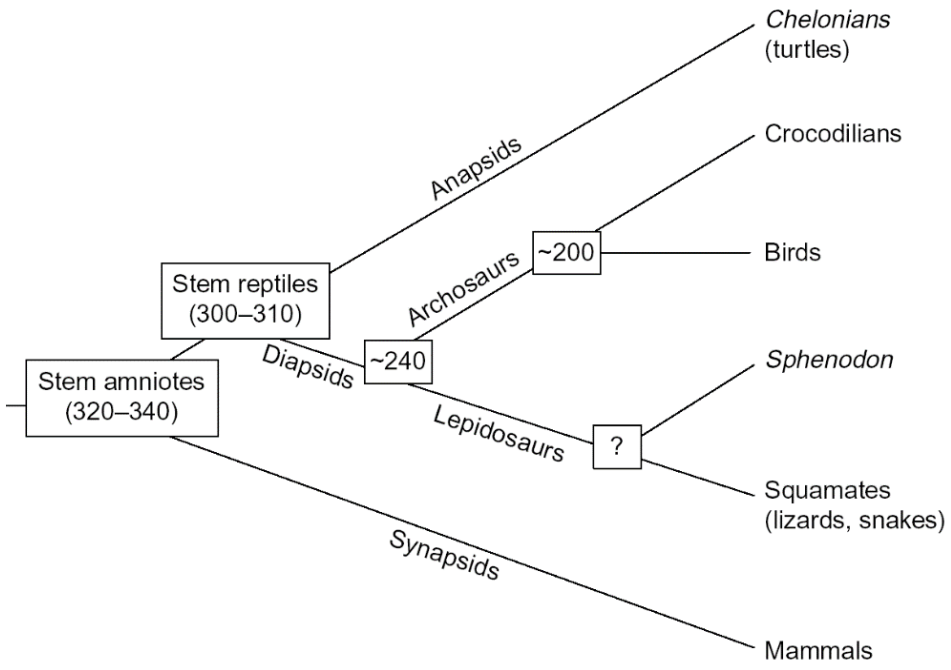

Figure 1.1 Simplified evolutionary filiations of amniotes. Numbers refer to estimated time of phyletic divergence in millions of years. Figure taken from (Bar, Lambert de Rouvroit, & Goffinet, 2000). Note: Other studies argue for turtles to be grouped with the diapsids (Rieppel, 2000), but there is still debate regarding the proper phylogeny of turtles (Gilbert & Corfe, 2013)

While all these animals may seem very different from each other, there are basic features of the stem amniote that persist in the evolved animals (though the form, function, and location of these features may have changed over time) (Figure 1.2).

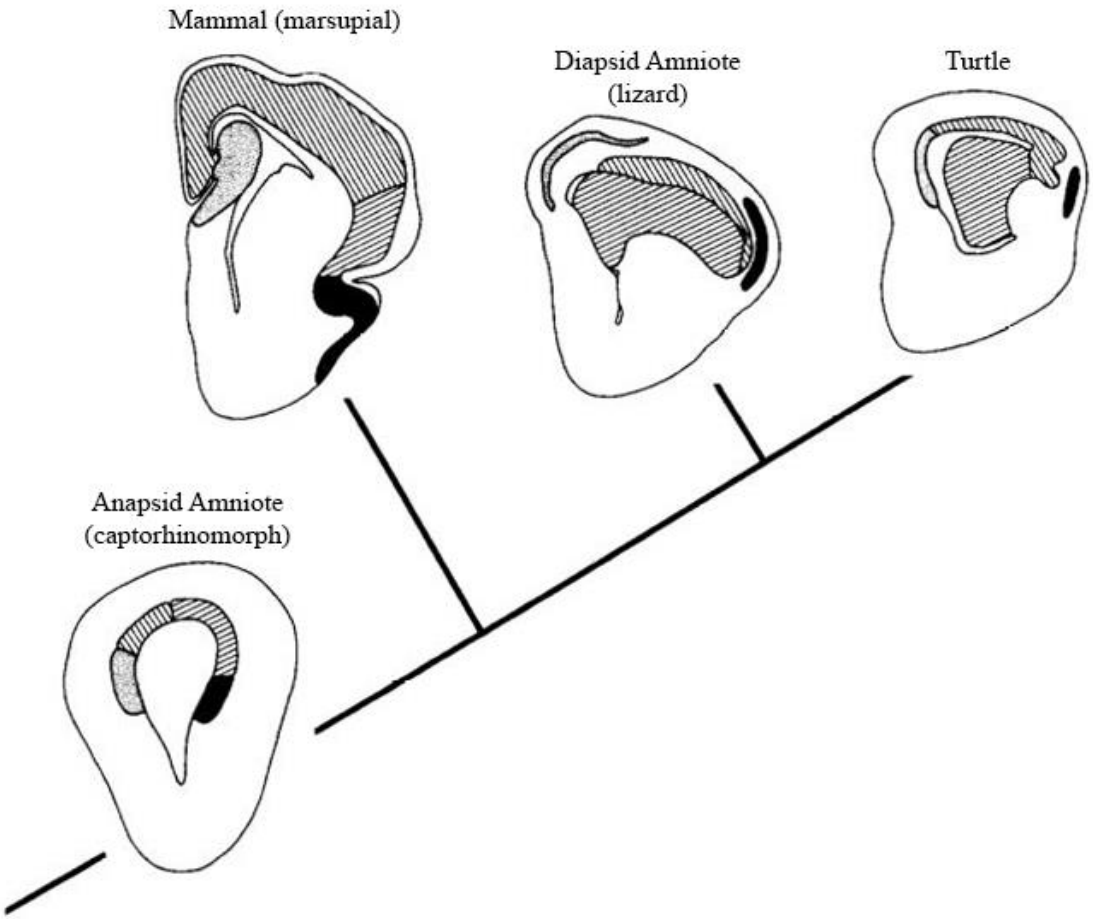

Figure 1.2 Dendrogram of amniotes with diagrams of transverse hemisections through the telencephalon. For each section, the midline is to the left and dorsal is towards the top. The labeling is as follows (starting with the black region moving counter clockwise on the captorhinomorph: lateral pallium, lateral dorsal pallium, medial dorsal pallium, and medial pallium. Modified from (Butler, 1994).

It is likely that the turtle cortex in particular may have retained many of the features of an ancestral form of mammalian cortex (Bar et al., 2000; Diamond & Hall, 1969; Kaas & Reiner, 1999; Northcutt, 1981; Reiner, 2000; Philip Steven Ulinski, 1983).

1.3.2 Functional Areas in the Turtle Brain

Within the turtle telencephalon, several distinct sensory regions can be found. In the lateral cortex we find the olfactory cortex, in the dorsal ventricular ridge we find a primary

auditory area and secondary visual area, and in the dorsal cortex, we find the primary visual cortex, which is the focus of our research (Figure 1.3). This is the area that we will discuss in further detail in the next few sections.

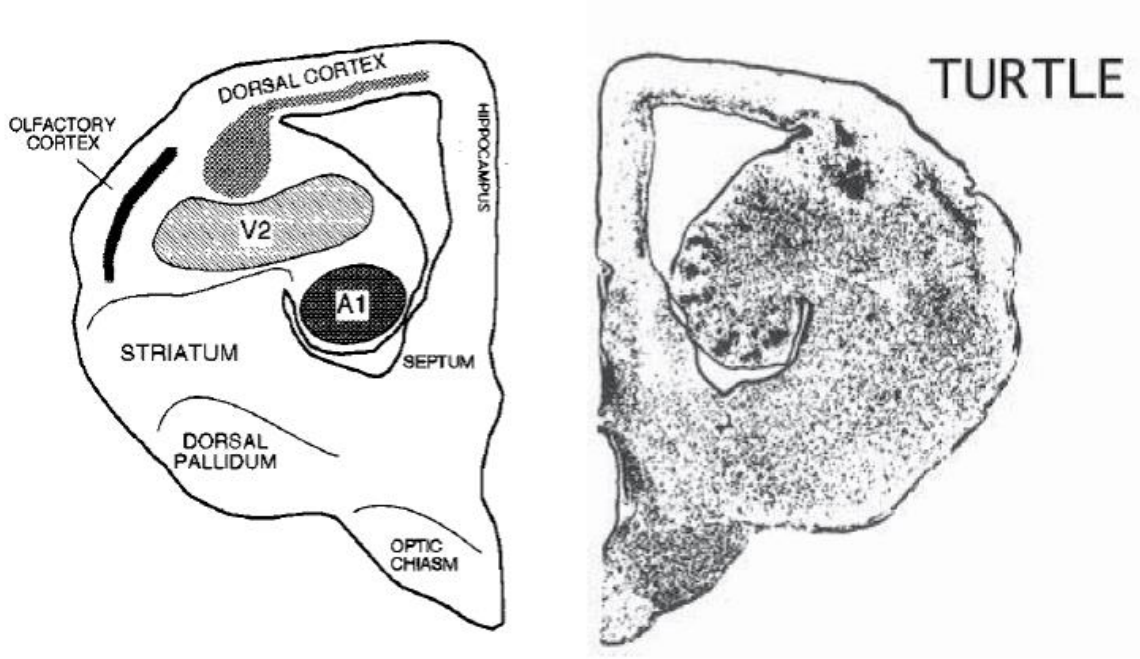

Figure 1.3 Photomicrograph and schematic illustration of the turtle telencephalon. The dorsal cortex contains the primary visual cortex, which is the focus of our studies. Taken from (Reiner, 2000).

1.3.3 Layered Cortical Structure

The cortices of reptiles and mammals are both arranged into layers with neurons forming local circuits both within as well as across layers. Among the reptiles, the radial organization of the turtle cortex is the most rudimentary (Bar & Goffinet, 2000). Turtles (along with fish and amphibians) have a three layer cortex (Figure 1.4) whereas the mammals have developed a six layer neocortex (though the three-layer cortex persists in mammalian hippocampus and olfactory cortex).

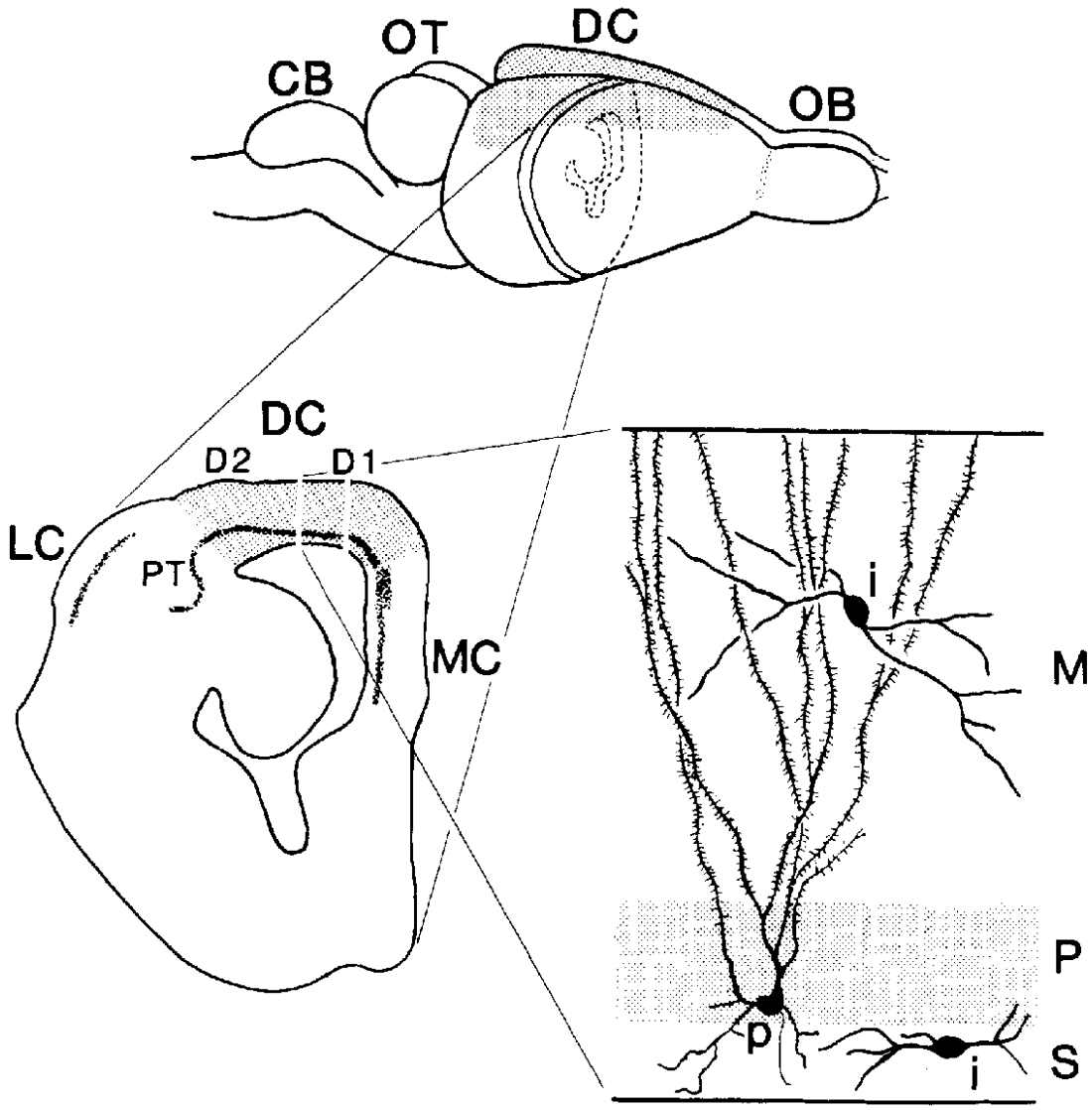

Figure 1.4 The turtle brain and cortex at multiple scales. **(Top)** Turtle brain shown indicating the cerebellum (CB), optic tectum (OT), dorsal cortex (DC) shaded grey, and the olfactory bulbs (OB). **(Bottom Left)** A blown up view of the cortex including the lateral cortex (LC), pallial thickening (PT), dorsal cortex subdivisions (D1 and D2), medial cortex (MC), and a darkened line extending from the pallial thickening into the dorsal cortex indicating the pyramidal cell layer. **(Bottom Right)** A blown up view of a section of dorsal cortex showing a pyramidal cell (p) and inhibitory cells (i) in the molecular layer (M), pyramidal cell layer (P), and subcellular layer (S). Figure taken from (Blanton, Shen, & Kriegstein, 1987).

Though we are far from understanding precisely how the 6 layer cortex evolved, it is thought that mutations affecting the expression of the protein reelin, play a key role in cortical lamination and laminar differentiation (Bar & Goffinet, 2000; Bar et al., 2000). Additionally, one

study suggests that cells serving in different functional roles (input and output) in the turtle pyramidal cell are correspond both in function and in gene expression to the pyramidal cells in different layers of the neocortex (Figure 1.5) (Dugas-Ford, Rowell, & Ragsdale, 2012).

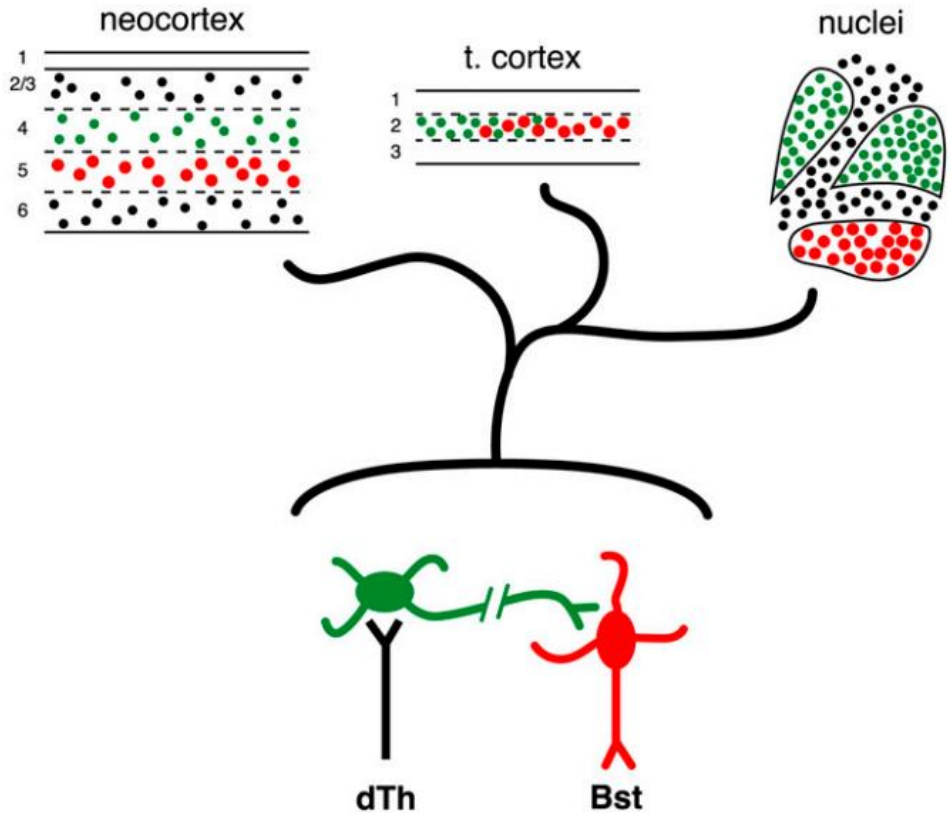

Figure 1.5 Structural diversity in the organization of conserved input and output cell types in amniote telencephalon. Organization of input cells (green) and output cells (red) in the neocortex **(Upper Left)**, turtle dorsal cortec **(Upper Center)**, and dorsal ventricular ridge **(Upper Right)**. **(Bottom)** The dorsal thalamus (dTh) and brainstem (Bst) are shown as a source of input and target for output, respectively. Figure taken from (Dugas-Ford et al., 2012).

1.3.4 Cell Types

Most neurons in the mammalian cortex can be sorted as either spiny (because their dendrites have little appendages called spines) or smooth cells (which don't have those appendages) (Shepherd, 2004). The turtle cortex also has both spiny and smooth cells (Figure 1.6), but they are arranged more simply in the turtle's three layer paleo cortex, with the spiny

pyramidal cells all lying in layer 2 (the pyramidal cell layer) and the smooth interneurons lying in layers 1 and 3.

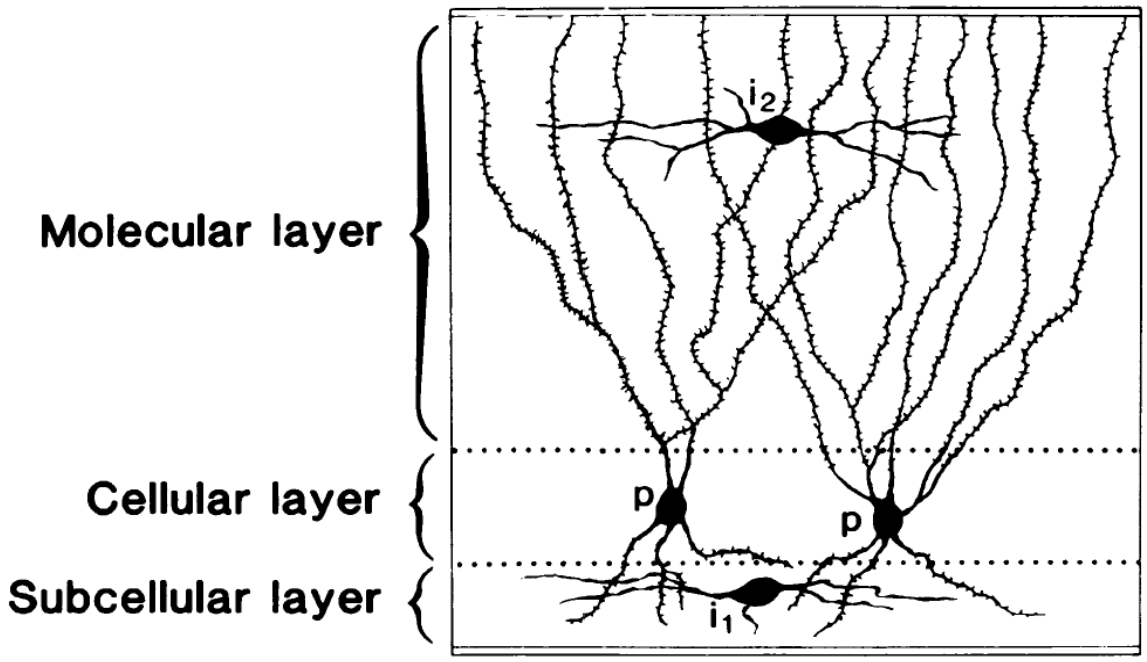

Figure 1.6 Spiny and smooth cells in turtle cortex. Spiny pyramidal cells (p) and smooth inhibitory stellate cells in the subcellular (i_1) and molecular (i_2) layers. Figure taken from (Shen & Kriegstein, 1986).

The dendritic arbors of turtle pyramidal cells are quite different from mammalian pyramidal cells. Whereas neocortical pyramidal cells often have one main apical dendritic branch extending from the soma with further oblique branches distal from the soma, most dendrites from turtle pyramidal cells are individual branches that extend all the way from the soma as seen in Figure 1.7 (Larkum, Watanabe, Lasser-Ross, Rhodes, & Ross, 2008).

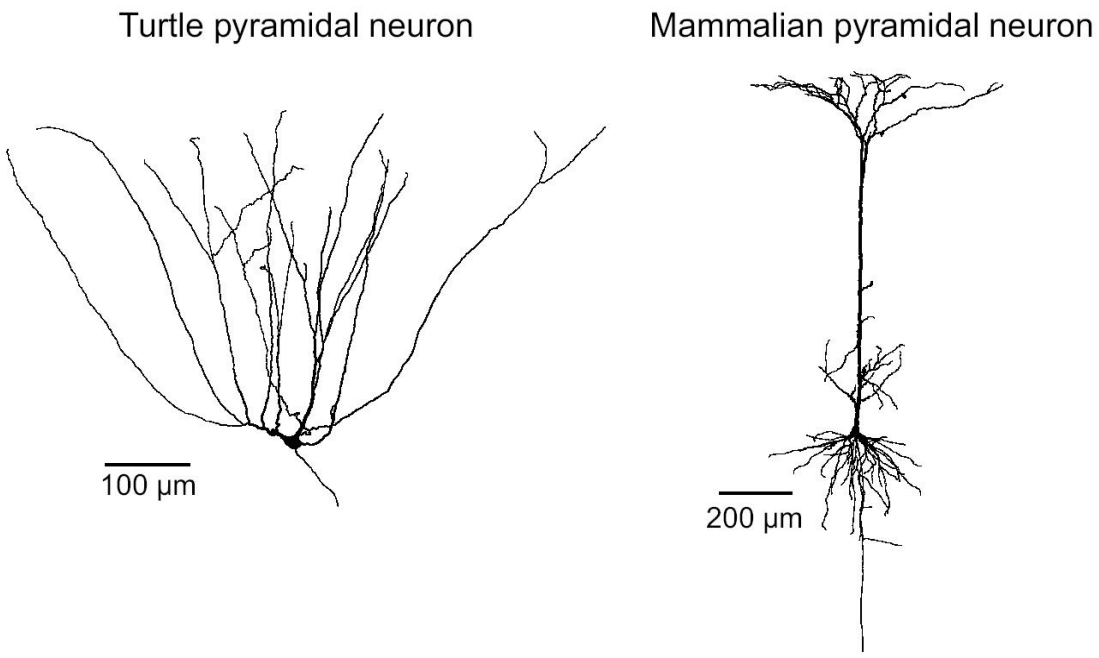

Figure 1.7 Pyramidal cells from turtle and rat. Outlines of pyramidal cells from turtle **(Left)** and rat layer 5 **(Right)** determined from biocytin fills. Modified from (Larkum et al., 2008).

1.4 Anatomy and Physiology of the Turtle Dorsal Cortex

Primary visual cortex receives sensory input directly from LGN axons making en passant synapses with pyramidal cells (Heller & Ulinski, 1987). There are also immense cortico-cortical connections providing both excitatory connections from other pyramidal cells (Cosans & Ulinski, 1990; Larson-Prior, Ulinski, & Slater, 1991) as well as inhibitory connections from GABAergic interneurons (Colombe, Sylvester, Block, & Ulinski, 2004). Individual pyramidal cells receive input from LGN cells covering a region of the visual field thought to represent azimuth lines (Mulligan & Ulinski, 1990).

1.4.1 Thalamic Input

The LGN (lateral geniculate nucleus) sends sensory signals into the turtle dorsal cortex through the lateral forebrain bundle (Figure 1.8) (Mulligan & Ulinski, 1990).

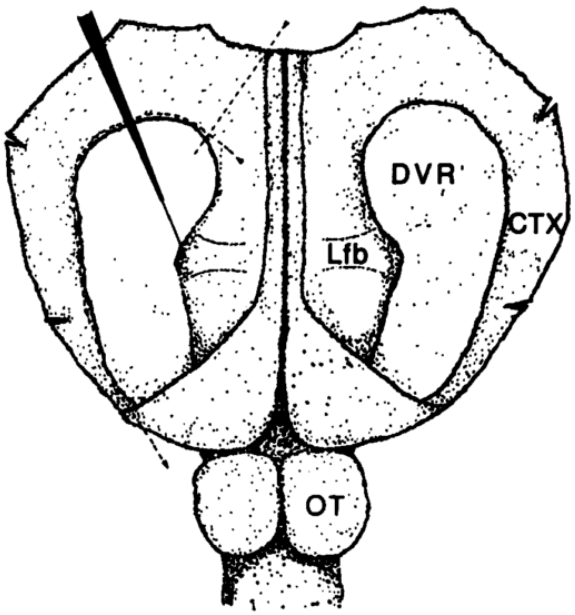

Figure 1.8 Drawing of the turtle whole-brain preparation showing the lateral forebrain bundle. This drawing shows the cortex (CTX), dorsal ventricular ridge (DVR), and lateral forebrain bundle after cuts have been made to the cortex and the cortex has been unfolded. Figure taken from (Mulligan & Ulinski, 1990).

After passing through the lateral forebrain bundle, the geniculate axons spread rostro-caudally, but generally extend radially towards the medial cortex as (Figure 1.9) (Mulligan & Ulinski, 1990).

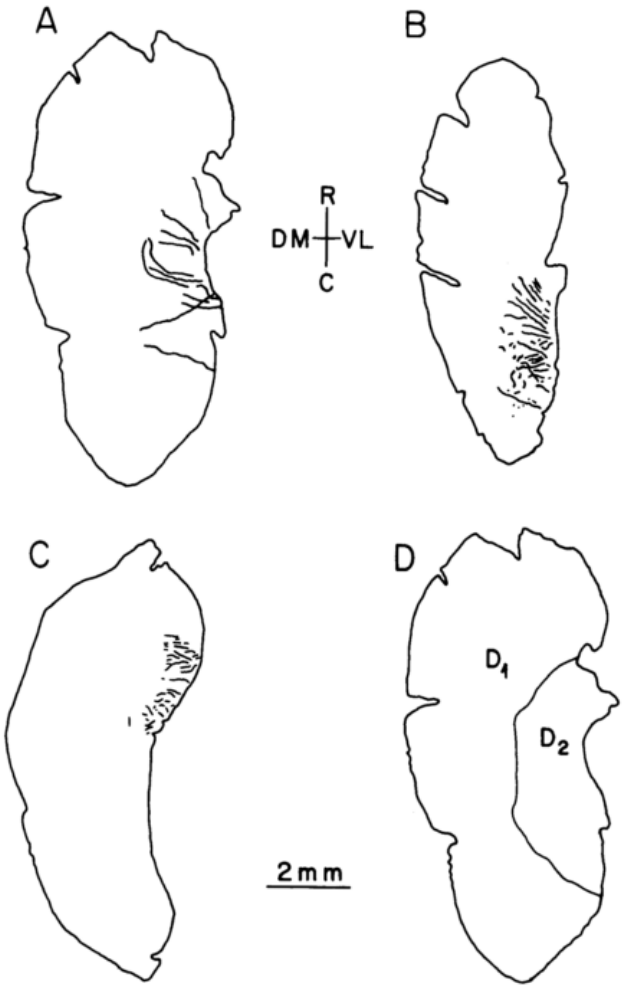

Figure 1.9 Geniculate axons in the dorsal cortex. **(A-C)** examples of the distribution of geniculocortical axons labeled by horseradish peroxidase injected in the lateral forebrain bundle. **(D)** The position of the visual cortex (D2). DM, dorsomedial; R, rostral; C, caudal; VL, ventrolateral. Figure taken from (Mulligan & Ulinski, 1990)

The geniculocortical axons pass beneath the DVR, pass through the pyramidal cell layer of the dorsal cortex and make en passant synapsis on the apical dendrites of the pyramidal cells (Figure 1.10) as well as forming synapses with interneurons..

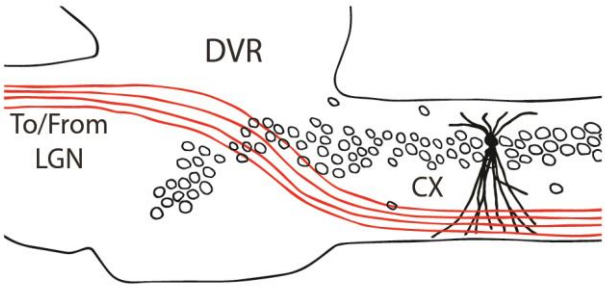

Figure 1.10 Schematic of turtle cortex with thalamic input and a sample pyramidal cell. Circles indicate pyramidal cell bodies. Axons to and from the LGN are shown in red, passing by the dorsal ventricular ridge. The dendritic tree is drawn for one pyramidal cell.

1.4.2 Cortico-Cortical Feedforward and Feedback Circuits

Most of the input to turtle pyramidal cells actually comes from other cells within the cortex. These connections are made in both feedforward and feedback circuitry (Figure 1.11). In the feedforward circuit, pyramidal cells receive excitatory input from other pyramidal cells and inhibitory input from subpial and stellate cells, all of which directly receive excitation from geniculate afferents. One factor that helps us appreciate the extent of the feedforward circuit is that the superficial layer-1 interneurons actually receive a higher density of afferent input than the pyramidal cells do (L. M. Smith, Ebner, & Colonnier, 1980).

In the feedback circuit, pyramidal cells receive inhibitory input from subpial, stellate, and horizontal cells after those cells have been excited by pyramidal cells.

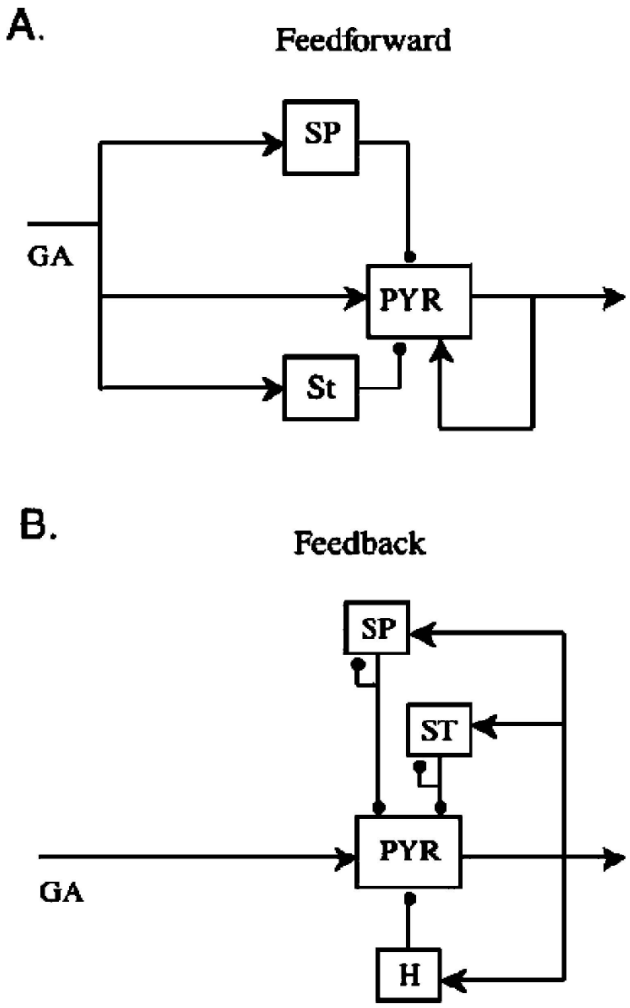

Figure 1.11 Turtle cortico-cortical feedforward and feedback circuits. The structure of anatomically feedforward **(A)** and feedback **(B)** circuits in the turtle cortex. Each box represents a population of cells. The figure shows geniculate afferents (GA), pyramidal cells (PYR), subpial cells (SP), stellate cells (ST), and horizontal cells (H). Connections ending with arrow heads are excitatory, and connections ending with circles are inhibitory. Figure taken from (W. Wang, Campaigne, Ghosh, & Ulinski, 2005).

1.5 Similarity to Mammalian Olfactory Cortex

It is thought that identifying the structural and functional similarities between reptilian dorsal cortex and mammalian olfactory cortex (which has persisted through evolution as a three layer cortex) could help reveal common organizational and computational principals and by

extension, some of the most primordial computations carried out in cortical networks (Fournier, Müller, & Laurent, 2014).

Mammalian olfactory cortex resembles turtle cortex in ways beyond its basic three layer structure. For instance, the olfactory cortex also makes local feedforward circuits with apical layer 1 inhibitory interneurons and feedback circuits with basal inhibitory interneurons (Fig12) (L B Haberly & Bower, 1984; Lewis B Haberly, 1985; Satou, Mori, Tazawa, & Takagi, 1983). Just as the turtle cortex pyramidal cells receive their sensory input through en passant synapses to the apical dendrites from the LGN, the olfactory cortex pyramidal cells receive their sensory input through en passant synapses to the apical dendrites from the lateral olfactory tract (LOT) (Figure 1.12) (Lewis B Haberly & Presto, 1986), and the superficial layer-1 interneurons in olfactory cortex also receive a higher density of afferent input than do the pyramidal cells (Stokes & Isaacson, 2010)

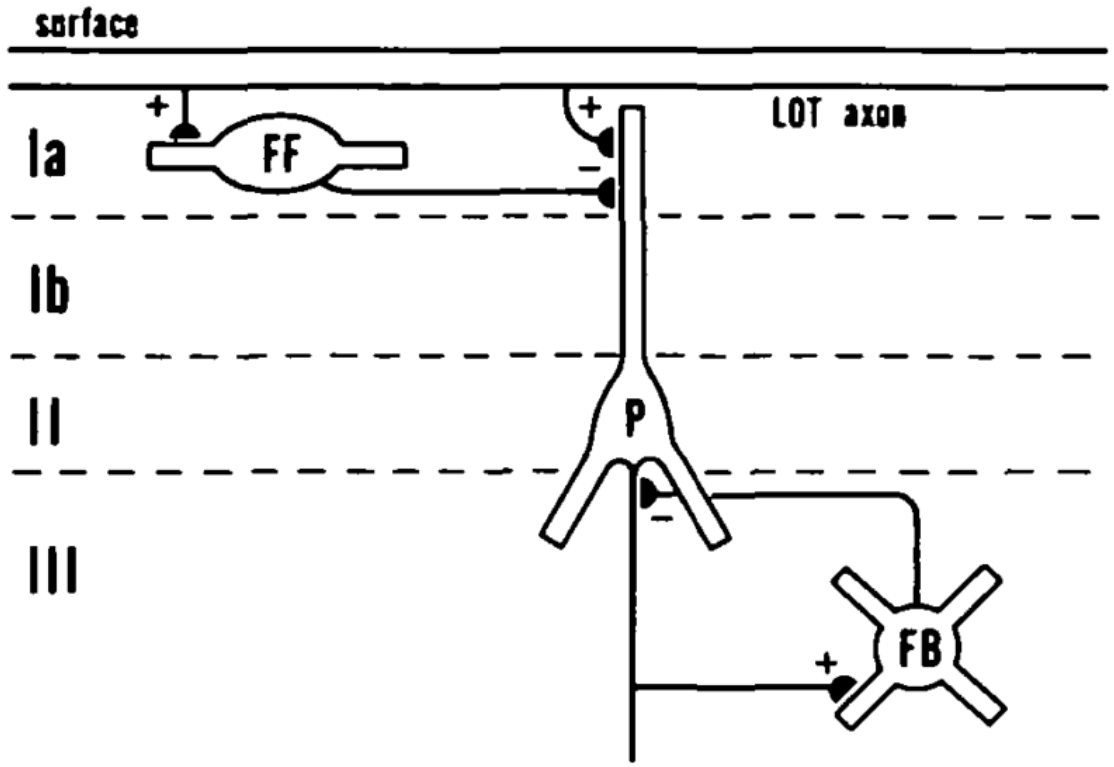

Figure 1.12 Inhibitory feedforward and feedback in olfactory cortex. Axons from the lateral olfactory tract (LOT), synapse onto both feedforward (FF) interneurons and ontho pyramidal cells (P). Feedback (FB) interneurons are excited by pyramidal cells, which the then inhibit. Figure taken from (Lewis B Haberly, 1985).

In addition to having these similar circuitries, the mammalian olfactory cortex also exhibits similar morphology. Whereas the dendritic tree of neocortical pyramidal cells tend to have a single main apical dendrititic branch extending from the soma, the pyramidal cells of olfactory cortex have many apical dendritic branches extending from the soma (Figure 1.13) just as we see in turtle cortex. It's also been shown that, like turtle pyramidal cells, olfactory cortex pyramidal cells are spiny (Johnson, Illig, Behan, & Haberly, 2000).

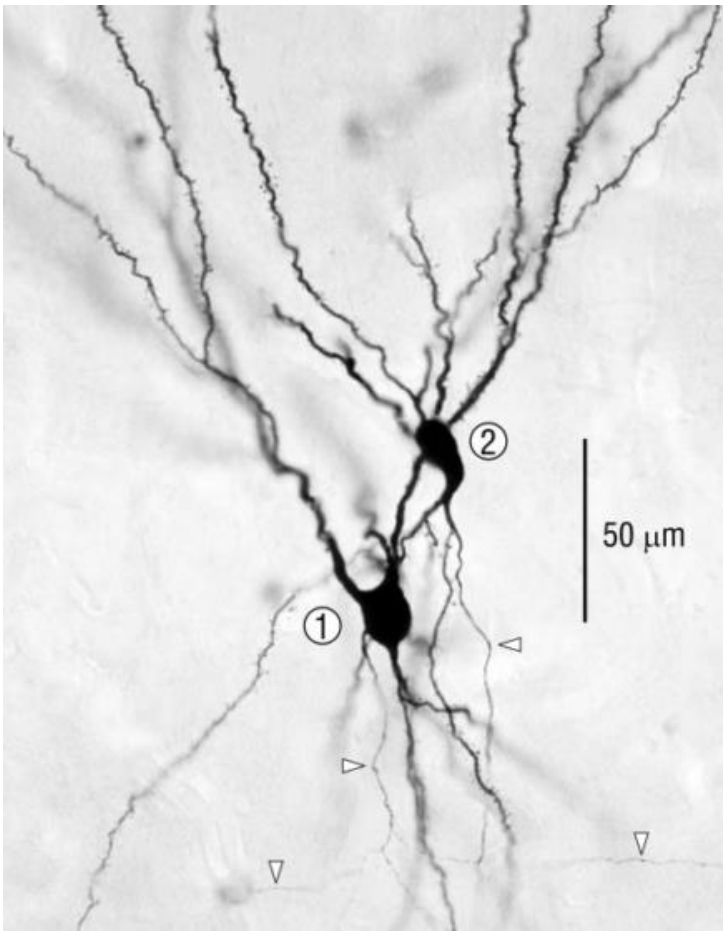

Figure 1.13 Pyramidal cells from olfactory cortex. Photomicrograph of two pyramidal cells in rat olfactory cortex. Arrowheads indicate axons. Figure taken from (Johnson et al., 2000)

1.6 Practical Advantages of Turtle

The turtle offers practical advantages for conducting experiments. Turtles are remarkably resistant to the effects of anoxia (Belkin, 1963; Clark & Miller, 1973). Consequently, unlike the mammalian brain, the turtle brain can be completely removed from the body and its circulatory and respiratory systems can remain active in a bath of oxygenated artificial cerebral spinal fluid for several hours. This allows us three great advantages: 1) complete control of the bathing medium (ACSF), 2) isolation from the noise and vibration associated with the heartbeat and respiration, and 3) control of and access to the cortical tissue (Hounsgaard & Nicholson, 1990).

1.7 Motivating Questions for the Turtle Cortical System

As we seek to better understand the structural and functional patterns that give rise to vision, olfaction, speech, memory, motor control and countless other fundamental functions the cortex participates in, we look for insights from many lines of research. We already know that the turtle cortex shares many features with mammalian hippocampus and olfactory cortex.

To gain further clues of the mechanisms underlying cortical processing, in Chapter 2 we will investigate the properties of local field potential and action potential activity in response to visual stimulation with complex movies, diffuse flashes, and stimuli involving simple motion, and we will discuss the extent to which these signal are specific to certain stimuli and how these signals vary throughout the visual cortex. In Chapter 3 we will focus on the nature of local field potential oscillations that occur spontaneously in visual cortex as well as in response to visual stimulation, with attention to the frequency profiles and the temporal properties of oscillations, as well as reproducing the experimental results with a model simulation. In chapter 4 we will study self-organized criticality in the turtle cortex by looking at activity across a range of scales along with a model simulation. Finally, in Chapter 6 we will discuss a myriad of additional results, observations, and questions that may lead to further insights into the workings of the cortex.

1.8 References

Bar, I., & Goffinet, A. (2000). Evolution of cortical lamination: the reelin/Dab1 pathway. *Novartis Foundation Symposium*. Retrieved from http://www.its.caltech.edu/~bi250b/2009/papers/Bar_Goffinet_2000.pdf

Bar, I., Lambert de Rouvroit, C., & Goffinet, A. M. (2000). The evolution of cortical development. An hypothesis based on the role of the Reelin signaling pathway. *Trends in*

Neurosciences, *23*(12), 633–8. Retrieved from http://www.ncbi.nlm.nih.gov/pubmed/11137154

Belkin, D. A. (1963). Anoxia: tolerance in reptiles. *Science (New York, N.Y.)*, *139*(3554), 492–493. doi:10.1126/science.139.3554.492

Blanton, M. G., Shen, J. M., & Kriegstein, A. R. (1987). Evidence for the inhibitory neurotransmitter gamma-aminobutyric acid in aspiny and sparsely spiny nonpyramidal neurons of the turtle dorsal cortex. *The Journal of Comparative Neurology*, *259*(2), 277–97. doi:10.1002/cne.902590208

Bullock, T. H. (1984). Comparative neuroscience holds promise for quiet revolutions. *Science*, *225*(4661), 473–478.

Butler, A. B. (1994). The evolution of the dorsal pallium in the telencephalon cladistic analysis and a new hypothesis of amniotes : *Brain Research Reviews*, *19*(1), 66–101.

Carlson, B. A. (2012). Diversity Matters: The Importance of Comparative Studies and the Potential for Synergy Between Neuroscience and Evolutionary Biology. *Archives of Neurology*, *69*(8), 987. doi:10.1001/archneurol.2012.77

Clark, V. M., & Miller, A. T. (1973). Studies on anaerobic metabolism in the fresh-water turtle (Pseudemys scripta elegans). *Comparative Biochemistry and Physiology. A, Comparative Physiology*, *44*, 55–62.

Colombe, J. B., Sylvester, J., Block, J., & Ulinski, P. S. (2004). Subpial and stellate cells: two populations of interneurons in turtle visual cortex. *The Journal of Comparative Neurology*, *471*(3), 333–51. doi:10.1002/cne.20037

Cosans, C. E., & Ulinski, P. S. (1990). Spatial organization of axons in turtle visual cortex: intralamellar and interlamellar projections. *Journal of Comparative Neurology*, *296*(4), 548–558. Retrieved from http://www.ncbi.nlm.nih.gov/pubmed/2358552

Diamond, I. T., & Hall, W. C. (1969). Evolution of neocortex. *Science (New York, N.Y.)*, *164*(3877), 251–262.

Dugas-Ford, J., Rowell, J. J., & Ragsdale, C. W. (2012). Cell-type homologies and the origins of the neocortex. *Proceedings of the National Academy of Sciences*, *109*(42), 16974–16979. doi:10.1073/pnas.1204773109

Fournier, J., Müller, C. M., & Laurent, G. (2014). Looking for the roots of cortical sensory computation in three-layered cortices. *Current Opinion in Neurobiology*, *31C*, 119–126. doi:10.1016/j.conb.2014.09.006

Gilbert, S. F., & Corfe, I. (2013). Turtle Origins: Picking Up Speed. *Developmental Cell*, *25*(4), 326–328. doi:10.1016/j.devcel.2013.05.011

Haberly, L. B. (1985). Neuronal circuitry in olfactory cortex: anatomy and functional implications. *Chemical Senses*, *10*(2), 219–238. doi:10.1093/chemse/10.2.219

Haberly, L. B., & Bower, J. M. (1984). Analysis of association fiber system in piriform cortex with intracellular recording and staining techniques. *Journal of Neurophysiology*, *51*(January), 90–112.

Haberly, L. B., & Presto, S. (1986). Ultrastructural analysis of synaptic relationships of intracellularly stained pyramidal cell axons in piriform cortex. *Journal of Comparative Neurology*, *248*(4), 464–474.

Hale, M. E. (2014). NeuroView Mapping Circuits beyond the Models : Integrating Connectomics and Comparative Neuroscience NeuroView. *Neuron*, *83*(6), 1256–1258. doi:10.1016/j.neuron.2014.08.032

Heller, S., & Ulinski, P. (1987). Morphology of geniculocortical axons in turtles of the genera Pseudemys and Chrysemys. *Anatomy and Embryology*, 2011. Retrieved from http://link.springer.com/article/10.1007/BF00309685

Hildebrand, J. G., & Shepherd, G. M. (1997). Mechanisms of olfactory discrimination: converging evidence for common principles across phyla. *Annual Review of Neuroscience*, *20*, 595–631. doi:10.1146/annurev.neuro.20.1.595

Hounsgaard, J., & Nicholson, C. (1990). The isolated turtle brain and the physiology of neuronal circuits. *Preparations of Vertebrate Central Nervous System In Vitro*, *6*, 155–181.

Johnson, D. M., Illig, K. R., Behan, M., & Haberly, L. B. (2000). New features of connectivity in piriform cortex visualized by intracellular injection of pyramidal cells suggest that "primary" olfactory cortex functions like "association" cortex in other sensory systems. *The Journal of Neuroscience : The Official Journal of the Society for Neuroscience*, *20*(18), 6974–6982.

Kaas, J. H., & Reiner, A. (1999). Evolutionary neurobiology: The neocortex comes together. *Nature*, *399*(6735), 418–419.

Larkum, M. E., Watanabe, S., Lasser-Ross, N., Rhodes, P., & Ross, W. N. (2008). Dendritic properties of turtle pyramidal neurons. *Journal of Neurophysiology*, *99*(2), 683–94. doi:10.1152/jn.01076.2007

Larson-Prior, L. J., Ulinski, P. S., & Slater, N. T. (1991). Excitatory amino acid receptor-mediated transmission in geniculocortical and intracortical pathways within visual cortex. *Journal of Neurophysiology*, *66*(1), 293–306. Retrieved from http://www.ncbi.nlm.nih.gov/pubmed/1681038

Mulligan, K. A., & Ulinski, P. S. (1990). Organization of geniculocortical projections in turtles: isoazimuth lamellae in the visual cortex. *Journal of Comparative Neurology*, *296*(4), 531–547. Retrieved from http://www.ncbi.nlm.nih.gov/pubmed/2358551

Northcutt, R. G. (1981). Evolution of the telencephalon in nonmammals. *Annual Review of Neuroscience*, *4*, 301–50. doi:10.1146/annurev.ne.04.030181.001505

Platt, M. L., & Spelke, E. S. (2009). What can developmental and comparative cognitive neuroscience tell us about the adult human brain? *Current Opinion in Neurobiology*, *19*, 1–5. doi:10.1016/j.conb.2009.06.002

Reiner, A. J. (2000). A hypothesis as to the organization of cerebral cortex in the common amniote ancestor of modern reptiles and mammals. *Novartis Foundation Symposium*, *228*, 83–102; discussion 102–13. Retrieved from http://www.ncbi.nlm.nih.gov/pubmed/10929318

Rieppel, O. (2000). Turtles as diapsid reptiles. *Zoologica Scripta*, *29*(July), 199–212. doi:10.1046/j.1463-6409.2000.00039.x

Romer, A. S. (1977). *Vertebrate Body*. (T. Parsons, Ed.) (5th ed.). W.B. Saunders Company.

Satou, M., Mori, K., Tazawa, Y., & Takagi, S. F. (1983). Interneurons mediating fast postsynaptic inhibition in pyriform cortex of the rabbit. *Journal of Neurophysiology*, *50*(1), 89–101.

Shen, J. M., & Kriegstein, A. R. (1986). Turtle hippocampal cortex contains distinct cell types, burst-firing neurons, and an epileptogenic subfield. *Journal of Neurophysiology*, *56*(6), 1626–49. Retrieved from http://www.ncbi.nlm.nih.gov/pubmed/2433411

Shepherd, G. M. (2004). *The synaptic organization of the brain* (Vol. 3). Oxford University Press New York.

Shepherd, G. M. (2011). *Introduction to Synaptic Circuits*. doi:10.1093/acprof

Smith, L. M., Ebner, F. F., & Colonnier, M. (1980). The thalamocortical projection in Pseudemys turtles: a quantitative electron microscopic study. *The Journal of Comparative Neurology*, *190*(3), 445–61. doi:10.1002/cne.901900304

Stokes, C. C. A., & Isaacson, J. S. (2010). From Dendrite to Soma: Dynamic Routing of Inhibition by Complementary Interneuron Microcircuits in Olfactory Cortex. *Neuron*, *67*(3), 452–465. doi:10.1016/j.neuron.2010.06.029

Ulinski, P. S. (1983). *Dorsal ventricular ridge: a treatise on forebrain organization in reptiles and birds*. J. Wiley.

Wang, W., Campaigne, C., Ghosh, B. K., & Ulinski, P. S. (2005). Two cortical circuits control propagating waves in visual cortex. *Journal of Computational Neuroscience*, *19*(3), 263–89. doi:10.1007/s10827-005-2288-5

Chapter 2: Visual Response Properties

As we seek to understand cortical processing, we expect to gain important insights from the turtle dorsal cortex, which is known to share many features with the mammalian hippocampus and olfactory cortex and thought to share many geniculo-cortical features that were common to the stem amniotes from which mammals evolved. To this end, we have used data from extracellular recordings from microelectrode arrays, to study the temporal and spatial properties of responses to stimuli as seen in both the local field potential and in the activity of action potentials. We find large receptive fields, responsiveness to a broad range of stimuli, correlation between different areas in the cortex, response variability, adaptation to both ongoing and visually evoked activity, a range of response latencies, and stimulus specific responses.

2.1 Introduction

2.1.1 Evolution and the Ancestral Visual Cortex

It is difficult to understand the mammalian cortico-thalamic system without also understanding its evolutionary origins. The brains of reptiles are simpler than their mammalian counterpart (Butler & Hodos, 2005). Turtles are of particular interest for comparative studies because they probably bear the strongest resemblance to the Triassic cotylosaurs (stem amniotes) from which they and all modern mammals evolved (Romer, 1977).

2.1.2 Previous Work on Turtle Cortex

Though we haven't yet seen the multitude of studies on turtles as we've seen with other preparations such as rat, mouse, and cat, the turtle preparation is becoming more appreciated for allowing the experimenter to study cortical processing from the subcellular level to the level of neuronal networks simultaneously, as well as being tolerant enough to a wide range of flexible modifications to meet the needs of a range of experiments with different technical demands (Hounsgaard & Nicholson, 1990).

The turtle dorsal cortex is a convergent zone for the visual, auditory, somatic, and other sensory systems (V. I. Gusel'nikov, Morenkov, & Pivovarov, 1972), but has mostly been investigated with respect to visual processing. There have been a handful of studies on the turtle visual cortex. Some have looked at spikes in response to diffuse flashes (V. I. Gusel'nikov et al., 1972; Kriegstein, 1987; Mancilla, Fowler, & Ulinski, 1998), the size and organization of the receptive field of spiking cells (P. Z. Mazurskaya, 1972), spiking responses to moving black dots (V. Gusel'nikov & Pivovarov, 1977), and even voltage sensitive dye studies (J C Prechtl, Cohen, Pesaran, Mitra, & Kleinfeld, 1997), but there have only been a few studies in turtle focusing on the local field potential (Bass, Andry, & Northcutt, 1983; Luo, Lu, Lu, Yang, & Gao, 2010; J C Prechtl, Bullock, & Kleinfeld, 2000; J C Prechtl, 1994; J. C. Prechtl & Bullock, 1994). Here, we have used the local field potential as our primary signal for probing receptive fields and other response properties.

2.1.3 Thalamic Response Properties

We're ultimately interested in how the cortex processes visual information. The clues we have at our disposal to work on this problem are the recordings or cortical neural activity.

Knowing that the activity we see in the cortex is the product of both cortico-cortical dynamics and external sensory input , it would seem that we have a better chance of understanding the circuitry and processing the cortex if we also know what is done (and what isn't done) outside of the cortex.

For instance we know that the size of receptive fields in LGN (lateral geniculate nucleus, the main source of sensory input to the cortex) cells is restricted to 30 degrees (Boiko, 1980) and that there are thalamic axons connecting to the cortex with receptive fields as small as 2-5 degrees (P. Z. Mazurskaya, 1972). Therefore, if we find considerably larger receptive fields in the cortex, we can infer that they arise from cortico-cortical connections or the convergence of afferents from many LGN cells.

We also know that sensitivity to the direction of motion of moving stimuli has been reported in only 9% of units in turtle thalamus, and the significance of these results is questionable (Boiko, 1980). Whether or not direction sensitivity exists in the thalamus affects how we think about its occurrence in the cortex.

2.1.4 Intracortical Connectivity

While it is important to understand the thalamic inputs to the cortex, a majority of the inputs to cortical neurons actually come from other cells within the cortex. In fact, only ~10% of the inputs to cortical cells come from the thalamus, with the rest coming from within the cortex (Douglas & Martin, 2004).

The extent to which the receptive field of individual cells in the visual cortex depends on the connectivity with other cortical cells has been demonstrated by comparing the normal

receptive field of a cortical cell to its receptive after applying pharmacological blockers to different areas of the cortex (P. Z. Mazurskaya, 1972). That study found that after applying blockers to other areas of the cortex, there would be gaps in the large receptive field that previously weren't present. This suggest that, for that cell, its responsiveness to certain regions of the visual field depended on receiving signals from the blocked region of the cortex.

2.2 Methods

2.2.1 Ex Vivo Eye-Attached Whole Brain Preparation

All procedures were approved by Washington University's Animal Care and Use Committees and conform to the guidelines of the National Institutes of Health on the Care and Use of Laboratory Animals. Adult red-eared turtles (Trachemys scripta elegans, 150 – 200 g weight, 12-15 cm carapace length) were studied. Rapid decapitation was performed following anesthetization with Propofol (10mg/kg) (Ziolo & Bertelsen, 2009). We then removed the brain with the right eye attached and proceeded to hemisect the eye.

To access the ventricular surface of the left visual cortex, we cut off ~1mm of the left olfactory bulb, which provided a hole to start a rostral-caudal cut through the medial cortex. This cut continued from the olfactory bulb into the natural separation of the medial cortex from the septum (about 1/3 of the cortex) and continued further along the same line for ~1-2 mm into the caudal cortex. Finally, two cuts were made from the medial cortex edge towards the dorsal cortex. These two cuts were started at roughly 1/3 and 2/3 the rostral-caudal length of the cortex and were made as short as possible while still allowing the cortex to be unfolded and pinned flat. This length was usually ~2 mm.

After making the cuts in the cortex, it was placed in the recording chamber on either a Sylgard or agar surface, and insect pins were used to pin the cortex flat. Our electrodes were then placed in the flattened cortex.

The eye and brain were continuously perfused with artificial cerebrospinal fluid (in mM; 85 NaCl, 2 KCl, 2 MgCl2, 45 Na HCO3, 20 D glucose, and 3 CaCl2 bubbled with 95% O2 and 5% CO2), adjusted to pH 7.4 at room temperature. To perfuse the eye without obstructing the image we project onto the retina, a small wick was made from a Kimwipe. The wick connected an ACSF feed located ~1 cm above and to the side of the eye to the inside edge of the hemisected eye. If any brain tissue were large enough to extend above the surface of the ACSF (e.g., the right cortex or the optic tecta), it would be cover with a small piece of Kimwipe so that it would also stay in contact with ACSF. Recordings began 2-3 hours after anesthetization.

2.2.2 Data Acquisition

Microelectrode Array Recordings

Data were collected at a 30 kHz sampling rate using the Cerebus data acquisition system by Blackrock Microsystems. Two different styles of microelectrode arrays were used for our recordings. For some recordings, we used a 96-channel Utah array (10x10 square grid, 400 µm inter-electrode spacing, 500 µm electrode length, no corner electrodes, Blackrock Microsystems). For others, we used an array of shank electrodes (4x4 array of shank electrodes with 8 recording sites on each electrode, 300 µm and 400 µm x and y distance between shanks and 100 µm between recording sites along a shank, Neuronexus). We attached either array to a post fastened to a micromanipulator (Sutter, MP-285). The Utah array was inserted the array to a depth of 250-500 µm starting from the ventricular side of the unfolded cortex such that the plane

of electrodes was parallel to the dorsal surface of cortex. The array of shank electrodes was inserted deep enough to span the entire depth of the cortex.

We recorded wideband (0.7 Hz – 15 kHz) extracellular voltages relative to a silver chloride pellet electrode in the tissue bath.

Single Electrode and Tetrode Recordings

For our experiments using single electrodes we used tungsten electrodes (500 kOhm part # WE30030.5H5 from MicroProbes and 1000 kOhm catalog # 573520 from AM Systems). For some experiments, we also used homemade tetrodes with resistances between 250 kOhms and 350 kOhms. These were made by twisting four 12.7 micron nickel chromium wires together, applying heat with a heat gun (Weller 6966C) and cutting the twisted wires at an angle to expose the ends for recording (Saha, Leong, Katta, & Raman, 2013). Recordings were taken in reference to a silver chloride ground wire sitting in the bath.

The signals from these electrodes were recorded with an AM Systems Model 1800 amplifier connected to a National Instruments PCI-6024E 12-bit DAQ board through a National Instruments BNC-2090. The data were collected at 20 kHz using Labview.

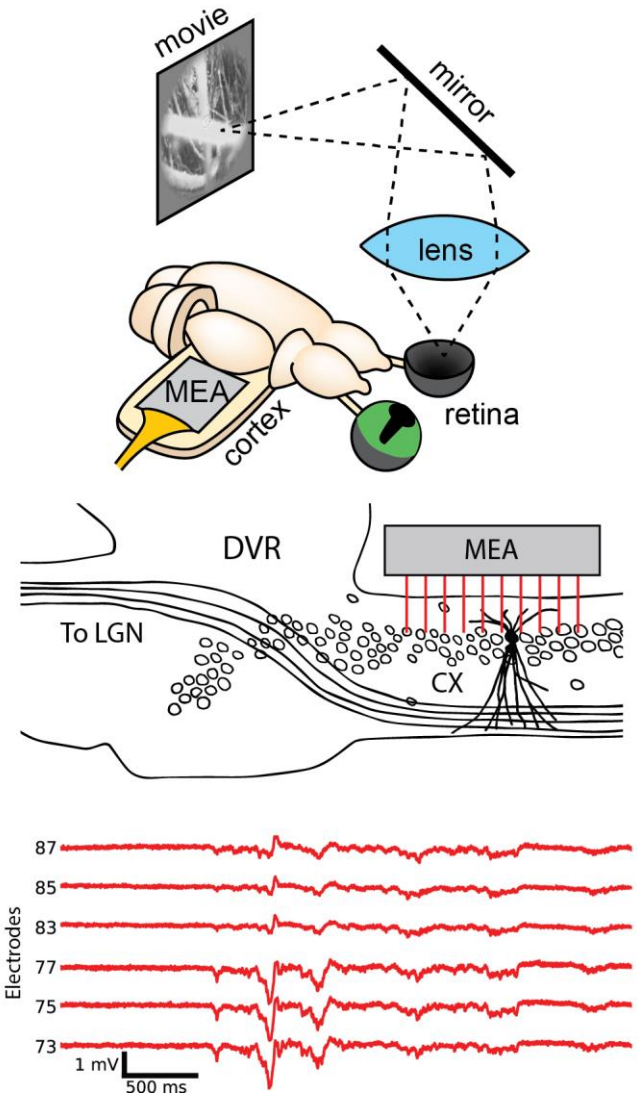

Figure 2.1 Experimental setup and raw data. **(A)** Our experimental set up for experiments done with a monitor and mirror. The visual stimuli are presented on a monitor. The image reflects off a mirror and through a lens to form a picture on the retina of the turtle's hemisected eye. The multielectrode array is placed in the unfolded cortex. **(B)** A side view of the cortex showing LGN axons passing through and then below the cellular layer of the cortex. The dentrites of one pyramidal cell are included to show the spatial extent of the dentritic arbors. In red are the electrodes from the MEA. **(C)** Six simultaneous raw extracellular voltage recordings from nearby electrodes recording responses to visual stimulation.

2.2.3 Visual Stimulation

For the included studies, three methods of visual stimulation were used.

LED Stimulation

For LED stimulation, a red LED was connected to the output of a National Instruments BNC-2090 terminal block connected to a National Instruments PCI-6024E DAQ board. This output was controlled with a custom LabView program on a computer running Windows 7. The mean light intensity at the retina was $60\ mW/m^2$.

Monitor/Mirror Stimulation

For monitor/mirror stimulation, a 19" LCD monitor (Samsung model Syncmaster T190, 1440x900 pixels, contrast ratio = 20000:1, response time = 2 ms) displayed the stimuli. This image was reflected off a mirror located across room above the tissue, and focused on the retina with a lens placed above the tissue. The mean light intensity at the retina from the monitor was $20\ mW/m^2$.

Projector Stimulation

For projector stimulation, a small projector was placed above the retina and focused with a system of lenses (Aaxa Technologies, P4X Pico Projector, 1440x900 pixels). The mean light intensity at the retina from the projector was $1\ W/m^2$

Both monitor/mirror and projector stimulation was provided using software written in python on a computer running Ubuntu 10.4. Visual stimuli included black dots moving on a white screen (Figure 2.2), naturalistic video, and red LED flashes.

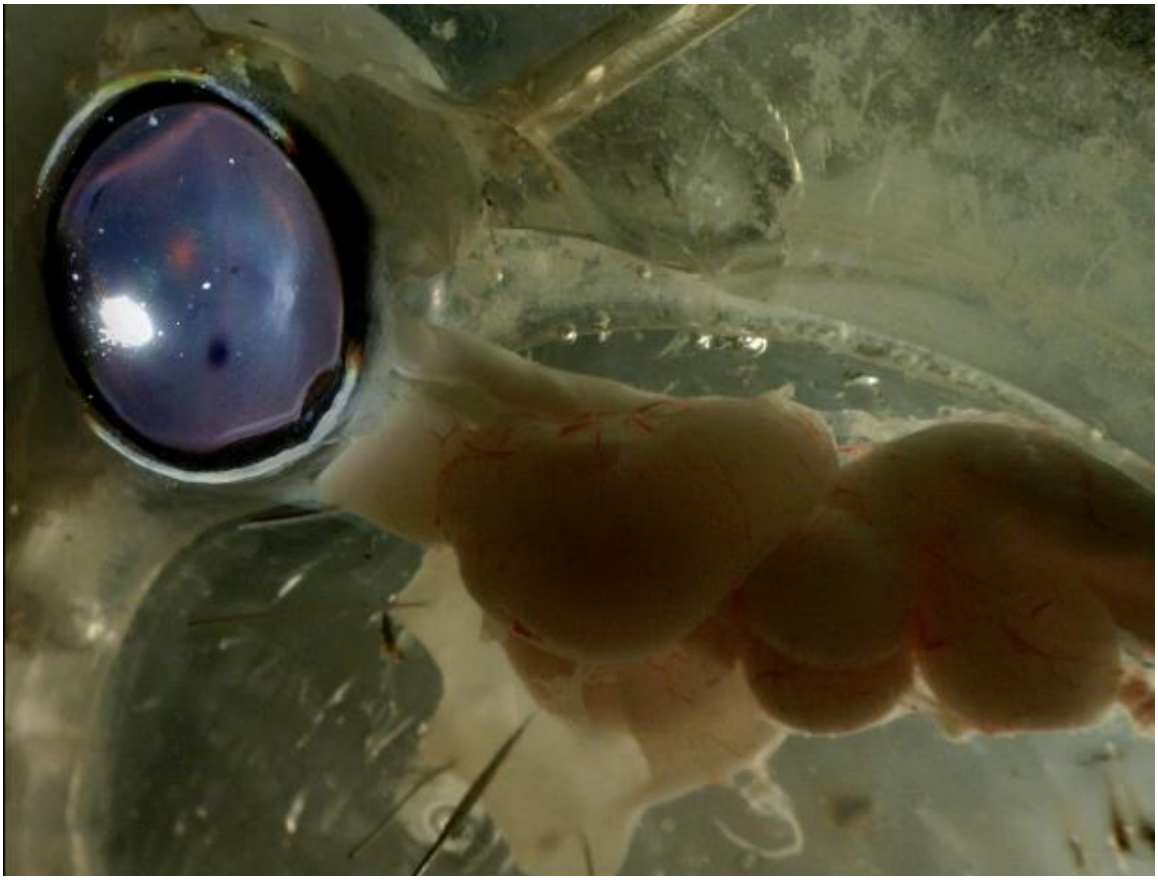

Figure 2.2 Turtle brain with electrode and stimulus. The dark spot in the hemisected eye is a black moving dot presented by the projector. An electrode is shown in the cortex near the DVR. For the sake of illustrating more clearly, this image is a composite of a well-lit picture and a snapshot from a video. During normal recordings the additional light needed to take the picture and the camera were not used.

2.2.4 Filtering for Local Field Potentials

To study LFPs, it is useful to filter out other frequencies. For our LFP analysis, we used the PyWavelets package to perform wavelet filtering (Wiltschko, Gage, & Berke, 2008). We used Daubechies wavelets with minimum level of 9 and a maximum level of 11. For our 30 kHz data, this corresponds to a pass band of ~7 Hz - 59 Hz.

2.2.5 Defining an LFP Event

There are many ways one can quantify the size of an LFP response. One method we use throughout this paper is to look for threshold crossings of the extracellular signal after filtering it (as described above) to the frequencies we're interested in. As a threshold for LFP events we used 3 standard deviations of the filtered signal. Therefore, when we refer to LFP event count, we are simply referring to a number of threshold crossings.

2.2.6 Determining Visually Responsive Electrodes

When recording from the 96 electrodes of the MEA, only a subset of electrodes would actually have a strong visual response. In order to get clean results it was necessary to do our analysis on only that subset of electrodes.

To consistently and systematically determine which electrodes to include, we created an algorithm to test for visual responsiveness. Roughly speaking, an electrode was considered visually responsive if the typical level of activity following visual stimulation was sufficiently greater that spontaneous ongoing level activity. Specifically, to accomplish this, we first chose some quantifiable measure of activity. Usually, this was the number of LFP events as defined above.

We then established the spontaneous ongoing level of activity, $a_{ongoing}$, by taking the average activity from 4 s windows immediately preceding the presentation of 12 stimuli. Similarly, the amount of visually evoked activity, a_{evoked}, was the average of the 4 s windows immediately following the onset of the 12 presented visual stimuli. We then calculate the decrease in activity (how much lower is the ongoing activity level than the evoked activity level)

as $d = \frac{a_{evoked} - a_{ongoing}}{a_{evoked}}$. Finally, we classify an electrode as visually responsive if the decrease in activity is greater than 0.75 (Figure 2.3).

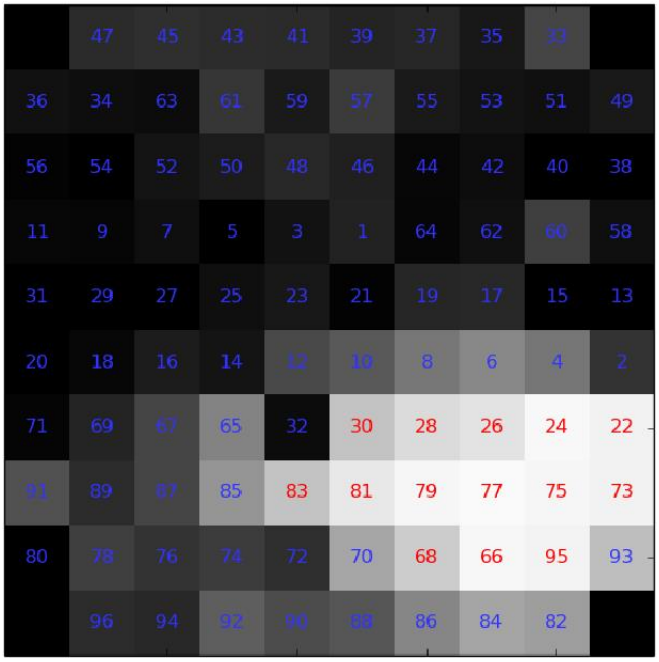

Figure 2.3 Visual responsiveness across the electrode array for Turtle 31. Each square represents an electrode. The background color for each square indicates the visual responsiveness with black being 0 and white being 1. The electrodes labeled in red have a visual responsiveness above the 0.75 threshold to be included in analyses, and the electrodes labeled in blue had subthreshold responsiveness.

2.2.7 Filtering for and Detecting Spikes

Filtering for spikes used the same wavelet filtering technique that was used for LFP, but with different parameters (Table 2.1).

Table 2.1 Filter and Threshold Settings for Spike Detection

Analysis	Min level	Max Frequency (Hz)	Max level	Min Frequency (Hz)	Threshold
Spike Latencies (Fig. 2.6)	3	3,750	7	117	-10 STD
T75 RF similarity (Fig. 2.17)	4	1,875	7	117	-100 μV
T7 Rastergrams (Fig. 2.16)	3	3,750	7	117	-60 μV

2.3 Temporal properties

2.3.1 Typical Durations of LFP Oscillations

LFP activity often presents as a transient oscillation (Figure 2.4). These oscillations are seen in both spontaneous and visually evoked activity. While at times these oscillations can be clearly dominated by one or two frequencies, at other times, the transient increases in LFP activity are made up of fluctuations covering a broad range of frequencies. Though the distributions of the durations of LFP oscillations can vary from electrode to electrode, peaks in these distributions are often found near 1 sec (see Chapter 3 for further details).

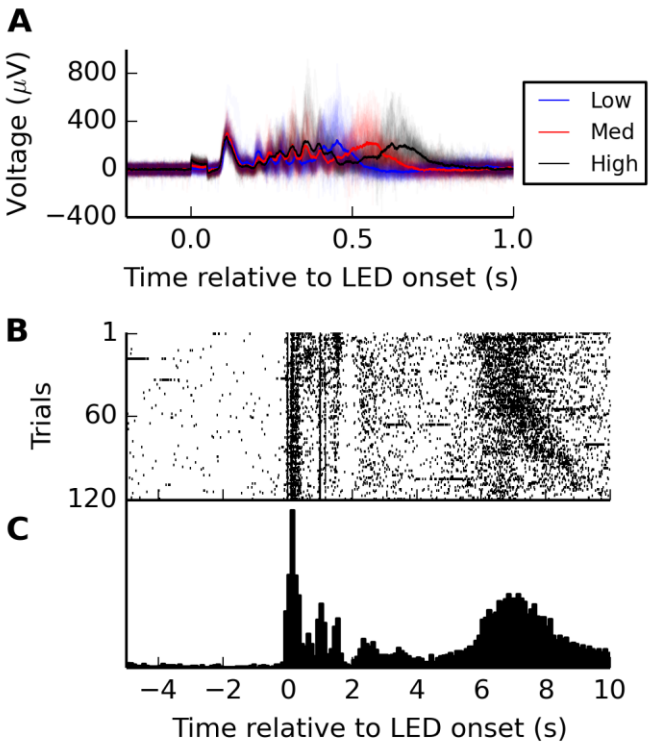

Figure 2.4 Temporal properties of visually evoked LFPs. **(A)** Individual LFP responses (thin, transparent traces, 60 trials per LED intensity, turtle 29, electrode 66) to 50 ms LED flashes of three different intensities with the average responses shown in bold. **(B)** Rastergram of LFP events after a 1 sec LED flash (turtle 2, electrode 65). **(C)** The peristimulus time histogram corresponding to the rastergram in (B).

2.3.2 Persistent Activity

When looking at visually evoked LFP activity, we typically see responses that last 500 - 2000 ms. In addition to this typical response, in many instances, we also see a second (or even third) period of activity after periods of relative inactivity. Often a period of increased activity occurs ~1 second after stimulus offset. We also see a reliably reproducible wave of activity up to 15 s after the presentation of a stimulus (Figure 2.5).

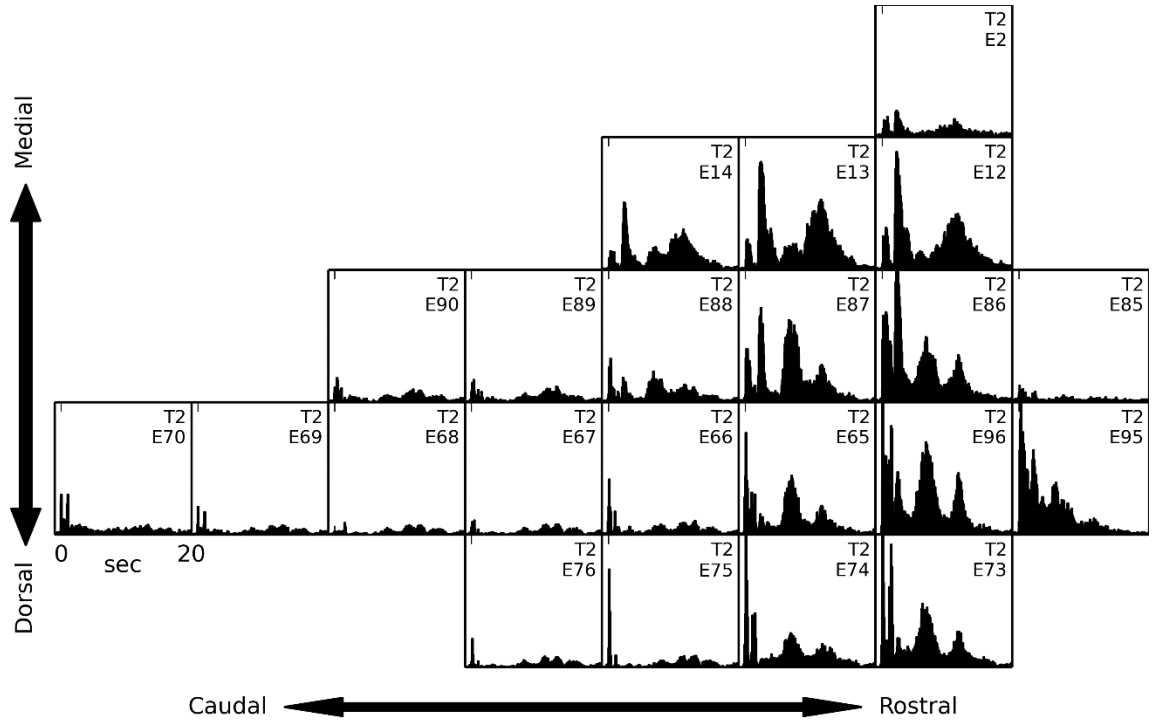

Figure 2.5 Turtle 2 peristimulus time histograms. PSTHs for several electrodes arranged as they were in the cortex showing LFP event in response to a brief LED flash (bin size = 50 ms, number of trials = 90).

2.3.3 Responses to Diffuse Flashes

Red LEDs were used to provide precisely timed diffuse stimulation of the entire retina. Responses to LED flashes were clearly dependent on flash intensity. One striking feature of the responses to LED flashes is that the evoked oscillations are phase coherent across trials revealing low frequency oscillations in the average response (Figure 2.4). It should be noted that most turtles did not have such a clearly dominant frequency in the average LED response (Supplementary Information 8, and that even when a turtle has this feature for some electrodes, it won't show up on all visually responsive electrodes (Figure 2.14).

When comparing responses to different intensities, we consistently found that, while all intensities had the same latency to response onset and were otherwise similar in their early response characteristics, the further into the response time course you go, the more distinct the responses to the different intensities are from one another. The clearest aspect of this is the overall duration of the responses. Higher LED intensities led to longer response durations.

2.3.4 Latency of Response

Many of our results involve relating the activity recorded in the cortex with stimuli presented to the retina. One important aspect of this relationship is how much delay there is between the presentation of the stimuli and the response caused by signal propagation time in the pathway leading to the cortical response. The is an interesting question in its own right, but also an important piece of information when it comes to interpreting the responses to stimuli that can't be characterized as occurring at only one instance in time.

We investigated the latency between stimulus presentation and an evoked response. When looking at the receptive fields determined by responses to moving dot stimuli, we tend to see the maximal convergence of the receptive field when applying a delay between response and stimulus of ~250-350 ms. That is to say that if we for each neural event detected, we attributed the region of visual field in which the dot was 250-350 ms prior, we saw the most overlap of the contributions to the visual field from dots moving at different angles (Supplementary Information 1). This is true for both spiking responses and LFP responses. As such, for all figures showing the receptive field as probed by moving dots, a 300 ms delay has been applied.

In addition to looking for the delay that provided the most convergence of the receptive field, we also looked at the latency to the first spike in response to stimuli with a precise ON time

covering the entire visual field. Though others have reported first spike latencies in visual cortex between 80 ms and 200 ms (P. Mazurskaya, 1973) and even as short as 25 – 150 ms (Bass et al., 1983), and latency to LFP response onset of 86 ± 4 ms (J. C. Prechtl & Bullock, 1994), we found, when looking at responses to a full screen flash or to the change from a blank screen to the start of a complex movie, a typical latency to first spike is around 200-500 ms (Figure 2.6). These results lend further support to the 300 ms delay we used for the moving dot receptive fields.

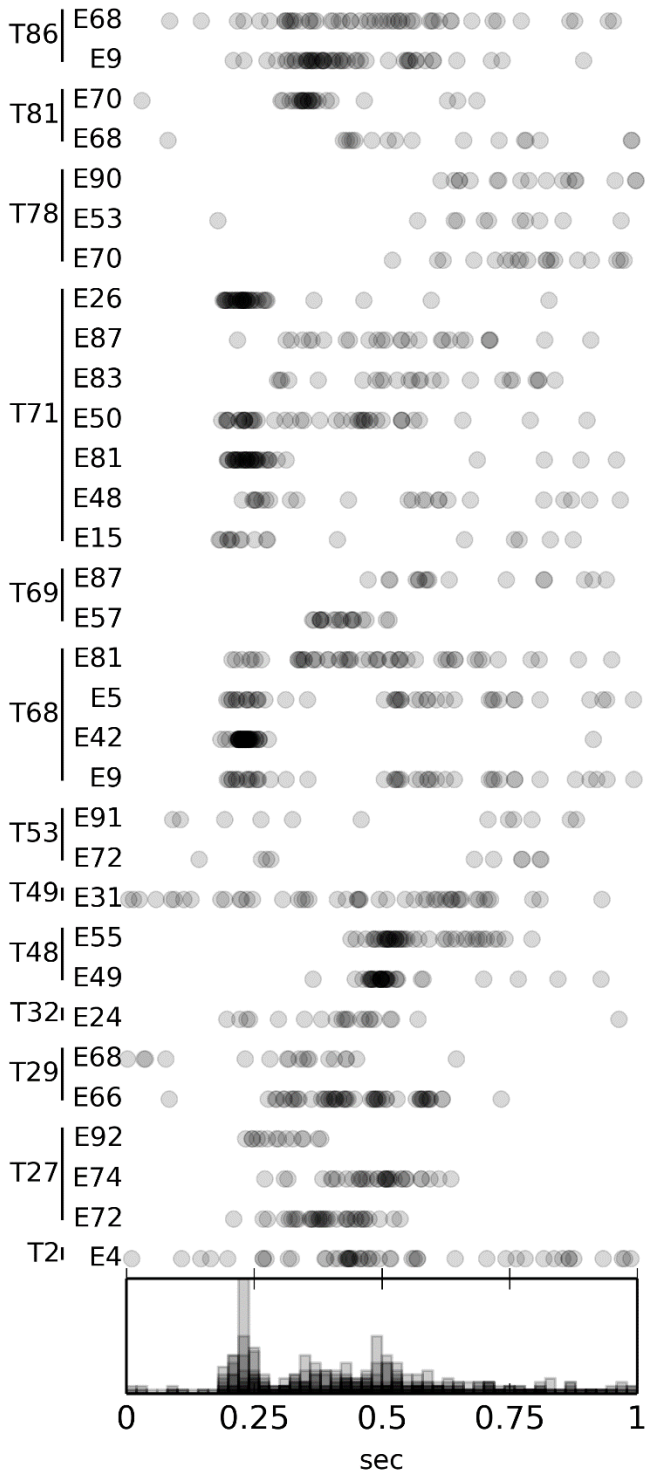

Figure 2.6 First spike latencies. **(Top)** The timing of the first spikes following either the onset of a red LED flash (turtles 2 -32) or the transition from a blank screen to the beginning of a complex movie (turtles 48-86). **(Bottom)** Summary histogram of all data.

2.4 Spatiotemporal properties

To probe the LFP receptive field we used black dots moving across a white background (8 degrees diameter dot moving at 40 deg/sec). Dots were tested with a range of angles of motion, and for each angle, dots were tested moving across several straight paths spanning the visual field.

2.4.1 Receptive Field Size

The receptive fields of both the LFP and individual cells in the visual cortex at times seem to span large areas of the visual field. It is common to see receptive fields that cover over half of the visual field. Our method of visualizing this is demonstrated in Figure 2.7 with further examples in Figure 2.8.

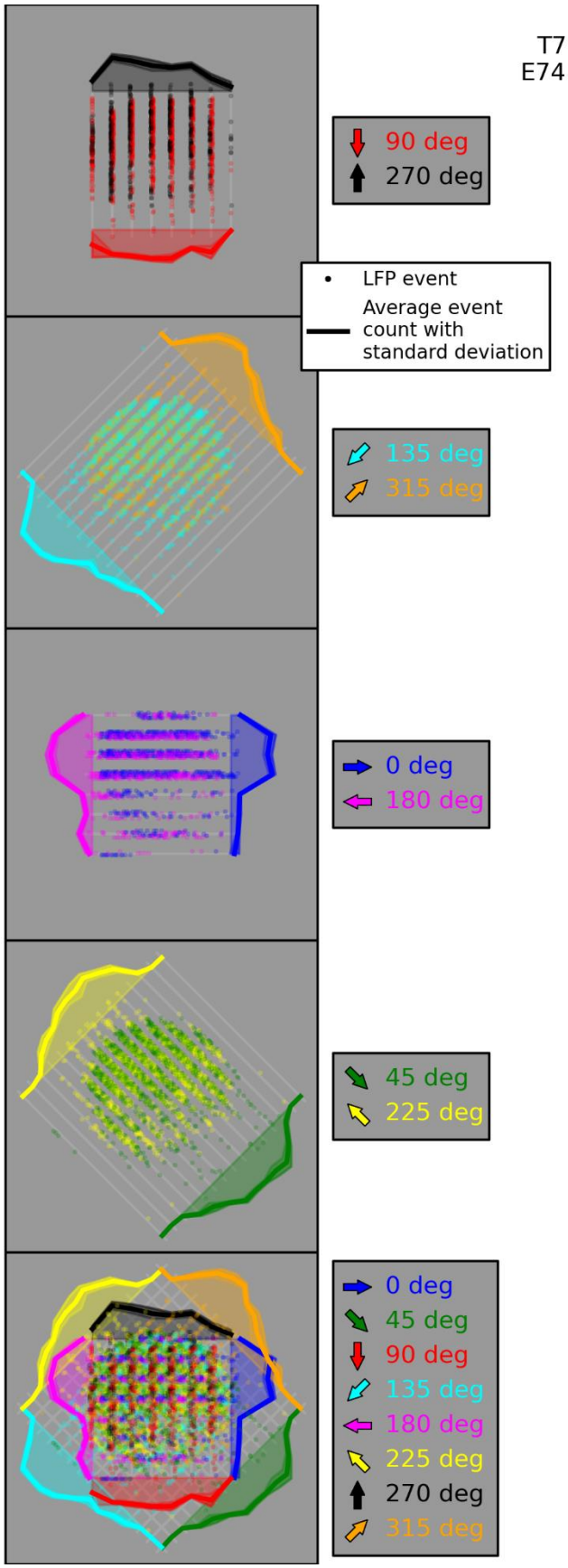

Figure 2.7 The LFP receptive field probed with moving dots. Each grey square represents the visual field. The paths that black dots moved along are represented by light grey lines. Dots indicate the location of a moving dot 300 ms before an LFP event was recorded. Dots are color coded according to the direction in which the dot was moving. To assist in visualizing trial-to-trial variability, the dots are plotted somewhat offset from the actual path traveled (a different amount for each trial). The solid lines show the average LFP event count for each path (averaged over multiple trials) with the standard deviation shown as the filled region around the average line. The top plot shows only the data for presentations of a dot moving 90 degrees or 270 degrees (with respect to the turtle's visual streak). The following three figures show the other three pairs of angles on their own, and the bottom figure shows all eight angles together.

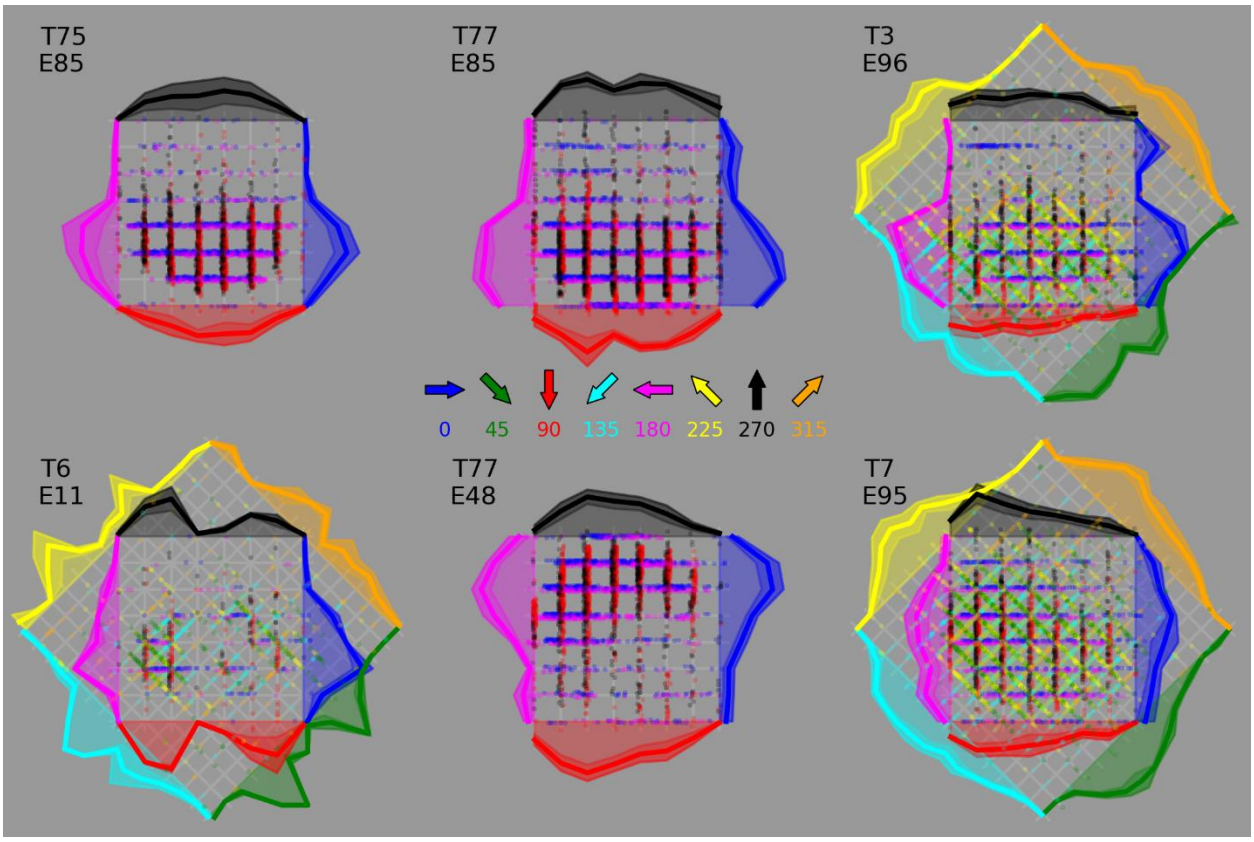

Figure 2.8 Six examples of LFP receptive fields probed with moving dots. Responses to black dots moving on a white screen from the LFP of single electrodes from 5 different turtles (the two center figures are different electrodes from the same turtle).

When we consider this in light of the small RFs in the LGN (P. Z. Mazurskaya, 1972), we come up with a few possible explanations. It could be that an individual cortical cell has a large RF because it receives input from many LGN cells whose RFs collectively span a large area of the visual field, but these seems unlikely given the proposed projections from LGN to cortex (Mulligan & Ulinski, 1990). Therefore, what seems more likely is that the large cortical RFs may be the result of individual cortical cells receiving input from many other cortical cells that each receive LGN input representing only a small portion of the visual field.

2.4.2 Direction Sensitivity

We found no examples of a cell or LFP being visually responsive to dots moving in only one direction.

By looking at the average LFP event counts for opposite angles in Figures 2.7 and 2.8, we can get a sense of whether a recording site shows sensitivity to one direction compared to the opposite direction. Overwhelmingly, we find that the average response curves to opposite directions are nearly mirror images of each other. This indicates that there is no opposite angle direction sensitivity in the LFP response (when quantifying the LFP response as the number of threshold crossing of the LFP).

2.5 Adaptation

The effects of adaptation in turtle visual cortex are clear, long lasting, and ubiquitous. Some studies described recovery times in visual cortex ranging from 0.5 min to 3 min (V. I. Gusel'nikov et al., 1972). Others showed nearly complete recovery in 16 sec (Luo et al., 2010).

An adapted response in the visual cortex can be the result of two different sources: the cortex may be adapting in such a way that it has a diminished response (relative to the unadapted state) to the same cortical input; or adaptation has taken place at an earlier stage in the visual pathway and the cortex is responding in a consistent way as before adaptation, but to a diminished cortical input. It is almost certainly the case that both of these effects contribute to the adaptation observed in the cortex.

2.5.1 Visual-Visual Adaptation

To test the effect of one stimulus on another we used moving dots, radially moving bars, and full field flashes. In the clearest demonstration of adaptation, when we presented a series of brief LED flashes to the retina, we reliably recorded a strong LFP response to the first flash, and either no response or a greatly diminished response to the subsequent flashes (Figure 2.9A). The extent to which the subsequent responses were diminished depended on the time in between flashes. Consistent with Luo 2010, this dependence was not all-or-none (Luo et al., 2010); in between the short inter-flash-intervals that completely abolished subsequent responses and the long inter-flash-intervals that seemed not to affect subsequent responses, there were intermediate inter-flash-intervals that resulted in somewhat diminished subsequent responses.

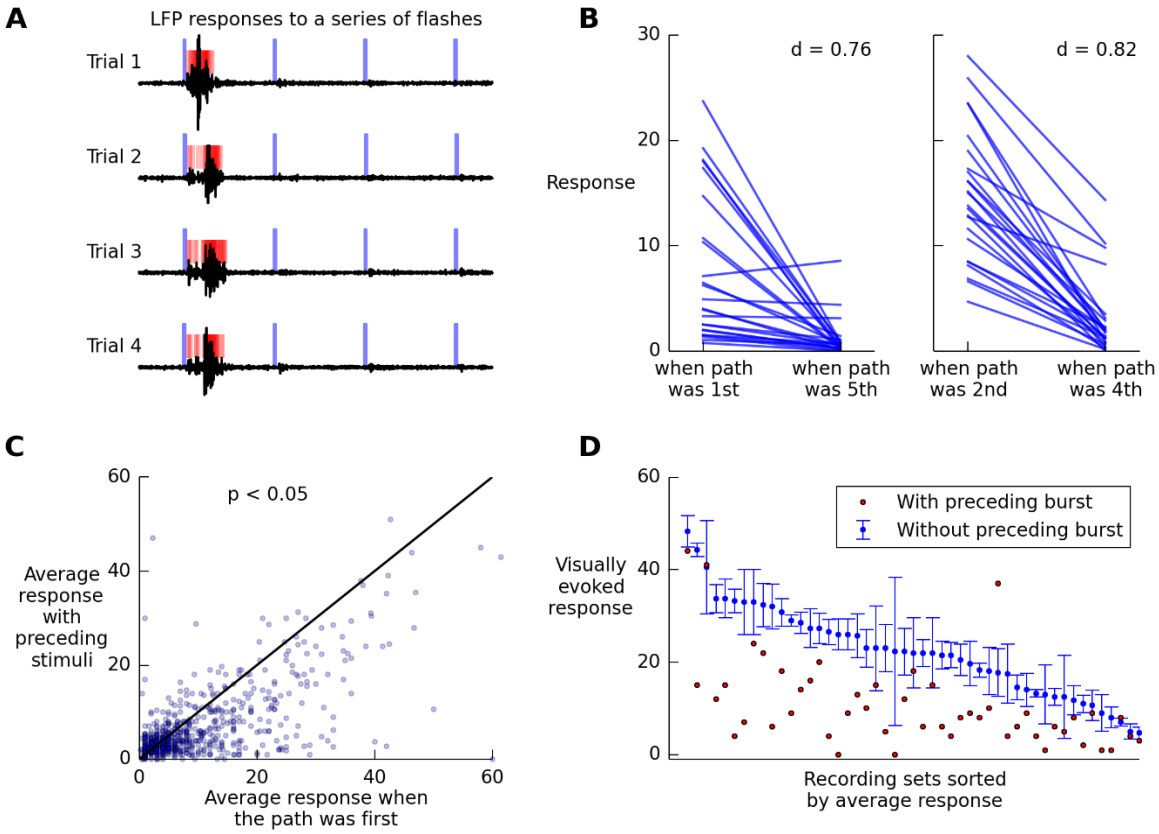

Figure 2.9: Adaptation to evoked and ongoing activity. **(A)** LFP responses to four repeated presentations of a series of four brief full field flashes (flash timing indicated by blue vertical bars). LFP threshold crossings are indicated by red rasters. **(B)** The responses to dots moving along 48 paths across (data coming from 3 turtles). For each path the response strengths when the path was an early stimulus in the series of stimuli (i.e., either the first or second path to be traveled) is compared against the response strengths when the same path was traveled later in the series of stimuli (i.e., either the fourth or fifth path to be traveled in the series of stimuli). Each point plotted is the average of 7-30 trials. The average decrease in response strength d is shown for both subplots. **(C)** The p-value is calculated for the hypothesis that the response when a path is presented first will be larger than when a path is presented after other stimuli (vs the null hypothesis that either response is equally likely to be the larger response). **(D)** Response strengths with and without preceding spontaneous activity. We show visual responses from several different stimuli. Red dots indicate individual responses to visual stimuli that were preceded by a strong burst of spontaneous activity within 5 s before the stimulus. For each of those recordings, the average response of the 2-4 trials of the same stimulus nearest in time to the recording that was preceded by a burst is shown in blue with error bars showing the standard deviation. These 2-4 reference recordings were selected from recordings that were not preceded by a spontaneous burst of activity. Each recording preceded by a spontaneous burst together with the 2-4 reference recordings are collectively referred to as a recording set.

We further demonstrated the effects of adaptation with more complex stimuli containing more spatial and temporal structure. To compare the effects of the order of presentation of stimuli for multiple stimuli, we used dots moving along different paths through the visual field. For 8 different angles, we moved dots across 5 paths in the visual field in an ordered sequence. For opposite angles, the paths overlapped but were in reversed order such that the path that was presented first at an angle of 0 degrees was presented last at 180 degrees. This allowed us to compare the response to presentation order while controlling for the area of the visual field being stimulated.

To quantify the effects of adaptation due to stimulus presentation order, we defined the decrease in response d as simply the average of the decreases for individual paths, where the decrease for an individual path was $1 - \frac{r_{late}}{r_{early}}$ where r_{late} is the strength of the response when the path was presented late in the series (either the fifth or fourth path to be presented), and r_{early} is the strength of the response when the path was presented early in the series (either first or second 1).

When we look at the response amplitude when a path was presented first compared to the same path being presented fifth (or second compared to fourth), we clearly see adaptation of responses to stimulation of one area of the visual field caused by previous stimulation of other areas of the visual field (Figure 2.9B).

On average, when a path was the fifth path to be traveled, the evoked response was 76% smaller than when it was the first path traveled. Similarly, when a path was the fourth path traveled, the evoked response was 81% smaller than when it was the second path traveled. The fact that the decrease in response strength was larger and more reliable for the second-fourth

pairs than it was for the first-fifth pairs is most likely due to complications near the edge of the visual field. The first/fifth paths were always on the very edge of the visual field. Consequently, the dots moving along those paths were not present on the retina nearly so long as dots moving across paths crossing a larger portion of the retina. In general, these outer paths evoked smaller responses than more interior paths. As such, these weaker responses may be more confounded by noise.

In a different set of experiments, adaptation to visual stimuli was studied while controlling for not only same path in the visual field, but also the direction of motion along that path. In contrast to the previous data set, in this data set the order in which the paths were traversed was randomized for each trial. Thus, a given path may have been the first path presented during one trial, but the fourth path presented during the next. This allowed us to separate the responses to a dot moving along any given path into trials for which the path was the first path to be presented and trials for which the path was not the first path presented. Using the same LFP threshold crossing described earlier, for each path, we calculated two average responses: the average first-presented response and the average nonfirst-presented response. For this data set, there were 10 seconds between dots moving on each path and either 118 s or 214 s between sets of paths for one angle and the next being stimulated. It is after that 118 s or 214 s, when we start paths for a new angle that we have a new first path. In Figure 2.9C the average response when a path was first is plotted against the average response to that same path when the path was not first. Because there were very few trials for any given angle-path combination, the results are somewhat scattered. But, when taken as a whole, for the 575 responsive points shown, we get a p-value of 1.7×10^{-20} for the claim that the average first path response should be greater than nonfirst path responses.

Visual stimulation with bars moving across the visual field also showed that the response to the bar presented first elicited a much greater response than any of the subsequent bars (Supplementary Information 9).

2.5.2 Ongoing-Visual Adaptation

While the preceding figures clearly demonstrate an adapted response to visual stimuli, they don't shed any light on the source of adaptation. It isn't clear if the adaptation is taking place in the cortex, at an earlier stage in the visual pathway, or (most likely) some combination of both effects. To better understand adaptation happening within the cortex, we looked at how visual responses adapted to spontaneous activity within the cortex (Figure 2.9D). Here we looked at repeated trials of a given stimulus and picked out the trials the had a large burst of LFP events (defined in methods) within the 5 seconds leading up to the stimulus presentation. We then plotted the subsequent visual response (red dots) along with the average response to 4 presentations of the same stimuli that did not have a large spontaneous burst preceding them (blue dots). To avoid having our results confounded by experimental rundown, we selected the 4 trials that occurred most closely in time to the trial which was preceded by spontaneous activity. From this figure, it is clear that spontaneous activity in the cortex can lead to a significant and reliable adaptation of subsequent visual responses.

2.6 Response Variability

We see large variability in the responses to repeated presentations of stimuli. This variability manifests in different ways. At times the strength of the response varies. At other times the response may be completely absent. Still at other times, there can be a response that is

varies not so much in its strength, but in its temporal or spectral properties (See Chapter 3 for variability in spectral properties).

2.6.1 All or None Response Variability

Figure 2.10 shows responses to moving dots. There seem to be two different visual responses (to dots moving along the 3rd and 4th paths). If we focus on the responses to the 3rd path, we see that of the 16 trials, there are only responses in 5 or 6 of them (first of those 'responses' is likely spontaneous activity, since it starts slightly before the stimulus).

On the other trials, there are no visible LFP oscillations. Two of the nonresponding trials might have been affected by adaptation from the bursts of activity preceding the stimulus (see Section 2.5 Adaptation), but that still leaves 8 nonresponsive trials. Similarly, the nonresponsive trials for the 4th path are likely due to the responses to the 3rd path that occurred just before the 4th path.

Interestingly, this all-or-none response variability was not seen for dots moving in the opposite direction along the same paths in a set of recordings taken over the same period of time (Supplementary Information 6).

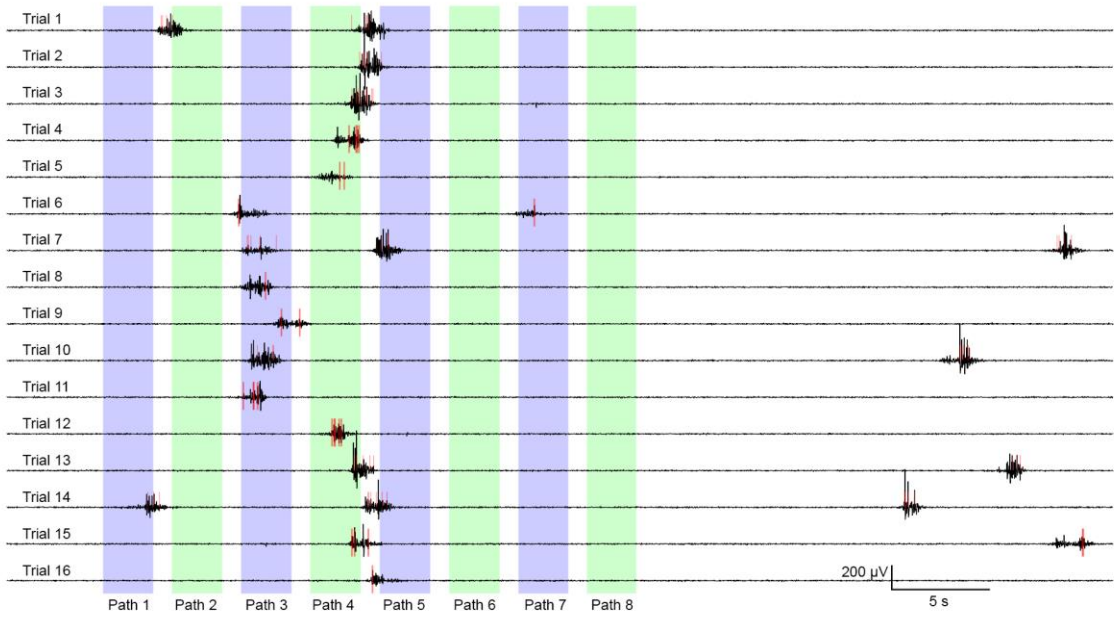

Figure 2.10 Response variability. LFP signal (black) with action potentials (red rasters) during 16 presentations (each row is a separate presentation) of 8 dots moving across the visual field following 8 different paths. The 8 colored columns indicate the timing of the 8 dots moving across the visual field.

2.6.2 Variability in Temporal Structure of Response

In Figure 2.9A we see four presentations of a series of flashes. All four trials elicit a strong response, but trial 1's response is markedly different from the other three. In trial 1 there is a large main oscillation that starts shortly after the flash. In contrast, for the other three trials, there is a small response right after the flash and then a larger main oscillation starts a bit later.

We also see variability in the temporal structure of the response in Figure 2.10. Not only do responses to both the 3rd and the 4th path have substantial differences in the time to response onset (sometimes varying by as much as a second), but they also vary in how that response plays out. For some trials (e.g., trials 1-3) we see roughly one large oscillation, and for others (e.g., trial 4) it looks more like a series of two smaller bursts.

2.6.3 Variability in Response Strength

Finally, Figure 2.10 also contains examples of response strength variability. If we compare the responses to the 3rd path in the 7th and 8th trial, we find markedly different amplitudes of response.

2.6.4 Discussion of Variability

This has also been seen in cat visual cortex in voltage sensitive dye recordings, in which much of the trial-to-trial variability could actually be explained by the ongoing activity in the cortex (Arieli, Sterkin, Grinvald, & Aertsen, 1996). That is to say that after subtracting the activity of the cortex immediately preceding the response, the variability of the responses were greatly reduced. More generally, it has been suggested that sensory responses should be thought of as not simply the product of a sensory input and some "default" anatomical connectivity, but instead the product of those along with learned expectations and environmental contingencies that can change continuously (Fontanini & Katz, 2008).

2.7 Response Similarity across the Cortex

When looking at the LFP receptive fields plotted for each electrode across the cortex, it appears that the RFs of nearby electrodes are more similar to each other than those of distant electrodes (Figure 2.11 and Supplementary Information 5 for an additional example).

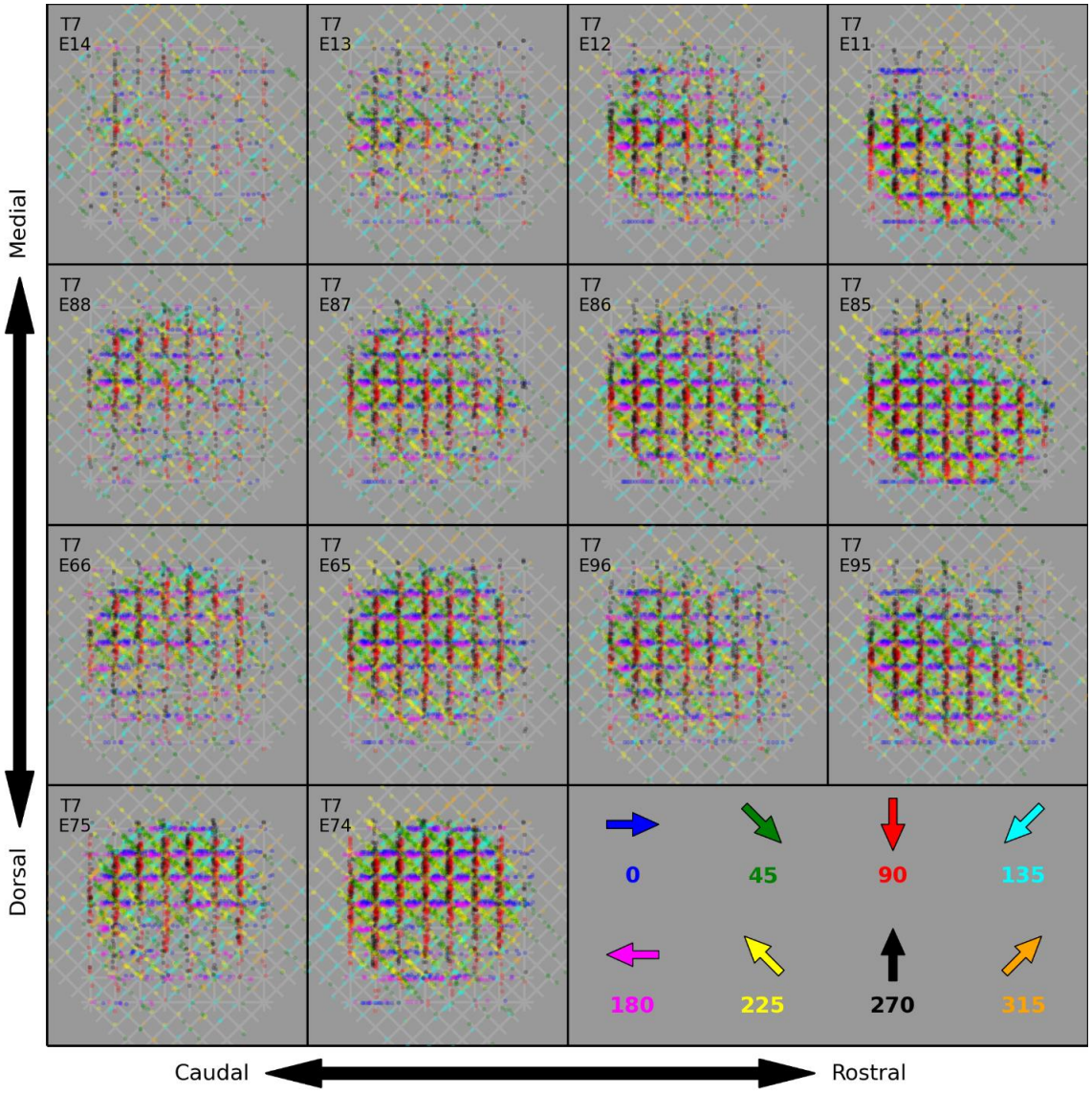

Figure 2.11 LFP receptive fields across the microelectrode array. The LFP receptive field as probed by moving dots is plotted for 14 visually responsive electrodes arranged as they are across the MEA (recorded from turtle 7).

It is important to consider whether these similarities are due to the LFP recording volume being large enough that neighboring electrodes are essentially measuring the same signal. In other words, when we see similar LFP signals on two electrodes, are we looking at two pictures of the same thing taken from slightly different angles, or are we looking at two pictures of different things that happen to be similar?

While there have been some recent claims that the spatial extent of the LFP can be as large as several millimeters (Kajikawa & Schroeder, 2011), it has usually been thought that the local field potential represents neural activity within roughly 150-400 μm of the electrode (Katzner et al., 2009; Dajun Xing, Yeh, & Shapley, 2009). The fact that we occasionally see bursts in narrow frequency bands on one electrode but not on the adjacent electrode is consistent with a smaller spatial extent for the LFP (Supplementary Information 7). This suggests that the similar receptive fields recorded at different electrodes (spaced 400 μm apart) are not merely measurements of the same signal generated by common sources, but are instead measurements of activity generated by different sources that happen to produce similar signals.

2.7.1 Defining Receptive Field Similarity

Beyond simply noticing that the LFP receptive fields of nearby electrodes seem similar, it is useful to quantify that similarity. To do so we calculated the amount of overlap between the RFs from pairs of electrodes. Specifically, we binned the dots paths in visual field (bin size = 8 visual degrees), calculated the normalized average LFP response to stimulation in each of those bins, and, for each electrode pair, we calculated the RF overlap (also called similarity) by summing the smaller of the two normalized response values (one for each electrode) over all bins.

The normalization of the average LFP response in each bin, was done by dividing the average response by the sum of the average responses over all bins (or, in the case of direction specific RF similarity, by dividing by the sum of the average responses over only the bins for the angle of interest). Consequently, the sum of the normalized responses over all bins was always one, the minimum similarity between two electrodes was zero, and the maximum was one.

2.7.2 Establishing Significance of Similarity

To quantify the significance of similarity between two electrodes, we recalculated the similarity between the two electrodes after shuffling the binned responses of one of the electrodes. This process was done 1,000 times. We then call the original similarity significant if it is higher than 95% of the shuffled similarities (Figure 2.12).

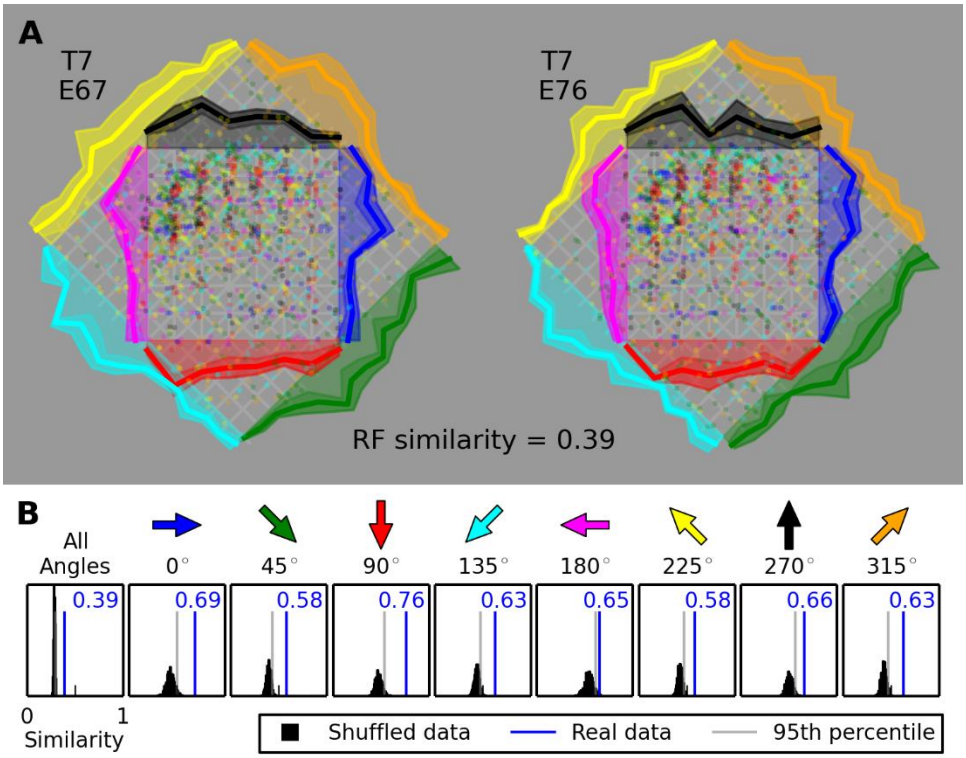

Figure 2.12 LFP receptive field similarity. **(A)** The LFP receptive fields for two electrodes from turtle 7 as plotted in Figure 2.7. **(B)** The similarity between the two receptive fields when the responses to dots moving at all angles are considered together, along with when we consider only the responses to dots moving at a specific angle. The black distributions are for 1,000 similarities calculated using shuffled data. The blue lines and numbers show the similarity of the real data for the two receptive fields, and the light grey line shows the similarity below which 95% of the shuffled similarities lie.

2.7.3 Receptive Field Similarity Results

For the four turtles that had several electrodes in visually responsive areas, we can look at RF similarity versus distance in more detail. To get a better picture of RF similarity, we plotted the similarity versus distance for a single electrode paired with all other electrodes. Then we made this plot for all visually responsive electrodes, and finally we arranged these plots in the same way the corresponding electrodes are arrange on the MEA (Figure 2.13).

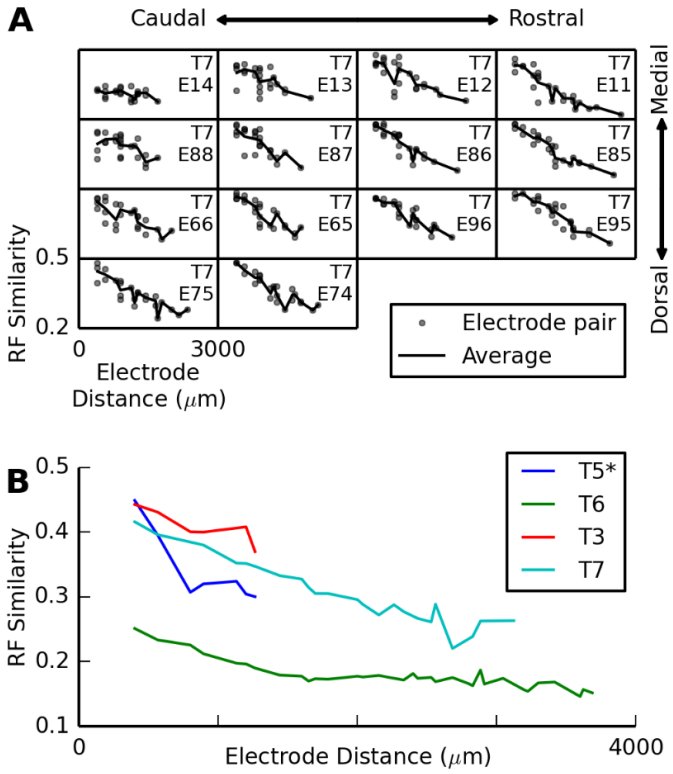

Figure 2.13 LFP receptive Field Similarity Versus Distance. **(A)** 14 plots of RF similarity versus electrode distance for 14 electrodes. The electrodes are arranged as they are on the MEA. Each point is the similarity of the LFP at that electrode with another visually responsive electrode. **(B)** The average LFP RF similarity at each electrode pair distance for all visually responsive electrode pairs for four turtle. *Turtle 5 was included here to show that its trend is consistent with the others, but the visual responses for turtle 5 were relatively weak. Therefore, in order to have enough visually responsive electrode pairs for turtle 5 we used a lower threshold (0.5) for visual responsiveness).

Looking at Figure 2.13A, we generally see mostly negative slopes. This indicates that receptive fields of nearby electrode pairs tend to be more similar to each other than the receptive fields of distant electrode pairs, which is consistent with the qualitative conclusions we came to earlier by simply looking at the receptive fields.

Additionally, it appears that the negative slope can be found more consistently for the rostral electrodes than for the caudal electrodes. The caudal electrodes tend to have slopes closer to zero. This means that the receptive fields at caudal electrode sites are no more (or only slightly more) similar to their neighbors than they are to distant electrodes. This is seen more clearly when looking at a larger section of the array and is a consistent result across turtles (Supplementary Information 2). It is worth noting that in a majority of cases, even the lower levels of similarity are still significantly more similar than shuffled data.

2.7.4 LED Flash Response Similarity

In addition to the amplitude of LFP response being similar in nearby electrodes (Figure 2.5 and Supplementary Information 4), if we look at the average responses to LED flashes across the electrode map, we can also see that the more detailed shape and timecourse of the LFP responses also seem to be similar in nearby electrodes (Figure 2.14).

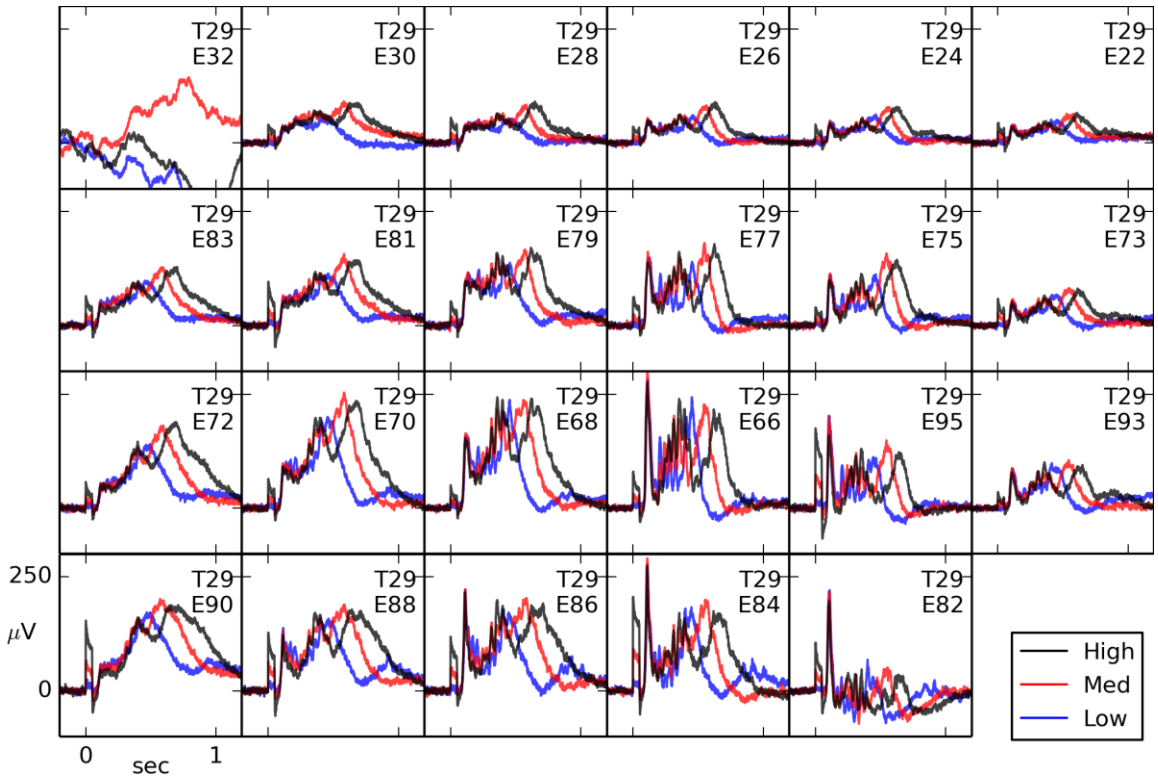

Figure 2.14 Average LED responses across the electrode array. The average responses to LED flashes of three different intensities (High, Med, and Low) shown for 23 electrodes from turtle 29. Left to right corresponds to caudal to rostral electrode arrangement, and top to bottom corresponds to medial to dorsal electrode arrangement.

2.8 Spike-LFP Correlation

In general, spikes are much less common in the absence of LFP activity than they are during a burst of LFP activity (Figure 2.15). This has been further quantified in Chapter 4 (section 4.5.3), in which there is a clear positive correlation between the number of action potential and the number of LFP peaks in 0.5 s windows.

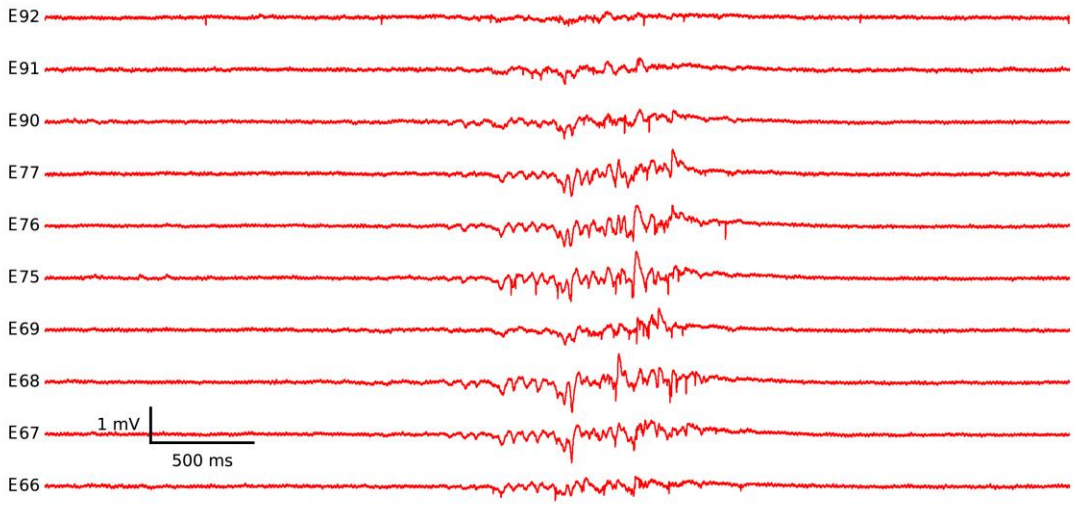

Figure 2.15 Action potentials during an LFP burst. Unfiltered simultaneous recordings from 10 electrodes from turtle 2.

In addition to looking at several electrodes with plenty of time preceding and following an LFP burst, we can also focus on a single highly responsive electrode and looked at multiple trials. Doing so shows that, during an evoked response, while both the LFP and the action potentials vary somewhat in their responses to each trial, the strength of their responses correlate very well with each other (Figure 2.16).

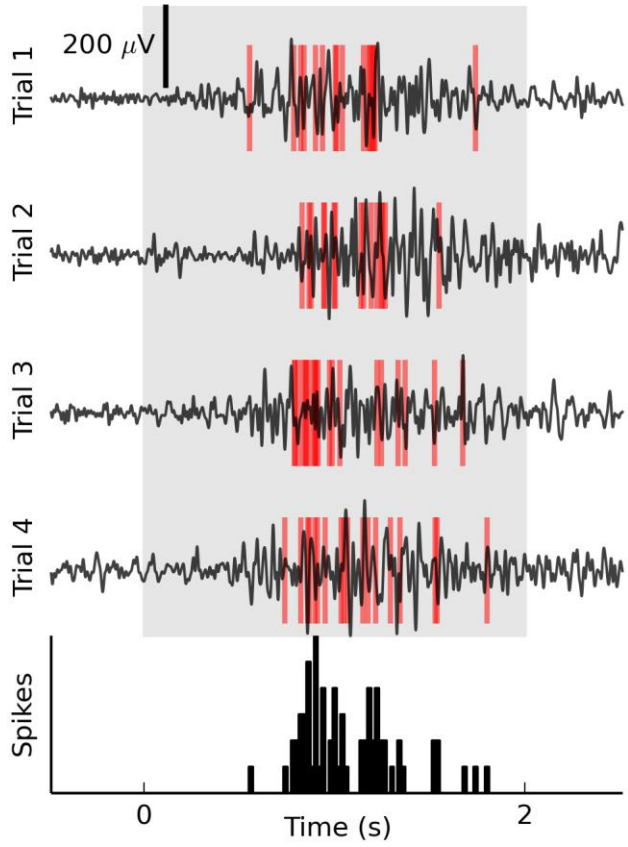

Figure 2.16 Action potential rastergrams with LFP. **(Top)** Four presentations of a moving dot moving across a white screen. Spikes (red) and LFP activity (black) are shown for each of the trials with **(bottom)** the peristimulus time histogram for the spikes shown below (turtle 7, electrode 95).

After recognizing that the two different measures of activity tend to be similar, it makes sense to quantify their similarity. We can do this in the same way that we calculated the receptive field similarity of the LFP signals from two separate electrodes (Figue 2.17).

The results of these studies were that, for a majority of the spiking/LFP comparisons, the spike data had a smaller RF, a less reliable response trial-to-trial, and the two RFs were significantly similar.

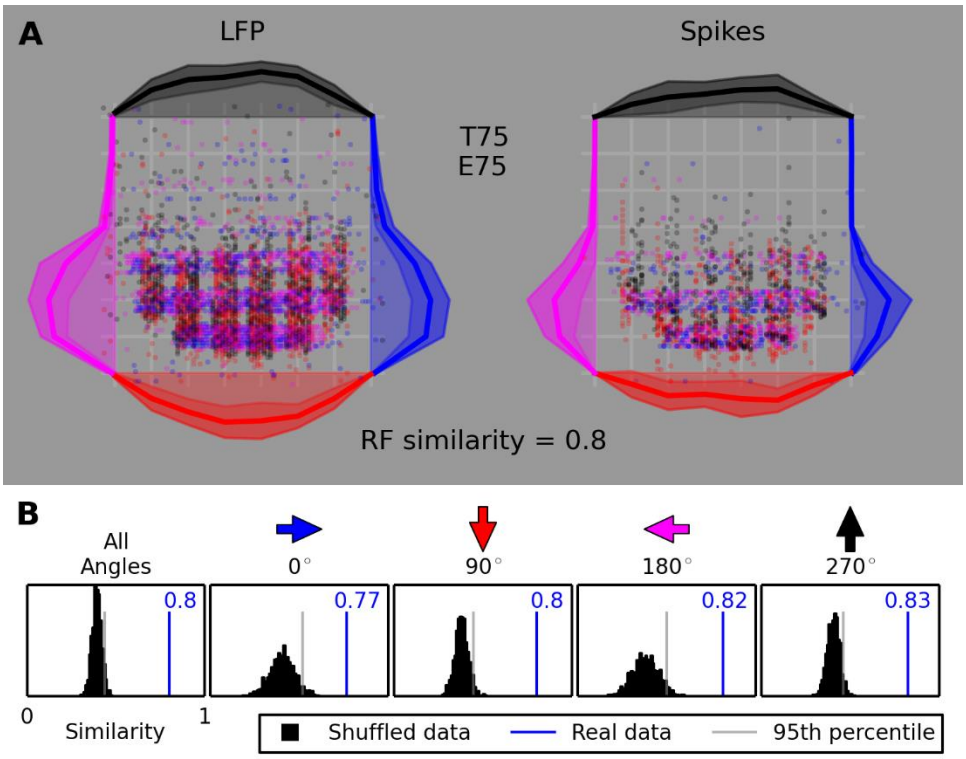

Figure 2.17 Spike-LFP receptive field similarity. **(A)** The LFP receptive field and spike receptive field for electrode 75 from turtle 7 (as plotted in Figure 2.12). **(B)** The similarity between the two receptive fields when the responses to dots moving at all angles are considered together, along with when we consider only the responses to dots moving at a specific angle. The black distributions are for 1,000 similarities calculated using shuffled data. The blue lines and numbers show the similarity of the real data for the two receptive fields, and the light grey line shows the similarity below which 95% of the shuffled similarities lie.

2.9 Color Sensitivity

To investigate the effects of color sensitivity, we compared the responses to different diffuse, full-field color changes. We found recording sites that respond to one change of colors, but not others and other recording sites whose responses seemed independent of color (Figure 2.18).

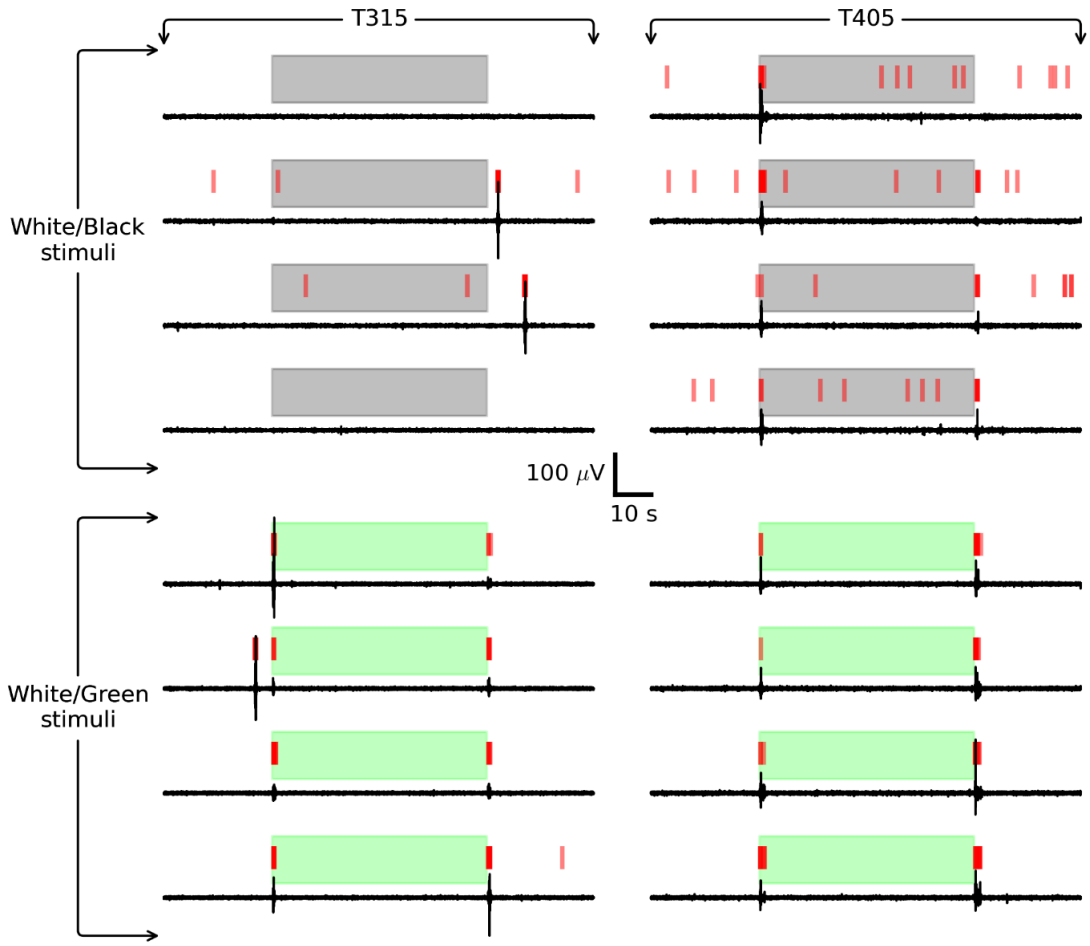

Figure 2.18 Color sensitivity in visually evoked LFP activity. Responses are shown for two turtles, turtle 315 **(Left)** and turtle 405 **(Right)**. **(Top)** LFP signal (black) and LFP events (red) shown for four trials of going from a white screen to a black screen and then back to white. **(Bottom)** same as the top but with a green screen instead of black.

2.10 Possible Mapping of the Visual Field to the Visual Cortex

For decades it has been reported that pyramids in turtle visual cortex respond to small moving stimuli spanning a very large portion of the visual field. While our results show large receptive fields for both single cell recordings and LFP's for single recording sites, when we looked for more detail in the spatial structure of the receptive fields, there is less of a consensus

regarding what to expect, and our results weren't always consistent with the existing predictions. Though there is not a clear and well defined retinotopic map to the cortex, there have been a few studies that report on projection at two steps leading from the retina to the cortex.

2.10.1 Naso-temporal Visual Field

Using retinal ablation and observing orthograde degeneration, Ulinski and Nautiyal reported that the nasal retina projects to the contralateral rostral LGN (and the temporal retina projects to the contralateral caudal LGN) (P S Ulinski & Nautiyal, 1988). Later, Mulligan and Ulinski used HRP stains and found that the rostral LGN projects to the caudal cortex (and the caudal LGN projects to the rostral cortex) (Mulligan & Ulinski, 1990). Combining these two observations Mulligan and Ulinski predicted that the nasal-temporal axis of visual space is represented along the rostro-caudal axis of the visual cortex. This prediction contradicted earlier results from Mazurskaya, who observed the opposite polarity in recorded evoked potentials in the visual cortex while presenting local visual stimulation to the retina (P. Mazurskaya, 1973).

Neither Mazurskaya's results nor Mulligan and Ulinski's predictions are consistent with our findings. We tested this with moving dots that followed straight paths from the top of the visual field to the bottom (as well as dots moving in the opposite direction). Eight of these vertical paths were spread out at different naso-temporal locations spanning the visual field. Only one dot (following one path) would move at a time. After moving these dots along the different paths we could look for naso-temporal response specificity at any given recording site in the cortex. With the microelectrode array, we could then see if the nasal-temporal response specificity changed as we compared data from electrodes in the rostral cortex with those from caudal cortex.

Our results show that, as you compare the naso-temporal response specificity of different recording sites, the strength of response specificity does change, but the pattern of specificity was approximately the same for all recording sites, and the variations from site to site did not follow any clear trend (e.g., rostral recording sites responding strongly to one area while caudal sites respond strongly to a different area) (Figure 2.19).

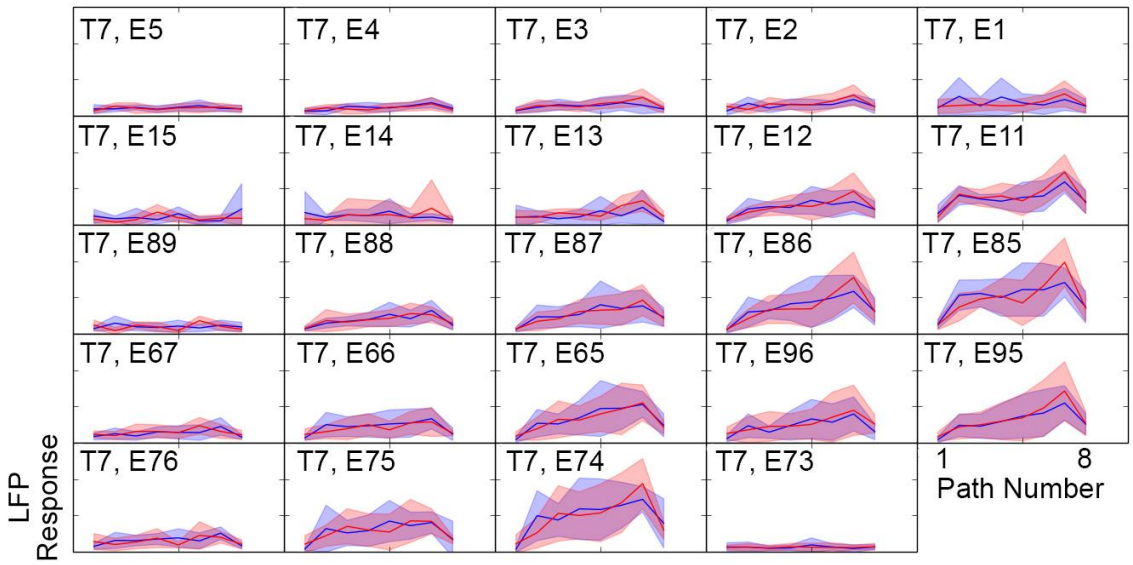

Figure 2.19 LFP responses to paths at different naso-temporal locations in the visual field. For 24 electrode we show the average responses (lines) and standard deviations (filled area around the lines), in response to dots moving along 8 different vertical paths arranged naso-temporally in the visual field. The two colors represent the two opposite angles that traverse the paths.

2.10.2 Dorso-Ventral Visual Field

By performing the same experiments with the visual stimuli rotated 90 degrees, we were able to investigate response specificity for different elevations in the visual field.

Ulinski and Nautiyal suggest that the dorso-ventral axis of the retina projects along the dorso-ventral axis of the LGN, but the data supporting this claim were much less clear than the data supporting conclusions about naso-temporal projections. Continuing along this visual

pathway, Mulligan and Ulinski reported that (at least some) neurons in any given dorso-ventral transect of the LGN project along the full lateral-medial extent of the cortex. Thus, a neuron located anywhere along a lateral-medial line in the cortex can respond to stimulation at any point along a particular vertical line in the visual field. In contrast with this prediction, we found recording sites that responded clearly to only the upper or only the lower visual field rather than stimulation at all elevations (Figure 2.20 electrodes 74 and 11).

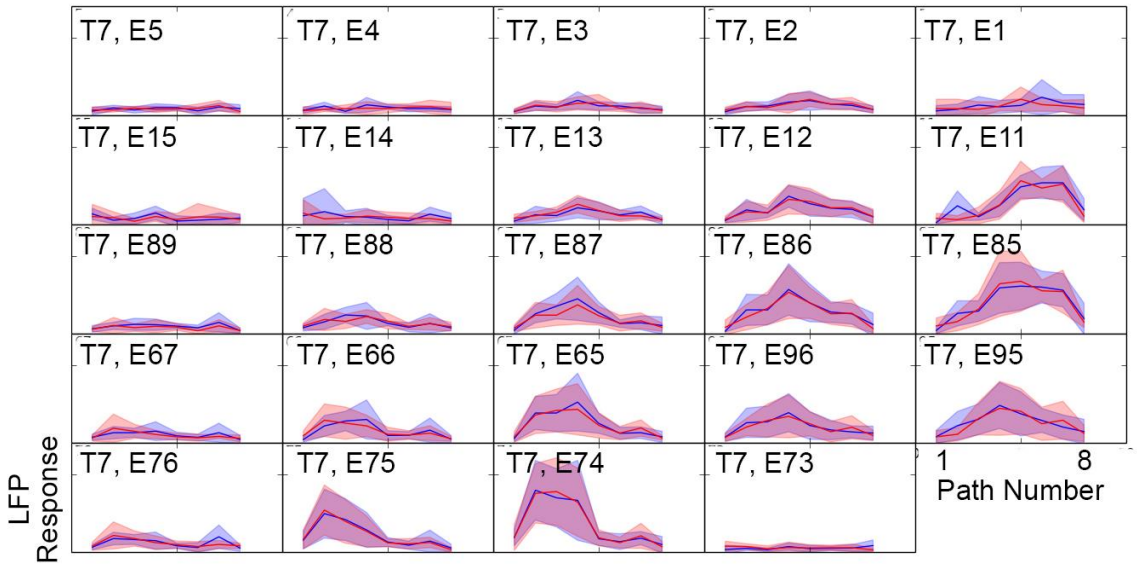

Figure 2.20 LFP responses to paths at different elevations in the visual field. For 24 electrode we show the average responses (lines) and standard deviations (filled area around the lines), in response to dots moving along 8 different horizontal paths arranged vertically in the visual field. The two colors represent the two opposite angles that traverse the paths.

2.11 Discussion

2.11.1 Similarity to Mammalian Inferior Temporal Cortex

IT (inferior temporal cortex) is a visually responsive area in mammals. Much of what we find in turtle cortex resembles what has been seen in mammalian IT. In IT they have also found responses to visual stimuli persisting up to 15 s (Fuster & Jervey, 1981). IT cells also tend to

have large receptive fields, respond to many stimuli, including moving stimuli, receive sensory input from both eyes, and have adaptation effects with interstimulus intervals less than 5 sec (Gross, Rocha-Miranda, & Bender, 1972).

Unlike, turtle visual cortex strong direction sensitivity has been observed in mammalian IT. Some of the direction sensitive IT cells had one clear preferred direction (termed unidirectional), but most were bidirection sensitive (they responded preferentially to both a direction and the opposite direction, but not perpendicular motion).This was demonstrated in IT using black bars sweeping across the visual field.

In contrast, our studies of direction sensitivity have used black dots that take up only a small portion of the visual field. Because there is an additional spatial component to our stimuli, we are only equipped to look for preference of one direction compared to the opposite direction (opposite directions cover the same spatial region).

Overwhelmingly, we have seen similar responses to opposite directions. This suggests that we don't have unidirectional sensitivity (at least not seen in the number of LFP events), but it doesn't preclude the possibility of bidirectional sensitivity. To test this, further studies should be done with moving bars that span the entire visual field.

2.11.2 Similarity to Mammalian Hippocampus and Piriform Cortex

Mammalian hippocampus has a similar structure to turtle cortex. Like turtle visual cortex, mammalian hippocampus has extensive feedback connections to its primary input source (entorhinal cortex) (Witter, 1993). In hippocampus oscillations are also found in the gamma band

(Bragin et al., 1995) and theta band with electrodes spanning several hundred microns having similar LFP signals (Buzsáki, 2002).

The olfactory or piriform cortex is also a three layer cortical structure, and has feedforward and feedback circuits that are similar to those found in turtle dorsal cortex (Lewis B Haberly, 1985) along with numerous other similarities(see Chapter 1). Further identifying structural and functional similarities between the turtle dorsal cortex and mammalian piriform cortex will likely help elucidate common organizational and computational principal of cortical networks (Fournier et al., 2014).

2.12 Supplementary Information

2.12.1 Convergence of Receptive Field with Applied Latency

It takes time for the signal elicited by visual stimuli to travel from the retina to the thalamus and then to the cortex. If we want to determine the receptive field represented by some signal (in this case, the LFP from an electrode), we need to be account for these delays.

One way that we have come up with estimates for what delay might be appropriate is to test a range of delays and see which delay reveals the most structure in the receptive field. Without any delay (Supplementary Figure 2.1) the contributions to the receptive field from dots moving at different angles only partially overlap, and consequently, the receptive field is quite large when taken as a whole. In contrast, when we apply a 300 ms delay, the contributions to the receptive field from different angles overlap nearly perfectly, and the receptive field as a whole is smaller and appears more structured.

It should be noted that the figures shown here have a smaller RF than is typical. Electrodes with smaller RFs were deliberately chosen to more clearly show the convergence of the RF with different delays.

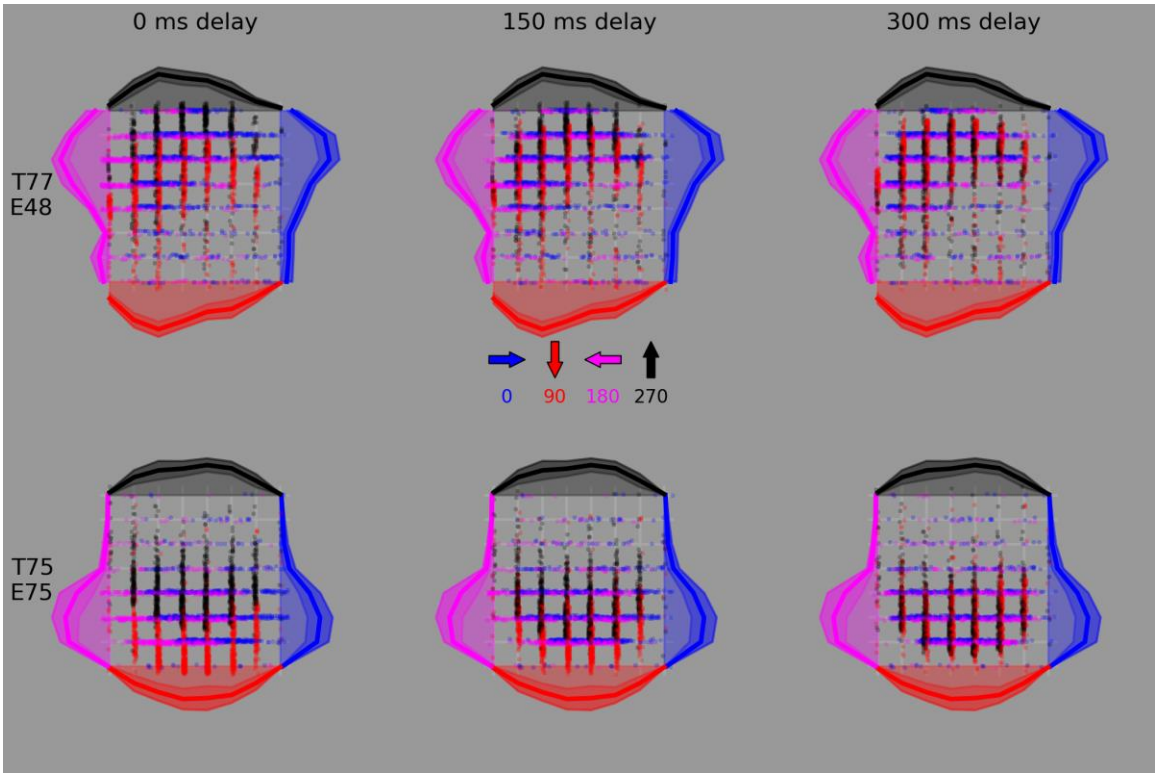

Supplementary Figure 2.1 Convergence of the receptive field with response delays. Receptive field plots for turtle 77 electrode 48 **(Top)** and turtle 75 electrode 75 **(Bottom)** made by applying stimulus response delays of 0 ms, 150 ms, and 300 ms.

The process above assumes that a smaller, more structured receptive field is 'right'. This seems like a reasonable assumption, but it is still worth mentioning.

We can actually gather another piece of evidence by applying multiple delays that does not require this assumption. We can establish an upper limit to the response latency by applying a latency large enough that we see a reliable response to times before a dot actually moves (Supplementary Figure 2.2). Looking at the red 90 degree responses for turtle 77 (or the black

270 degree responses for turtle 75), we see that the differences in response onset for the various paths that can be seen for 250 ms and 300 ms delays start to be cut off for 350 ms delays (i.e., the earliest responses are no longer shown because they don't correspond to a location on the path because at that time, no dot was moving along a path). This gives us an upper limit of 350 ms (in this case) for response latency.

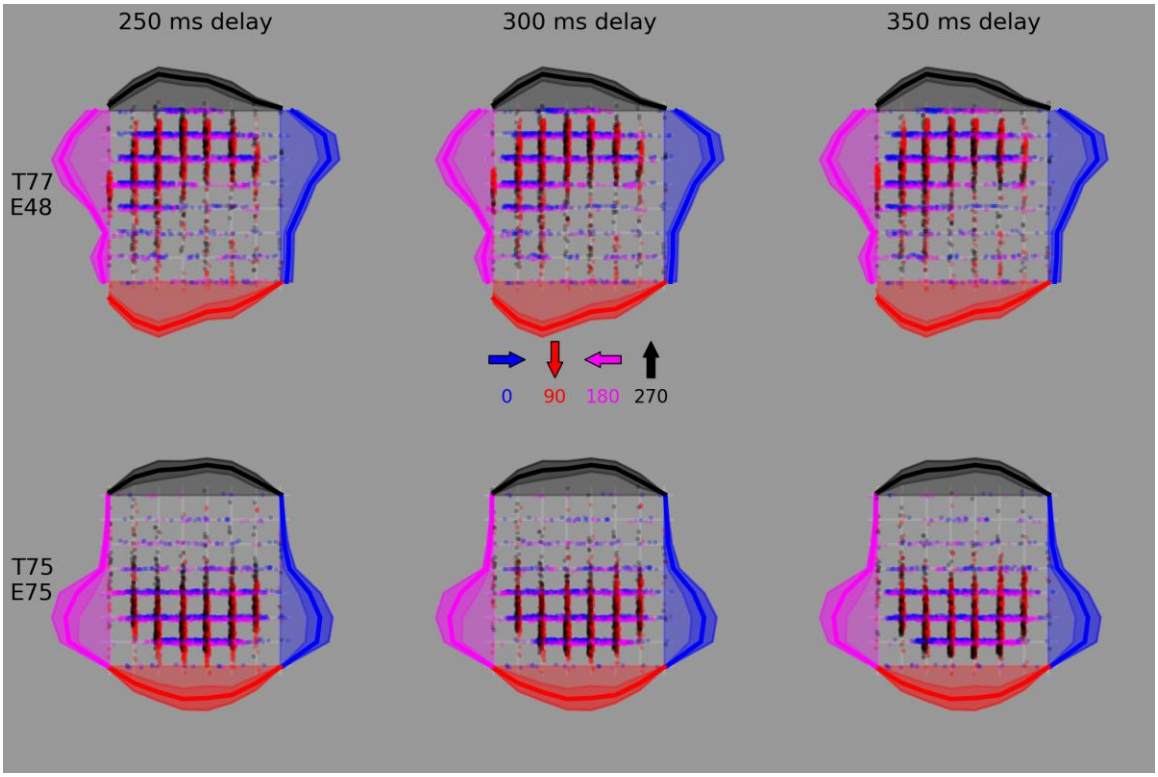

Supplementary Figure 2.2 Limits of the visual field provide upper limits to response latency. Receptive field plots for turtle 77 electrode 48 **(Top)** and turtle 75 electrode 75 **(Bottom)** made by applying stimulus response delays of 0 ms, 150 ms, and 300 ms.

2.12.2 Receptive Field Similarity versus Electrode Pair Distance across the MEA for 3 Turtles

A trend in receptive field similarity versus distance is to find a negative slope. That is to say that similarity decreases when electrode pair distance increases. Zooming out we see a trend in the strength of this trend throughout the cortex. It is often the case that this trend is strongest in

one area of the cortex (typically a rostral area) and is less apparent in other areas (Supplementary Figures 2.3-6).

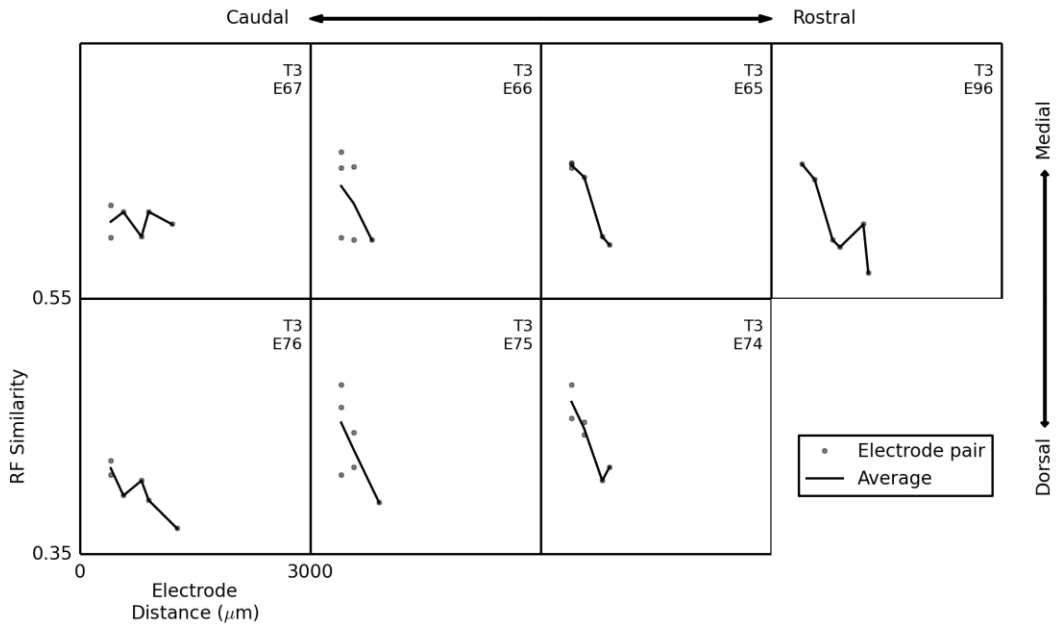

Supplementary Figure 2.3 Receptive field similarity versus distance for Turtle 3. Plots of RF similarity versus electrode distance for several electrodes. The electrodes are arranged as they are on the MEA. Each point is the similarity of the LFP at that electrode with another visually responsive electrode.

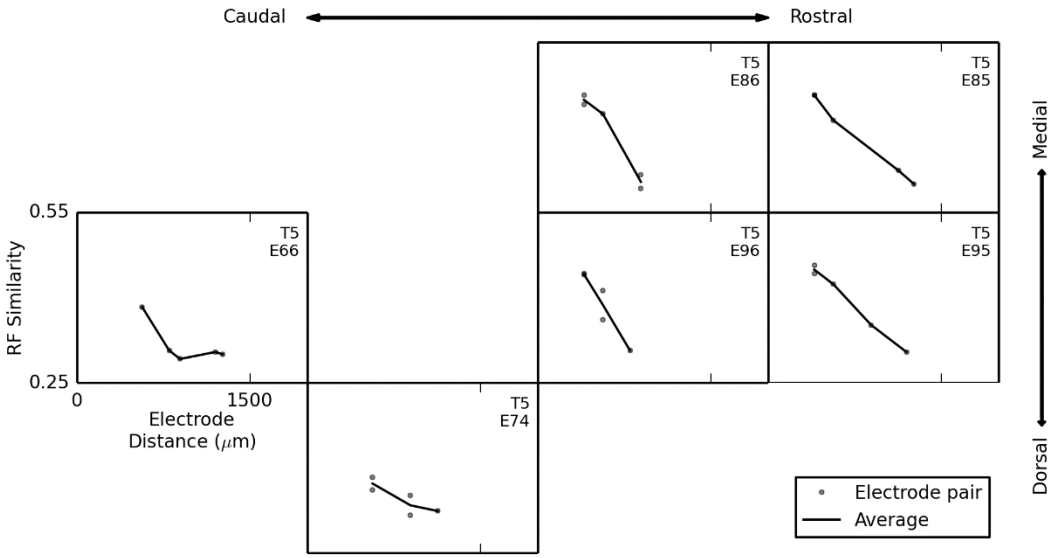

Supplementary Figure 2.4 Receptive field similarity versus distance for Turtle 5. Plots of RF similarity versus electrode distance for several electrodes. The electrodes are arranged as they are on the MEA. Each point is the similarity of the LFP at that electrode with another visually responsive electrode.

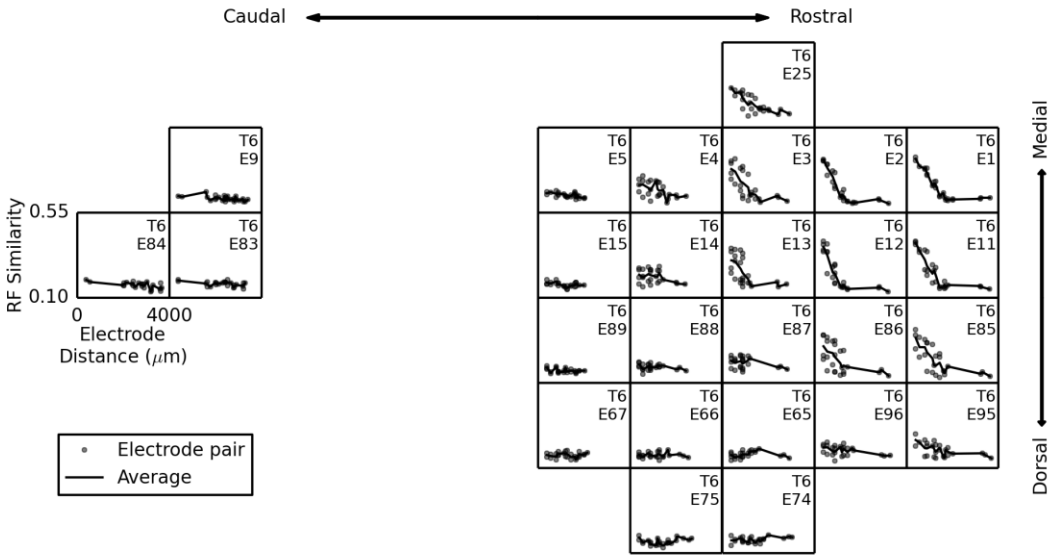

Supplementary Figure 2.5 Receptive field similarity versus distance for Turtle 6. Plots of RF similarity versus electrode distance for several electrodes. The electrodes are arranged as they are on the MEA. Each point is the similarity of the LFP at that electrode with another visually responsive electrode.

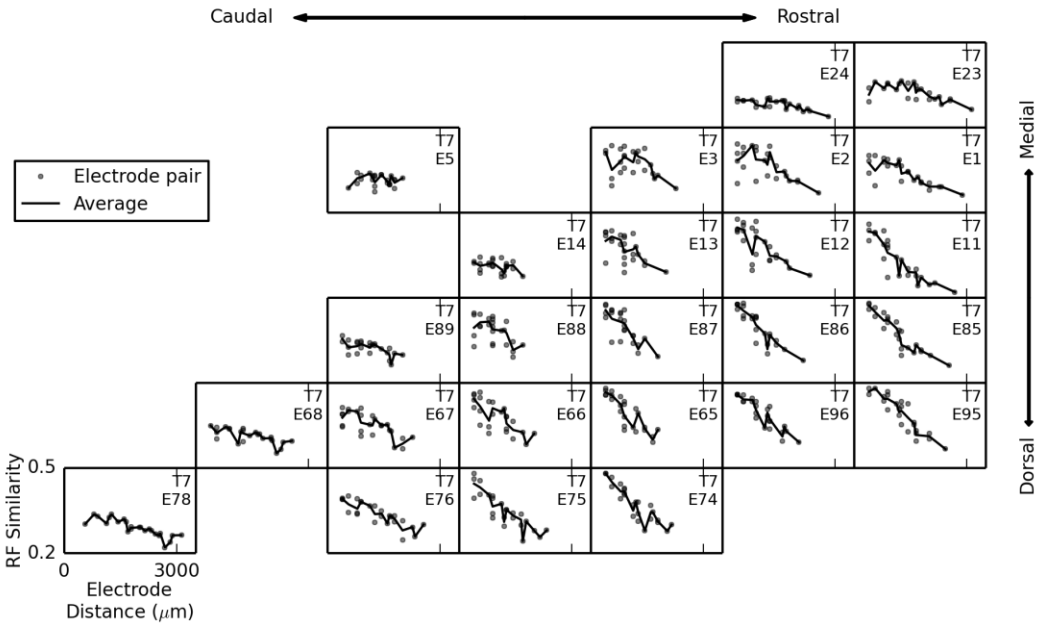

Supplementary Figure 2.6 Receptive field similarity versus distance for Turtle 7. Plots of RF similarity versus electrode distance for several electrodes. The electrodes are arranged as they are on the MEA. Each point is the similarity of the LFP at that electrode with another visually responsive electrode.

2.12.3 Possible Direction Sensitivity in Spiking Data

It's difficult to draw conclusions regarding direction sensitivity from much of our spiking data because 1) we haven't systematically gone through all of our data to identify visually responsive units as we've done for the LFP on every electrode, and 2) when it seems that we are looking at visually responsive units, the responses are often so sparse that it's tough to establish significance or clear patterns.

With that in mind there are some indications that we might expect direction sensitivity from individual cells in turtle cortex. For instance, consider the receptive field shown for spiking activity in Supplementary Figure 2.7. We should be careful drawing conclusions from a data set including only 6 spikes, but I would argue that we have strong evidence suggesting that the

timing of those 6 spikes are far from random. The probability of 6 random spikes all occurring during motion in 1 direction (out of 4 possible directions) is already less than 1%. That they would further have occurred on all of (but no more than) a group of four adjacent paths and only at the location corresponding to ~25% from the beginning of the path is substantially less probable. Finally, that the receptive field is substantially similar to the LFP receptive field from the same electrode also suggests that the six spikes represent some real structure.

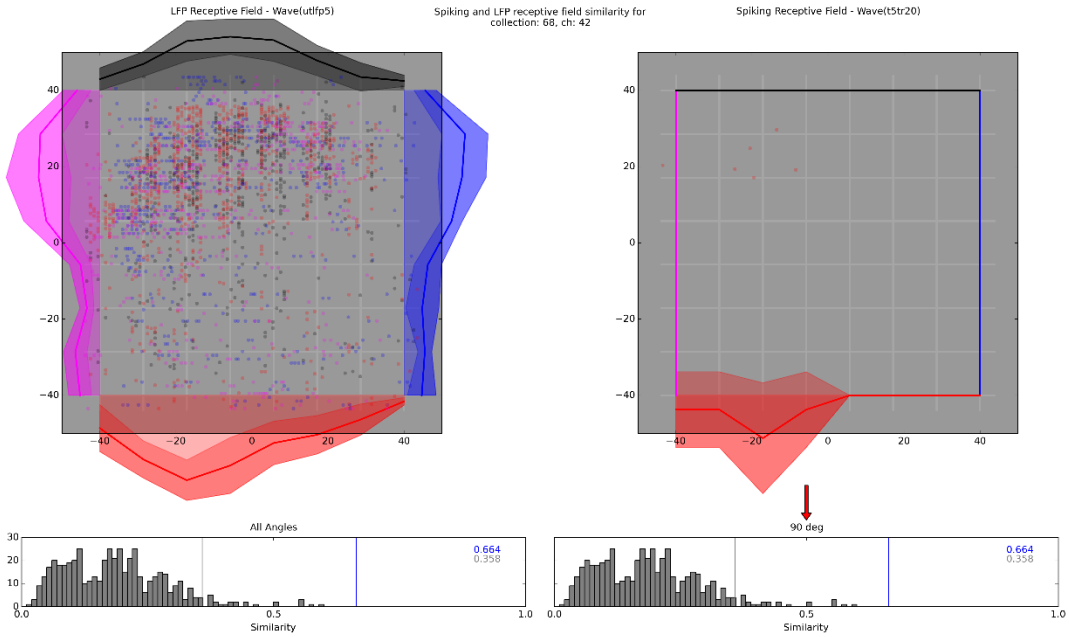

Supplementary Figure 2.7 Possible direction sensitivity and spike-LFP receptive field similarity. **(Right)** Receptive field of a spiking cell. **(Left)** Receptive field of the LFP picked up by the same electrode. **(Bottom)** An indication of the similarity between the two receptive fields showing a comparison with shuffled data.

It is worth noting one way the preceding reasoning could at times be misleading. Occasionally, a cell will be very quiet for a long time and the in a small period of time (maybe a second or two) fire a quick burst of action potentials. In that case, all the aforementioned 'unlikely' events could quite simply be explained by calling the six spikes a single burst event.

That is clearly not what happened in this case. There was at least 30 s between each of the six recorded spikes, and most between most of the spikes there was even a presentation of dots moving at other angles.

We can even argue that this is an example of unidirectional sensitivity (sensitivity to only one direction as opposed to a direction and its opposite, which is bidirectional sensitivity). In nearly all cases the LFP receptive field showed equally strong responses to dots moving in opposite directions. Here that clearly isn't the case. Again, we should consider whether we can draw meaningful conclusions from only 6 spikes.

Each path in the visual field was presented 8 times. Therefore, seeing 6 spikes in the 32 presentations (from the 4 paths that had spikes), suggests that the probability of a spike being evoked by a dot moving along one of those paths is 19%. If a dot moving in the opposite direction for the same 4 paths was equally as likely to evoke a spike, then the probability of not seeing a single spike for the 32 presentations along those paths is ~0.1%.

2.12.4 LED Peristimulus Time Histograms for Several Turtles

Peristimulus time histograms of LFP events are useful for illustrating the temporal patterns of typical responses. By plotting these for several electrodes across the MEA, we get a sense for the extent to which these properties vary throughout the cortex (Supplementary Figures 2.8-14).

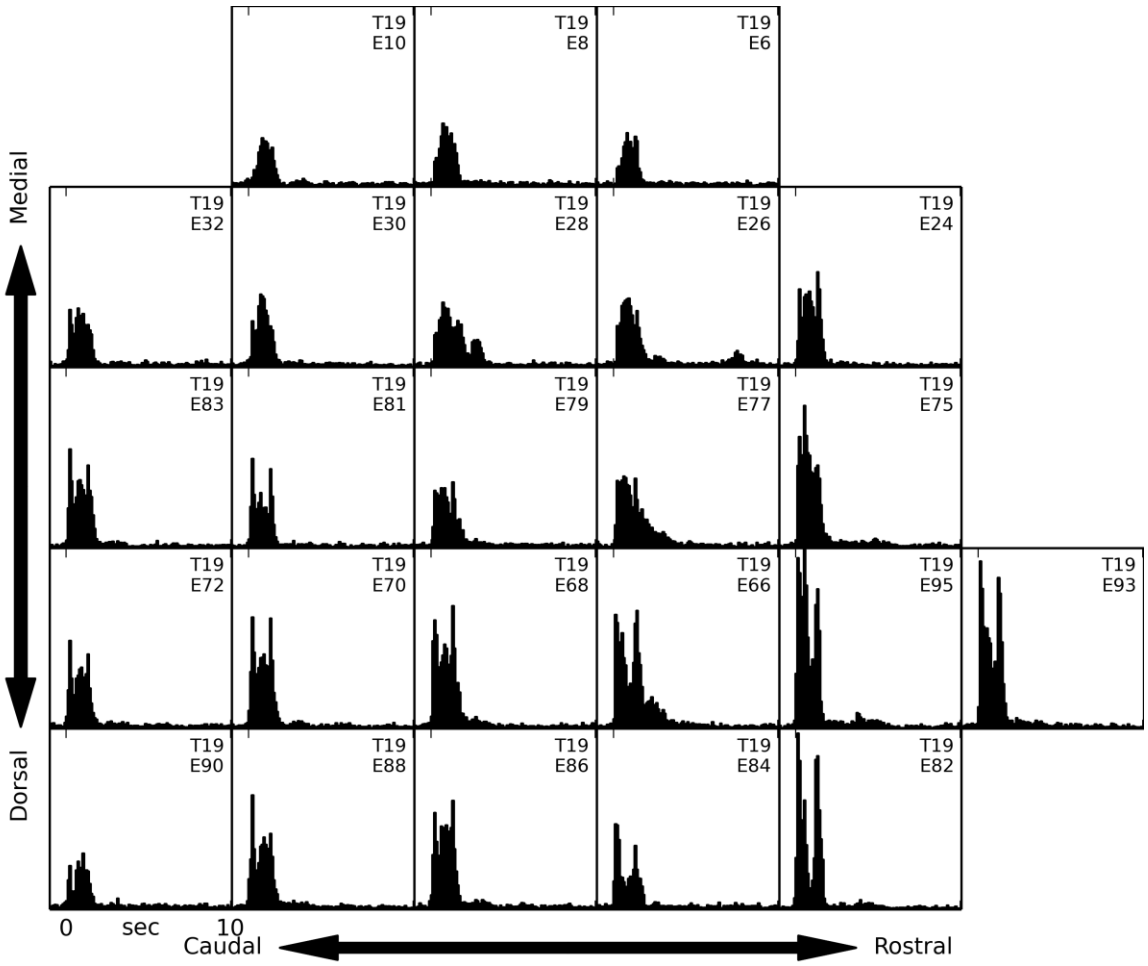

Supplementary Figure 2.8 Peristimulus Time Histograms for several electrodes, Turtle 19. The electrodes are arranged as they were in the cortex. The PSTHs show LFP events in response to a brief LED flash (bin size = 50 ms, number of trials = 90).

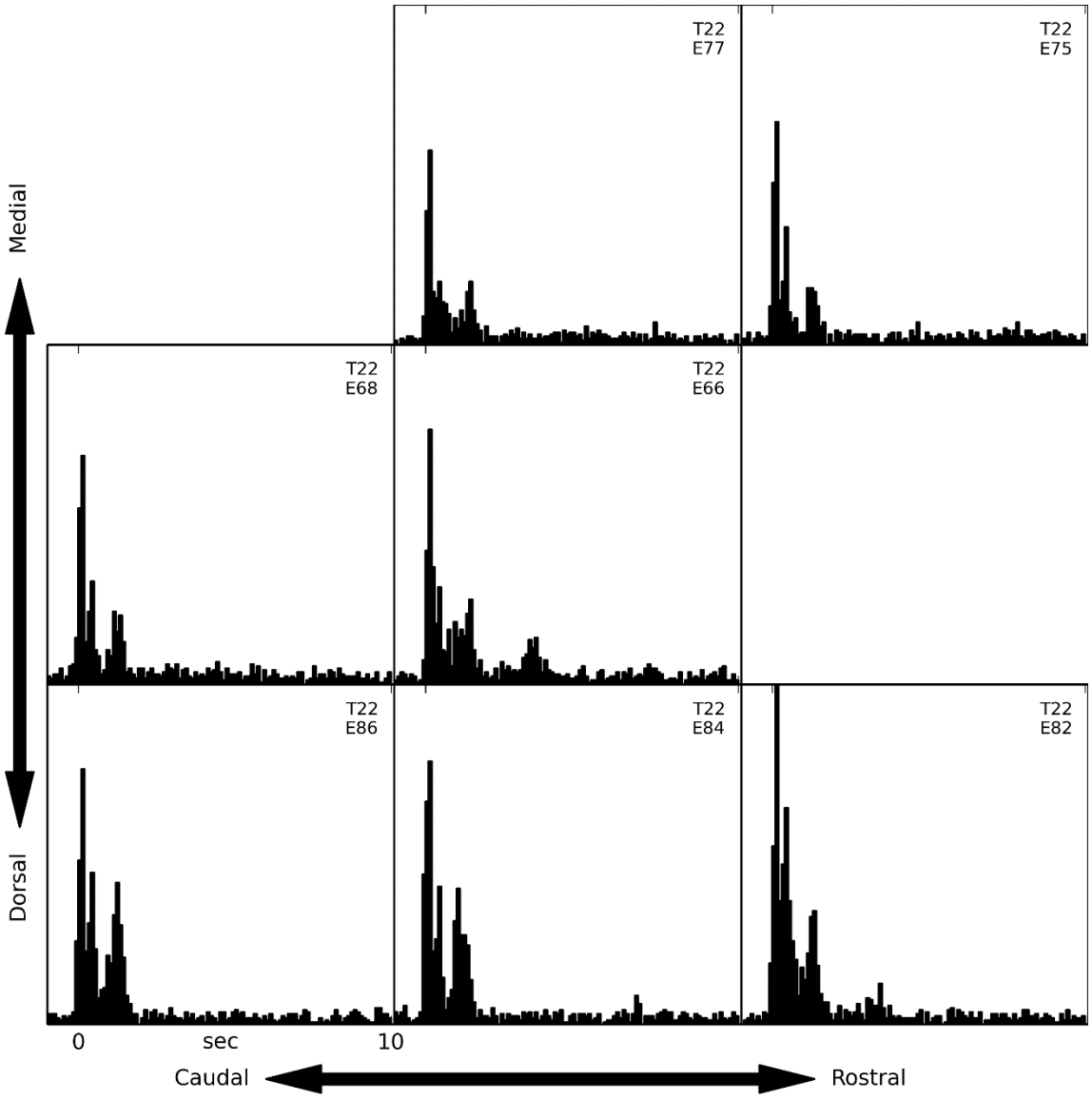

Supplementary Figure 2.9 Peristimulus Time Histograms for several electrodes, Turtle 22. The electrodes are arranged as they were in the cortex. The PSTHs show LFP events in response to a brief LED flash (bin size = 50 ms, number of trials = 90).

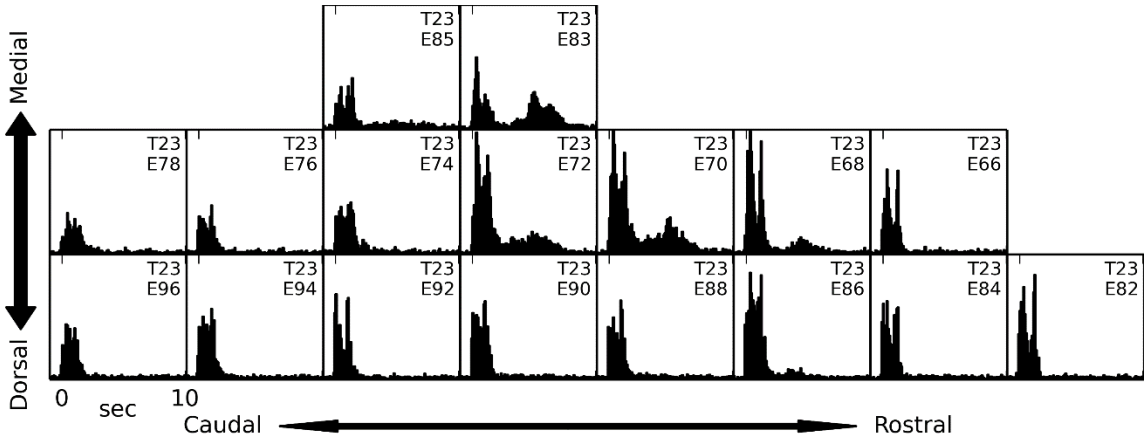

Supplementary Figure 2.10 Peristimulus Time Histograms for several electrodes, Turtle 23. The electrodes are arranged as they were in the cortex. The PSTHs show LFP events in response to a brief LED flash (bin size = 50 ms, number of trials = 90).

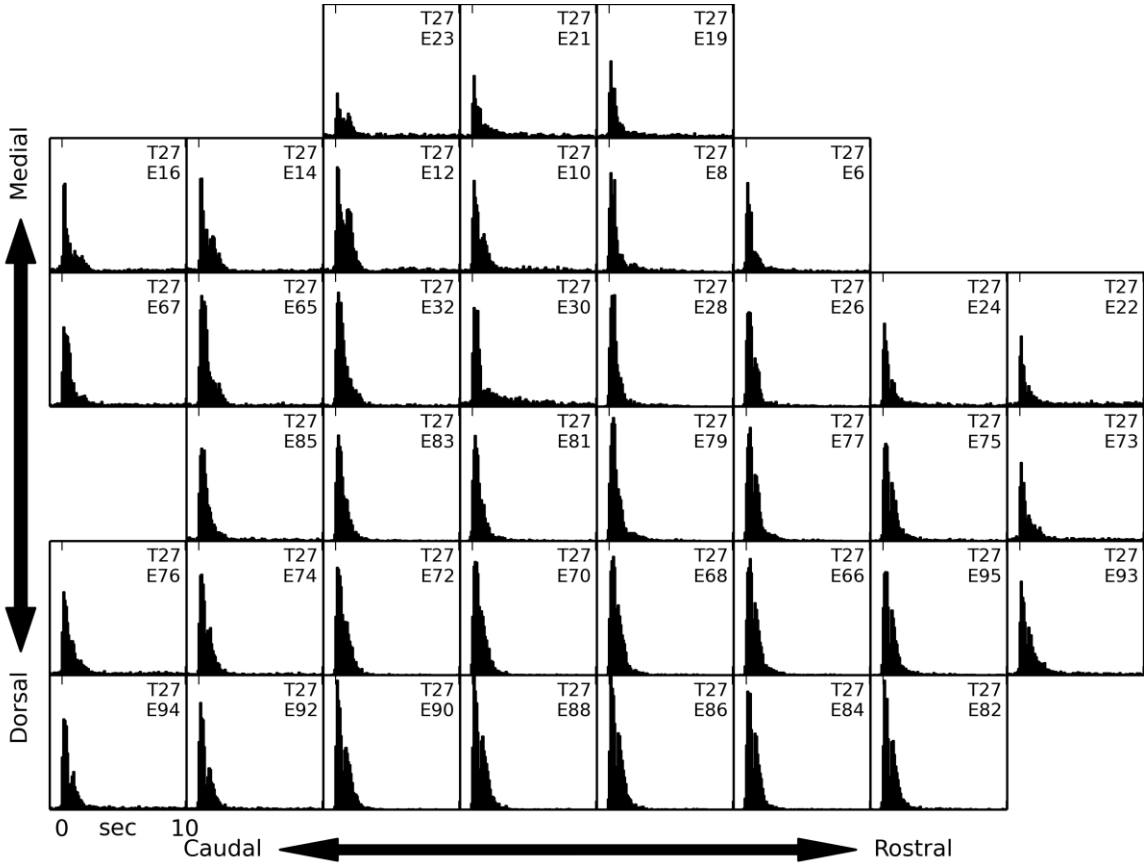

Supplementary Figure 2.11 Peristimulus Time Histograms for several electrodes, Turtle 27. The electrodes are arranged as they were in the cortex. The PSTHs show LFP events in response to a brief LED flash (bin size = 50 ms, number of trials = 90).

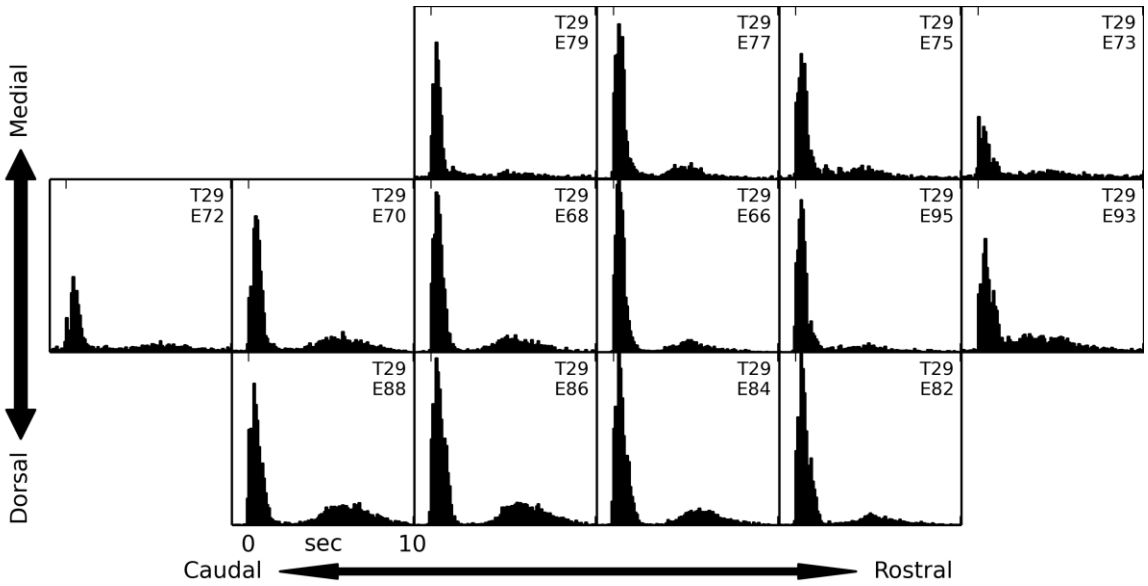

Supplementary Figure 2.12 Peristimulus Time Histograms for several electrodes, Turtle 29. The electrodes are arranged as they were in the cortex. The PSTHs show LFP events in response to a brief LED flash (bin size = 50 ms, number of trials = 90).

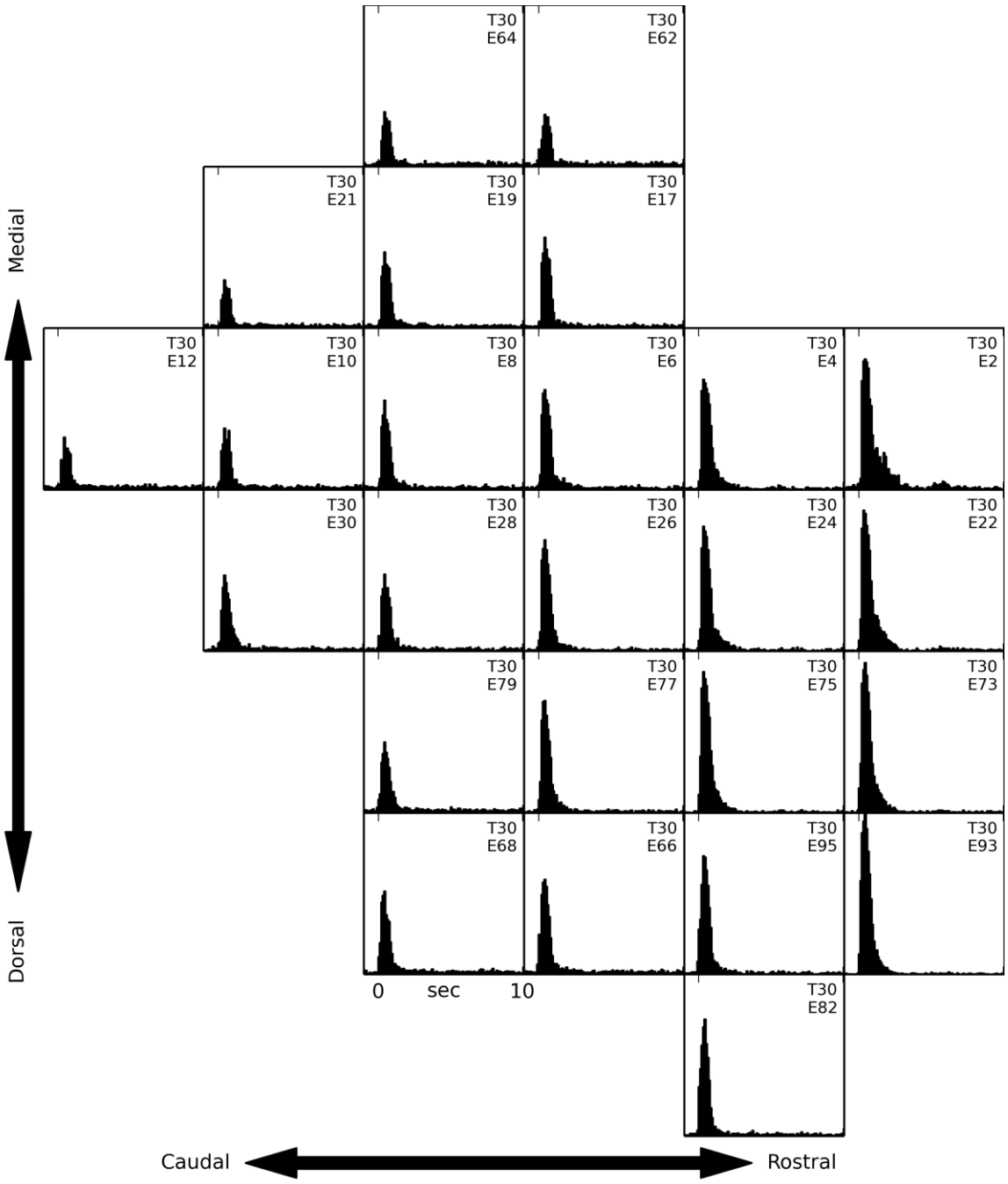

Supplementary Figure 2.13 Peristimulus Time Histograms for several electrodes, Turtle 30. The electrodes are arranged as they were in the cortex. The PSTHs show LFP events in response to a brief LED flash (bin size = 50 ms, number of trials = 90).

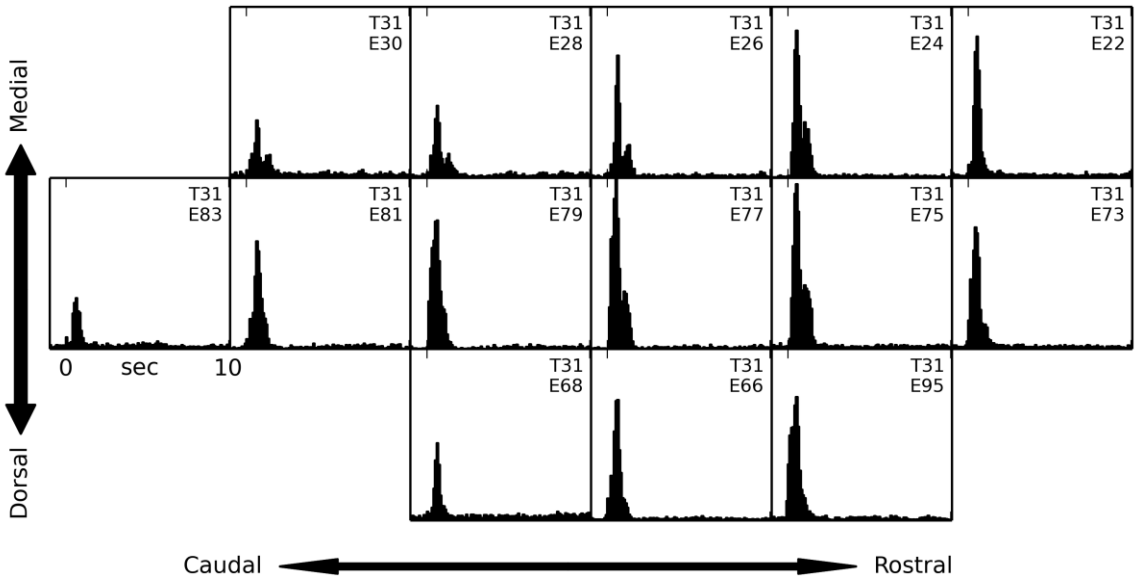

Supplementary Figure 2.14 Peristimulus Time Histograms for several electrodes, Turtle 31. The electrodes are arranged as they were in the cortex. The PSTHs show LFP events in response to a brief LED flash (bin size = 50 ms, number of trials = 90).

2.12.5 Additional Moving Dot Receptive Field across the Electrode Array

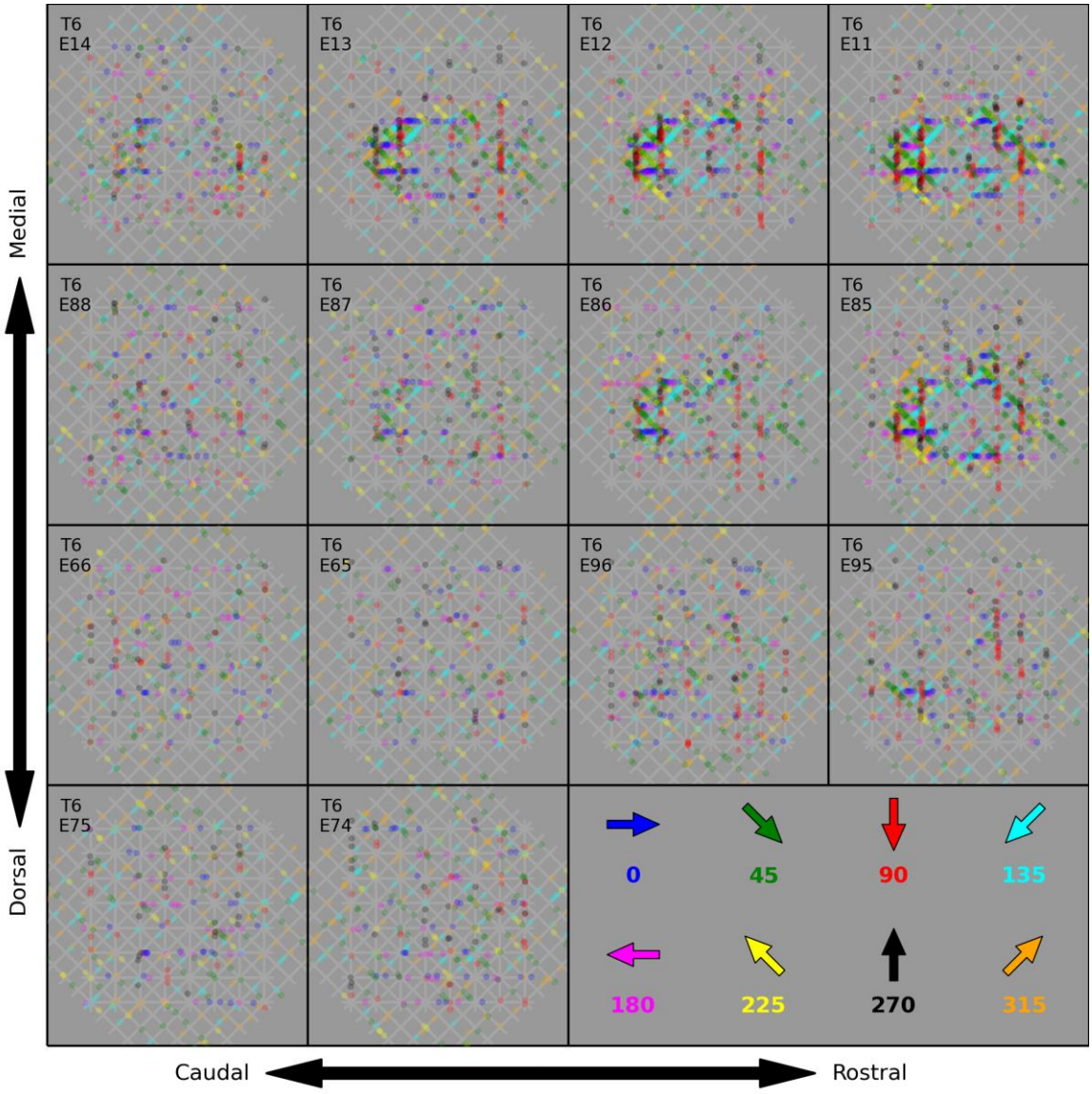

Supplementary Figure 2.15 LFP receptive fields across the microelectrode array for Turtle 6. The LFP receptive field as probed by moving dots is plotted for 14 visually responsive electrodes arranged as they are across the MEA.

2.12.6 Reliable Responses to Moving Dot Stimuli

In Figure 2.10 we showed a set of responses demonstrating several types of response variability. Here we show a set of responses to a different stimuli (dots moving in the opposite direction), which exhibit far less response variability.

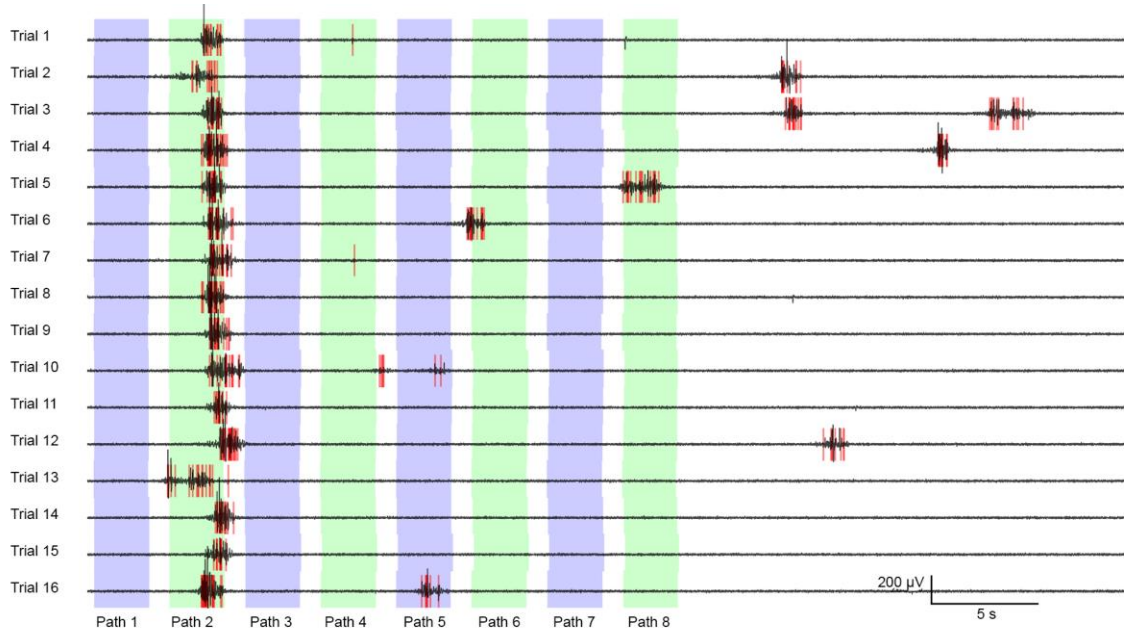

Supplementary Figure 2.16 Reliable responses to moving dot stimuli. LFP signal (black) with action potentials (red rasters) during 16 presentations (each row is a separate presentation) of 8 dots moving across the visual field following 8 different paths. The 8 colored columns indicate the timing of the 8 dots moving across the visual field.

2.12.7 Clues Regarding the Spatial Extent of the Local Field Potential

If we want to claim that there is any meaning behind the LFP recorded at two different electrodes being similar, we should convince ourselves that they are simply recording the same signals. To this end, we split the LFP into many narrow frequency bands and compared the activity on two neighboring electrodes (Supplementary Figure 2.17). While most of the activity on one electrode is also seen on the neighboring electrode (though maybe with a different

amplitude), there are events that occur on only one of the electrodes. This shows that there are contributions to the LFP that can be seen clearly on one electrode but not seen at all 400 μm away and lends support to the claim that the similarity of LFP activity isn't merely a result of recording from largely overlapping regions.

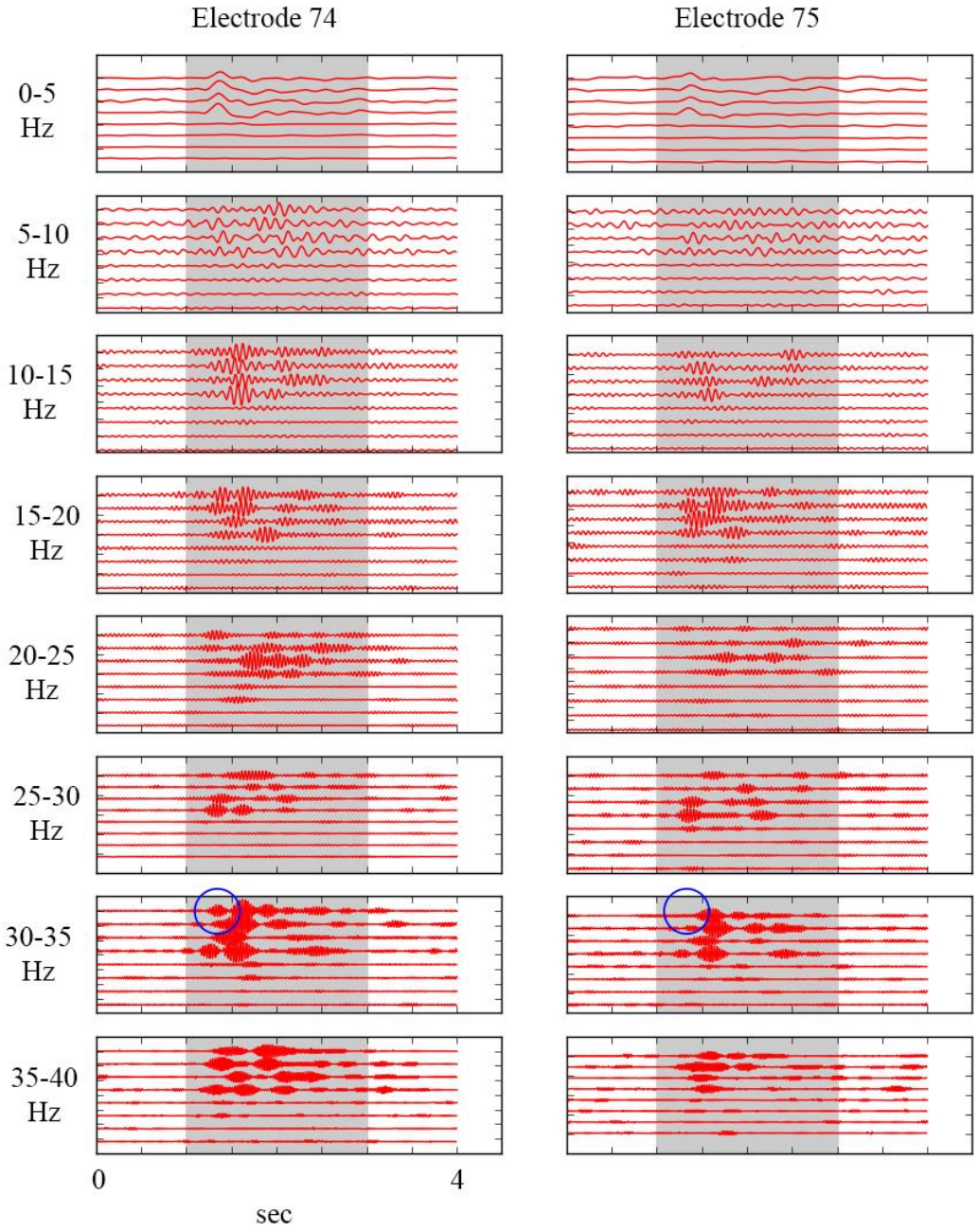

Supplementary Figure 2.17 Differences in LFP activity in adjacent electrodes. Responses to a black dot moving across a white screen for two electrodes separated by 400 µm. The signal is shown after filtering in 8 different narrow frequency bands. The 8 red paths shown in each box are 8 repetitions of the same stimulus. The blue circle highlights an example of an oscillation being present on one electrode but not the other.

2.12.8 Additional Average LED Responses

As seen in Figure 2.4, at times the LFP response to an LED flash can have a dominant frequency present even in the average, but a single dominant frequency can't be found in all turtles Supplementary Figure 2.18.

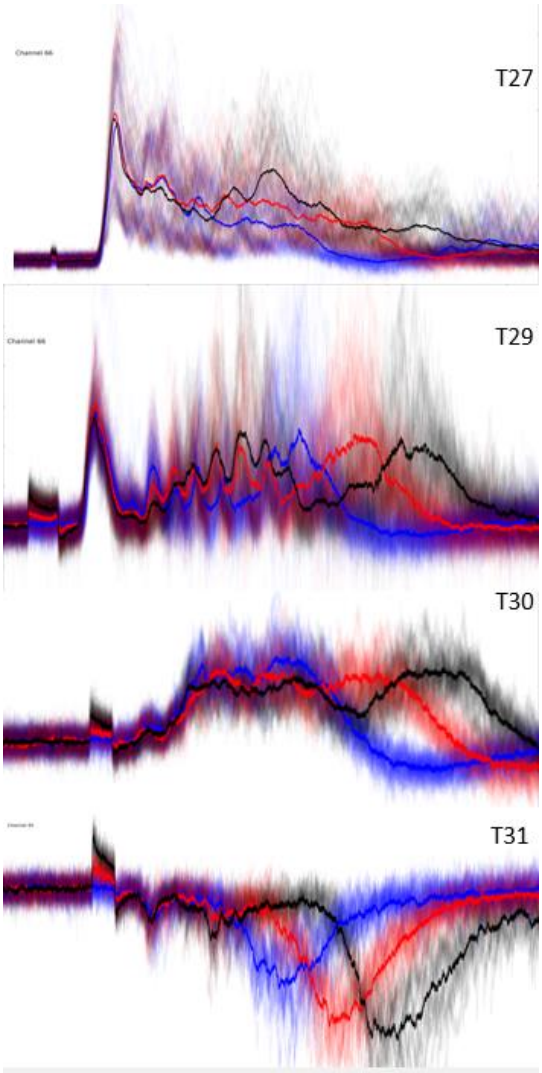

Supplementary Figure 2.18 Average responses to LED flashes for several turtles. Responses shown for LED flashes of three different intensities: low (blue), medium (red), and high (black). The averages are shown as bold lines with the individual trials shown as thinner slightly transparent lines.

2.12.9 Adaptation with Moving Bar Stimuli

Clear adaptation to visually evoked activity is seen in response to bars moving across the visual field in different direction. In Supplementary Figure 2.19 we see the strongest response to the bar that moved first in the series of 8 bars moving, and we see the weakest response to the bar that moved second. The order of the angles in which the bars moved was not the same for each trial, which tells us that the differences in response strengths can't simply be explained by direction sensitivity, and much more likely are due to adaptation effects.

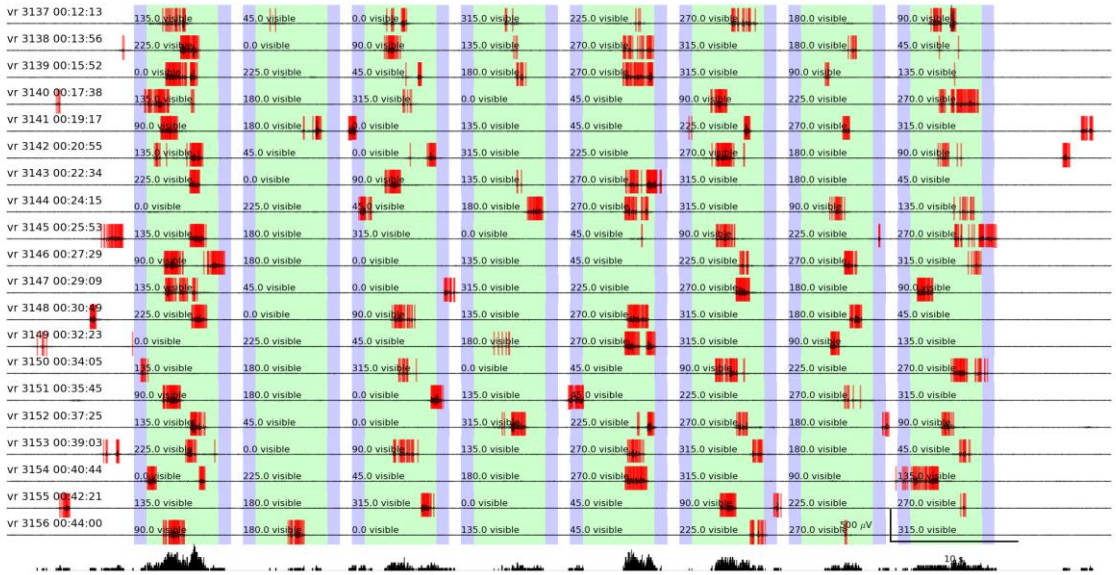

Supplementary Figure 2.19 LFP and action potential responses to moving bars. The LFP is shown in black. Action potentials are indicated by red rasters. Each row is a separate trial, each colored column indicates the timing of a bar moving across the visual field. The histogram along the bottom is a peristimulus time histogram for the action potential data.

2.13 References

Arieli, A., Sterkin, A., Grinvald, A., & Aertsen, A. (1996). Dynamics of ongoing activity: explanation of the large variability in evoked cortical responses. *Science (New York, N.Y.), 273*(5283), 1868–71. Retrieved from http://www.ncbi.nlm.nih.gov/pubmed/8791593

Bass, A., Andry, M., & Northcutt, R. G. (1983). Visual activity in the telencephalon of the painted turtle, Chrysemys picta. *Brain Research*, *263*, 201–210. Retrieved from http://www.sciencedirect.com/science/article/pii/000689938390313X

Boiko, V. (1980). Responses to visual stimuli in thalamic neurons of the turtle Emys orbicularis. *Neuroscience and Behavioral Physiology*, 2011. Retrieved from http://link.springer.com/article/10.1007/BF01148461

Bragin, A., Jandó, G., Nádasdy, Z., Hetke, J., Wise, K., & Buzsáki, G. (1995). Gamma (40-100 Hz) oscillation in the hippocampus of the behaving rat. *The Journal of Neuroscience : The Official Journal of the Society for Neuroscience*, *15*(January), 47–60.

Butler, A. B., & Hodos, W. (2005). *Comparative Vertebrate Neuroanatomy: Evolution and Adaptation: Second Edition*. *Comparative Vertebrate Neuroanatomy: Evolution and Adaptation: Second Edition* (pp. 1–715). John Wiley and Sons.

Buzsáki, G. (2002). Theta oscillations in the hippocampus. *Neuron*, *33*, 325–340. doi:10.1016/S0896-6273(02)00586-X

Douglas, R. J., & Martin, K. A. C. (2004). Neuronal circuits of the neocortex. *Annual Review of Neuroscience*, *27*, 419–51. doi:10.1146/annurev.neuro.27.070203.144152

Fontanini, A., & Katz, D. B. (2008). Behavioral states, network states, and sensory response variability. *Journal of Neurophysiology*, *100*, 1160–1168. doi:10.1152/jn.90592.2008

Fournier, J., Müller, C. M., & Laurent, G. (2014). Looking for the roots of cortical sensory computation in three-layered cortices. *Current Opinion in Neurobiology*, *31C*, 119–126. doi:10.1016/j.conb.2014.09.006

Fuster, J. M., & Jervey, J. P. (1981). Inferotemporal neurons distinguish and retain behaviorally relevant features of visual stimuli. *Science (New York, N.Y.)*, *212*(4497), 952–955. doi:10.1126/science.7233192

Gross, C. G., Rocha-Miranda, C. E., & Bender, D. B. (1972). Visual Cortex Properties of Neurons in Inferotemporal of the Macaque. *J Neurophysiol*, *35*, 96–111.

Gusel'nikov, V. I., Morenkov, E. D., & Pivovarov, A. S. (1972). Unit responses of the turtle forebrain to visual stimuli. *Neuroscience and Behavioral Physiology*, *5*(3), 235–42. Retrieved from http://www.ncbi.nlm.nih.gov/pubmed/4570704

Gusel'nikov, V., & Pivovarov, A. (1977). Postsynaptic excitation and in hibition in neurons of the turtle general cortex in response to moving stimuli. *Neurophysiology*, *9*(3), 194–199. Retrieved from http://link.springer.com/article/10.1007/BF01063391

Haberly, L. B. (1985). Neuronal circuitry in olfactory cortex: anatomy and functional implications. *Chemical Senses*, *10*(2), 219–238. doi:10.1093/chemse/10.2.219

Hounsgaard, J., & Nicholson, C. (1990). The isolated turtle brain and the physiology of neuronal circuits. *Preparations of Vertebrate Central Nervous System In Vitro*, *6*, 155–181.

Kajikawa, Y., & Schroeder, C. E. (2011). How local is the local field potential? *Neuron*, *72*(5), 847–858. doi:10.1016/j.neuron.2011.09.029

Katzner, S., Nauhaus, I., Benucci, A., Bonin, V., Ringach, D. L., & Carandini, M. (2009). Local origin of field potentials in visual cortex. *Neuron*, *61*(1), 35–41. doi:10.1016/j.neuron.2008.11.016

Kriegstein, A. R. (1987). Synaptic responses of cortical pyramidal neurons to light stimulation in the isolated turtle visual system. *The Journal of Neuroscience : The Official Journal of the Society for Neuroscience*, *7*(8), 2488–92. Retrieved from http://www.ncbi.nlm.nih.gov/pubmed/3612249

Luo, Q., Lu, H., Lu, H., Yang, Y., & Gao, J.-H. (2010). Comparison of visually evoked local field potentials in isolated turtle brain: patterned versus blank stimulation. *Journal of Neuroscience Methods*, *187*(1), 26–32. doi:10.1016/j.jneumeth.2009.12.005

Mancilla, J. G., Fowler, M., & Ulinski, P. S. (1998). Responses of regular spiking and fast spiking cells in turtle visual cortex to light flashes. *Visual Neuroscience*, *15*(5), 979–93. Retrieved from http://www.ncbi.nlm.nih.gov/pubmed/9764539

Mazurskaya, P. (1973). Retinal projection in the forebrain ofEmys orbicularis. *Neuroscience and Behavioral Physiology*. Retrieved from http://link.springer.com/article/10.1007/BF01186006

Mazurskaya, P. Z. (1972). Organization of receptive fields in the forebrain of Emys orbicularis. *Neuroscience and Behavioral Physiology*, *6*(6), 311–318.

Mulligan, K. A., & Ulinski, P. S. (1990). Organization of geniculocortical projections in turtles: isoazimuth lamellae in the visual cortex. *Journal of Comparative Neurology*, *296*(4), 531–547. Retrieved from http://www.ncbi.nlm.nih.gov/pubmed/2358551

Prechtl, J. C. (1994). Visual motion induces synchronous oscillations in turtle visual cortex. *Proceedings of the National Academy of Sciences of the United States of America*, *91*(26), 12467–71. Retrieved from http://www.pubmedcentral.nih.gov/articlerender.fcgi?artid=45459&tool=pmcentrez&rendertype=abstract

Prechtl, J. C., & Bullock, T. H. (1994). Event-related potentials to omitted visual stimuli in a reptile. *Electroencephalography and Clinical Neurophysiology*, *91*, 54–66. doi:10.1016/0013-4694(94)90018-3

Prechtl, J. C., Bullock, T. H., & Kleinfeld, D. (2000). Direct evidence for local oscillatory current sources and intracortical phase gradients in turtle visual cortex. *Proceedings of the National Academy of Sciences of the United States of America*, *97*(2), 877–82. Retrieved from

http://www.pubmedcentral.nih.gov/articlerender.fcgi?artid=15424&tool=pmcentrez&rendertype=abstract

Prechtl, J. C., Cohen, L. B., Pesaran, B., Mitra, P. P., & Kleinfeld, D. (1997). Visual stimuli induce waves of electrical activity in turtle cortex. *Proceedings of the National Academy of Sciences of the United States of America*, *94*(14), 7621–6. Retrieved from http://www.pubmedcentral.nih.gov/articlerender.fcgi?artid=23872&tool=pmcentrez&rendertype=abstract

Romer, A. S. (1977). *Vertebrate Body*. (T. Parsons, Ed.) (5th ed.). W.B. Saunders Company.

Saha, D., Leong, K., Katta, N., & Raman, B. (2013). Multi-unit Recording Methods to Characterize Neural Activity in the Locust (Schistocerca Americana) Olfactory Circuits. *Journal of Visualized Experiments*, (January), 1–10. doi:10.3791/50139

Ulinski, P. S., & Nautiyal, J. (1988). Organization of retinogeniculate projections in turtles of the genera Pseudemys and Chrysemys. *The Journal of Comparative Neurology*, *276*(1), 92–112. doi:10.1002/cne.902760107

Wiltschko, A. B., Gage, G. J., & Berke, J. D. (2008). Wavelet Filtering before Spike Detection Preserves Waveform Shape and Enhances Single-Unit Discrimination. *Journal of Neuroscience*, *173*(1), 34–40. doi:10.1016/j.jneumeth.2008.05.016.Wavelet

Witter, M. P. (1993). Organization of the entorhinal-hippocampal system: a review of current anatomical data. *Hippocampus*, *3 Spec No*, 33–44. doi:10.1002/hipo.1993.4500030707

Xing, D., Yeh, C.-I., & Shapley, R. M. (2009). Spatial spread of the local field potential and its laminar variation in visual cortex. *The Journal of Neuroscience : The Official Journal of the Society for Neuroscience*, *29*(37), 11540–9. doi:10.1523/JNEUROSCI.2573-09.2009

Ziolo, M. S., & Bertelsen, M. F. (2009). Effects of propofol administered via the supravertebral sinus in red-eared sliders. *Journal of the American Veterinary Medical Association*, *234*, 390–393. doi:10.2460/javma.234.3.390

Chapter 3: Oscillations

Functional roles of rhythmic oscillations in cognition are still a matter of debate in the neuroscience community. They are generally thought of as a core mechanism in synchronizing brain signals through bursts of oscillations. Using time-frequency analyses of the local field potential (LFP) recorded from turtle primary visual cortex, we found a large variability from electrode-to-electrode and turtle-to-turtle. Results also indicate a broad distribution of oscillation durations (ranges up to 2 s) and peak frequencies with little or no correlation between these two quantities. Visual inspection doesn't reveal any qualitative discrepancies between ongoing and stimulus-evoked oscillations. These results were verified by our simulated network. This study suggest that neuronal oscillations in turtle primary visual cortex have a stochastic nature and aren't sufficiently reliable to serve as a communication signal.

3.1 Introduction

3.1.1 Motivation

Rhythmic oscillations have been found in many species and many brain structures (for a review see (X. Wang, 2010)). They have been discovered in cat neocortex (Bouyer, Montaron, & Rougeul, 1981), rat hippocampus (J Csicsvari, Hirase, Czurkó, Mamiya, & Buzsáki, 1999), human motor cortex and olfactory bulb (Adrian, 1950; Jasper & Penfield, 1949), visual and

auditory cortices of monkeys (Brosch, Budinger, & Scheich, 2002; Friedman-Hill, Maldonado, & Gray, 2000), and auditory cortex of rats (Franowicz & Barth, 1995) to name a few. Despite the fact that they have been studied extensively, the functional significance of these oscillations is still unclear. It has been hypothesized that rhythmic oscillations provide temporal windows for long-range communication between multiple regions (Buzsáki & Draguhn, 2004; Pascal Fries, Nikolić, & Singer, 2007; Pascal Fries, 2005; Gray & Singer, 1989; Lisman & Idiart, 1995). To this end the phase of the oscillations should be conserved over a period of time (autocoherent), which happens not to be the case (Burns, Xing, & Shapley, 2011; Burns, Xing, Shelley, & Shapley, 2010). Neuronal oscillations, however, exist even in brain slices (Cardin et al., 2009; Compte et al., 2008; Miles & Poncer, 1993; Whittington, Traub, & Jefferys, 1995).

3.1.2 Questions to address

To serve as a feature binding (Eckhorn et al., 1988) and phase coding signal, neuronal oscillations need to be similar and very reliable. The aim of this study is to address whether oscillations in primary visual cortex of turtles are coherent enough to function as a clock signal. There is a large controversy about the relationship between peak frequency and gamma band (30-100Hz) power in the cortex. On one hand, empirical relationships have been proposed (Henrie & Shapley, 2005; Lima, Singer, Chen, & Neuenschwander, 2010), but on the other hand, none of these relationships are consistent (Gieselmann & Thiele, 2008; Jia, Xing, & Kohn, 2013). Therefore, our study is particularly focused on characterizing oscillatory responses in V1 (primary visual cortex).

3.1.3 Structure of the Paper and Summary of Results

To address these questions, we recorded *ex vivo* from primary visual cortex in turtles using MEAs (micro electrode arrays). In line with previous work (Delano, Pavez, Robles, & Maldonado, 2008; D. Xing et al., 2012), a large variability of the duration and peak frequency of oscillatory bursts has been observed. Moreover, a large variation is seen between electrodes and preparations. Qualitative discrepancies between ongoing and stimulus-evoked oscillations are discussed. We recreated these dynamics in a network with recurrent connections, Poissonian inputs, and balanced excitation/inhibition. Using complex time-frequency analysis, we test the autocoherent oscillator (ACO) hypothesis for experimentally recorded LFPs and instantaneous population rate of the computational network.

3.2 Materials and Methods

3.2.1 Ex-vivo eye-attached whole-brain preparation

Adult red-ear turtles (Trachemys scripta elegans, 150-200g weight, 12-15cm carapace length) were used in this study. Procedures used in this study were approved by the Washington University Institutional Animal Care and Use Committee and conform to the guidelines of the National Institutes of Health on the Care and Use of Laboratory Animals. Rapid decapitation was performed after anesthetization with Propofol (10mg/kg) following established procedures (Ziolo & Bertelsen, 2009).

The brain was surgically removed from the skull with the right eye attached and continuously perfused with artificial cerebral spinal fluid bubbled with 5% carbogen. The anterior half of the right eye was removed to provide a clear path to project an image onto the

retina (Figure 3.1). Starting from the left olfactory bulb, a rostro-caudal incision was made along the medial cerebral hemisphere allowing us to unfold the cortex and expose the ventricular surface of the visual cortex.

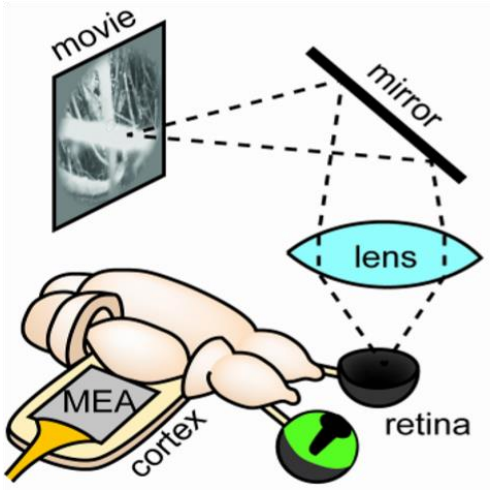

Figure 3.1: Turtle ex-vivo preparation. Visual stimuli are reflected off a mirror and focused on the retina with a lens placed above the tissue.

3.2.2 Visual Stimulation

For the included studies, three methods of visual stimulation were used:

LED Stimulation

For LED stimulation, a red LED was connected to the output of a National Instruments BNC-2090 terminal block connected to a National Instruments PCI-6024E DAQ board. This output was controlled with a custom LabView program on a computer running Windows 7.

Monitor/Mirror Stimulation

For monitor/mirror stimulation (Figure 3.1), a 19 LCD monitor (Samsung model Syncmaster T190) displayed the stimuli. This image was reflected off a mirror located across room above the tissue, and focused on the retina with a lens placed above the tissue.

Projector Stimulation

For projector stimulation, an AAXA P4 X projector was placed above the retina and focused with a system of lenses. Both monitor/mirror and projector stimulation was provided using software written in python on a computer running Ubuntu 10.4.

Visual stimuli included black dots moving on a white screen, naturalistic video, and red LED flashes.

3.2.3 MEA recordings and data acquisition

Data were collected at a 30 kHz sampling rate using the Cerebus data acquisition system by Blackrock Microsystems. Two different styles of microelectrode arrays were used for our recordings. For some recordings, we used a 96-channel array (10 × 10 square grid, 400μm interelectrode spacing, 500μm electrode length, no corner electrodes, Blackrock Microsystems). For others, we used an array of shank electrodes (4×4 array of shank electrodes with 8 recording sites on each electrode, 300μm and 400μm x and y distance between shanks and 100μm between recording sites along a shank). We attached either array to a post fastened to a micro-manipulator (Sutter, MP-285) and inserted the array to a depth of 500μm starting from the ventricular side of the unfolded cortex such that the plane of the tips of the electrodes was parallel to the dorsal surface of the cortex. We recorded wide-band (0.7–15 kHz) extracellular voltages relative to a silver chloride pellet electrode in the tissue bath.

3.3 Data Analysis

3.3.1 Burst Detection

To detect bursts of fluctuations in the LFP, we filtered the raw signal using 9 different 10 Hz wide passbands from 10 to 100 Hz. We then took the Hilbert transform of each of these filtered signals and normalized it by dividing by its mean value. Finally, we created a new signal by taking the maximum value from all 9 normalized Hilbert transforms at every time step. This new array indicates whether there was substantial activity in any of the 9 pass bands we considered. This signal was used to look for bursts of oscillations.

To do so we looked at all the crossing of both a high threshold (6 std) and a low threshold (4 std). Each time the signal crosses the high threshold it becomes part of a burst, and the onset (and offset) of each burst is defined by extending forward (and backward) in time from the high threshold crossing until more there is more than 250ms to the next low threshold crossing. The data used for burst duration distributions came for multihour recordings including a mixture of visually evoked and dark periods.

3.3.2 Relative Power

Taking the PSD of the voltage signal can be useful to learn about the spectral properties during that time, but there are a few drawbacks to simply looking at the PSD. Typically, when looking at an evoked response or any event of neural activity, we are interested in how that activity is different than the ongoing spontaneous activity. If we simply look at the PSD we don't get this information. For instance, if there were consistent ongoing high power in a band near 80 Hz, then seeing a peak at 80 Hz during a period of evoked activity would not indicate that any

information was carried by that high power. Also, if one wishes to look at the changes in power of many electrodes, one might be misled by different electrodes having different impedances. To deal with both of these issues, we define something called the relative power.

We examined visually evoked LFP responses to look for trends in the frequency profiles. Our primary measure of power at a given frequency is the relative power. The relative power is the power during a 2 s period after a stimulus onset divided by a baseline power (Figure 3.2). The baseline power was calculated by taking the average of the power spectral densities of all the 2 s periods before the stimulus onsets, during which any recorded activity was not visually evoked. To calculate the power spectral densities, we downsampled our recordings to 3 kHz and then performed multitaper (3 tapers) spectral estimations of 500 ms sliding windows (sliding by 50 ms) covering the 2 s periods. The average of powers from these sliding windows was used as the power to then calculate relative power from.

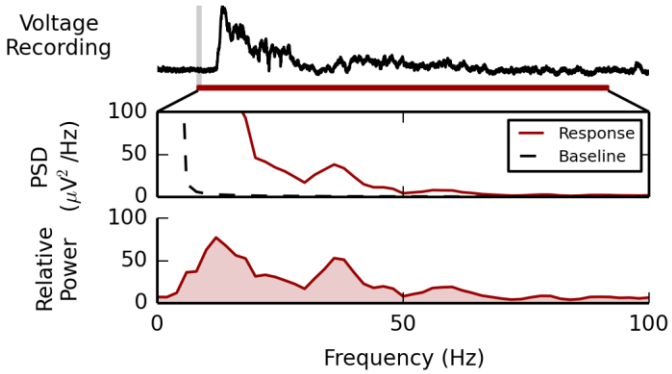

Figure 3.2: Relative power of a voltage recording. **(Top)** A 2 s sample extracellular voltage trace is shown. **(Middle)** The power spectral density of this signal (red curve) and of an average baseline (dashed curve). **(Bottom)** The relative power of this signal (relative to the average baseline).

3.3.3 Peak Frequency

To allow for the detection of peaks in relative power at more than one frequency for a single trial, we looked at more than simply the maximum value in the relative power. Instead, we started with all local maxima in relative power, and called any given maxima a peak frequencies if it met three conditions: 1) there must be a neighborhood around that frequency in which the relative power at some higher frequency (and lower frequency unless the neighborhood includes 0 Hz) was at most $\frac{1}{4}$ the relative power at the putative peak frequency, 2) in this neighborhood, the putative peak frequency must have the highest relative power, and 3) the relative power at the putative peak frequency must be at least 4 (i.e., the evoked power must be at least 4 times the baseline power).

3.3.4 Continuous Gabor Transform

The Fourier transform of a signal allows us to have frequency components with extremely high resolution. But, based on uncertainty principles, we lose all control on spatial duration: we know what frequency components exist in the signal, but we do not know when in time different components are triggered. To gain information about the temporal dynamics of the signal, we have to give up some frequency precision. The Gabor short-time Fourier transform is designed for this purpose. The signal is first multiplied by a window function, also called Gabor filter, and the resulting signal is Fourier transformed to render the time-frequency content.

$$G_x(t,f) = \int_{-\infty}^{\infty} d\tau x(\tau)\psi(\tau - t, f) = R(t,f)e^{j\phi(t,f)} \quad (1)$$

where x(t) is the signal to be transformed. The Gabor filter can be defined as follows

$$\psi(t,f) = \frac{1}{\sigma\sqrt{2\pi}} e^{-\frac{(t-t_0)^2}{2\sigma^2}} e^{-j2\pi ft} \quad (2)$$

where t_0 and σ are the center and temporal extent of the window function.

The Continuous Gabor Transform (CGT) results in a complex matrix with its absolute values as power and its phases as the phase of the signal for that time and frequency component. Using these values, parametric trajectories can be plotted in polar coordinate with the radius as the amplitude and phase of the complex numbers during time. We define a frequency component that can be modeled as a sinusoidal function with a fixed phase as autocoherent (ACO). For ACO signals, parametric trajectories with residual phase (sinusoidal phase subtracted from original phase) should be confined to a region in the plot. Circular variation (CV) is a measure of localization of trajectories in phase portrait and can be it can be defined as,

$$CV(f) = 1 - \left|\frac{\Sigma_t R(t,f) e^{j\phi(t,f)}}{\Sigma_t R(t,f)}\right| \quad (3)$$

CV is always normalized to be between zero and one, with zero for the most coherent (sinusoidal) and one for completely random signals (Burns et al., 2010).

3.4 Computational Model

We used a network model of leaky integrate-and-fire cortical neurons. This network model was composed of three neuronal populations: 2000 regular spiking (RS) pyramidal neurons, 250 fast spiking (FS) interneurons, and 250 low-threshold spiking (LTS) interneurons. The connections are random and all connections, except inhibition from FS on LTS, are present. Using electrophysiological data, RS, FS, and LTS impacts were modeled as AMPA, fast, and slow GABA currents respectively. Detailed values are shown for each figure separately.

Thalamo-cortical inputs were provided as Poisson-like spike trains for all three populations and modeled as AMPA currents. Network activity is defined using the instantaneous population rate, which is obtained by summing over all spikes from all neurons in 0.5 ms time bins. This is analogous to the experimentally recorded LFP.

3.5 Results

3.5.1 Variability in Oscillatory Bursts

The relative power at a given frequency represents the extent to which the power in that frequency has increased beyond an average baseline level calculated from periods without stimuli. Figure 3.3 shows recordings from four nearby electrodes in response to 50 ms red LED flashes. The top plot shows 1 s voltage traces with their relative power shown immediately belowe. Beneath that, the relative power is shown for 30 more trials and the average relative powers are shown in the last row. Interestingly, the relative power often has peaks within narrow frequency bands, and multiple peaks can be present simultaneously. It is useful to think of each peak as being generated by some neural circuit. Several types of variability in the peak frequencies are worth mentioning:

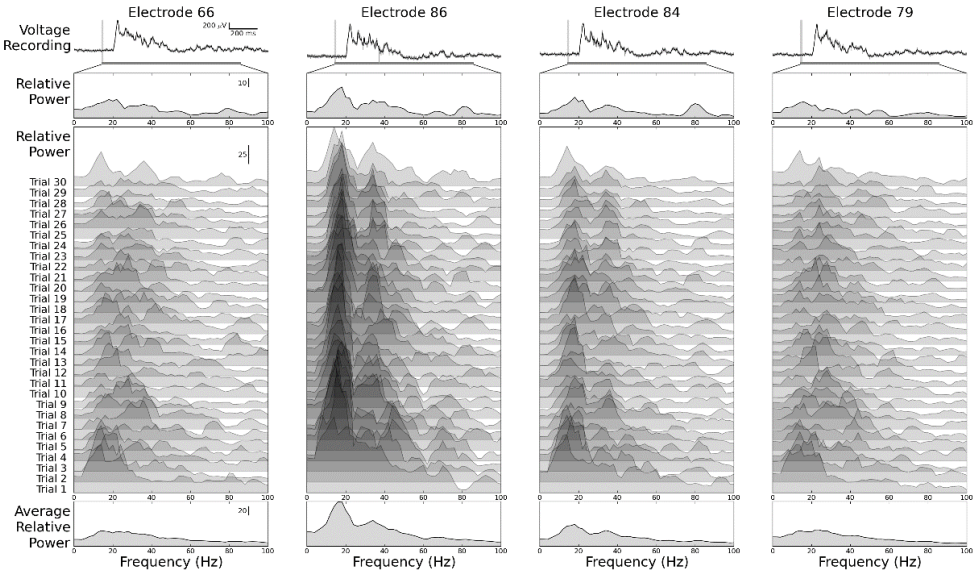

Figure 3.3 Variability in oscillatory bursts. Recordings from four nearby electrodes in response to 50 ms red LED flashes. The top plot shows one second voltage traces with their relative power plotted for that single trial in second row. Beneath that, the relative power is shown for 30 more trials and the last row shows the average relative powers over all trials.

Trial-to-Trial Variability

Each set of 30 repeated trials demonstrate that there can be significant trial-to-trial variability. While there is consistently an increase in power at some low frequency, the sharpness of the peak frequencies and the centers of those peaks vary from trial to trial. Often, there are certain frequencies that have high relative powers in most trials but not all. This suggests that there is a neural network that is typically activated by the given stimulus, but occasionally it is either inactive or overwritten by a more active network motif.

Electrode-to-Electrode Variability

For a single trial, peaks in relative power are often shared with nearby electrodes, but different peaks may see their maximal relative power at different electrodes. In some instances two distant electrodes may share peaks that do not show up on electrodes in between. In some

data sets, it appears that one subset of electrodes tends to have a specific peak frequency, while another subset tends to have a different peak frequency. These electrode subsets often overlap. More detailed correlation exists between electrodes in the time domain using narrow filters corresponding to the frequency bands identified by the relative power plots.

Another type of variability not indicated by figure 3.3 is stimulus-to-stimulus variability. There could be a huge variability in relative power peaks in response to different stimuli presented (data not shown). All these variability types indicate the versatile functional roles of oscillatory bursts in information processing in visual cortex.

3.5.2 Duration Distributions

Understanding the role of oscillation variability in cognitive processes requires characterizing properties of oscillatory epochs. This also helps in constructing computational models. Considering the synchronizing role for neuronal oscillations in the brain, raises a question about the existence of a characteristic duration and frequency for oscillation epochs. Neuronal rhythms should last as long as the brain is processing information while frequency should remain unchanged.

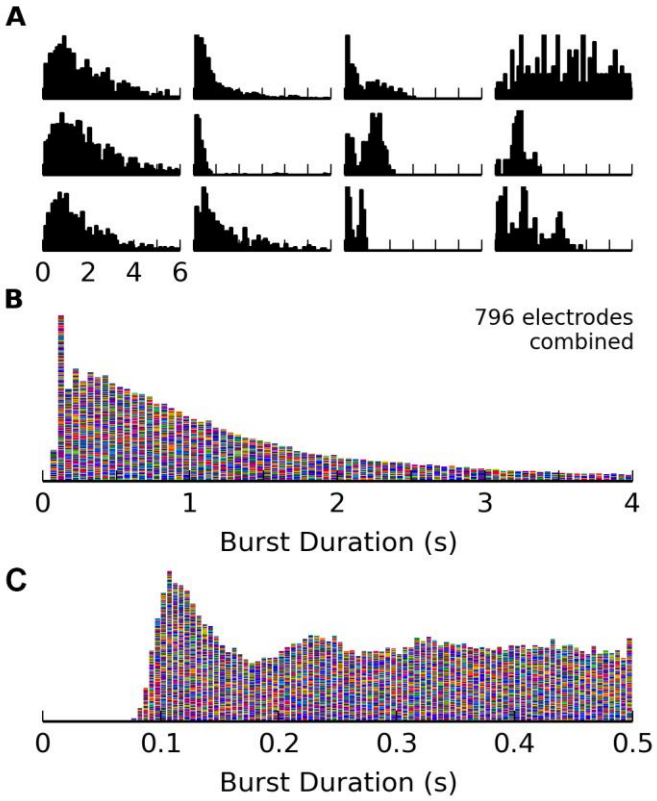

Figure 3.4 Burst duration distributions. **(A)** Burst duration distributions for a single electrode from twelve different turtles. They have been arranged by column purely by visual inspection to demonstrate a few recurring features: a broad, gamma-like distribution peaked at duration near 1 s; a narrow distribution with most bursts being less than 1 s; bimodal distributions; and three other distributions without any particular common feature simply to further illustrate the diversity of burst duration distributions. **(B)** The distribution of the burst durations from 796 electrodes recorded from 51 turtles combined with 50 ms bins for the histogram. The contribution from each turtle is colored differently from the others near it, by simply cycling through 8 colors. **(C)** The same data shown in (B) zoomed in to show just the first 500 ms of the response using 5 ms bins for the histogram.

Using the Hilbert transform (see Materials and Methods, Burst detection), we explored patterns in burst duration profiles. Figures 3.4A,B show duration profiles for 796 electrode recordings from 51 turtles. Burst duration distributions for a set of 12 electrodes are shown in figure 3.4A. A few recurring features are seen in these 12 distributions: a broad, gamma-like distribution peaked at duration near 1 s; a narrow, exponential-like distribution with most bursts being less than 1 s; bimodal distributions with most bursts being less than 2s; along with three

other distributions without any particular common feature simply to further illustrate the diversity of burst duration distributions.

While we see clear and sometimes complicated structure in the distributions for individual electrodes, the combined distribution of many electrodes has a simpler structure and can be described quite simply. Figures 3.4B,C show the distribution of the bursts from 51 turtles (total 796 electrodes) combined. When combining this many distributions, the main feature that persists is the dominance of short bursts.

An added benefit of using this larger data set is that we have enough data to increase our temporal precision. In Figure 3.4B, at the resolution used to bin the data, it's unclear if the first few bins are following much of a trend. By decreasing our bin size to 5 ms and zooming in to just the first 500 ms of the distribution, we can see smoother patterns, the peaks of which may correspond to common stereotypical distributions for individual electrodes.

The speculation is that there could be a space dependence for oscillation features. Since we recorded from a slightly different location each time, we would end up with different duration distributions. Another possibility could be that different internal states of the brain at the time of presenting the stimulus might differentially affect burst durations. Brain response is a complex interaction of inputs from sensory systems combined with the spontaneous activity (the internal state) of the brain at that time. Because we have no control over the internal state, we expect a variety of responses even when presenting the same stimulus.

3.5.3 Peak Frequency Distributions

Duration variability shouldn't be an issue on its, own especially when durations are an order of magnitude longer than the time scale on which neuronal circuits process information and oscillations can still be used as a long range communication and linking means. However, *frequency* variability could have an adverse impact on the function of oscillations in the cortex. We examined visually evoked LFP responses to look for patterns in the frequency profiles. Our primary measure of power at a given frequency is the relative power (see Materials and Methods, Relative power). Using our approach (see Material and Methods, Peak frequency) we were able to detect peaks in relative power at more than one frequency for a single trial. Distributions of relative power peak frequencies for a single electrode from twelve different turtles are shown in figure 3.5. At first glance, the diversity of profiles is noticeable. Profiles have been arranged to demonstrate a few recurring features: a broad distribution of peak frequencies primarily between 10 Hz and 40 Hz with a gamma-like distribution; a very narrow distribution less than 20 Hz; a narrow distribution less than 20 Hz along with occasional peak frequencies covering a broad range of frequencies; and three additional distributions to further demonstrate the diversity of distributions.

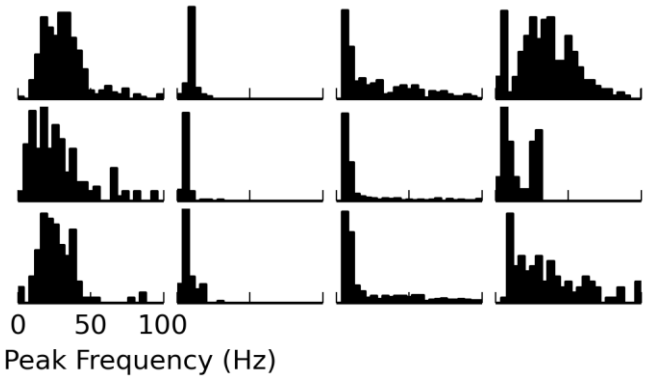

Figure 3.5 Distributions of relative power peak frequencies. Distributions shown for twelve single electrodes from twelve different turtles. They have been arranged to demonstrate a few recurring features: a broad distribution of peak frequencies primarily between 10 Hz and 40 Hz; a narrow distribution less than 20 Hz; a narrow distribution less than 20 Hz along with occasional peak frequencies covering a broad range of frequencies; and three additional distributions to further demonstrate the diversity of peak frequency distributions.

3.5.4 Test of autocoherency

Here we tested to see whether oscillations have the properties of a ”clock” signal. A deterministic mechanism can lead to ACO oscillation, which provides a unique reference time for precise temporal encoding of visual information. The reason for our focus is that ACO oscillations are immensely supported by experimental data (Jozsef Csicsvari, Jamieson, Wise, & Buzsáki, 2003; Gray & Singer, 1989). Thus, the result of this test helps to keep or rule out many computational models and clarifies the situation.

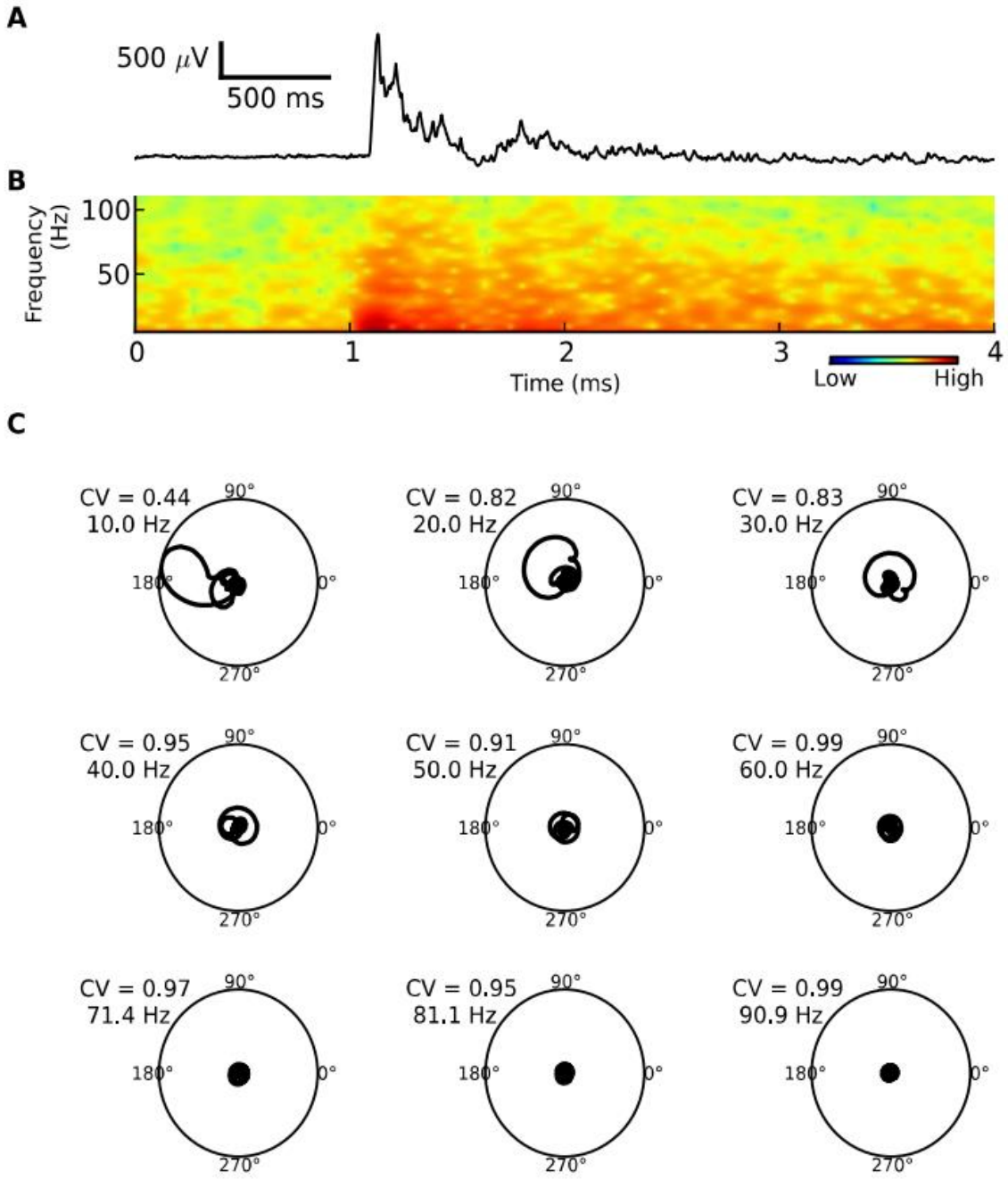

Figure 3.6 Non-autocoherency of oscillatory bursts. **(A)** A 4 s voltage trace from one of the electrodes. A 10 ms red flash is triggered at 1 s. **(B)** Power spectrum of the signal for frequencies less than 100 Hz. It shows an increase in power at the onset of the stimulus. **(C)** Parametric phase portraits of the data shown in A for frequencies from 10 to 100 Hz with the increments of 10 Hz. Exact frequency and CV are shown at the top of the polar plots.

To this end, we use a time-frequency analysis method first proposed by Burns et al. (Burns et al., 2010). Their ACO test for the data from monkey V1 showed that oscillations in the gamma-band don't have the properties of a "clock" signal. Moreover, they showed that ACO signals exist in EEG recordings in alpha rhythms. To quantify autocoherency, they used circular variation (CV; see Methods and Materials) as a measure of localization of parametric paths in phase space. The CV is the ratio of the average complex coefficients from CGT normalized by the average amplitudes of the coefficients. A CV close to zero indicates that trajectories are localized in a sector of space and phase is nearly conserved, an ACO oscillation. A CV close to one implies that the phase path is wandering all over the space and oscillations are non-ACO.

Figure 3.6 shows the results for a 4 s LFP trace from turtle V1. For the LFP trace shown in figure 3.6A, a 10 ms red LED flash was presented at one second. Figure 3.6B shows the power spectrum of this trace for a wide range of frequencies (5 Hz - 110 Hz). This plots shows an elevation in the alpha and gamma frequency bands. Phase portraits are plotted in polar coordinates and are shown in Figure 3.6C. Frequency for each parametric trajectory is listed at its top with a CV value. The radius of the trajectories is the amplitude of the coefficients, which are actually the square root of the power, and the phase is the phase of the coefficients with phase of a pure sine wave subtracted. Except for the alpha band all other CVs are very large and close to one, which indicates non-ACO of oscillations in the gamma band. However, ACO oscillations have been observed in rat hippocampus on shorter time scales, ~100 ms (Montgomery & Buzsáki, 2007; Montgomery, Sirota, & Buzsáki, 2008). Therefore, we also tested CV values during just elevated power, from 1 s to 1.5 s period, and the results were robust.

Figure 3.7 shows histograms of CVs for 9 frequency bands over a large number of recording sessions (3146). Each histogram is for 2 sec of LFP recording in response to LED

flashes. CVs are widely distributed from 0.3 to 1 in the alpha band (10 Hz – 30 Hz) with a slightly left-skewed distribution. This fails to reject autocoherency of oscillations and thus, there isn't a conclusive result on autocoherency of oscillations. In contrast, very sharp distributions of CVs close to 1 indicate the nonautocoherency of oscillations in gamma band frequencies. These results, which are in line with those presented in Burns et al. 2010 (Burns et al., 2010), indicate that gamma-band rhythms cannot be trusted as a unique reference time in time scales of 500 ms, but alpha-band oscillations can function as a clock signal in order to synchronize distant brain regions and help to bind features of visual stimuli.

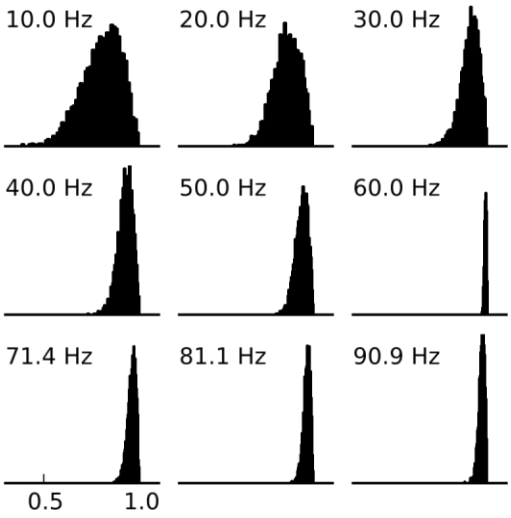

Figure 3.7 CV histograms for alpha and gamma rhythms. Each inset is a CV histogram for 3146 instances of 2 sec LFP recordings in response to 10 ms red LED flashes at the frequency listed on its top. Broad distributions of CVs in alpha-band (10-30 Hz) fail to reject autocoherency of oscillations. In contrast, very sharp distribution of CVs indicates the non-autocoherency of oscillations.

3.6 Computational Model Results

3.6.1 Duration and Peak Frequency PDF

The computational model is built with three types of cells: one excitatory and two interneuron types (see Materials and Methods). In other work (being prepared for publication) we showed that changing the LTS time constants changes the duration of oscillations but keeps frequency intact and, on the other hand, changing the FS time constants affects the frequency but not the duration. With that in mind, for this study, we ascribe normally distributed values to each time constant. All other parameters used for this study are the same as that previous work. These parameters lead to a broad duration distribution comparable to what we've seen from experiment. However, it is incapable of generating a wide distribution of frequencies from alpha to gamma band. Figure 3.8B shows a normal distribution of frequencies (57 ± 11, mean ± std). Another aspect of the data that cannot be seen in the model results is the variability in the shape of the distributions. Figure 3.8A and B are the typical, if not only, shapes that can be produced in the model.

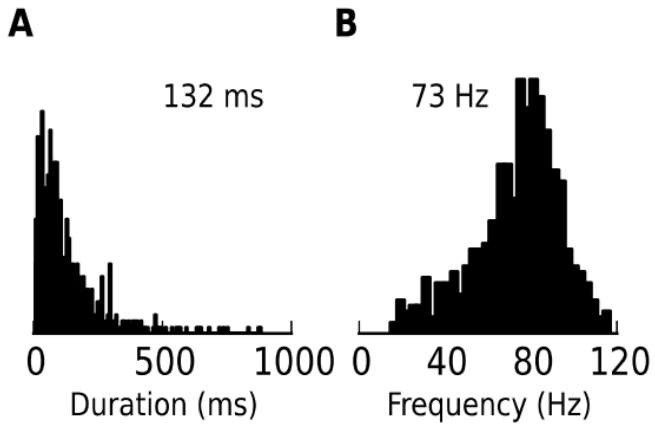

Figure 3.8 Duration and peak frequency distribution in simulated model. **(A)** Drawing rise and decay time constants in FS and LTS cells from normal distributions broadens the duration PDF of population rate signal. **(B)** Distributed time constants also shift the peak frequency distribution to lower values with the mean in the middle of gamma band. For both insets time constants are as follows (mean ± std): LTS rise 10 ± 2, LTS decay 70 ± 15, FS rise 2 ± 0.3, FS decay 10 ± 1

3.6.2 Test of ACO

We showed that recorded LFP activity doesn't show ACO in gamma-band, but does show ACO in alpha-band. Now we test the concept that a deterministic oscillation underlies the alpha- and gamma-band peaks observed in the population rate signal of the model. The clock hypothesis is a prominent observation in experimental studies of wide-band generally and gamma-band specifically. Therefore, it is a crucial criterion to narrow down all neuronal network models and proposed mechanisms for generating oscillations to a handful of them.

This test has been done in other work we are preparing for publication. The network shows an epoch of oscillation around 60 Hz while CVs for all frequency bands from 20–100 Hz are very close to one, which indicates that oscillations are nonACO. This model is able to capture this feature of oscillations by having a stochastic mechanism for generating variable phase rhythms. It predicts that, for a constant visual (external) input, the time-scale on which oscillations are ACO is set by the internal dynamics of the network, which are obviously shorter

than the time scale of persistent activity (~1 s). However, the model is incapable of generating ACO alpha rhythms. Randomness of duration and peak frequency observed for recorded LFPs, can be fulfilled by having a noisy external input to the neurons of the network. We believe that this noise has a critical role in generating alpha- and gamma-band peaks with variable phase. Another sophisticated mechanism is needed to lead to ACO alpha-band activity.

3.7 Discussion

3.7.1 Results Summary

This study is a comprehensive assessment of neuronal oscillations of turtle V1 cortex in terms of their power, duration, peak frequency, and phase. Results indicate that a huge variability exists among electrodes and trials. This pertains to the information processing happening in underlying neuronal circuits and the state of the cortex at that time. Large variability can be seen from stimulus-to-stimulus as well (data not shown). Huge variability seen in duration and peak frequencies disallows straightforward functional roles for oscillations. Non-ACO of oscillations prevents the brain from using gamma-band oscillatory epochs as a means to synchronize distant brain regions on long time scales of ~500 ms. However, there are two points worth mentioning. First of all, temporally unstructured dynamics could be resolved on shorter time scales of 100 ms, on which gamma oscillations could be a clock signal. Second, our analysis doesn't reject the possibility of alpha-band rhythms to be ACO and to be used as a universal reference time. This raises a very important question: what are the functional roles of gamma-band oscillations? Moreover, what approaches should be taken to evaluate functional roles of oscillations in general?

3.7.2 Underlying Mechanisms for Oscillations

The simplest mechanism that can be devised for generation of oscillations in any frequency band in the LFP is a network of cells rhythmically firing at that frequency. However, experimental work suggest that neurons fire irregularly (J Csicsvari et al., 1999; P Fries, Reynolds, Rorie, & Desimone, 2001) and sparsely (J Csicsvari et al., 1999; Jozsef Csicsvari et al., 2003; Engel, Koning, Gray, & Singer, 1990) even when oscillations are present in the LFP signals of the network. Theoreticians showed that ACO oscillations emerge in a population of inhibitory neurons (X. J. Wang & Rinzel, 1993; X.-J. Wang & Rinzel, 1992). These early models indicated that recurrent interaction among inhibitory cells is the key underlying mechanism for the emergence of oscillations (Skinner, Kopell, & Marder, 1994). Numerous models included both excitatory and inhibitory cells proposed for generation of oscillations especially in gamma bands (N Brunel & Hakim, 1999; Nicolas Brunel & Wang, 2003; Geisler, Brunel, & Wang, 2005; X J Wang, Golomb, & Rinzel, 1995). All these models demonstrate ACO oscillations in which phase is conserved over a period of time determined by the quality of external drive since they use a deterministic mechanism for generating oscillations (Burns et al., 2010).

3.7.3 Functional Implications of the Variability of Oscillations

During the past two decades, a surge of research on oscillations has happened and a wealth of promising papers have been published discussing how cortical oscillations may contribute to cognitive functions (Başar, Başar-Eroglu, Karakaş, & Schürmann, 2000; Başar, 1999; Herrmann, Munk, & Engel, 2004; Ward, 2003) (for a review on oscillation functional roles see (X. Wang, 2010)). One hypothesis for the role of neural oscillations is the concept of phase coding (G. Buzsaki & Chrobak, 1995; Buzsáki & Draguhn, 2004; Gyorgy Buzsaki, 2006; Pascal

Fries et al., 2007; Harvey, Collman, Dombeck, & Tank, 2009). This hypothesis states that the timing of spikes with respect to the phase of ongoing network oscillations carries information about the presented stimulus. Another essential role that has been conceived for rhythmic oscillations is that they serve as a ”clock” signal (Pascal Fries et al., 2007; Pascal Fries, 2005; Lisman & Idiart, 1995; Singer & Gray, 1995). In this view, the brain uses oscillations for precise temporal encoding and for this purpose, the phase of the oscillations should be conserved during evoked response.

Some studies, on the other hand, show that gamma-band activity is a stochastic process and is too random to serve as a clock signal for synchronizing brain regions over the length of the stimulus (Burns et al., 2011, 2010; D. Xing et al., 2012). Their experimental results (D. Xing et al., 2012) indicate that gamma activity has an identical temporal structure in both awake and anesthetized monkeys and their modeling results, in line with others (Kang, Shelley, Henrie, & Shapley, 2010), suggest that gamma-band dynamics could be replicated in a recurrent network with Poisson-distributed inputs and is unlikely to be a reference time. Another study (Ray & Maunsell, 2010) also shows that gamma-band activity is unlikely to serve as a feature binding signal in visual cortex, since neighboring sites have a different frequency profile in response to a single Gabor patch. To resolve this old-standing controversy and evaluate the importance of oscillations in neuronal circuits, a real-time analysis should be done while controlling the occurrence of oscillations (Rutishauser, Kotowicz, & Laurent, 2013). Using this approach while the animal is performing a task, the roles of oscillations can be explored.

3.8 References

Adrian, E. D. (1950). The electrical activity of the mammalian olfactory bulb. *Electroencephalography and Clinical Neurophysiology*, *2*, 377–388. doi:10.1016/0013-4694(50)90075-7

Başar, E. (1999). Brain Function and Oscillations Volume II: Integrative Brain Function. Neurophsyioloy and Cognitive Processes. *Springer Series in Synergetics*.

Başar, E., Başar-Eroglu, C., Karakaş, S., & Schürmann, M. (2000). Gamma, alpha, delta, and theta oscillations govern cognitive processes. *International Journal of Psychophysiology*, *39*, 241–248. doi:10.1016/S0167-8760(00)00145-8

Bouyer, J. J., Montaron, M. F., & Rougeul, A. (1981). Fast fronto-parietal rhythms during combined focused attentive behaviour and immobility in cat: cortical and thalamic localizations. *Electroencephalography and Clinical Neurophysiology*, *51*(78), 244–252. doi:10.1016/0013-4694(81)90138-3

Brosch, M., Budinger, E., & Scheich, H. (2002). Stimulus-related gamma oscillations in primate auditory cortex. *Journal of Neurophysiology*, *87*, 2715–2725. doi:10.1152/jn.00583.2001

Brunel, N., & Hakim, V. (1999). Fast global oscillations in networks of integrate-and-fire neurons with low firing rates. *Neural Computation*, *11*, 1621–1671. doi:10.1162/089976699300016179

Brunel, N., & Wang, X.-J. (2003). What determines the frequency of fast network oscillations with irregular neural discharges? I. Synaptic dynamics and excitation-inhibition balance. *Journal of Neurophysiology*, *90*(1), 415–30. doi:10.1152/jn.01095.2002

Burns, S. P., Xing, D., & Shapley, R. M. (2011). Is gamma-band activity in the local field potential of V1 cortex a "clock" or filtered noise? *The Journal of Neuroscience : The Official Journal of the Society for Neuroscience*, *31*(26), 9658–9664. doi:10.1523/JNEUROSCI.0660-11.2011

Burns, S. P., Xing, D., Shelley, M. J., & Shapley, R. M. (2010). Searching for autocoherence in the cortical network with a time-frequency analysis of the local field potential. *The Journal of Neuroscience : The Official Journal of the Society for Neuroscience*, *30*(11), 4033–4047. doi:10.1523/JNEUROSCI.5319-09.2010

Buzsaki, G. (2006). *Rhythms of the Brain*. Oxford University Press.

Buzsaki, G., & Chrobak, J. J. (1995). Temporal structure in spatially organized neuronal ensembles: A role for interneuronal networks. *Current Opinion in Neurobiology*, *5*, 504–510. doi:10.1016/0959-4388(95)80012-3

Buzsáki, G., & Draguhn, A. (2004). Neuronal oscillations in cortical networks. *Science (New York, N.Y.)*, *304*(2004), 1926–1929. doi:10.1126/science.1099745

Cardin, J. A., Carlén, M., Meletis, K., Knoblich, U., Zhang, F., Deisseroth, K., … Moore, C. I. (2009). Driving fast-spiking cells induces gamma rhythm and controls sensory responses. *Nature*, *459*(7247), 663–7. doi:10.1038/nature08002

Compte, A., Reig, R., Descalzo, V. F., Harvey, M. A., Puccini, G. D., & Sanchez-Vives, M. V. (2008). Spontaneous high-frequency (10-80 Hz) oscillations during up states in the cerebral cortex in vitro. *The Journal of Neuroscience : The Official Journal of the Society for Neuroscience*, *28*(51), 13828–13844. doi:10.1523/JNEUROSCI.2684-08.2008

Csicsvari, J., Hirase, H., Czurkó, A., Mamiya, A., & Buzsáki, G. (1999). Oscillatory coupling of hippocampal pyramidal cells and interneurons in the behaving Rat. *The Journal of Neuroscience : The Official Journal of the Society for Neuroscience*, *19*(1), 274–287.

Csicsvari, J., Jamieson, B., Wise, K. D., & Buzsáki, G. (2003). Mechanisms of gamma oscillations in the hippocampus of the behaving rat. *Neuron*, *37*, 311–322. doi:10.1016/S0896-6273(02)01169-8

Delano, P. H., Pavez, E., Robles, L., & Maldonado, P. E. (2008). Stimulus-dependent oscillations and evoked potentials in chinchilla auditory cortex. *Journal of Comparative Physiology. A, Neuroethology, Sensory, Neural, and Behavioral Physiology*, *194*(8), 693–700. doi:10.1007/s00359-008-0340-4

Eckhorn, R., Bauer, R., Jordan, W., Brosch, M., Kruse, W., Munk, M., & Reitboeck, H. J. (1988). Coherent oscillations: a mechanism of feature linking in the visual cortex? Multiple electrode and correlation analyses in the cat. *Biological Cybernetics*, *60*, 121–130. doi:10.1007/BF00202899

Engel, A. K., Koning, P., Gray, C. M., & Singer, W. (1990). Stimulus-dependent neuronal oscillations in cat visual cortex: Inter-columnar interaction as determined by cross-correlation analysis. *European Journal of Neuroscience*, *2*, 588–606. doi:10.1111/j.1460-9568.1990.tb00449.x

Franowicz, M. N., & Barth, D. S. (1995). Comparison of evoked potentials and high-frequency (gamma-band) oscillating potentials in rat auditory cortex. *Journal of Neurophysiology*, *74*(1), 96–112.

Friedman-Hill, S., Maldonado, P. E., & Gray, C. M. (2000). Dynamics of striate cortical activity in the alert macaque: I. Incidence and stimulus-dependence of gamma-band neuronal oscillations. *Cerebral Cortex (New York, N.Y. : 1991)*, *10*, 1105–1116. doi:10.1093/cercor/10.11.1105

Fries, P. (2005). A mechanism for cognitive dynamics: Neuronal communication through neuronal coherence. *Trends in Cognitive Sciences*, *9*(10), 474–480. doi:10.1016/j.tics.2005.08.011

Fries, P., Nikolić, D., & Singer, W. (2007). The gamma cycle. *Trends in Neurosciences*, *30*(7), 309–16. doi:10.1016/j.tins.2007.05.005

Fries, P., Reynolds, J. H., Rorie, A. E., & Desimone, R. (2001). Modulation of oscillatory neuronal synchronization by selective visual attention. *Science (New York, N.Y.)*, *291*(5508), 1560–3. doi:10.1126/science.291.5508.1560

Geisler, C., Brunel, N., & Wang, X.-J. (2005). Contributions of intrinsic membrane dynamics to fast network oscillations with irregular neuronal discharges. *Journal of Neurophysiology*, *94*, 4344–4361. doi:10.1152/jn.00510.2004

Gieselmann, M. A., & Thiele, A. (2008). Comparison of spatial integration and surround suppression characteristics in spiking activity and the local field potential in macaque V1. *The European Journal of Neuroscience*, *28*(3), 447–59. doi:10.1111/j.1460-9568.2008.06358.x

Gray, C. M., & Singer, W. (1989). Stimulus-specific neuronal oscillations in orientation columns of cat visual cortex. *Proceedings of the National Academy of Sciences of the United States of America*, *86*(5), 1698–702. Retrieved from http://www.pubmedcentral.nih.gov/articlerender.fcgi?artid=286768&tool=pmcentrez&rendertype=abstract

Harvey, C. D., Collman, F., Dombeck, D. A., & Tank, D. W. (2009). Intracellular dynamics of hippocampal place cells during virtual navigation. *Nature*, *461*(7266), 941–946. doi:10.1038/nature08499

Henrie, J. A., & Shapley, R. (2005). LFP Power Spectra in V1 Cortex : The Graded Effect of Stimulus Contrast, 479–490. doi:10.1152/jn.00919.2004.

Herrmann, C. S., Munk, M. H. J., & Engel, A. K. (2004). Cognitive functions of gamma-band activity: Memory match and utilization. *Trends in Cognitive Sciences*, *8*(8), 347–355. doi:10.1016/j.tics.2004.06.006

Jasper, H., & Penfield, W. (1949). Electrocorticograms in man: effect of voluntary movement upon the electrical activity of the precentral gyrus. *Archiv Für Psychiatrie Und Nervenkrankheiten*, *183*(1-2), 163–174.

Jia, X., Xing, D., & Kohn, A. (2013). No Consistent Relationship between Gamma Power and Peak Frequency in Macaque Primary Visual Cortex. *The Journal of Neuroscience*, *33*(1), 17–25. doi:10.1523/JNEUROSCI.1687-12.2013

Kang, K., Shelley, M., Henrie, J. A., & Shapley, R. (2010). LFP spectral peaks in V1 cortex: network resonance and cortico-cortical feedback. *Journal of Computational Neuroscience*, *29*(3), 495–507.

Lima, B., Singer, W., Chen, N.-H., & Neuenschwander, S. (2010). Synchronization dynamics in response to plaid stimuli in monkey V1. *Cerebral Cortex (New York, N.Y. : 1991)*, *20*(7), 1556–73. doi:10.1093/cercor/bhp218

Lisman, J. E., & Idiart, M. A. P. (1995). Storage of 7 plus/minus 2 short term memories in oscillatory subcycles. *Science*, *267*, 5203.

Miles, R., & Poncer, J. C. (1993). Metabotropic glutamate receptors mediate a post-tetanic excitation of guinea-pig hippocampal inhibitory neurones. *The Journal of Physiology*, *463*, 461–473.

Montgomery, S. M., & Buzsáki, G. (2007). Gamma oscillations dynamically couple hippocampal CA3 and CA1 regions during memory task performance. *Proceedings of the National Academy of Sciences of the United States of America*, *104*(36), 14495–14500. doi:10.1073/pnas.0701826104

Montgomery, S. M., Sirota, A., & Buzsáki, G. (2008). Theta and gamma coordination of hippocampal networks during waking and rapid eye movement sleep. *The Journal of Neuroscience : The Official Journal of the Society for Neuroscience*, *28*(26), 6731–6741. doi:10.1523/JNEUROSCI.1227-08.2008

Ray, S., & Maunsell, J. H. R. (2010). Differences in gamma frequencies across visual cortex restrict their possible use in computation. *Neuron*, *67*(5), 885–96. doi:10.1016/j.neuron.2010.08.004

Rutishauser, U., Kotowicz, A., & Laurent, G. (2013). A method for closed-loop presentation of sensory stimuli conditional on the internal brain-state of awake animals. *Journal of Neuroscience Methods*, *215*(1), 139–55. doi:10.1016/j.jneumeth.2013.02.020

Singer, W., & Gray, C. M. (1995). Visual feature integration and the temporal correlation hypothesis. *Annual Review of Neuroscience*, *18*, 555–586. doi:10.1146/annurev.ne.18.030195.003011

Skinner, F. K., Kopell, N., & Marder, E. (1994). Mechanisms for oscillation and frequency control in reciprocally inhibitory model neural networks. *Journal of Computational Neuroscience*, *1*, 69–87. doi:10.1007/BF00962719

Wang, X. (2010). Neurophysiological and Computational Principles of Cortical Rhythms in Cognition. *Physiological Reviews*, *90*(3), 1195–1268. doi:10.1152/physrev.00035.2008.

Wang, X. J., Golomb, D., & Rinzel, J. (1995). Emergent spindle oscillations and intermittent burst firing in a thalamic model: specific neuronal mechanisms. *Proceedings of the National Academy of Sciences of the United States of America*, *92*(June), 5577–5581. doi:10.1073/pnas.92.12.5577

Wang, X. J., & Rinzel, J. (1993). Spindle rhythmicity in the reticularis thalami nucleus: Synchronization among mutually inhibitory neurons. *Neuroscience*, *53*(4), 899–904. doi:10.1016/0306-4522(93)90474-T

Wang, X.-J., & Rinzel, J. (1992). Alternating and Synchronous Rhythms in Reciprocally Inhibitory Model Neurons. *Neural Computation*. doi:10.1162/neco.1992.4.1.84

Ward, L. M. (2003). Synchronous neural oscillations and cognitive processes. *Trends in Cognitive Sciences*, *7*(12), 553–559. doi:10.1016/j.tics.2003.10.012

Whittington, M. A., Traub, R. D., & Jefferys, J. G. R. (1995). Synchronized oscillations in interneuron networks driven by metabotropic glutamate receptor activation. *Nature*, *373*(6515), 612–615.

Xing, D., Shen, Y., Burns, S., Yeh, C.-I., Shapley, R., & Li, W. (2012). Stochastic Generation of Gamma-Band Activity in Primary Visual Cortex of Awake and Anesthetized Monkeys. *Journal of Neuroscience*, *32*(40), 13873–13880. doi:10.1523/JNEUROSCI.5644-11.2012

Ziolo, M. S., & Bertelsen, M. F. (2009). Effects of propofol administered via the supravertebral sinus in red-eared sliders. *Journal of the American Veterinary Medical Association*, *234*, 390–393. doi:10.2460/javma.234.3.390

Chapter 4: Neuronal Avalanches

Adaptation maintains cortical neuronal networks in a dynamic state that is thought to optimize aspects of sensory information processing. Although adaptation depends on multi-scale interactions among many neurons, most previous work has focused on single neurons; how adaptation manifests at the population level is largely unknown. Here we measured population activity in visual cortex during visual stimulation. At stimulus onset, large-scale activity was dominant; during adaptation, diverse multi-scale activity emerged. Emergence of multi-scale activity during adaptation was reproduced in a computational model with external inputs and synaptic depression. In the model, adaptation tunes the system towards the boundary of two regimes: one with dominant large-scale activity, the other with dominant small-scale activity. Near this regime boundary, activity has no dominant scale, exhibits power-law statistics, and follows specific scaling laws. Our experiments confirm these predictions, indicating that adaptation maintains scale-free cortex dynamics, which have long been hypothesized to optimize information processing.

4.1 Introduction

A long-standing hypothesis at the interface of physics and neuroscience is that neural networks self-organize to the critical point of a phase transition, thereby optimizing aspects of

sensory information processing (Beggs, 2008; Plenz, Niebur, & Schuster, 2014; Woodrow L Shew & Plenz, 2013). This idea is partially supported by strong evidence for critical dynamics observed in the cerebral cortex (Beggs & Plenz, 2003; Friedman et al., 2012; Haimovici, Tagliazucchi, Balenzuela, & Chialvo, 2013; Klaus, Yu, & Plenz, 2011; Petermann et al., 2009; Priesemann, Valderrama, Wibral, & Le Van Quyen, 2013; W. L. Shew, Yang, Yu, Roy, & Plenz, 2011), but the impact of sensory input on these dynamics is largely unknown. Thus, the foundations of this hypothesis – the self-organization process and how it manifests during strong sensory input – remain unstudied experimentally. Here we show in visual cortex and in a computational model that strong sensory input initially elicits cortical network dynamics that are not critical, but adaptive changes in the network rapidly tune the system to criticality. This conclusion is based on observations of multifaceted scaling laws predicted to occur at criticality (Friedman et al., 2012; Sethna, Dahmen, & Myers, 2001). Our findings establish sensory adaptation as a self-organizing mechanism which maintains criticality in visual cortex during sensory information processing.

Sensory nervous systems adapt, dynamically tuning interactions among large networks of neurons, to cope with a changing environment (Bialek, 2012; Kohn, 2007). The principles governing such adaptation at the macroscopic level of neuronal network dynamics are not well understood. Computational models and theory suggest that such adaptation can maintain critical network dynamics (A. Levina, Herrmann, & Geisel, 2007; Anna Levina, Herrmann, & Geisel, 2009; Meisel & Gross, 2009), but these previous studies did not consider the strongly driven regime that is expected during intense sensory input. Indeed, sufficiently strong input may increase the overall excitability of a network by bringing neurons closer to their firing thresholds and potentially tipping the network into a high firing rate regime that is inconsistent with critical

dynamics (Supplementary Information 1). Thus, the question remains: does strong sensory input drive cortical network dynamics away from criticality or can adaptation counteract this tendency and maintain the critical regime?

4.2 Methods

4.2.1 Ex vivo eye-attached whole brain prep

All procedures were approved by Washington University's and University of Arkansas' Institutional Animal Care and Use Committees and conform to the guidelines of the National Institutes of Health on the Care and Use of Laboratory Animals. Adult red-eared turtles (n=9, Trachemys scripta elegans, 150 – 200 g weight, 12-15 cm carapace length) were studied. Following anesthesia (Propofol 10 mg/kg) and decapitation, we surgically removed the brain, optic nerves, and eyes, from the cranium (Supplementary Information 9). One eye was hemisected and drained, thus exposing the retina for visual stimulation; the other eye was removed. Two cuts allowed the cortex to be unfolded, exposing the ventricular surface, thus facilitating the subsequent insertion of the microelectrode array. The eye and the brain were continuously perfused with artificial cerebrospinal fluid (in mM; 85 NaCl, 2 KCl, 2 MgCl2, 45 Na HCO3, 20 D glucose, and 3 CaCl2 bubbled with 95% O2 and 5% CO2), adjusted to pH 7.4 at room temperature. Recordings began 2-3 hrs after induction of anesthesia.

4.2.2 Microelectrode array measurements

We recorded wideband (0.7 Hz – 15 kHz) extracellular voltages relative to a silver chloride pellet electrode in the bath at 30 kHz sample rate (Blackrock Microsystems, Cerebus).

With post-processing filtering (band-pass 5-100 Hz) we extracted local field potential (LFP). We used two different electrode arrays. The first was a 96-channel microelectrode array (10x10 square grid, 400 µm inter-electrode spacing, 500 µm electrode length, no corner electrodes, Blackrock Microsystems). Using a micromanipulator (Sutter, MP-285), we inserted this array to a depth of 250-500 µm with the plane of electrodes parallel to the dorsal surface of cortex. The second array was comprised of a three dimensional grid of electrodes (4x4x8 grid, 16 shanks, 8 electrodes per shank, 300 µm inter shank spacing, 100 µm interelectrode spacing on each shank, Neuronexus). This second array was inserted to a depth such that electrodes spanned the cortex from the ventricular to the dorsal surface. We analyzed data from electrodes that were located with the visually responsive region of cortex (Supplementary Information 2). This included between 13 and 28 electrodes (19 on average) for 10x10 electrodes and approximately 48 electrodes for the 3D grid electrodes.

4.2.3 Visual stimuli

Visual stimuli (two types of grayscale movie, black dots moving on a white background, uniform black to gray transition) were created by a computer and delivered with either a miniature video projector (Aaxa Technologies, P4X Pico Projector) or an LCD monitor (Samsung 19", 1440x900 pixels, contrast ratio = 20000:1, response time = 2 ms). The projector/monitor image was focused onto the retina with additional lenses (Figure 4.1a). The mean light intensity (irradiance) at the retina was 20 mW/m2.for the monitor and 1 W/m2 for the projector. In two experiments, we also used brief flash from a light emitting diode (LED, 60 W/m2 at retina) placed near the retina to stimulate with a 1 s flash. Additional details about the stimuli including timing are in Supplementary Information 10.

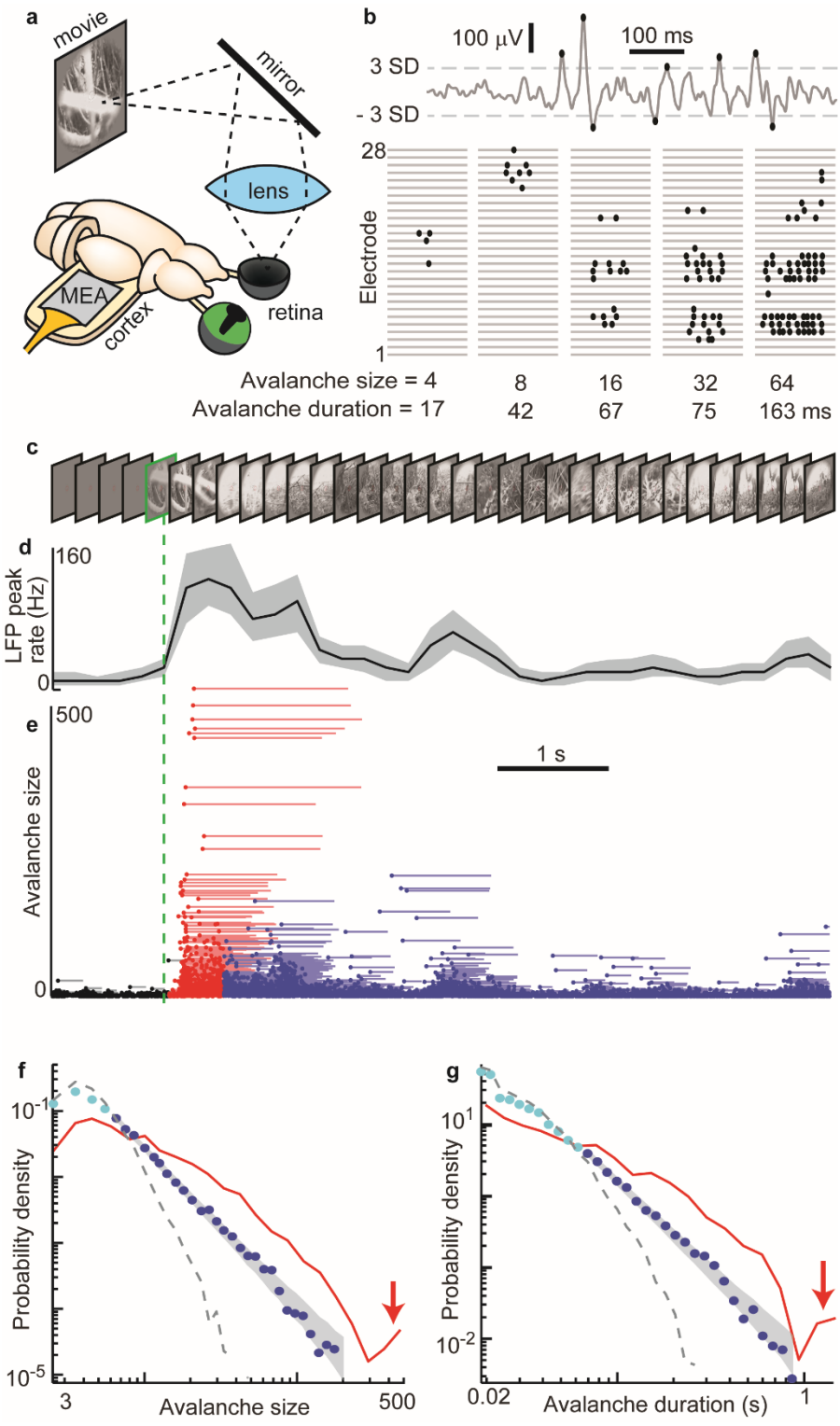
a
movie
mirror
lens
MEA
cortex
retina
b
100 µV
100 ms
3 SD
- 3 SD
28
Electrode
1
Avalanche size = 4
8
16
32
64
Avalanche duration = 17
42
67
75
163 ms
c
d
160
LFP peak rate (Hz)
0
e
500
1 s
Avalanche size
0
f
10^{-1}
Probability density
10^{-5}
3
Avalanche size
500
g
10^{1}
Probability density
10^{-2}
0.02
Avalanche duration (s)
1

Figure 4.1 Visually driven network dynamics are power law distributed after non-power law transient. **(a)** *Ex vivo* whole brain with eyes attached. Visual stimuli are projected onto the intact retina while activity is recorded with a 96-channel microelectrode array (MEA) inserted into the unfolded visual cortex. **(b)** Avalanches are defined as spatiotemporal clusters of large amplitude LFP peaks (black dots). Five example avalanches are displayed with one dot per LFP peak. Avalanche size = number of LFP peaks; duration = time between the first and last peaks. **(c)** Natural movie visual stimulus (subset of 1 frame per 200 ms shown). **(d)** At movie start (green dashed line), there is a transient increase in stimulus-triggered average LFP peak rate. Average is over 315 movie presentations. Gray region delineates quartiles. **(e)** Stimulus-triggered avalanche size time series reveals tendency for very large avalanches during the transient response (red). Later, during the visually-driven steady state, less extreme avalanches occur (blue). Each point represents one avalanche. The line following each point indicates avalanche duration. Responses to 315 repeats of movie stimulation are overlaid. **(f,g)** Probability density functions for sizes and durations of avalanches during the transient response (red line) and during the visually-driven steady-state (blue dots). Large avalanches (arrow) occur during the transient response, yielding bimodal distributions of avalanche sizes and durations. Avalanches during the visually-driven steady state are power law distributed over the range indicated with dark blue dots. Gray shading indicates the range (0.05-0.95) of expected probabilities for a perfect power law with the same number of samples as the experiment. Jittering the times of LFP peaks destroys the power-law (dashed line) by abolishing large sized avalanches. Panels d-g are from one experiment with one turtle.

4.2.4 Avalanche analysis

The first step of avalanche detection was to compute the standard deviation of every LFP trace. Next we defined an *'LFP peak'* as a period of time during which an LFP trace fluctuates beyond 3 to 4 standard deviations, due to either a positive or negative deflection (Figure 4.1b). For each LFP peak, we determined the time of its extreme value and the identity of the channel on which it was recorded. The channel information was used to exclude from analysis LFP peaks which were not within visual cortex. An avalanche was defined as a spatiotemporal cluster of consecutive LFP peaks with inter-peak intervals not exceeding a temporal threshold ΔT (channel information does not play a role in avalanche definition). ΔT was chosen to be the average inter-peak interval (<IPI>, inverse of population LFP peak rate), resulting in $\Delta T = 24 \pm 18$ ms (mean ±

SD). Avalanche duration was defined as the difference between the first and last LFP peak time within the avalanche. The size of an avalanche was defined as the number of LFP peaks comprising the avalanche. Avalanches analyzed separately depending on whether they occurred during the transient period or visually-driven steady state period. Robustness of results to changes in ΔT and definitions of time periods are in Supplementary Information 11.

4.2.5 Power law fitting and fit quality, q

Using maximum likelihood methods (Clauset, Shalizi, & Newman, 2009; Klaus et al., 2011), we fit a truncated power law (truncated at both the head and tail) to the avalanche distributions during visually-driven steady state (Supplementary Information 12). The fitting function for the avalanche size distribution was $f(S) = S^{-\tau}(\sum_{x=x_0}^{x_M} x^{-\tau})^{-1}$, where the maximum size x_M was assumed to be the largest observed size. The minimum size x_0 and the exponent τ were fitting parameters. Since avalanche duration is a non-integer variable, the fitting function for the duration distribution was $g(D) = (1-\alpha)(y_M^{1-\alpha} - y_0^{1-\alpha})^{-1} D^{-\alpha}$, where the maximum y_M was taken as the largest observed duration, and y_0 and α were fitting parameters. Exponents τ and α between -1 and -4 in increments of 0.01 were tried. Minimum values x_0 and y_0 were tried increasing from 0, but only up to the point when the fitted power law matches the data well enough to have a Kolmogorov-Smirnov statistic $KS < 1/\sqrt{N_{samp}}$, where N_{samp} is the number of avalanches comprising the dataset (Supplementary Information 12). For fitting model data size and duration distributions, we used the fitting function *f*(*S*) above, because both size and duration are discrete variables for the model.

After finding the best-fit power law, the next step was to assess goodness-of-fit q (Clauset et al., 2009; Klaus et al., 2011). We compared the experimental data to 1000 surrogate data sets drawn from the best-fit power law distribution with the same number of samples as the experimental data set. The deviation between the surrogate data sets and a perfect power law was quantified with the KS statistic. The quality q of the power law fit was defined as the fraction of these surrogate KS statistics which were greater than the KS statistic for the experimental data. We use a very conservative criterion, $q>0.1$, for judging the data to be power law distributed. This is demonstrated visually in Figure 4.1f,g and Figure 4.2e,f by plotting the experimental distribution over a gray band which delineates the 5-95 percentiles of the surrogate data sets.

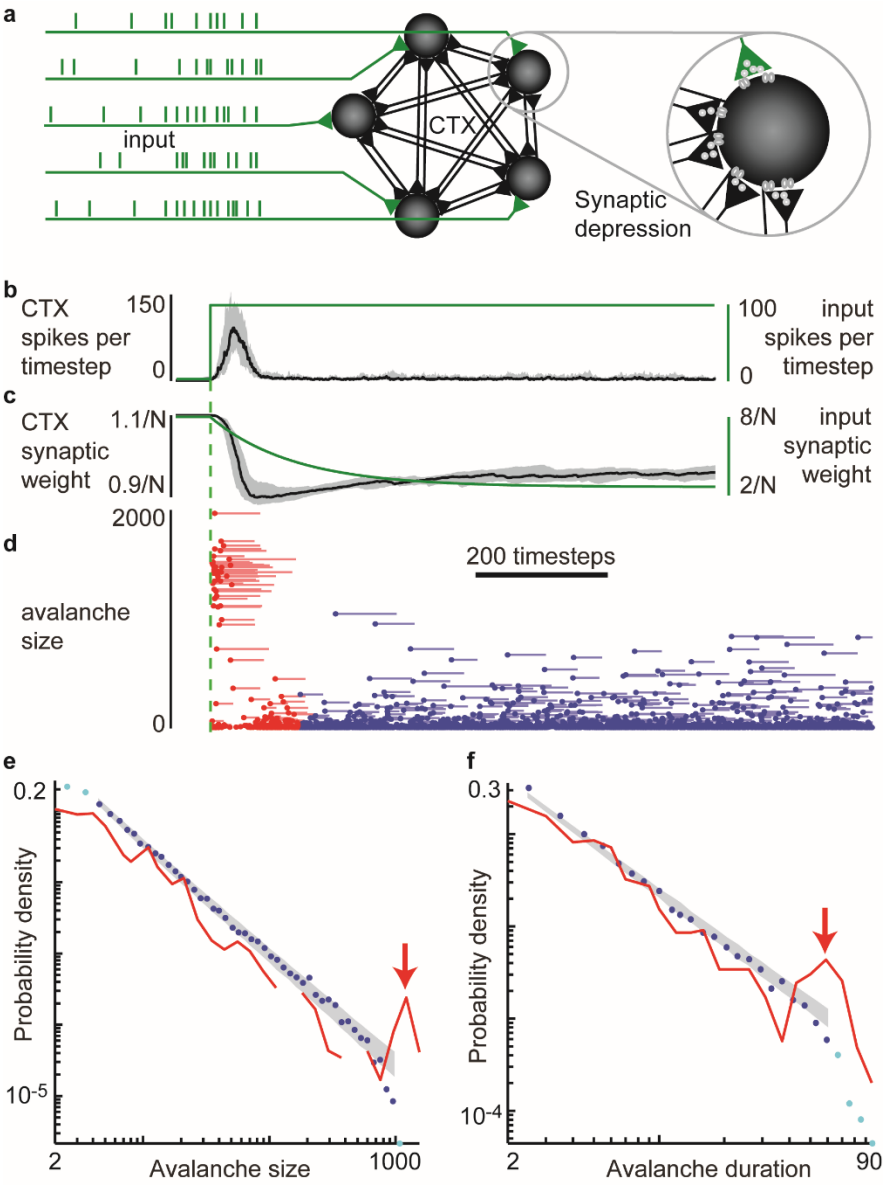
a
input
CTX
Synaptic
depression
b
CTX
spikes per
timestep
150
0
100
input
spikes per
timestep
0
c
CTX
synaptic
weight
1.1/N
0.9/N
8/N
input
synaptic
weight
2/N
d
2000
avalanche
size
0
200 timesteps
e
0.2
Probability density
10^{-5}
2
Avalanche size
1000
f
0.3
Probability density
10^{-4}
2
Avalanche duration
90

Figure 4.2 Depressing synapses tune model dynamics to critical regime after noncritical transient. **(a)** Conceptual cartoon illustrating model features, including recurrent synapses (black) and input synapses (green) which change strength according short-term depression. **(b)** A step increase in input (green, input spikes per timestep for whole network) causes a transient increase in the population spike rate of the network (black, median). Time series is averaged over 40 trials. Gray region delineates quartiles. **(c)** Following the input rate increase, there is a relatively slow decrease in median synaptic strength for both recurrent (black) and input (green) synapses (average over 40 trials). Gray region delineates quartiles. Dashed line marks stimulus onset. **(d)** Stimulus-triggered avalanche time series. During a transient period after increase in input rate, avalanches of very large size occur (red). **(e)** Distributions of avalanche size during the transient period (red) reveal a 'bump' in the avalanche size distribution at large size (arrow). Avalanche sizes are power law distributed after synapses have adapted (blue). Gray shading indicates the range (0.05-0.95) of expected probabilities for a perfect power law with the same number of samples. **(f)** Avalanche durations follow a similar trend. Model parameters: low input R=0.05, high input R=100, default synapses Λ_0=1.1, 30% subsampling, 5000 timesteps computed after increase in R.

4.2.6 Computational Model

$N = 1000$ all-to-all connected binary neurons received input from outside the network. The 'strength' of the synapse from neuron *j* onto neuron *i* at time *t* is determined by the corresponding element of the synaptic weight matrix $W_{ij}(t)$. 20% of neurons are inhibitory, i.e., with negative entries in the weight matrix. $\Omega_i(t)$ is the strength of the input synapse onto neuron *i* (all excitatory). The binary state $s_i(t+1)$ of neuron *i* ($s = 0$ inactive, $s = 1$ spiking) is determined probabilistically based on the sum $p(t+1)$ of its inputs $p(t+1) = \Omega_i(t)\sigma_i(t) + \sum_{j=1}^{N} W_{ij}(t)s_j(t)$. If $0 < p < 1$, then the neuron fires with probability p. If $p \geq 1$, then the neuron fires with probability 1. If $p \leq 0$, then the neuron does not fire. Time is discrete and state updates are synchronous. The input $\sigma_i(t)$ from the *i*th input synapse is binary (1 with probability *r*). The onset of stimulation is modelled as a step increase from r=5x10^{-5} to

either *r*=0.02 or *r*=0.1. In Figs. 4.2 and 4.3, we report the population input rate of $R = Nr$. The update rules for synaptic dynamics are $W_{ij}(t+1) = W_{ij}(t) + \tau_r^{-1}\left(W_{ij}^o - W_{ij}(t)\right) - \tau_d^{-1} W_{ij}(t) s_j(t)$

and $\Omega_i(t+1) = \Omega_i(t) + \tau_r^{-1}\left(\Omega_i^o - \Omega_i(t)\right) - \tau_d^{-1}\Omega_i(t)\sigma_i(t)$. The default weight matrix was constructed such that its largest eigenvalue Λ_0 has absolute value equal to either 1.0, 1.05, or 1.1 (Supplementary Information 7). A largest eigenvalue of 1.0 corresponds approximately to an average synaptic weight of 1/N and is known to result in critical dynamics for models with static synapses (Larremore, Shew, & Restrepo, 2011). Synapses depress with a time constant of $\tau_d = 20$ timesteps following a presynaptic spike and recover exponentially with a time constant of $\tau_r = 400$ timesteps.

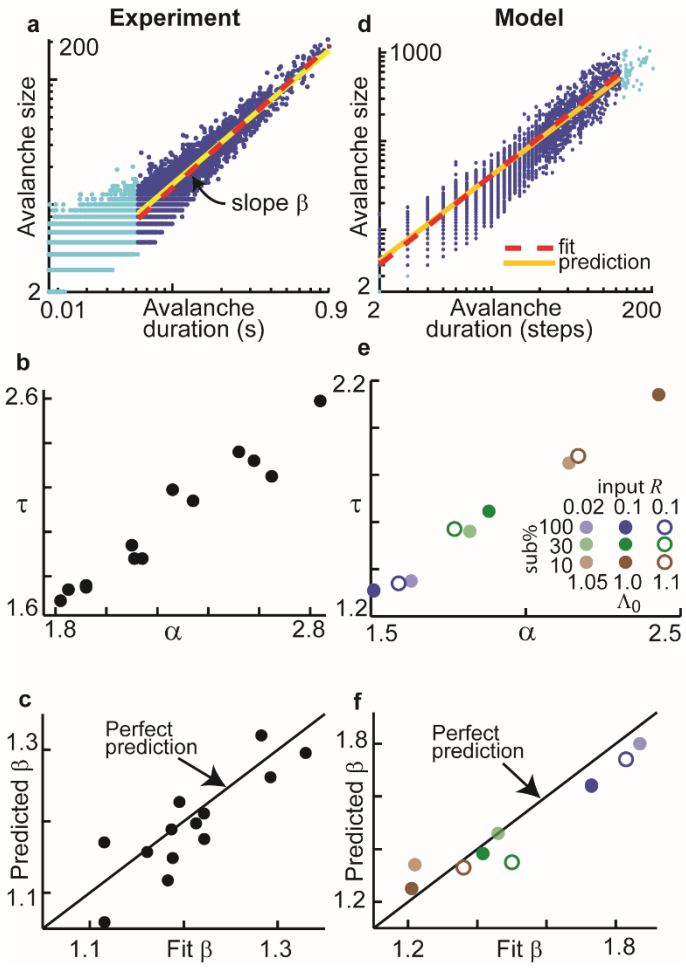

Figure 4.3 Steady state visually-driven avalanches follow predictions for critical regime. **(a)** Each point displays the size and duration of one avalanche (from one experiment, one turtle, same as Figure 4.1). Avalanches from the visually-driven steady state are shown. The linear relationship on logarithmic axes reveals a power law relationship between avalanche size and duration as predicted by criticality theory: $S \sim D^{\beta}$. The slope of the best-fit line (red) matches with the predicted $\beta = (\alpha - 1)/(\tau - 1)$ (yellow). **(b)** In different experiments, different values were found for duration exponents α and size exponents τ. **(c)** Different best-fit β were found for different turtles. Predicted β matched the best-fit β in the visually-driven steady state. Line indicates identical match. **(d-f)** Computational model displays the same relationship among power law exponents as found experimentally. Different size and duration exponents (e) were obtained by varying the input rate R, the degree of subsampling, and default synapse strengths Λ_0 (see inset legend).

Each avalanches is initiated by external input. Upon reaching a timestep with no active cortical neurons, the avalanche is considered to be ended. We simulated 30 trials of step increase in input. In each trial, we ran the model for 5000 timesteps following the onset of increased

input. Subsampling (Figure 4.3) entailed analyzing the spikes from a randomly chosen 30% or 10% of the network.

4.3 Results

Here we addressed this question in turtle visual cortex and in a companion computational model. In our experiments, we obtained long-duration recordings of population neural activity (local field potential, LFP) using a microelectrode array inserted into the geniculo-recipient dorsal cortex (visual cortex) of the turtle eye-attached whole-brain *ex vivo* preparation (Saha, Morton, Ariel, & Wessel, 2011) (Figure 4.1a and Supplementary Information 2). We measured multi-scale spatiotemporal patterns of neural activity while visually stimulating the retina. Similarly, in our model we studied changes in neural network activity in response to changes in external input. Experimentally and in the model, we assessed whether the measured dynamics were near or far from criticality. For this, we examined statistics and spatiotemporal scaling laws of "neuronal avalanches", which are bouts of elevated population activity with correlations in space and time (Beggs & Plenz, 2003) (Figure 4.1b). In brief, a neuronal avalanche is defined as a group of LFP peaks, occurring on any electrode, irrespective of location, and separated by inter-peak intervals less than a specified time (Methods). For experiments in which spikes (i.e., multiunit activity) were also measureable, we confirmed that the rate of LFP peaks increases with the rate of spikes (Supplementary Information 3). Thus, a period of time with many LFP peaks, e.g., a neuronal avalanche, reflects an increase in population spike rate in the cortex.

At the onset of stimulation, we observed that LFP amplitude, LFP peak rate, and avalanches were typically large scale – not consistent with critical dynamics – during a transient period (Figs. 4.1c-e and Supplementary Information 4). More specifically, avalanche sizes *S* and

durations *D* were often bimodally distributed during the transient (Figure 4.1f,g and Supplementary Information 5). Following this large-scale transient response, LFP amplitude decreased and avalanches became more diverse in spatiotemporal scale (Figure 4.1e), resulting in power-law distributions, $P(S) \sim S^{-\tau}$ (Figure 4.1f) and $P(D) \sim D^{-\alpha}$ (Figure 4.1g) over a wide range of sizes and durations. This fact is supported by rigorous maximum likelihood fitting methods (Clauset et al., 2009; Klaus et al., 2011) and strict statistical criteria for fit quality ($q > 0.1$, Methods).

These conclusions held for nine turtles and four types of visual stimuli (n = 13 data sets; complex movies, static gray screen, diffuse flashes, moving dots) with power law quality values $q = 0.31 \pm 0.13$ (mean ± SD). Importantly, the different visual stimuli had very different spatiotemporal structure, yet all resulted in power law avalanche distributions. This indicates that the power laws were due to inherent neuronal network dynamics rather than externally imposed statistics of the stimulus. Notably, randomizing the recorded LFP peak times abolished the power law distributions of avalanche size and duration, thus demonstrating the importance of correlations, (Figure 4.1f,g). Moreover, activity recorded outside visual cortex was not power law distributed (Supplementary Information 6).

What biophysical mechanisms could mediate self-organization towards scale-free population activity during visual processing? To address this question, we investigated a parsimonious model network of probabilistic integrate-and-fire neurons with all-to-all connectivity (Figure 4.2a) (Haldeman & Beggs, 2005; Kinouchi & Copelli, 2006; W. L. Shew et al., 2011). A subset of neurons (20%) was inhibitory. Motivated by previous experiments (Chung, Li, & Nelson, 2002) and models (A. Levina et al., 2007), we modeled adaptation as

short-term synaptic depression with recovery (Methods). However, our model differed from previously studied models as detailed in Supplementary Information 7. We studied how the model dynamics and avalanche statistics change due to increasing the input rate. During a transient period after increasing the input rate, the population spike rate increased and synapses depressed (Figure 4.2b,c). During the transient, avalanches also increased dramatically in size and duration (Figure 4.2d), qualitatively similar to the experimental observations (Figure 4.1e). Avalanche size and duration distributions during the transient period displayed a distinct bimodal character consisting of small and large avalanches (Figure 4.2e,f), qualitatively similar to what we found experimentally (Figure 4.1f,g) and inconsistent with a power law. Following the transient jump in population activity, the network dynamically reached a new steady-state of population activity and average synaptic strength (Figure 4.2b,c). In this driven steady state, during continued high external input rate, the simulated neuronal avalanche size and duration distributions were power laws ($q > 0.1$) (Figure 4.2e,f, Supplementary Information 7).

In the model, a sufficiently strong increase in input rate transiently tips the system into a regime without critical dynamics (Supplementary Information 1). Adaptation then tunes the system to a critical regime. Given the similarity between our model results and our experiment, it is tempting to conclude that the experimentally observed power law avalanche distributions occurred because adaptation tunes the visual cortex to criticality. However, caution is called for, because power laws provide necessary, but insufficient evidence for the critical regime (Beggs & Timme, 2012; Sornette, 2006; Stumpf & Porter, 2012). Therefore, additional tests are needed to determine whether criticality underlies the experimentally observed power laws.

Two such tests arise from a particular relationship between the size and duration of avalanches, which is predicted to occur at criticality(Friedman et al., 2012; Sethna et al., 2001)

and confirmed by our model (Figure 4.3d-f, Supplementary Information 1 and 7). First, the average avalanche size increases with duration according to a specific function $S \sim D^{\beta}$. Second, the exponent β is predicted to depend on the exponents τ and α as $\beta = (\alpha - 1)/(\tau - 1)$. (A third additional test is confirmed in Supplementary Information 8.)

Our experiments confirmed both these predictions (Figure 4.3a-c). First, we showed that avalanche size scales with duration according to a power law (Figure 4.3a). Second, we determined the "best-fit β" from the size versus duration data for each experiment (Figure 4.3a). Next we computed the "predicted β" using the observed exponents τ and α. For different turtles and different visual stimuli, we obtained a range of exponents; $1.7 < \tau < 2.6$ and $1.8 < \alpha < 2.8$ (Figure 4.3b). Importantly, the observed values of τ and α provided a good prediction, $\beta = (\alpha - 1)/(\tau - 1)$, of the best-fit β for all experiments (Figure 4.3c, Supplementary Information 5).

The experimentally observed range of the values for the exponents τ and α (Figure 4.3b) raises an important question as to the origin of this variability. In the model, we demonstrated that τ and α depended on three factors (Figure 4.3e): 1) the subsample fraction, 2) the external input rate, and 3) the default synaptic strength (parameterized by the largest eigenvalue Λ_0 of the default synaptic weight matrix (Larremore et al., 2011), see Supplementary Information 7). Subsampling, i.e., creating avalanche distributions based on spikes from a subset of all model neurons, tended to increase τ and α, consistent with previous studies (Priesemann et al., 2014; Ribeiro, Ribeiro, Belchior, Caixeta, & Copelli, 2014). The effects of input rate and default synapse strengths depended on the level of subsampling. Importantly, the various combinations of τ and α observed in the model preserve the size versus duration scaling relationship (Figure 4.3f), similar to what we found experimentally (Figure 4.3c). We note that the near linear

relationship between τ and α (Figure 4.3b,e) has not, to our knowledge, been predicted theoretically.

4.4 Discussion

The close match between our experimental observations and our model results, suggest that adaptation plays a crucial role in tuning cortical circuits towards the critical regime during vision. Why should adaptation in sensory cortex tune the network to operate near a critical regime? Previous computational studies and cortex slice experiments suggest that the critical regime optimizes several aspects of information processing (reviewed in ref. 3) including dynamic range (Kinouchi & Copelli, 2006; Larremore et al., 2011; W. L. Shew, Yang, Petermann, Roy, & Plenz, 2009) and information transmission (Beggs & Plenz, 2003; W. L. Shew et al., 2011). Our observation that transient response to stimulus onset is not critical suggests that sensory cortex dynamically adapts to gain the functional benefits of critical dynamics during strong sensory input.

The critical regime has long been hypothesized to be a target of homeostatic processes in neural networks. This could be achieved by some 'top-down' mechanism (e.g., neuromodulators like dopamine (Gireesh & Plenz, 2008)) that tunes the network or as the result of local self-organization (Bak, Tang, & Wiesenfeld, 1987; Bornholdt & Röhl, 2003; A. Levina et al., 2007; Meisel & Gross, 2009). In either case, one concern with this hypothesis has been that, theoretically, the critical regime occupies an infinitesimal volume in state space (the boundary between two different regimes), which may be too small a target to hit for a real biological tuning process contending with noise and imperfections. Recent theoretical findings mitigate this concern, showing that in networks with complex structure, the critical regime expands,

occupying a substantial region (Griffiths phase) in state space (Moretti & Muñoz, 2013). Thus, our experiments, together with previous theory, establish the critical regime as a viable target for adaptive self-tuning during cortical sensory information processing.

4.5 Supplementary Information

4.5.1 Weakly Driven Versus Strongly Driven Model Network Dynamics

Our modelling efforts highlight an important distinction between weakly and strongly driven systems. For simplicity, we first consider a model with static synapses (Supplementary Figs. 4.1,4.2). In contrast with our dynamic model, here we fixed synaptic weight matrices W and Ω and did not implement the dynamic rules for changing synapse strengths. Otherwise, the model was identical to the dynamic model. In the weakly driven case, the timescales of driving and avalanches are well separated. In this case, interactions among neurons (e.g., synapse strengths, number of connections per neuron, relative strength of excitatory versus inhibitory synapses) determine whether or not a system produces critical dynamics (i.e., power law avalanche distributions and size vs duration scaling). More succinctly, in the weakly driven case, a synaptic weight matrix with largest eigenvalue $\Lambda=1$ defines criticality (Larremore et al., 2011). In contrast, in the strongly driven case, non-critical dynamics may occur, even with 'structurally critical' synapses, i.e., $\Lambda=1$. In the case of strong drive and depressing synapses (Figure 4.2), both the intensity of external input and Λ are dynamic variables. If synaptic depression sufficiently decreases effective input to the cortex and Λ is near unity after such depression, only then will critical dynamics result. In conclusion, to maintain critical dynamics and associated functional advantages, a system must account for both Λ and the level of external drive it receives.

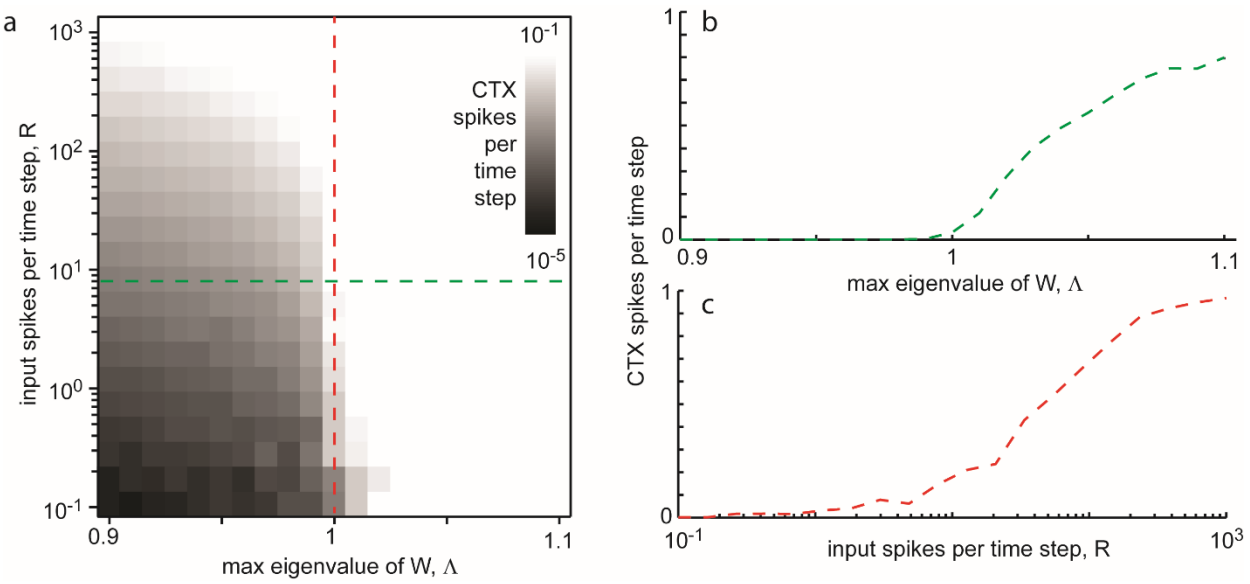

Supplementary Figure 4.1. Sufficiently strong input results in a noncritical dynamics. These results are from our model with static synapses. The synaptic weight matrix is fixed. Otherwise the model is identical to the model presented in the main text. **(a)** Population spike rate (gray scale) varies with both the strength of synapses (parameterized by Λ, the absolute value of the largest eigenvalue of the synaptic weight matrix) and the input rate (total spikes per time step for the whole network). The color scale is logarithmic. **(b)** Phase transition from subcritical to supercritical dynamics as synapse strength is increased. Critical dynamics occur at Λ≈1. Input rate is fixed just below R=10 spikes per time step. Corresponds to the green dashed line in panel a. **(c)** Increasing from low to high input rates causes a transition from critical dynamics (R < ~10 spikes per time step) to non-critical dynamics for high input rates. Synapses are fixed at Λ=1. Corresponds to the red dashed line in panel a.

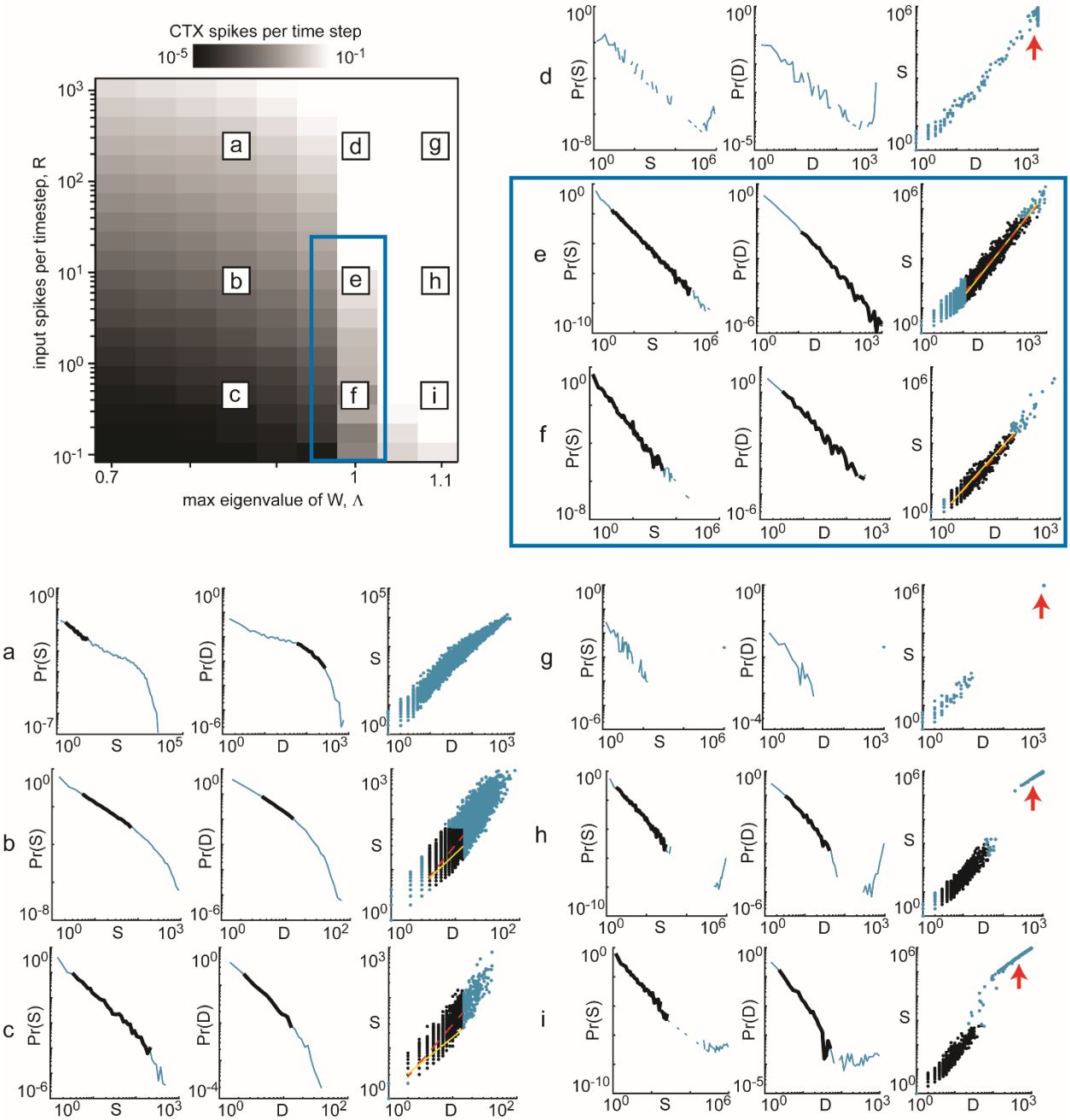
CTX spikes per time step
10^{-5}
10^{-1}
input spikes per timestep, R
max eigenvalue of W, Λ
0.7
1
1.1
a
b
c
d
e
f
g
h
i
Pr(S)
Pr(D)
S
D

Supplementary Figure 4.2. Strong drive and Λ far from 1 preclude critical dynamics. **(upper left)**A phase diagram like that shown in Supplementary Figure 4.1a. The letters a-i indicate the parameters corresponding to the example avalanche distributions and scaling laws shown in panels a-i. The blue box encloses the two examples that match best with our experimental observations. **(panels a-i)***LEFT*: Avalanches size S probability density function. Heavy black line: range of power law scaling. Blue: full range. *MIDDLE*: Avalanche duration D probability density function. *RIGHT*: Avalanche size versus duration. Red dashed lines: best fit S vs D scaling relationship. Yellow lines: predicted S vs D scaling. Red arrows: Indicate the large avalanches (bimodally distributed) that occur for Λ>1(g,h,i) or for intense input with Λ=1 (d). Note that critical dynamics (large range of power law scaling and well-predicted S vs D scaling) are not found if either Λ is far from 1 or if the input rate is too high.

4.5.2 Visual Cortex in Turtles

Turtle visual cortex is defined by the geniculo-recipient area of the dorsal cortex (Cosans & Ulinski, 1990; Mulligan & Ulinski, 1990). We accepted a recording channel as part of visual cortex when its average LFP response to visual stimulation exceeded a given threshold. For the 10x10 grid electrodes, we identified visually responsive channels based on stimulus-triggered average maps of the absolute value of LFP (for an example see Supplementary Figure4.3b). For the 3D grid electrodes, we placed the entire array in visual cortex, but used data from every other electrode along each shank (total of about 48 electrodes). Based on this approach, visual cortex included between 13 and 28 electrodes (19 on average) for 10x10 electrodes and approximately 48 electrodes for the 3D grid electrodes. Importantly, the visually responsive region defined by our approach was always centered on rostral dorsal cortex (Supplementary Figure4.3c), which is where previous anatomy studies have identified LGN projections to cortex(Mulligan & Ulinski, 1990; P. Ulinski, 2007).

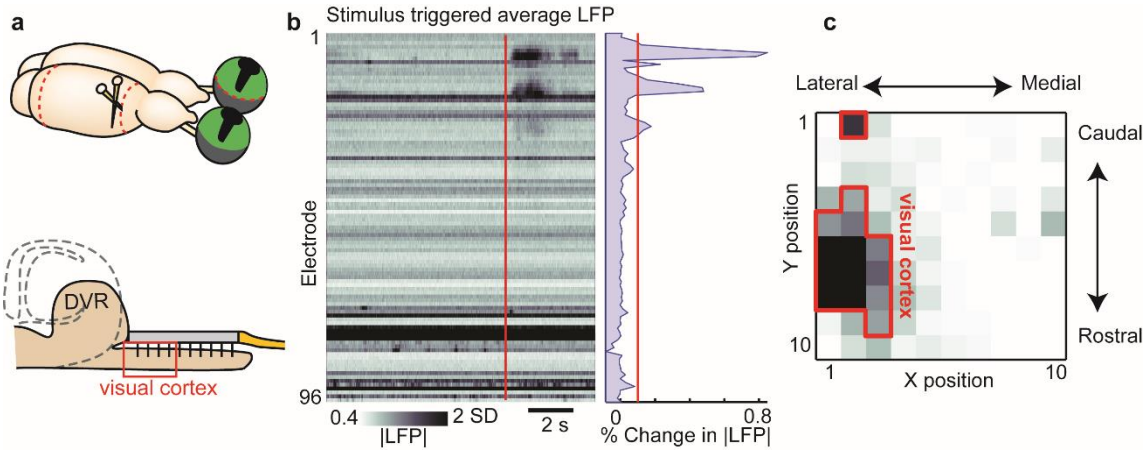

Supplementary Figure 4.3. Delineating visual cortex based on visually responsive channels. **(a)** The whole brain is removed from the turtle with eyes attached. The ventricle beneath the cortex allows the unfolding of the cortex without severing afferent/efferent fibers. A 96-channel microelectrode array (MEA) is inserted into the unfolded visual cortex and surrounding cortical regions. DVR = Dorsal Ventricular Ridge. **(b, left)** Stimulus triggered average |LFP| is shown for every electrode in the 96 channel array. Each row of the image represents one electrode. Time advances from left to right. The red line is the time the stimulus was turned on. Grayscale indicate magnitude of |LFP| normalized by SD averaged over 45 trials. Note that some channels have significant LFP amplitude, but little response to stimulus. These channels are located in the medial cortex, outside visual cortex (compare to Supplementary Figure4.8 data). **(b, right)**Percent change in |LFP| relative to the pre-stimulus baseline is plotted for every electrode. The post-stimulus time window is 4 s. We define a channel as visually responsive if the % change in |LFP| exceeds a threshold (10% in this example). **(c)** Each pixel in this image represents the % change in |LFP| for one electrode (same data as Middle panel). The pixels are spatially arranged according to actual electrode positions. The visually-responsive (above-threshold) channels are shown outlined in red. In all turtles, the visually-responsive channels were primarily in the rostral-lateral corner of the array. Note that this figure is relevant for experiments with the 10x10 microelectrode arrays. In contrast, the three dimensional grid array covered less area was positioned such that all electrodes were in the visually responsive area.

4.5.3 LFP-Spike Relationship

Our two primary reasons for analyzing LFP peaks rather than spikes were that 1) spikes were not always clearly measurable in our experiments and 2) that LFP may better represent a large population of neurons. Here we show that the rate of LFP peaks rises with the rate of multi-unit spikes for one turtle that did have clearly measurable spikes. This relationship suggests that

although we specify avalanche size in terms of number of LFP peaks, the avalanche may be interpreted as comprised of a roughly proportional number of spikes.

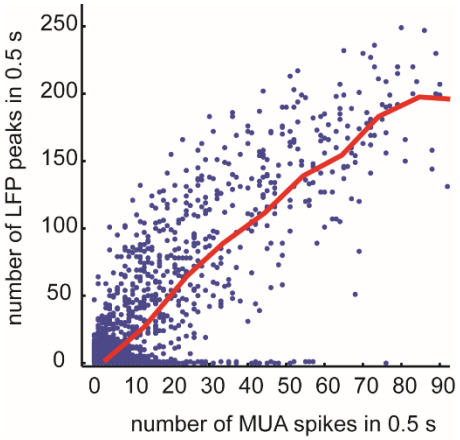

Supplementary Figure 4.4. LFP peak rate increases with multi-unit spike rate. Each point represents the numbers of peaks and spikes counted in one 0.5 s period. This was done in consecutive 0.5 s windows over the entire recording. The red line is the average of the points. Multi-unit activity was detected with a 5 SD threshold after band-pass filtering 300 - 3000 Hz.

4.5.4 Spatiotemporal Dynamics of Visually-Driven Population Activity (Beyond LFP Peaks)

The data we present in our main results are based on LFP peaks and their statistics. Here we present some alternative perspectives showing the spatiotemporal dynamics of continuous LFP signals.

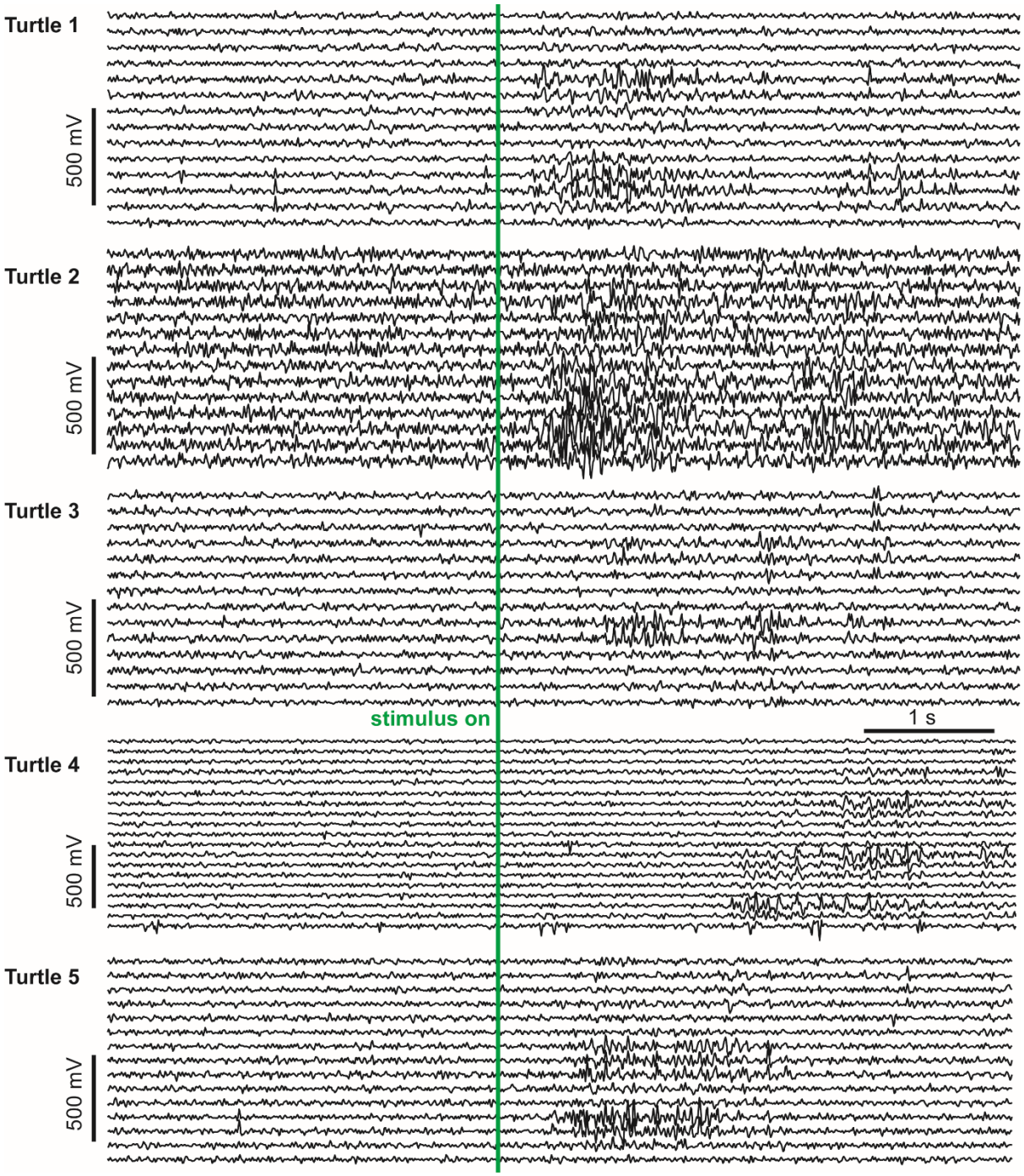

Supplementary Figure 4.5. Examples of raw data. Shown are examples of raw LFP traces (from all visually responsive electrodes) for the first five turtles. For turtles 1 and 2, the stimulus (onset at green line) was a complex movie. For turtles 3-5, the stimulus was black dot scanning across a white background.

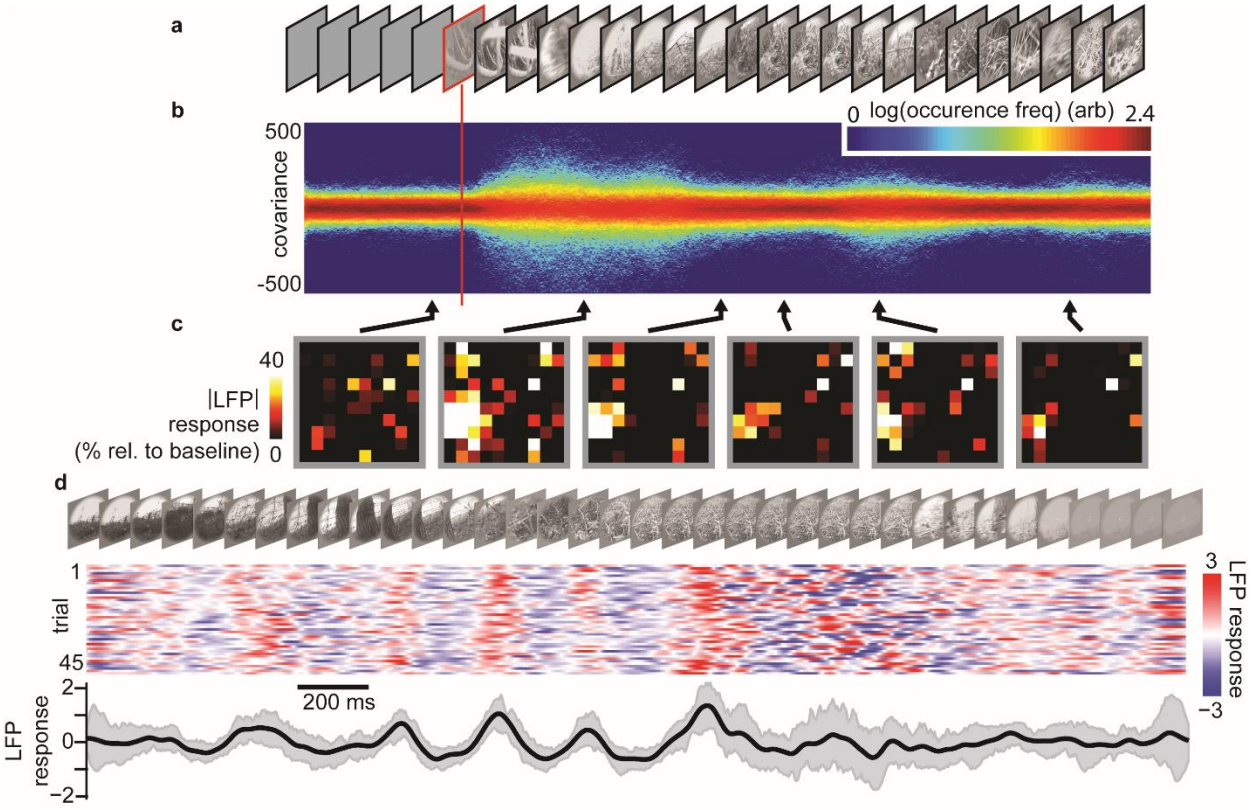

Supplementary Figure 4.6. Spatiotemporal dynamics of visually driven population activity. (**a**) Natural movie visual stimulus (for clarity, a subset of frames is shown). (**b**) At movie start, there is a transient increase in pairwise covariance of LFP. Each vertical strip of this plot displays one distribution of pairwise covariance computed during a 300 ms sliding time window (10 ms slide step). Data is from 45 repeated movie presentations. Color indicates how often a given covariance was observed. (**c**) Spatial patterns of stimulus-triggered average |LFP|. Each image represents the average LFP (% change relative to pre-stimulus baseline) at all 96 channels on the array at the time indicated by each arrow. (**d**) Low frequency LFP (1-5 Hz) recorded at one channel during repeated presentation (n = 45 trials) of the natural movie. For each trial (row), LFP amplitude is represented (color coded) in terms of z-score (difference from mean, normalized by SD). Small variability (gray) about the cross-trial average (black) demonstrates reliability of response to repeated stimuli. Frame-specific changes in LFP indicate stimulus specificity of response. The gray shaded region delineates quartiles.

4.5.5 Avalanche Distributions and Scaling Relations for All Experiments

The following 13 plots (Supplementary Figure 4.7) shows avalanche size and duration distributions for all experiments. Each plot includes probability density functions (PDF) with logarithmic bins **(top left, top middle)** as well as cumulative distribution functions **(bottom left,**

bottom middle) for three data sets: 1) avalanches that occurred during the visually-driven steady state (blue), 2) avalanches during the transient (red), and 3) avalanches based on temporally jittered LFP peaks (T_j=10 s) from the visually-driven steady state (gray). In addition, we show the size versus duration scaling plot **(top right)** comparing the predicted scaling (yellow line) with the best fit scaling (red dashed line). In all plots, dark blue points represent the range of avalanches that best fits a truncated power law. The light blue points indicate the range that is outside the fitted range. In the PDF plots, the gray band delineates the range of expected probabilities for N avalanches drawn from a perfect power law distribution with the same exponent as the best fit power law for the data. Here, N is the number of experimentally observed avalanches within the fitting range. Finally each plot specifies what values were found for power law exponents τ and α, the parameter ΔT used in the avalanche analysis, the deviations δ between the best fit power law and the other distributions, the power law quality q, predicted β, best fit β, the total number of avalanches N_a, and the number of avalanches included in the fitted range for sizes (N_{fS}) and durations (N_{fD}).

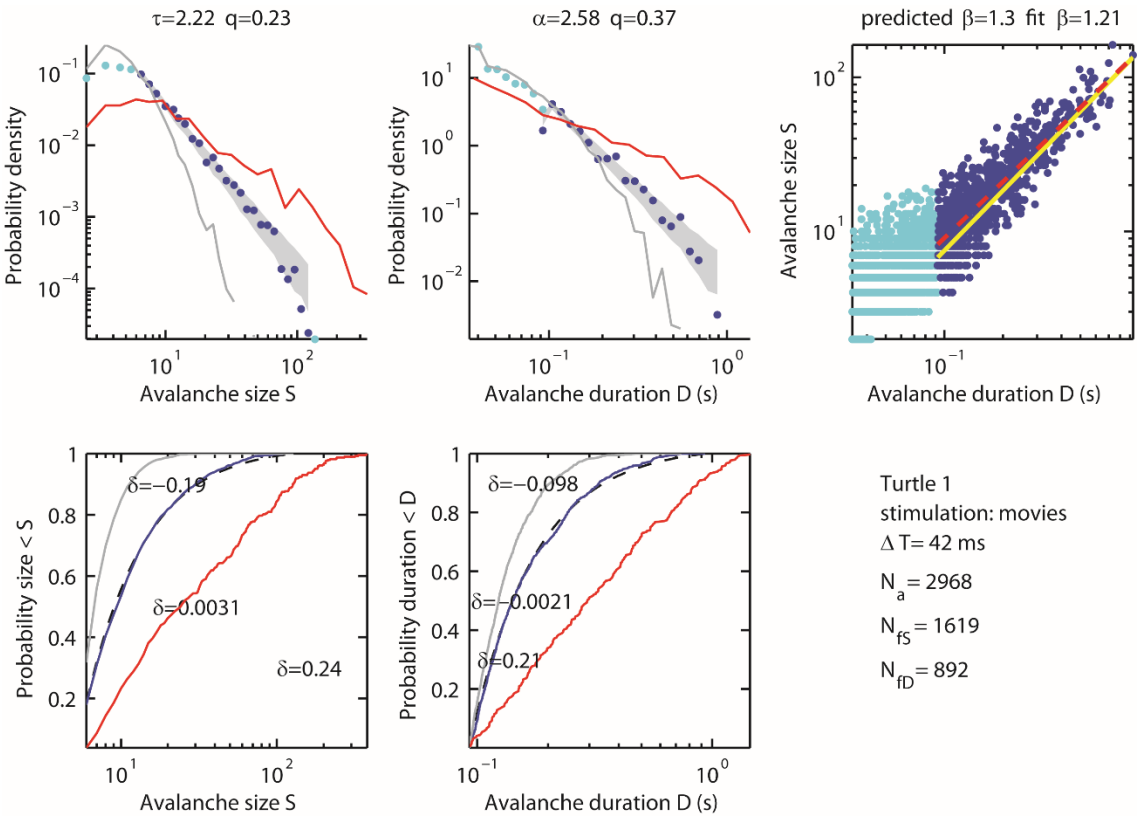

Supplementary Figure 4.7. Avalanche distributions and scaling laws for all experiments. A general caption for this figure and the following 12 figures is given above in Supplementary Information 5.

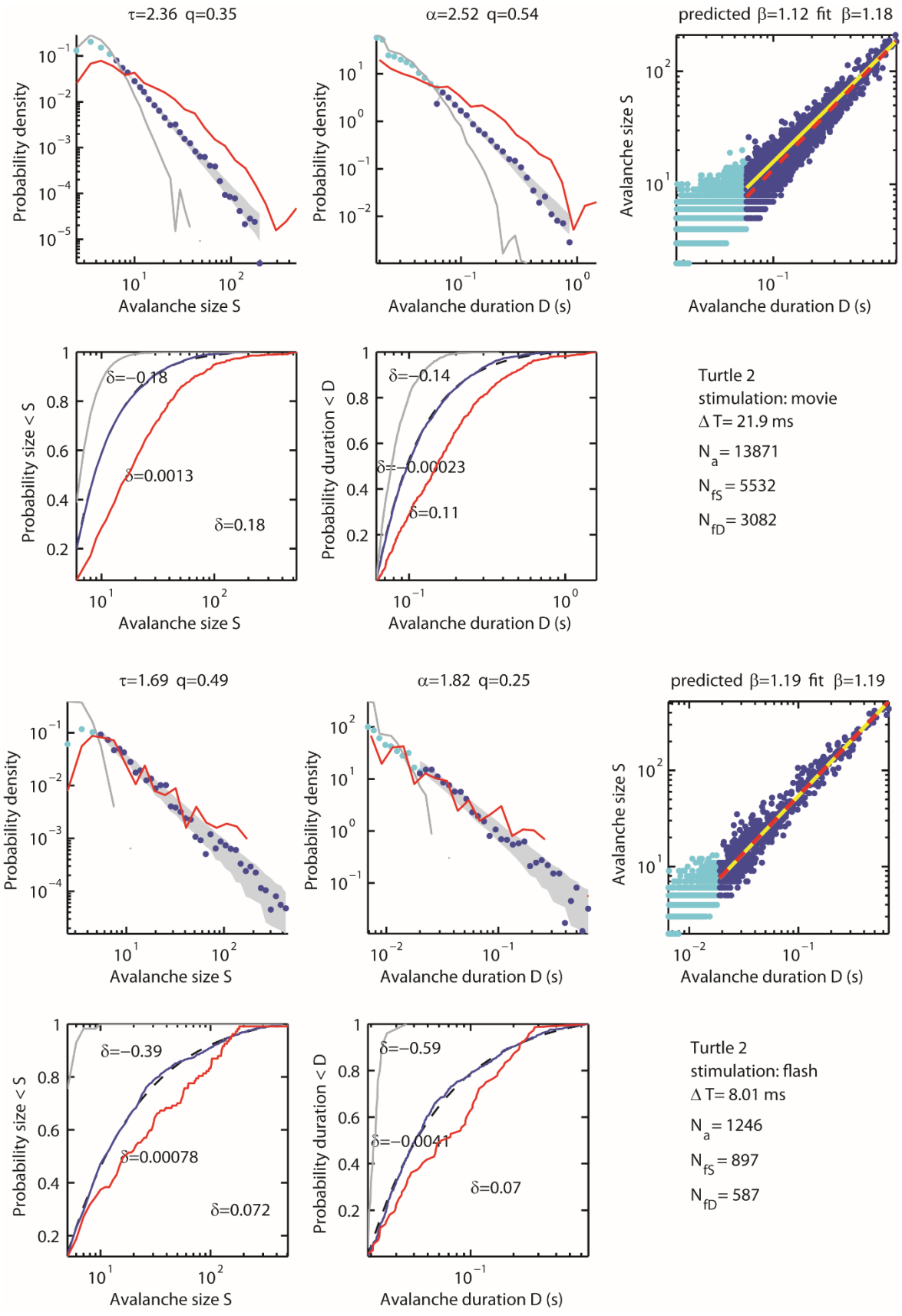
τ=2.36 q=0.35
α=2.52 q=0.54
predicted β=1.12 fit β=1.18
Probability density
Avalanche size S
Avalanche duration D (s)
Avalanche size S
Probability size < S
δ=−0.18
δ=0.0013
δ=0.18
Probability duration < D
δ=−0.14
δ=−0.00023
δ=0.11
Turtle 2
stimulation: movie
Δ T= 21.9 ms
N a = 13871
N fS = 5532
N fD = 3082
τ=1.69 q=0.49
α=1.82 q=0.25
predicted β=1.19 fit β=1.19
δ=−0.39
δ=0.00078
δ=0.072
δ=−0.59
δ=−0.0041
δ=0.07
Turtle 2
stimulation: flash
Δ T= 8.01 ms
N a = 1246
N fS = 897
N fD = 587

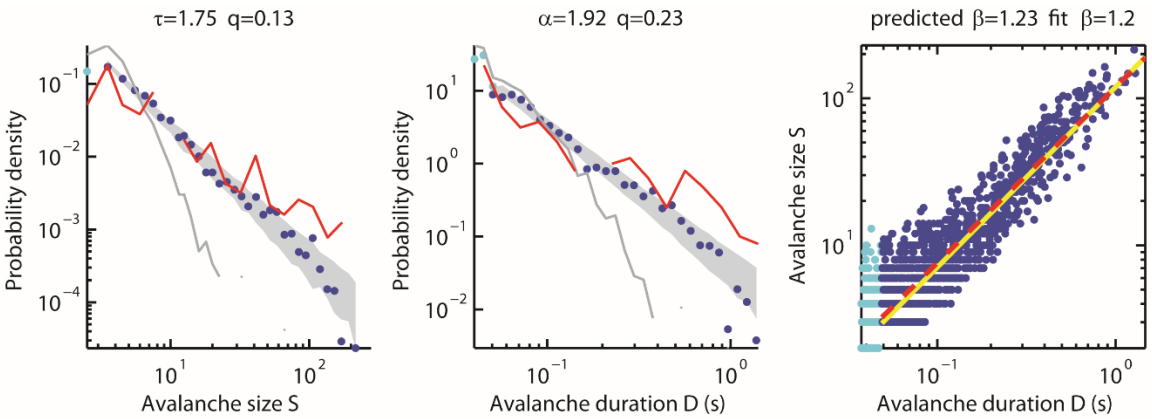

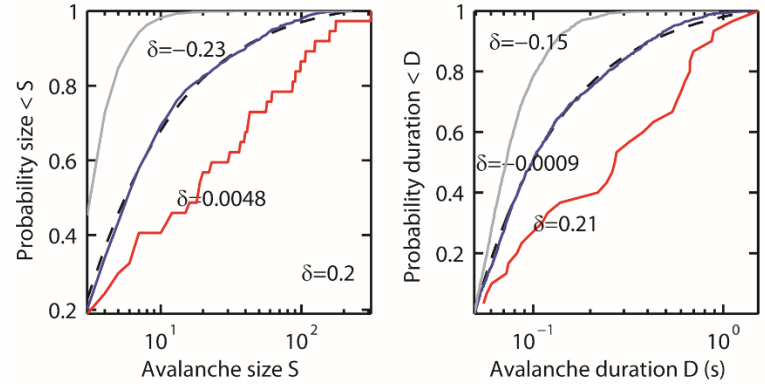

Turtle 3
stimulation: dots
$\Delta T = 47$ ms
$N_a = 1638$
$N_{fS} = 1393$
$N_{fD} = 1134$

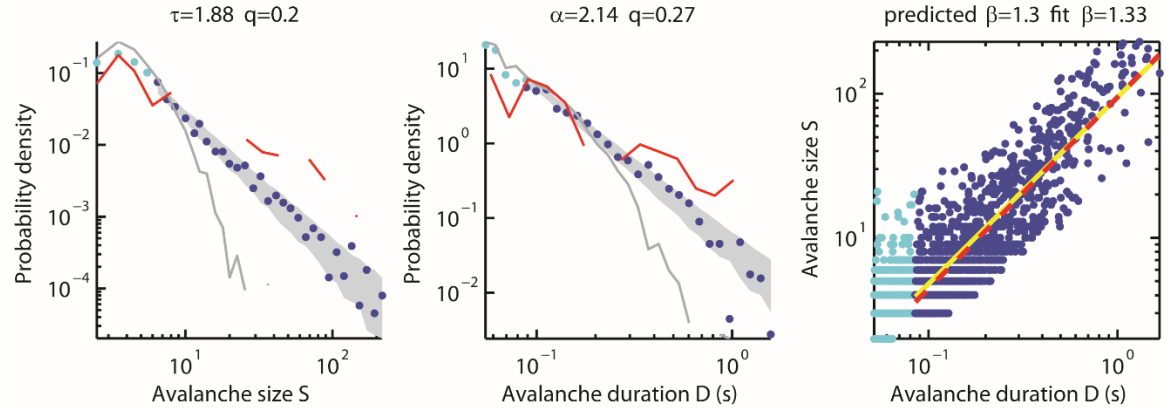

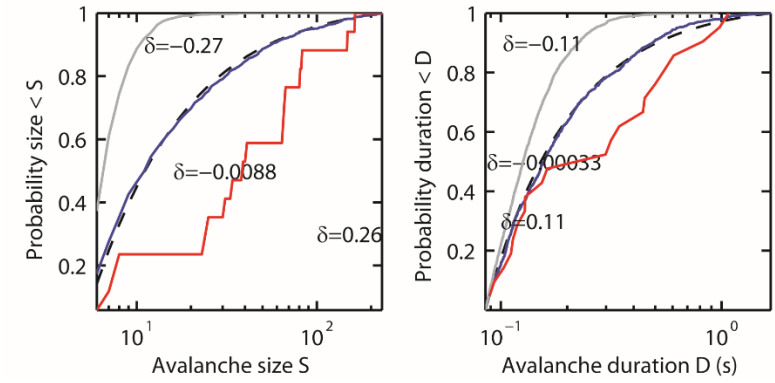

Turtle 4
stimulation: dots
$\Delta T = 64.3$ ms
$N_a = 1920$
$N_{fS} = 824$
$N_{fD} = 1129$

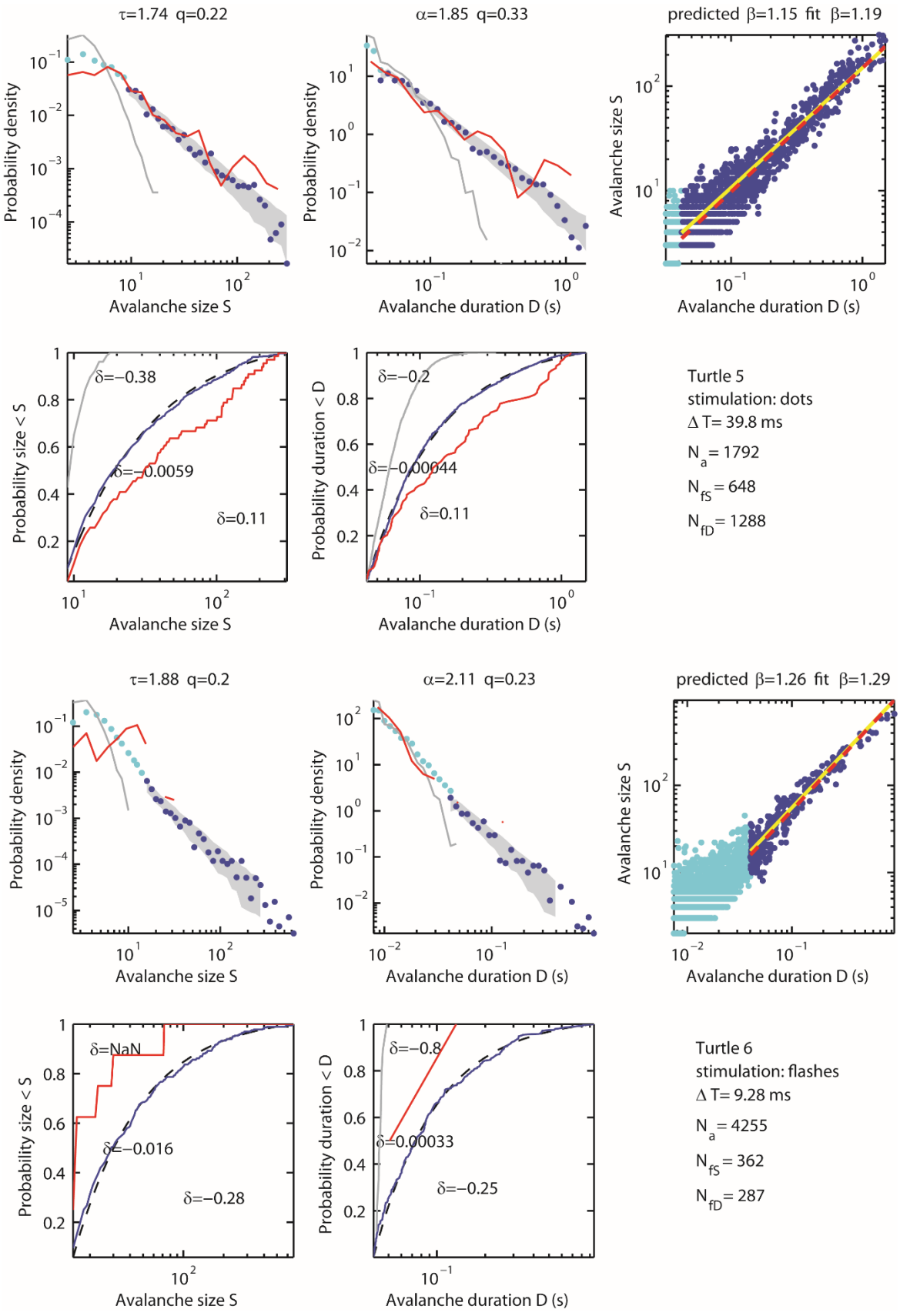
τ=1.74 q=0.22
α=1.85 q=0.33
predicted β=1.15 fit β=1.19
Probability density
Avalanche size S
Avalanche duration D (s)
Avalanche size S
Probability size < S
δ=−0.38
δ=−0.0059
δ=0.11
Probability duration < D
δ=−0.2
δ=−0.00044
δ=0.11
Turtle 5
stimulation: dots
Δ T= 39.8 ms
N a = 1792
N fS = 648
N fD = 1288
τ=1.88 q=0.2
α=2.11 q=0.23
predicted β=1.26 fit β=1.29
δ=NaN
δ=−0.016
δ=−0.28
δ=−0.8
δ=−0.00033
δ=−0.25
Turtle 6
stimulation: flashes
Δ T= 9.28 ms
N a = 4255
N fS = 362
N fD = 287

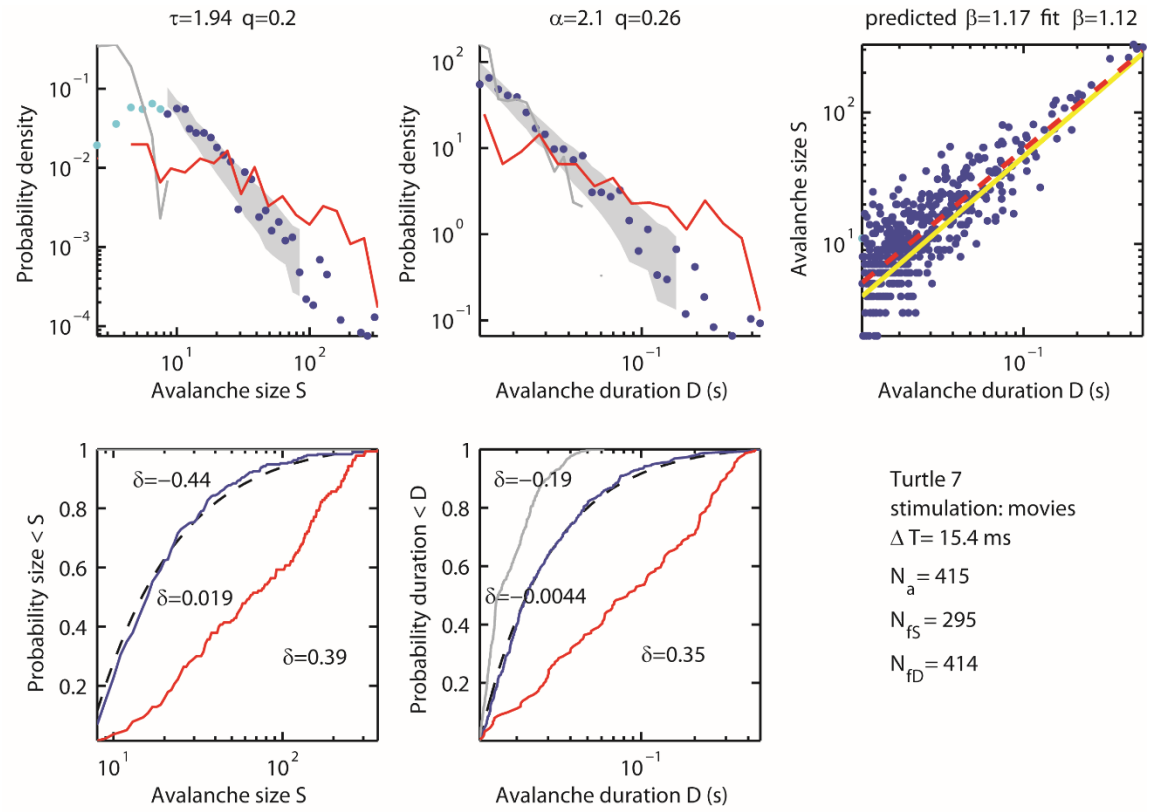
τ=1.94 q=0.2
α=2.1 q=0.26
predicted β=1.17 fit β=1.12
Probability density
Avalanche size S
Avalanche duration D (s)
Avalanche size S
Probability size < S
Probability duration < D
δ=−0.44
δ=0.019
δ=0.39
δ=−0.19
δ=−0.0044
δ=0.35
Turtle 7
stimulation: movies
Δ T= 15.4 ms
N a = 415
N fS = 295
N fD = 414

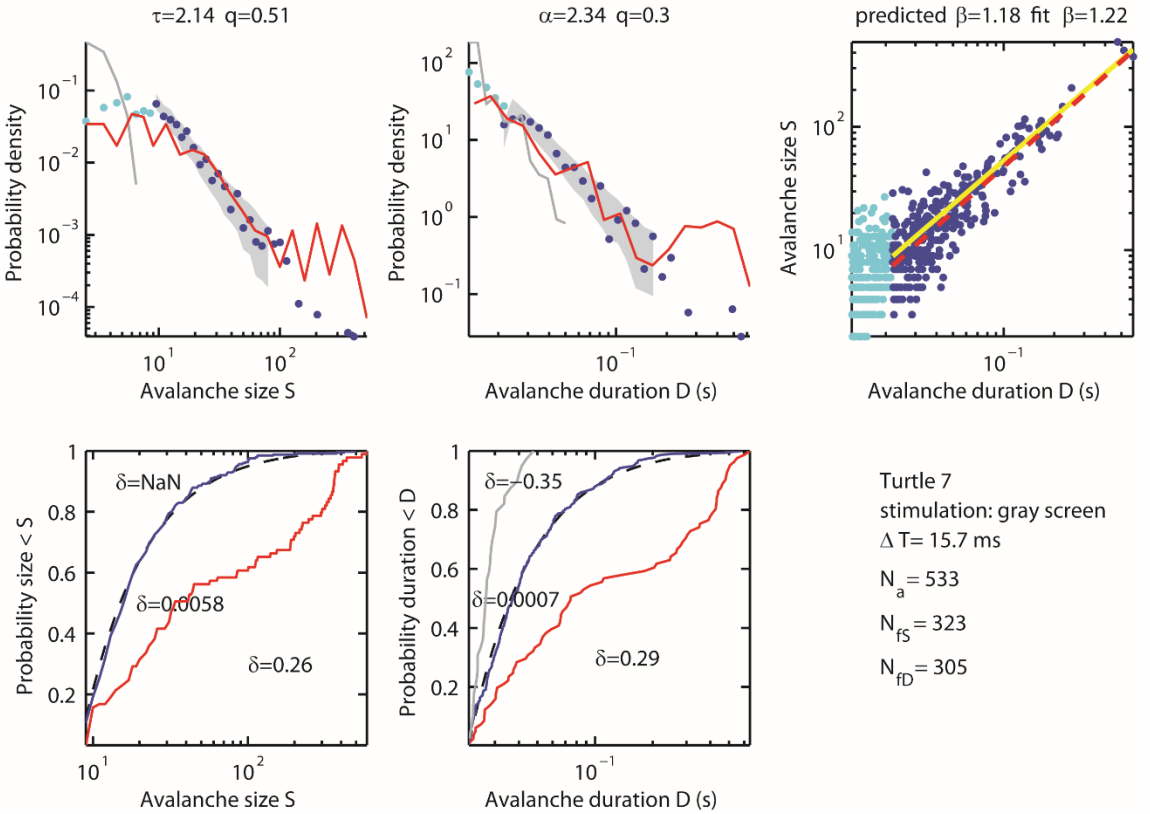
τ=2.14 q=0.51
α=2.34 q=0.3
predicted β=1.18 fit β=1.22
Probability density
Avalanche size S
Avalanche duration D (s)
Avalanche size S
Probability size < S
Probability duration < D
δ=NaN
δ=0.0058
δ=0.26
δ=−0.35
δ=0.0007
δ=0.29
Turtle 7
stimulation: gray screen
Δ T= 15.7 ms
N a = 533
N fS = 323
N fD = 305

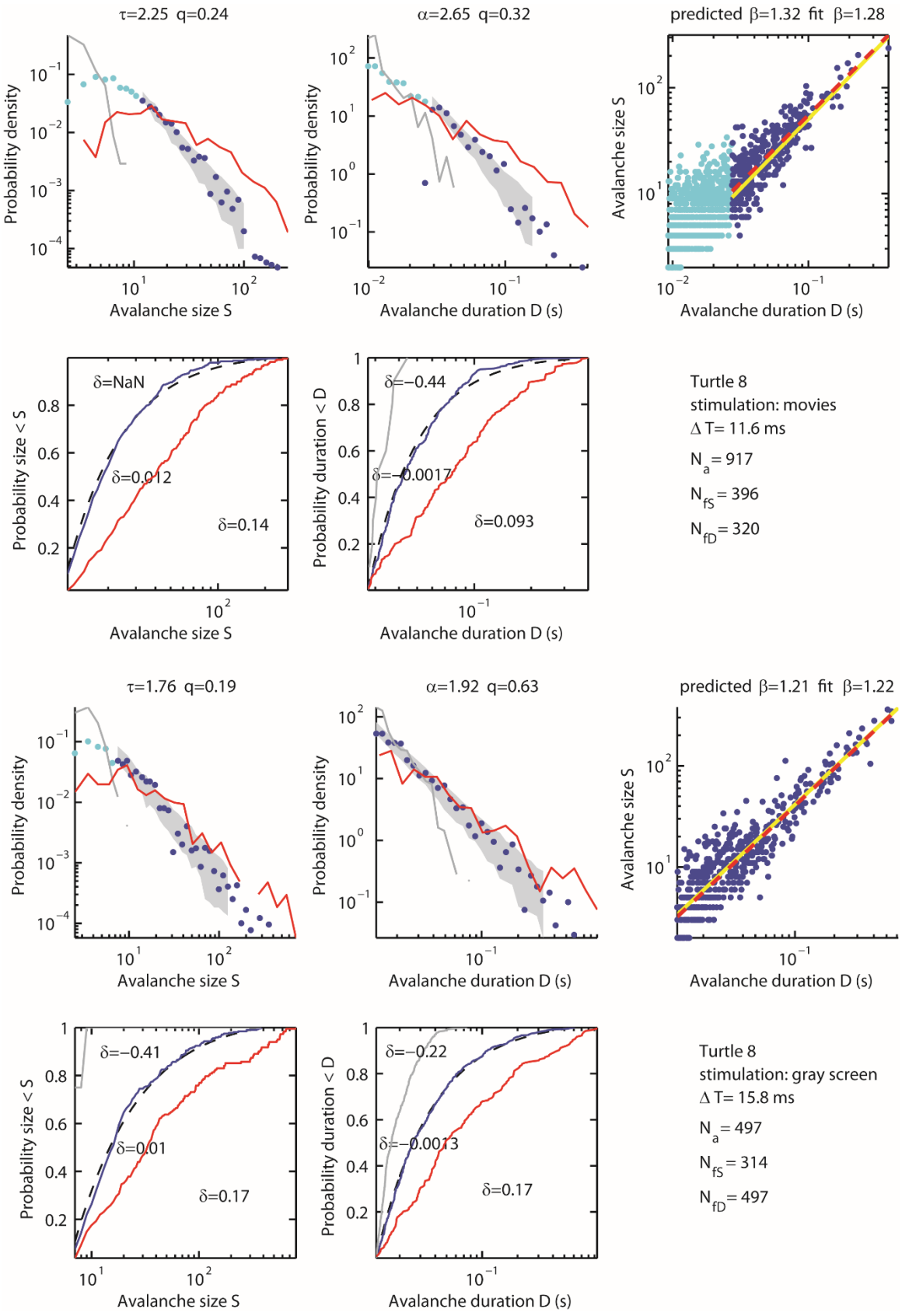
τ=2.25 q=0.24
α=2.65 q=0.32
predicted β=1.32 fit β=1.28
Probability density
Avalanche size S
Avalanche duration D (s)
Avalanche size S
δ=NaN
δ=0.012
δ=0.14
Probability size < S
Probability duration < D
δ=−0.44
δ=−0.0017
δ=0.093
Turtle 8
stimulation: movies
Δ T= 11.6 ms
N a = 917
N fS = 396
N fD = 320
τ=1.76 q=0.19
α=1.92 q=0.63
predicted β=1.21 fit β=1.22
δ=−0.41
δ=−0.01
δ=0.17
δ=−0.22
δ=−0.0013
δ=0.17
Turtle 8
stimulation: gray screen
Δ T= 15.8 ms
N a = 497
N fS = 314
N fD = 497

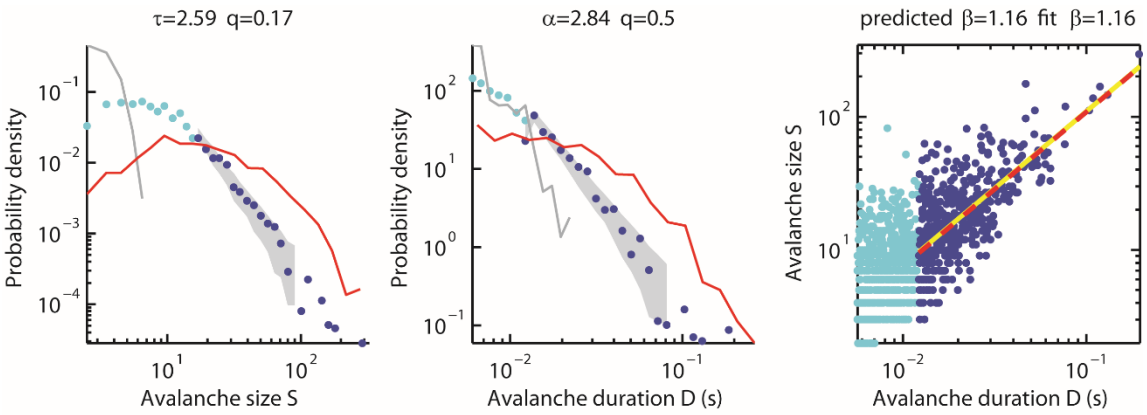

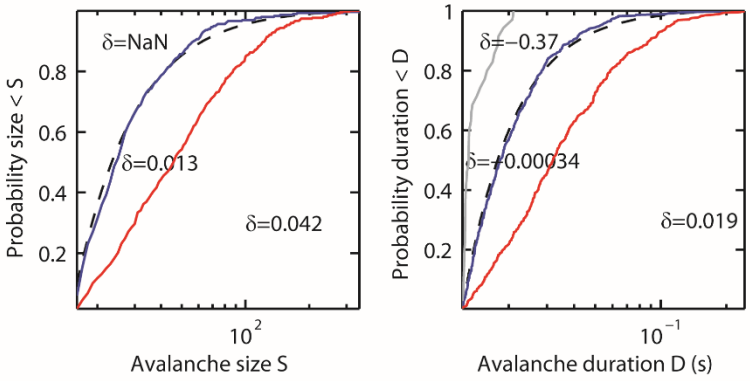

Turtle 9
stimulation: movie
Δ T= 7.06 ms
N_a = 1036
N_{fS} = 300
N_{fD} = 447

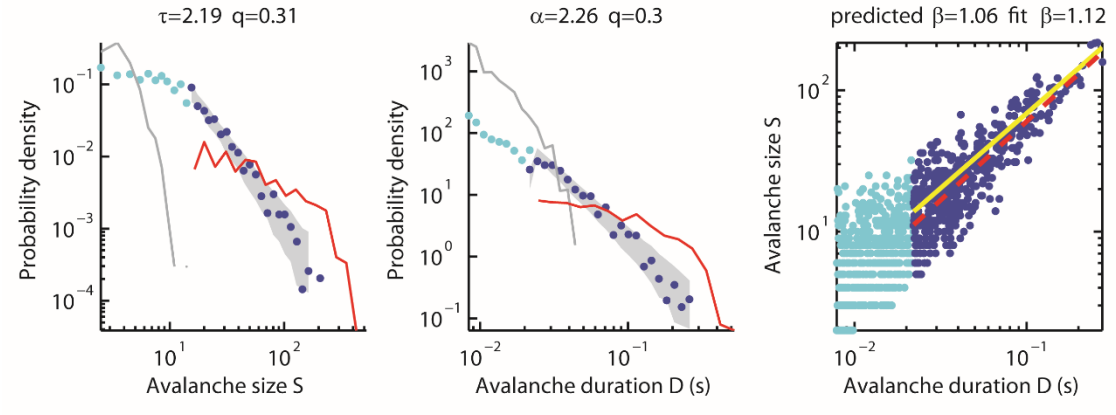

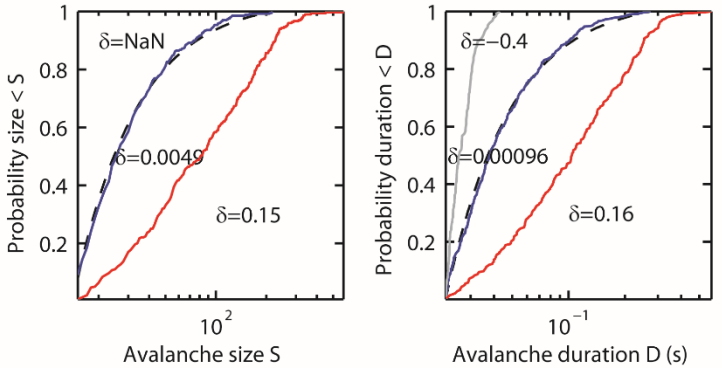

Turtle 9
stimulation: gray screen
Δ T= 9.8 ms
N_a = 987
N_{fS} = 407
N_{fD} = 475

4.5.6 Avalanche Statistics outside Visual Cortex

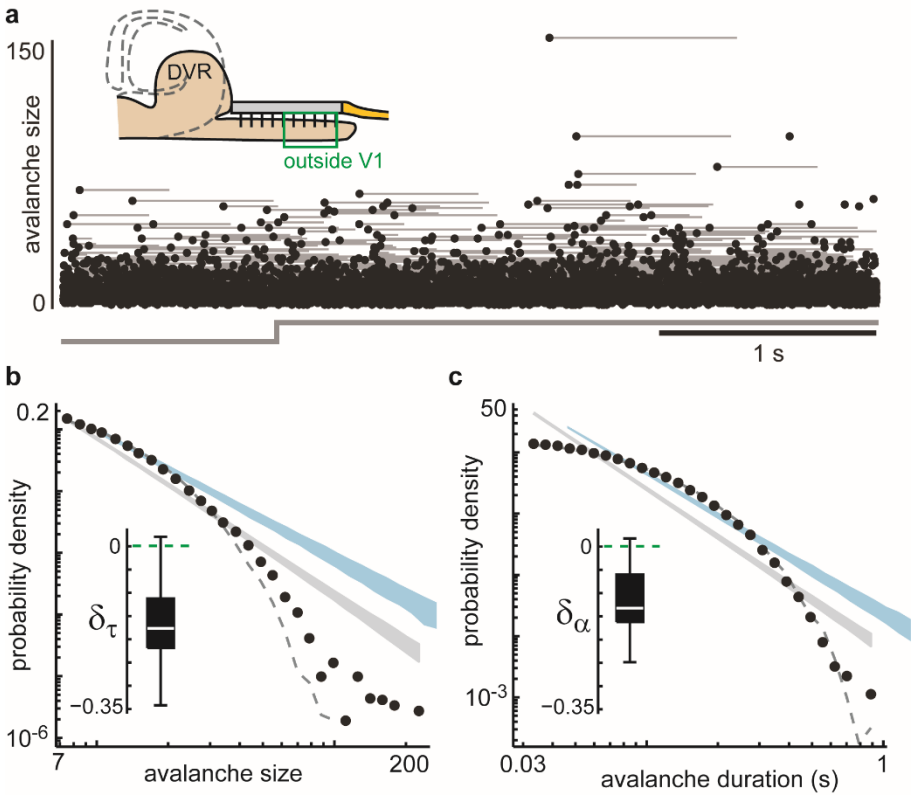

Supplementary Figure 4.8 Critical dynamics are not a universal feature of cortical circuits: no power laws outside visual cortex**.** Here we present recordings from outside visual cortex (Supplementary Figure 4.3)in the cortical region adjacent to visual cortex, known as medial cortex, the putative homolog of mammalian hippocampus(P. Ulinski, 2007). (**a**) Stimulus-triggered avalanche size time series confirms that, among electrodes outside visual cortex, the cortex is active, but activity is independent of visual response. Each point represents one avalanche. Avalanche durations are represented by the gray line to the right of each point. The avalanches recorded during 45 repeats of movie stimulation are overlaid. **(b,c)** Outside visual cortex, avalanche size (b) and duration (c) distributions are not power laws. For comparison, the best fit power law is represented by the gray shaded region and the power law for avalanches within visual cortex is shown in blue (data from same turtle as Figure 4.1). Jittering LFP peak times (dashed) leaves avalanche size statistics largely unchanged, indicating that cross-channel correlations are weak outside visual cortex. Inset summarizes the deviation from the visual cortex power law for all experiments. While fitting power laws to activity outside of visual cortex (Supplementary Figure 4.8), we did not fit the y_0 parameter, because such fitting resulted in y_0 very close to y_M excluding the vast majority of the dataset. This fact is further demonstration that the data are not power law outside visual cortex. Likewise x_0 was not a fitting parameter for activity outside visual cortex.

4.5.7 Details and Example Data from Model with Adapting Synapses

Our model with adapting synapses was designed to test the idea that short-term depression may account for our primary experimental observation: power law avalanches after a transient period of depressive adaptation. The model consisted of $N = 1000$ all-to-all connected binary neurons (mimicking cortex). In addition, each neuron receives input from outside the network (mimicking thalamic drive). The 'strength' of the synapse from cortical neuron *j* onto neuron *i* at time *t* is determined by the corresponding element of the synaptic weight matrix $W_{ij}(t)$. 20% of neurons are inhibitory. All the output synapses of inhibitory neurons are modeled with negative entries in the weight matrix. Similarly, $\Omega_i(t)$ is the strength of the thalamocortical synapse onto neuron *i* (all excitatory). The binary state $s_i(t+1)$ of neuron *i* ($s = 0$ inactive, $s = 1$ spiking) is determined probabilistically based on the sum $p(t+1)$ of its inputs

$$p(t+1) = \Omega_i(t)\sigma_i(t) + \sum_{j=1}^{N} W_{ij}(t)s_j(t)$$

If $0 < p < 1$, then the neuron fires with probability p . If $p \geq 1$, then the neuron fires with probability 1 (p is very rarely >1). If $p \leq 0$, then the neuron does not fire (p is very rarely <0). Time is discrete and state updates are synchronous. The input $\sigma_i(t)$ from the *i*th thalamocortical synapse is 1 with probability *r* and zero with probability 1- *r*, for all *i*. To simulate the onset of visual stimulation, we implement a step increase from r=5x10^{-5} to either r=0.02 or r=0.1. In the main text and in figures (Figures 4.2, 4.3, Supplementary Figs. 4.1, 4.2, 4.9) we report the population input rate of $R = Nr$,which specifies the total number of input spikes per timestep for

the whole network. Data from both of these situations is summarized in Figure 4.3 and Supplementary Figure 4.9.

At time $t = 0$ the cortico-cortical synapse matrix is equal to the default matrix W_{ij}^{0}. The default matrix is constructed as follows. Initially all entries are drawn from a uniform distribution on $[0,1]$. Then a randomly chosen subset of 20% of columns are multiplied by -1 (these are the inhibitory output synapses). Then, the weight matrix is normalized so that its largest eigenvalueΛ_0 has absolute value equal to either 1.0, 1.05, or 1.1. Data generated with these different model parameters is summarized in Figure 4.3 and Supplementary Figure 4.9. A largest eigenvalue of 1.0 corresponds approximately to an average synaptic weight of 1/N and is known to result in critical dynamics for models with static synapses and weak input (Larremore et al., 2011) (Supplementary Figs 4.1, 4.2). The initial thalamocortical synapses Ω_i^0 are all equal to $8/N$. Both the corticocortical and thalamocortical synapses are dynamic in an activity-dependent manner, similar to previous models (A. Levina et al., 2007; Anna Levina et al., 2009). They depress with a time constant of $\tau_d = 20$ timesteps following a presynaptic spike. They also recover exponentially with a time constant of $\tau_r = 400$ timesteps. These timescales for depression and recovery were chosen so that the synapses reach a steady state in less than about 500 timesteps, which is consistent the timescales of adaptation we observed experimentally, if we interpret one timestep as approximately 1 ms. The discrete time update rules for synaptic dynamics are

$$W_{ij}(t+1) = W_{ij}(t) + \frac{1}{\tau_r}\left(W_{ij}^{o} - W_{ij}(t)\right) - \frac{1}{\tau_d} W_{ij}(t) s_j(t)$$

$$\Omega_i(t+1) = \Omega_i(t) + \frac{1}{\tau_r}\left(\Omega_i^o - \Omega_i(t)\right) - \frac{1}{\tau_d}\Omega_i(t)\sigma_i(t)$$

In this model, avalanches are initiated by thalamocortical input and sustained by a combination of corticocortical interactions plus thalamocortical input. Upon reaching a timestep with no active cortical neurons, the avalanche is considered to be ended. Model avalanche size and duration distributions were treated with the same statistical tests as the experimental data.One exception to this was that, for the model data, the upper cutoff x_M was a fitting parameter, but in experiments it was fixed. This was done because in the model there was a clear cutoff at large size avalanches that needed to be accounted for.

We used this model to simulate 30 repetitions of step increase in thalamocortical drive. The transient period in the model was defined in the same way as the experiments and was typically 200-300 timesteps. We ran the model for 5000 timesteps following the onset of increased drive. This allowed us to obtain distributions based on thousands of avalanches; a similar number of avalanches was found in experiments (Supplementary Table 1). We also used the model to investigate how greater or lesser degrees of subsampling might impact the statistics of avalanche distributions during the visually-driven steady state (Figure 4.3, Supplementary Figure 4.9). Our findings are consistent with previous studies of subsampling, which found that increasing subsampling in densely connected networks steepens the avalanche distributions (Priesemann et al., 2014; Ribeiro et al., 2014).

Comparison to related models

Although the synaptic dynamics in our model was motivated by the model studied by Levina et al. (2007), our model differs in important ways from Levina et al's model. Our neurons are leaky, as in numerous recent studies of criticality in neural systems (Kinouchi & Copelli,

2006; Larremore et al., 2011; Woodrow L Shew, Yang, Petermann, Roy, & Plenz, 2009; S.-J. Wang, Hilgetag, & Zhou, 2011); they do not integrate inputs over indefinite time intervals. We set the timescale of depression to be somewhat slower 20 timesteps than the ~5 timesteps for Levina et al. We chose this timescale to approximately match the observed duration of the transient response in our experiments. Another difference is that we include inhibitory neurons, similar to other recent studies (Larremore, Shew, Ott, Sorrentino, & Restrepo, 2014; S.-J. Wang et al., 2011; Yang, Shew, Roy, & Plenz, 2014). Finally, we consider the strongly driven case, whereas Levina et al. maintained a separation of timescales that is typical in models of self-organized criticality. In contrast, Hartley et al. (2014) considered a range of different driving including similar rates of external input to what we studied here. Interestingly, Hartley et al. concluded that strong drive does not preclude critical dynamics. We suspect that this apparent discrepancy with our results is due their defining avalanches using a very short ΔT for segmenting avalanches and implementing continuous time modeling, but this possibility remains to be verified in further studies.

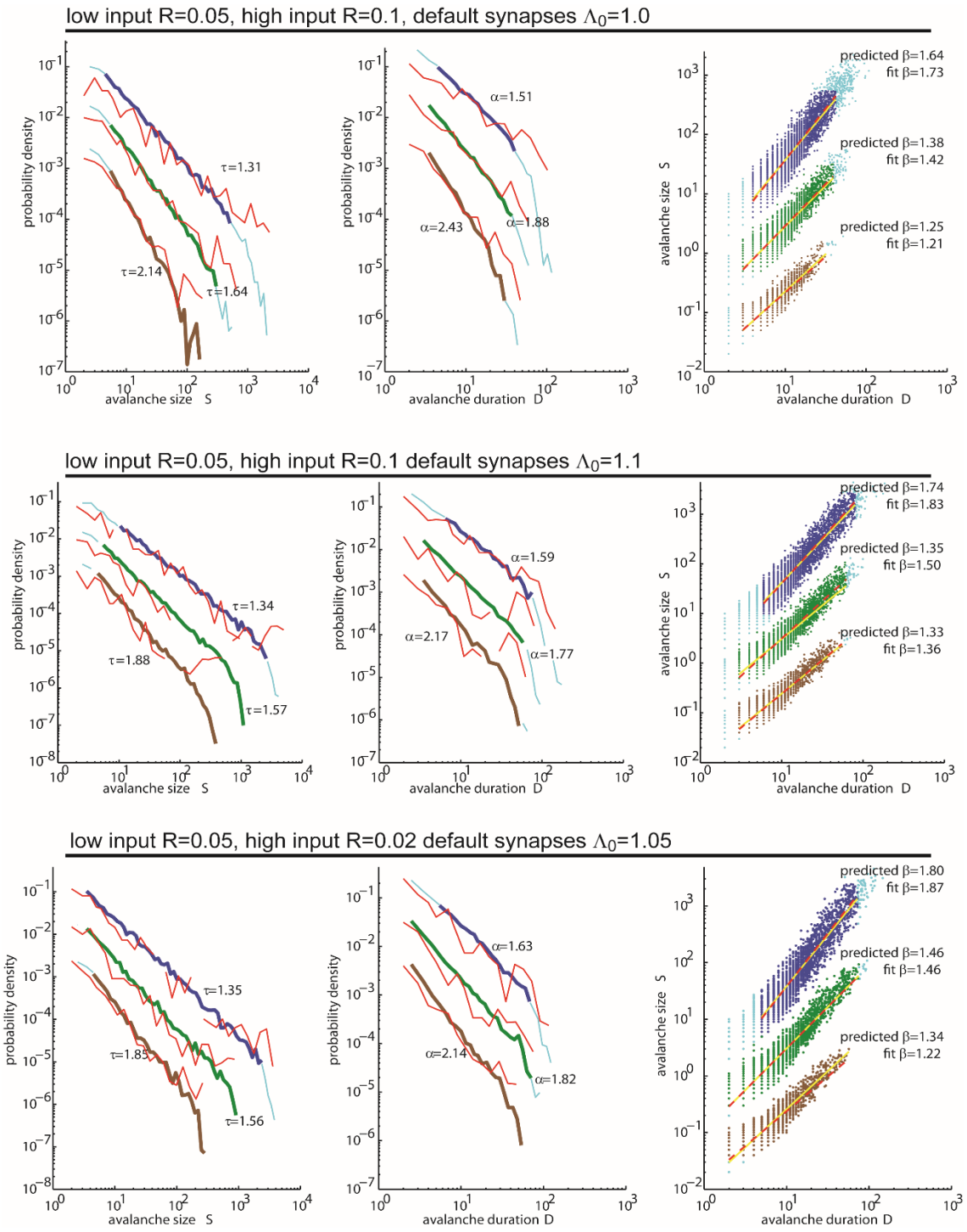
low input R=0.05, high input R=0.1, default synapses Λ0=1.0
probability density
avalanche size S
τ=1.31
τ=2.14
τ=1.64
avalanche duration D
α=1.51
α=2.43
α=1.88
avalanche size S
predicted β=1.64
fit β=1.73
predicted β=1.38
fit β=1.42
predicted β=1.25
fit β=1.21
avalanche duration D
low input R=0.05, high input R=0.1 default synapses Λ0=1.1
probability density
avalanche size S
τ=1.34
τ=1.88
τ=1.57
avalanche duration D
α=1.59
α=2.17
α=1.77
avalanche size S
predicted β=1.74
fit β=1.83
predicted β=1.35
fit β=1.50
predicted β=1.33
fit β=1.36
avalanche duration D
low input R=0.05, high input R=0.02 default synapses Λ0=1.05
probability density
avalanche size S
τ=1.35
τ=1.85
τ=1.56
avalanche duration D
α=1.63
α=2.14
α=1.82
avalanche size S
predicted β=1.80
fit β=1.87
predicted β=1.46
fit β=1.46
predicted β=1.34
fit β=1.22
avalanche duration D

Supplementary Figure 4.9 Detailed examples from model with dynamic synapses. In Figure 4.3 of the main manuscript, we summarize the exponents and scaling relations for nine different sets of model parameters. Here we show the corresponding avalanche distributions and scaling laws for each of these different model data sets. Each row is for a different level of input R and default synapses Λ_0. For a given R and Λ_0, we show the effects of subsampling (green – fully sampled, blue-30% subsampled, brown-10% subsampled). Red distributions represent avalanches during the transient following the increase in drive. The best fit power law exponents α and τ as well as the scaling exponents β are displayed for each condition. In the probability distributions the light blue portions of each line are outside the range of power law scaling.

4.5.8 Empirical Branching Function Versus ΔT

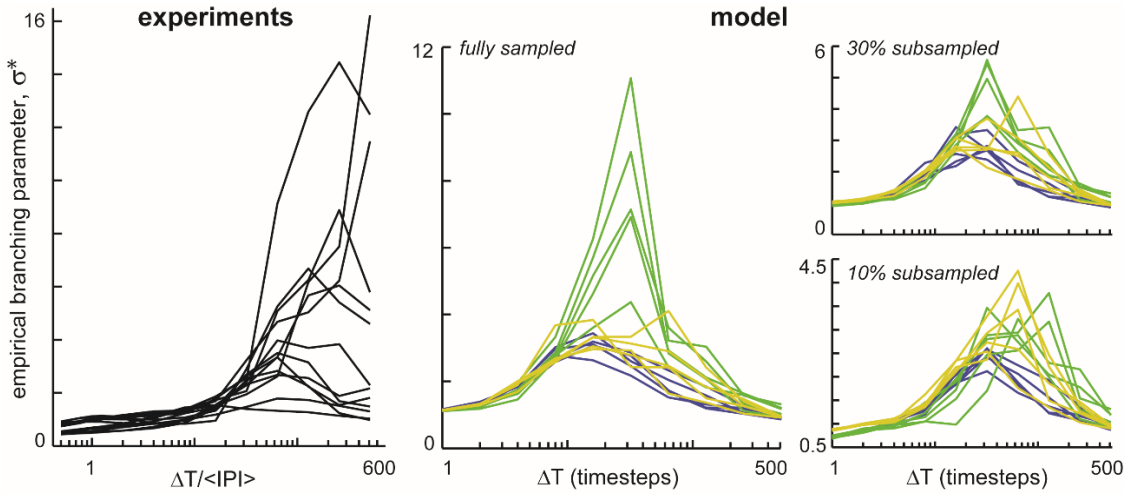

Supplementary Figure 4.10 Empirical branching parameter versus ΔT curves support the hypothesis that visually-driven steady state activity and our model operate in critical regime. Here we study the empirical branching parameter σ* following previously developed methods (Priesemann et al., 2014). In brief, for the experiments **(LEFT)**, we computed the ratio of the number of LFP peaks observed in a time bin of duration ΔT to the number observed in the previous time bin. This ratio was averaged over all consecutive pairs of time bins to obtain σ*. This was then repeated for a different sized time bin to determine how σ* depends on ΔT. As shown in previous work (Priesemann et al., 2014), if this curve reaches a peak significantly above σ*=2 then this may be considered as evidence for critical dynamics. **(MIDDLE)** Results from the model with adapting synapses. Different colors represent different model parameters (green: Λ_0=1.1, R=0.1; purple Λ_0=1.0, R=0.1; yellow Λ_0=1.05, R=0.02). **(RIGHT)** Results from the model with two different levels of subsampling (top 30%; bottom 10%).

4.5.9 Ex vivo eye-attached whole-brain preparation

Following anesthesia (Propofol 10 mg/kg) and rapid decapitation with a guillotine, we surgically removed the brain, optic nerves, and eyes, from the cranium as described earlier (Kriegstein, 1987; Mancilla et al., 1998; D M Senseman, 1996). In brief, during surgery we cut the conjunctiva and extraocular muscles to free the eyes from their orbits. After removing the brain from the skull, we made a cut rostro-caudally along the medial cortex, starting at the ventricle of the olfactory bulb. This cut preserves the normal afferent input of the visual cortical area, because the geniculocortical pathway traverses the lateral cortical wall within the lateral forebrain bundle (Mulligan & Ulinski, 1990). Subsequently, two medio-lateral cuts to the telencephalon at its anterior and posterior ends prepared for unfolding of the hemisphere and exposing the ventricular surface (Supplementary Figure 4.3a). The contralateral eye was hemisected and drained of its vitreous, thus exposing the retina; the ipsilateral eye was removed. The preparation was transferred to the perfusion chamber positioned on an air table with the eye-cup beneath a focusing lens (Figure 4.1a). The unfolded cortex was pinned with short pieces of tungsten wires (25 µm diameter) to an agar block in the recording chamber with the ventricular side up, thus facilitating the subsequent insertion of the microelectrode array.

4.5.10 Details and timing of visual stimuli

Visual stimuli were created by a computer and delivered with either of two methods. In the first method, an LCD monitor (Samsung 19”, 1440x900 pixels, contrast ratio = 20000:1, response time = 2 ms). The image on the monitor was projected onto the retinal surface of the hemisected eye-cup with a converging lens system (Figure 4.1a). The mean light intensity (irradiance) at the retina was 20mW/m^2.A monitor pixel corresponded to 7 µm on the retina or

~0.08^{o} of visual angle (Ariel & Kogo, 2001; Northmore & Granda, 1991).This first method was used in turtles 1-5. In the second method, visual stimuli were projected directly onto the retina with a miniature video projector (Aaxa Technologies, P4X Pico Projector) with additional lenses. Resolution was similar to method 1, but the mean light intensity was higher, 1 W/m^2. This method was used for turtles 7-9.For turtle 6 and one additional experiment with turtle 2, we used brief flash from a light emitting diode (LED) placed near the retina to stimulate as described further below. For the LED, the light intensity was 60 W/m^2 (flash duration 1 s).Stimuli were created using *psychopy*, an open-source psychophysics module written for the Python programming language(Peirce, 2008). Software tools were written to allow the experimenter to characterize the projection of the computer screen onto the retina (Saha et al., 2011). A computer game controller was used to position stimulus image and the eye-cup interactively. The eye-cup parameters, including the position and orientation of the visual streak, and the size and position of the optic disk were documented. An image based on these parameters overlaid on the eye cup preparation (in the recording chamber) when projected through the focusing system. The image was not corrected for curvature of the retina. Two of the turtles were presented with gray-scale naturalistic movies ("CatCam" (Betsch, Einhäuser, Körding, & König, 2004)) as used in studies of the mammalian geniculocortical system (Mante, Bonin, & Carandini, 2008). The movie clip was 10 s in duration and presented in blocks of 45 repetitions at 20 s intervals. 15 min of gray screen was presented between blocks. Three turtles were presented with a previously studied, 5 s duration "motion enhanced" movie (Nishimoto & Gallant, 2011). The screen was black before movie presentation. These three turtles were also presented with a 5 s uniform gray screen, preceded by black screen. The movies were alternated with the gray screen stimuli, presented 80 times at 35 s intervals. Three turtles were presented with black dots (6 deg) moving (6 deg/s)

linearly across a white background. 8 directions of motion were used, each repeated 8 times in pseudorandom order. For each direction, a dot traversed the visual field on 8 to 15 paths during an 86 - 182 s period followed by 5 minutes of darkness before starting the next direction. Two turtles were presented with diffuse red LED flashes (1 s in duration, 2 min intervals, 200 repetitions). The movies and dots were generated on the projection systems described above. For diffuse flashes, the LED was positioned 2 cm above the retina, diffusely illuminating the entire retina. As specified in Supplementary Table 1, some turtle were tested with two different types of visual stimuli.

4.5.11 Robustness to changes in ΔT and defining transient, visually-driven steady state, and ongoing time periods

An avalanche was defined as a spatiotemporal cluster of consecutive LFP peaks with inter-peak intervals not exceeding a temporal threshold ΔT (Methods). Consistent with previous studies (Beggs & Plenz, 2003), ΔT was chosen to be the average inter-peak interval (<IPI>, inverse of population LFP peak rate). This resulted in ΔT in the range 7 to 64 ms (24 ± 18ms, mean ± SD). We note that avalanche statistics and scaling laws were robust to deviations in ΔT within about ±30% from <IPI> (Supplementary Figs. 4.11, 4.12).

The transient time periods T were determined based on the overlaid avalanche time series of all trial of visual stimuli (e.g., Figs. 4.1e, 4.2d). T was computed automatically by first calculating an envelope curve of the avalanche time series defined as the 90 percentile of the avalanche time series in consecutive time bins. Then T was defined as the full width at half max of this envelope curve. This resulted in T ranging from 108 to 784 ms (423 ± 202 ms, mean ± SD, see also Supplementary Table 1). The visually-driven steady state time periods were defined

as any period of visual stimulation, excluding the transient period. Thus, the visually-driven steady state period ended when the visual stimulus ended. One exception was for the two experiments with LED flash stimuli, for which a sustained neural response continued long after the flash ended. For these, we included the sustained response (10 s) as part of the visually-driven period. Ongoing time periods were defined as all periods when no visual stimulus was presented.

Avalanches that started within a period were assigned to that period, irrespective of whether the avalanche extended into the next period. One exception was that avalanches in the ongoing period that ended during the transient period were excluded from analysis. We also note that we excluded avalanches within periods of time when the LFP peak rate was nonstationary over long time scales (Supplementary Figure 4.13). Data from outside visual cortex was not analyzed except for the data shown in Supplementary Figure 4.8.

Most previous studies of neuronal avalanches which have focused on ongoing activity recorded in mammalian cortex. Although ongoing activity was not the focus of our work, we note that, in some experiments, ongoing avalanches were power law distributed similar to the visually-driven avalanches steady state (Supplementary Figure 4.14 top). However, in several experiments the rate of ongoing LFP peaks was too low to obtain enough avalanches to draw sound statistical conclusions about how ongoing avalanches were distributed (Supplementary Figure 4.14 bottom). Rates of LFP peaks, durations of recording periods, and numbers of avalanches for each of the three different periods (transient, steady-state visually-driven, ongoing) are shown in Supplementary Table 4.1.

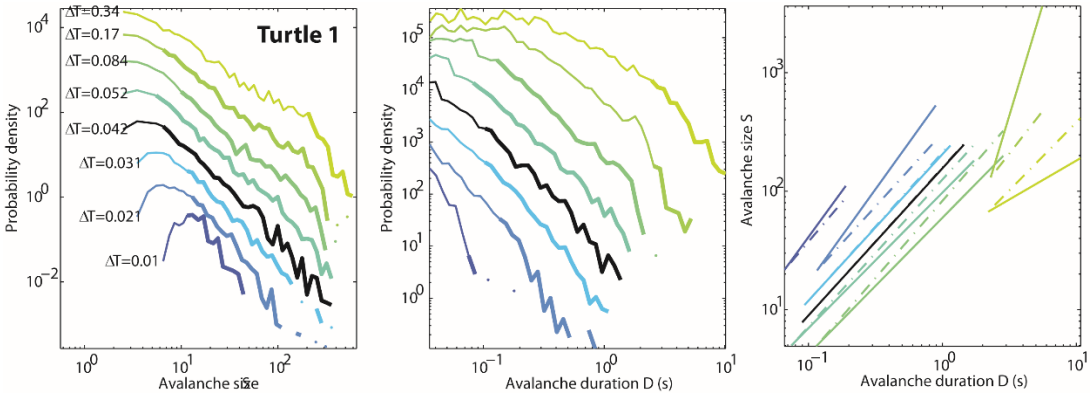

Supplementary Figure 4.11 Dependence of experimental results on choice of ΔT. The figure together with the following 12 plots shows how the form of avalanche size and duration distributions as well as scaling between size and duration depends on ΔT. ΔT values are specified in seconds. In all figures, the black curve represents the actual ΔT=<IPI> used in the manuscript. **(LEFT, MIDDLE)** In each distribution the range that was determined to be well-fit by a truncated power law is shown with a heavier line. (When the range is very small, the distribution is not well fit by a power law.) **(RIGHT)** The right panel compares the predicted size versus duration scaling (dash dot line) and the best fit scaling (solid line) for each ΔT. Points are omitted for clarity. Notice that values of ΔT within about ±30% from the <IPI> still give a reasonable scaling relation, but more severe changes in ΔT result in non-power law size and duration distributions and/or poor prediction of the scaling relation.

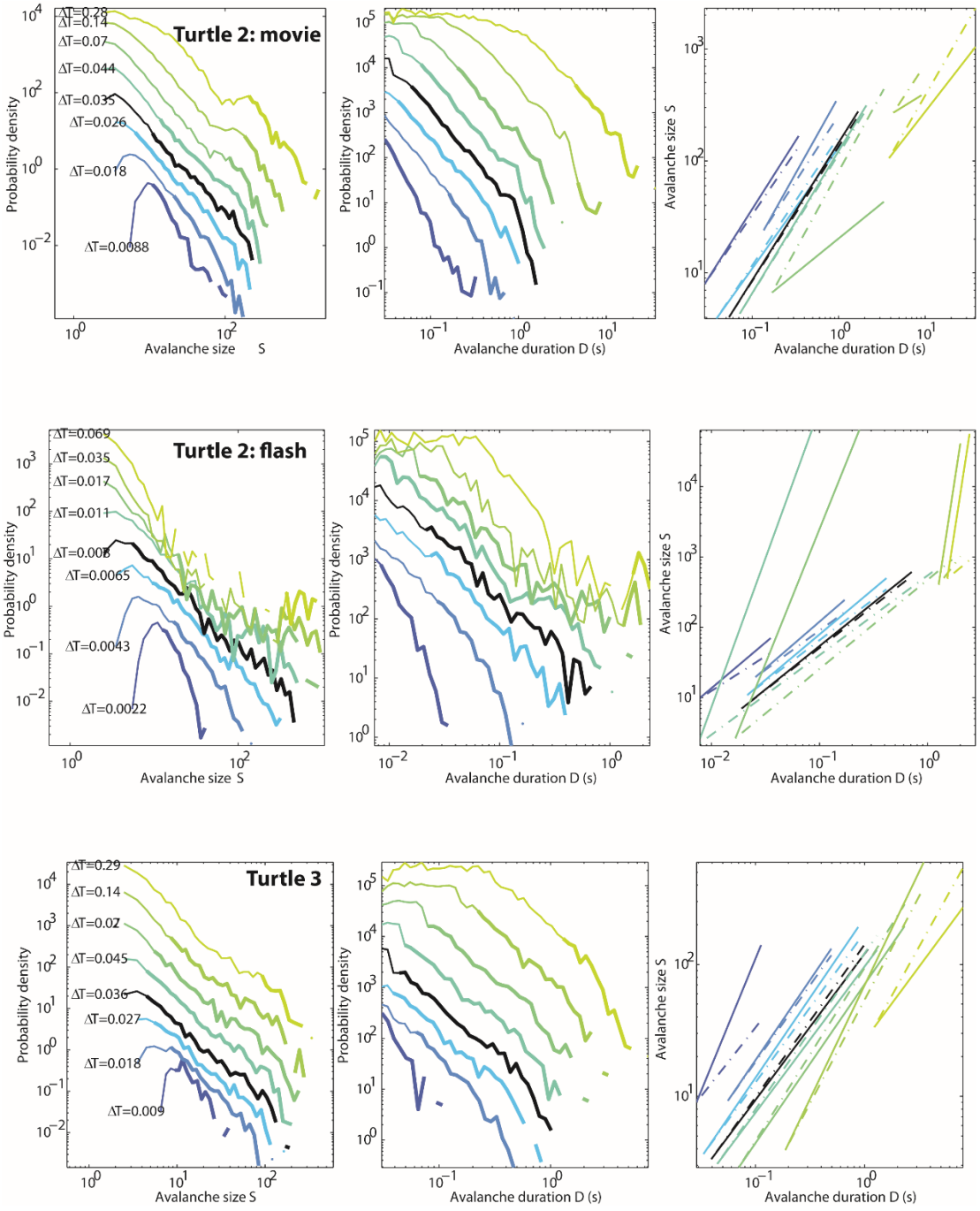
Turtle 2: movie
ΔT=0.28
ΔT=0.14
ΔT=0.07
ΔT=0.044
ΔT=0.035
ΔT=0.026
ΔT=0.018
ΔT=0.0088
Probability density
Avalanche size S
Probability density
Avalanche duration D (s)
Avalanche size S
Avalanche duration D (s)
Turtle 2: flash
ΔT=0.069
ΔT=0.035
ΔT=0.017
ΔT=0.011
ΔT=0.008
ΔT=0.0065
ΔT=0.0043
ΔT=0.0022
Probability density
Avalanche size S
Probability density
Avalanche duration D (s)
Avalanche size S
Avalanche duration D (s)
Turtle 3
ΔT=0.29
ΔT=0.14
ΔT=0.07
ΔT=0.045
ΔT=0.036
ΔT=0.027
ΔT=0.018
ΔT=0.009
Probability density
Avalanche size S
Probability density
Avalanche duration D (s)
Avalanche size S
Avalanche duration D (s)

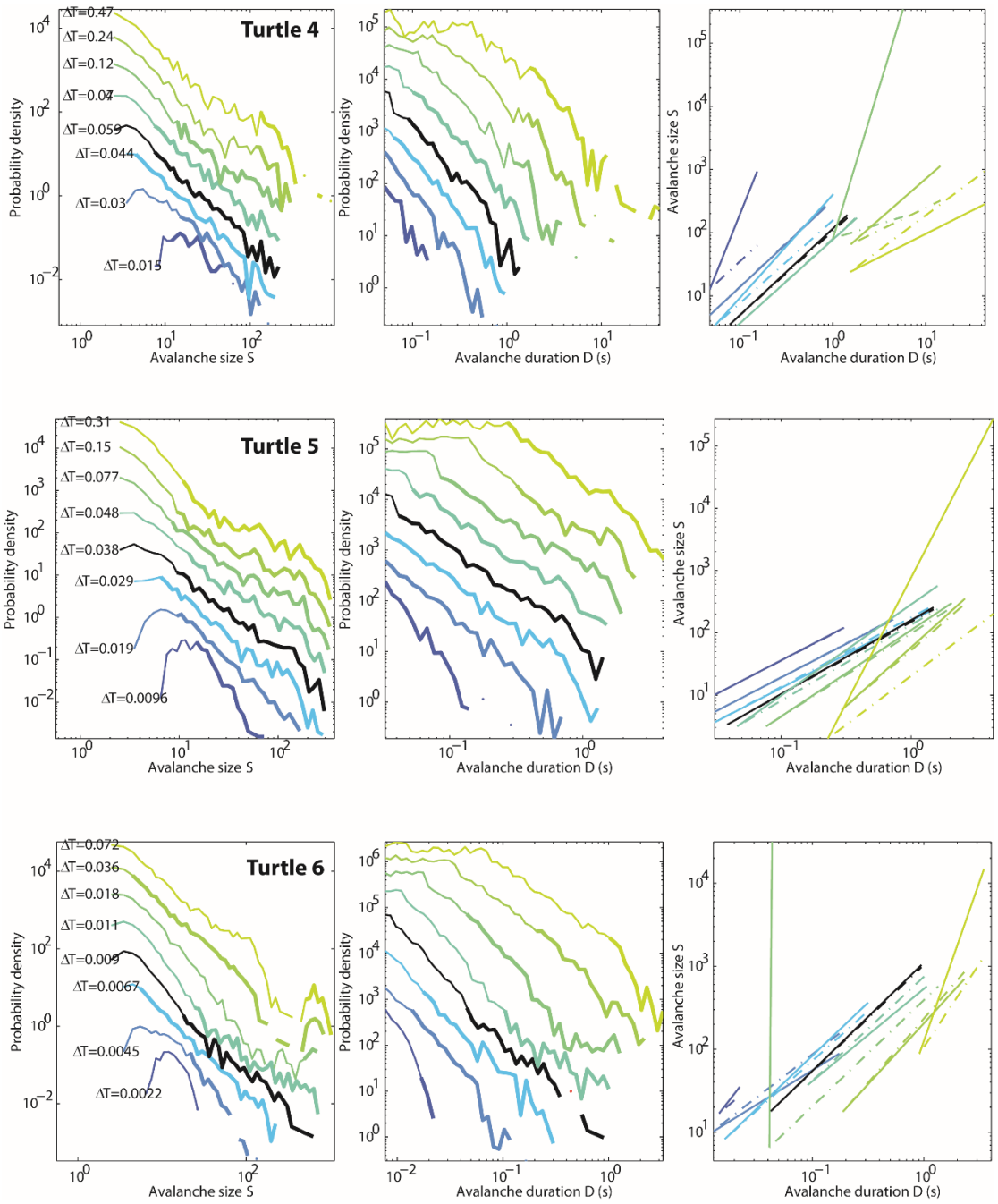
Turtle 4
ΔT=0.47
ΔT=0.24
ΔT=0.12
ΔT=0.07
ΔT=0.059
ΔT=0.044
ΔT=0.03
ΔT=0.015
Probability density
Avalanche size S
Probability density
Avalanche duration D (s)
Avalanche size S
Avalanche duration D (s)
Turtle 5
ΔT=0.31
ΔT=0.15
ΔT=0.077
ΔT=0.048
ΔT=0.038
ΔT=0.029
ΔT=0.019
ΔT=0.0096
Probability density
Avalanche size S
Probability density
Avalanche duration D (s)
Avalanche size S
Avalanche duration D (s)
Turtle 6
ΔT=0.072
ΔT=0.036
ΔT=0.018
ΔT=0.011
ΔT=0.009
ΔT=0.0067
ΔT=0.0045
ΔT=0.0022
Probability density
Avalanche size S
Probability density
Avalanche duration D (s)
Avalanche size S
Avalanche duration D (s)

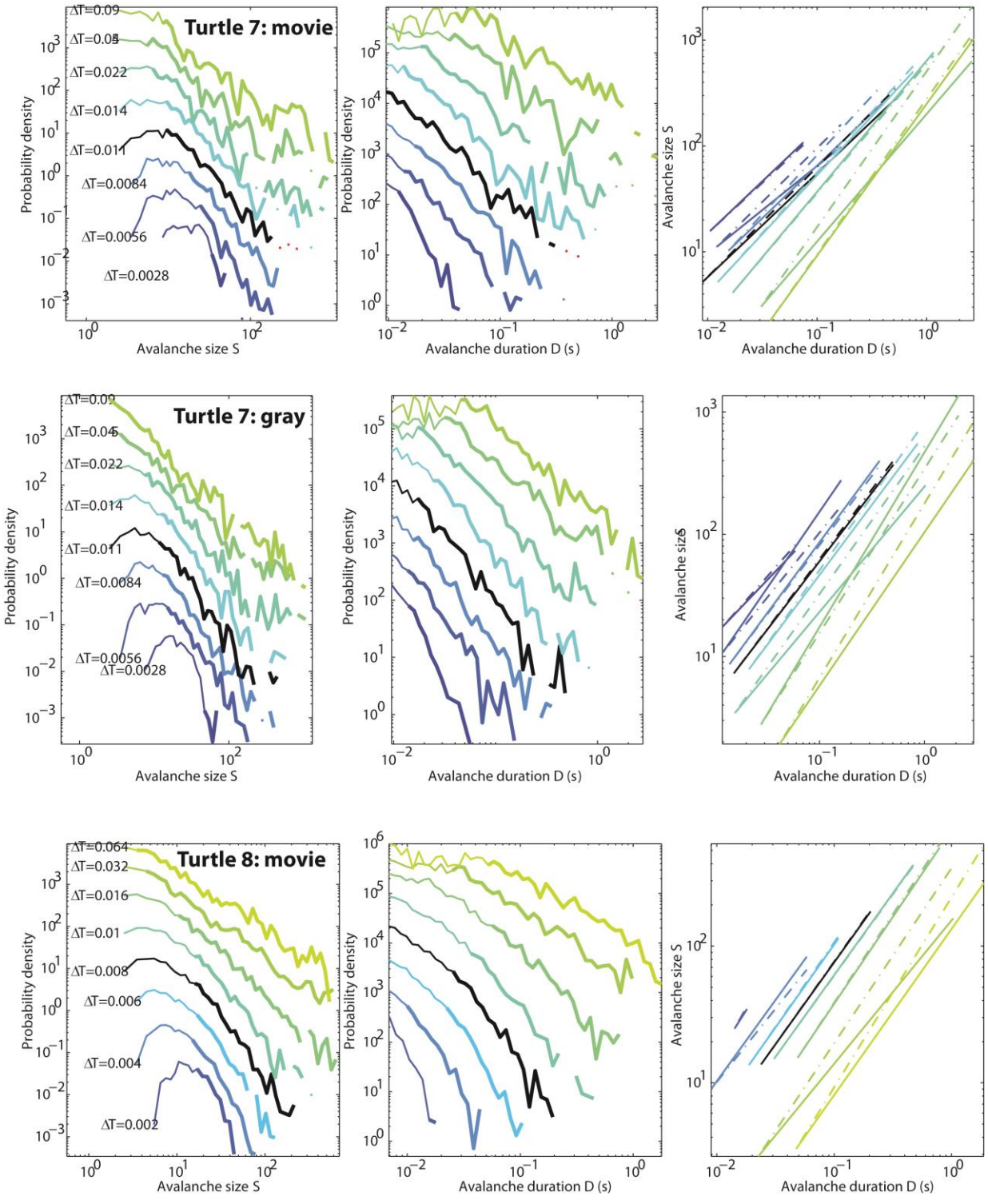
Turtle 7: movie
ΔT=0.09
ΔT=0.045
ΔT=0.022
ΔT=0.014
ΔT=0.011
ΔT=0.0084
ΔT=0.0056
ΔT=0.0028
Probability density
Avalanche size S
Avalanche duration D (s)
Avalanche size S
Avalanche duration D (s)
Turtle 7: gray
ΔT=0.09
ΔT=0.045
ΔT=0.022
ΔT=0.014
ΔT=0.011
ΔT=0.0084
ΔT=0.0056
ΔT=0.0028
Probability density
Avalanche size S
Avalanche duration D (s)
Avalanche size S
Avalanche duration D (s)
Turtle 8: movie
ΔT=0.064
ΔT=0.032
ΔT=0.016
ΔT=0.01
ΔT=0.008
ΔT=0.006
ΔT=0.004
ΔT=0.002
Probability density
Avalanche size S
Avalanche duration D (s)
Avalanche size S
Avalanche duration D (s)

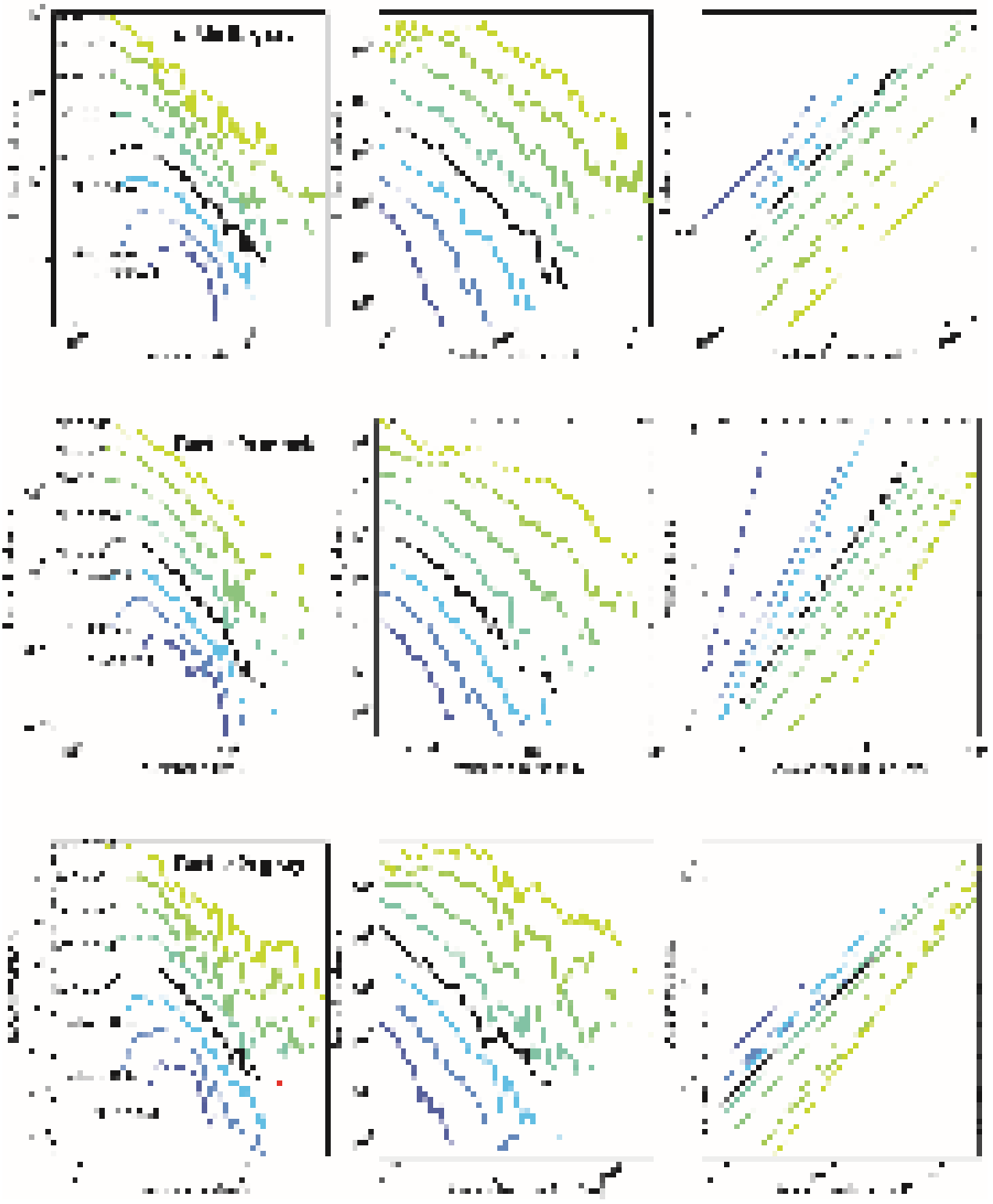

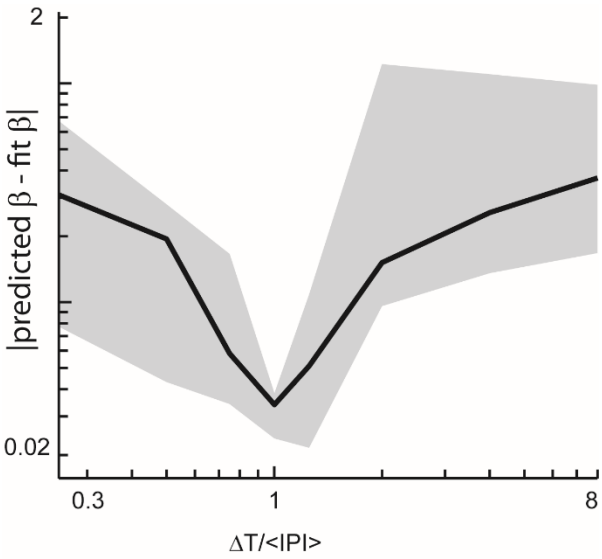

Supplementary Figure 4.12 Good prediction of scaling relation occurs if ΔT is chosen nearby <IPI>. This plot summarizes one feature of the series of plots in Supplementary Figure 4.11. It summarizes how well the predicted scaling relation matches the best fit scaling relation and how this depends on ΔT. Here it is clear that a small difference (good prediction) occurs in a range of approximately ±30% around ΔT=<IPI>.

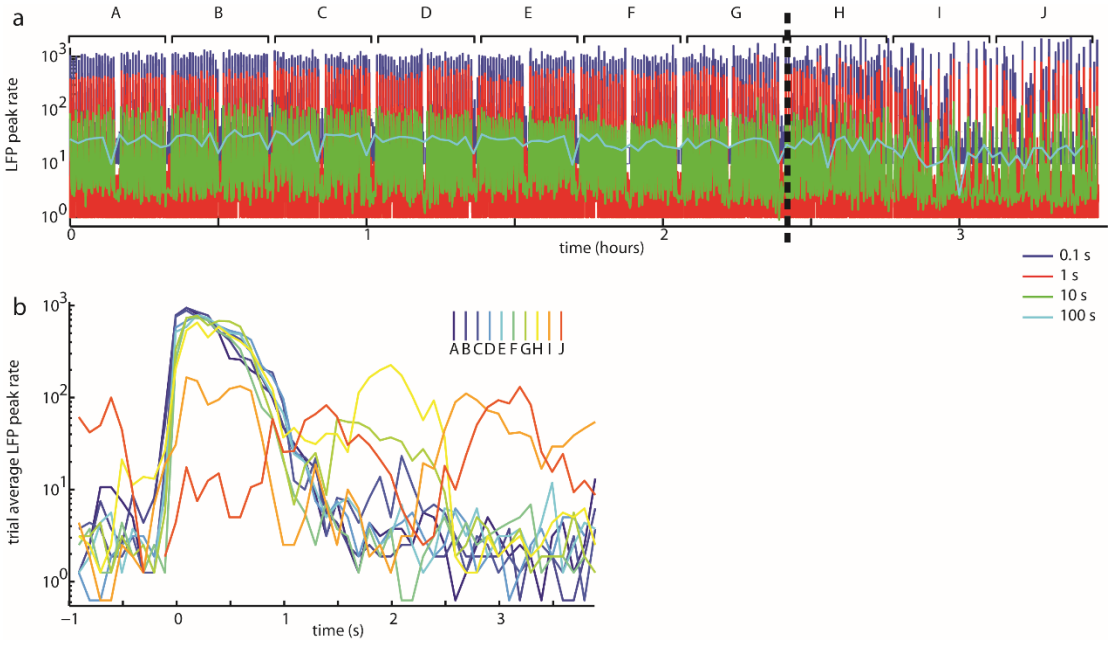

Supplementary Figure 4.13 Stationarity of experimental system. **(a)** The rate of LFP peaks recorded over the course of multiple hours is steady (one representative example experiment shown). Each rate time series was computed by counting LFP peaks in consecutive time windows of duration dt and normalizing by dt. Durations dt=0.1, 1, 10, and 100 s were used (colors indicated in legend). The apparent 10 min cyclic pattern is due the timing of repeated visual stimulus presentation. Note that after about 2.5 hours (epochs labeled H, I and J), non-stationarity sets in. In all experiments, we include data in our analysis only during stationary periods. **(b)** The stimulus-triggered average response to repeated visual stimulation is also steady (except for epoch H, I, and J). The color code corresponds to the periods labeled alphabetically in panel a.

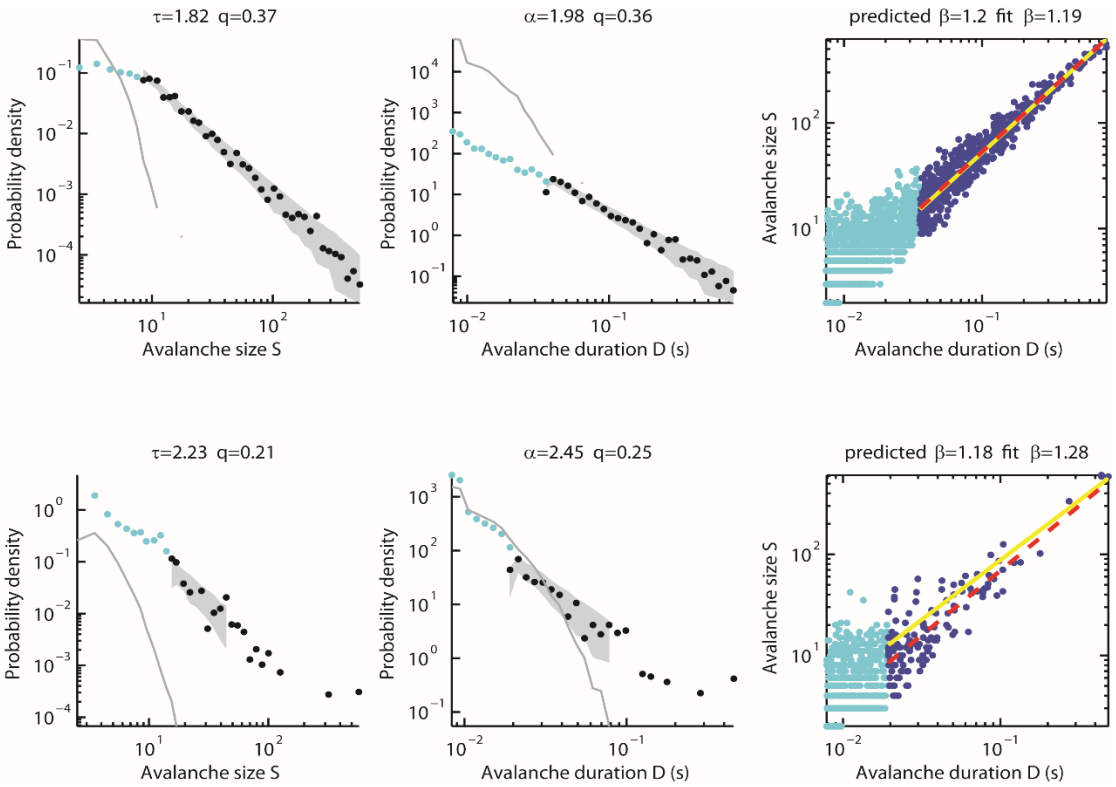

Supplementary Figure 4.14 Ongoing activity exhibited critical dynamics in a subset of experiments. **(top)** In some of our experiments, ongoing activity also exhibited strong evidence for critical dynamics, similar to the visually-driven steady state avalanches. These cases are consistent with previous studies of neuronal avalanches in mammals, which have primarily been based on ongoing activity. **(bottom)** In other experiments, we observed that ongoing activity occurred at such low rate that statistically sound conclusions were not possible.

Supplementary Table 1. Basic statistics for each experiment.

			5	6	7	7	8	8	9	9
		Stimulation type	movie	movie	flash	dots	dots	dots	flash	movie	gray	movie	gray	movie	gray
total recording time (s)		**ongoing**	3263.8	6818.3	7010.3	6260.9	11963.4	9061.5	11950.8	2673.3	2287.0	589.8	1996.8	3800.4	4836.0
		transient	134.3	172.4	6.7	107.7	62.7	275.2	30.7	21.6	22.6	25.4	22.3	49.4	41.8
		visually-driven steady state	3474.8	6127.6	199.6	5035.6	4059.6	6980.0	2227.6	196.4	170.8	71.8	151.9	227.6	317.1
		all	6872.9	13118.3	7216.7	11404.3	16085.8	16316.7	14209.2	2891.3	2480.5	687.1	2171.0	4077.5	5194.9
rate of recorded LFP peaks (Hz)		**ongoing**	5.8	10.8	7.6	3.8	3.8	2.9	5.5	12.9	25.6	59.4	53.4	42.5	45.2
		transient	92.4	100.6	357.2	5.7	5.7	9.6	52.7	391.6	303.6	530.8	411.5	604.7	828.0
		visually-driven steady state	16.9	31.3	196.6	7.4	8.8	7.6	38.8	101.0	115.1	275.9	165.2	91.8	92.4
number of avalanches	**ongoing**	**total**	900	667	1096	1090	2679	721	1692	88	218	416	583	255	1115
		in ongoing size distribution fitting range	*304*	*268*	*404*	*554*	*259*	*544*	*1016*	*67*	*145*	*204*	*444*	*167*	*97*
		in ongoing duration distribution fitting range	*272*	*208*	*489*	*588*	*1437*	*313*	*507*	*52*	*172*	*227*	*471*	*254*	*132*
	transient	**total**	447	915	126	39	28	123	57	152	116	267	203	555	318
	visually-driven steady state	**total**	2968	13871	1246	1638	1920	1792	4255	415	533	917	497	1036	987
		in size distribution fitting range	*964*	*5532*	*897*	*1393*	*824*	*648*	*362*	*295*	*323*	*396*	*314*	*300*	*407*
		in duration distribution fitting range	*892*	*3082*	*587*	*1134*	*1129*	*1288*	*287*	*414*	*305*	*320*	*497*	*447*	*475*
		jitter time Tj (s)	1.4	1.4	1.2	0.9	2	1.1	1.1	1.1	2	1.5	1.8	1.9	1.2
		transient time (s)	0.746	0.547	0.108	0.436	0.302	0.784	0.256	0.260	0.293	0.462	0.306	0.618	0.380

4.5.12 Power law fitting and the measure δ

To test whether evoked and ongoing avalanches were distributed according to a power law, we carried out a two-step analysis. First, we identified the best-fit power law using established maximum likelihood methods (Clauset et al., 2009; Klaus et al., 2011; Langlois, Cousineau, & Thivierge, 2014). As in previous studies, we assumed that there is a lower size limit, below which power law statistics are not expected (Clauset et al., 2009; Langlois et al., 2014). The rationale for this assumption was that some measurement noise is unavoidable and likely to be uncorrelated across channels, thus resulting in some small size 'noise-corrupted' avalanches. In line with this idea, we found that avalanches that were shorter than approximately ΔT in duration were distributed quite differently than larger duration avalanches (Supplementary Figure 4.15). For this reason, in all of our figures (except Supplementary Figure 4.15) we plot avalanches with durations exceeding 0.8ΔT. An important difference between our method and the typical approach (Clauset et al., 2009) is that we assumed that avalanches are also limited in how large they can be. Such avalanche size and duration limits have been recognized in other work as well (Klaus et al., 2011; Langlois et al., 2014). Thus, we identified the maximum likelihood truncated power law fit to our data. This approach obviates the need for comparing to similar distributions (e.g., power law with exponential cutoff (Clauset et al., 2009; Klaus et al., 2011)), because the truncation cuts off such end effects already. Since our definition of avalanche size is a discrete, integer variable, the fitting function for the avalanche size distribution was

$$f(S) = \frac{S^{-\tau}}{\sum_{x=x_0}^{x_M} x^{-\tau}}$$

The maximum size x_M was assumed to be the largest size actually observed in the experimental data. We note that, in our experiments, unlike many previous experiments in mammals, we did not observe a clear size cutoff at the number of channels used to record. This reflects the tendency for a single channel to have many LFP peaks during a single avalanche. The minimum size x_0 and the power law exponent τ were fitting parameters. Since avalanche duration is a non-integer variable, the fitting function for the avalanche duration distribution was

$$g(D) = \frac{D^{-\alpha}}{\int_{y_0}^{y_M} y^{-\alpha} dy} = \frac{1-\alpha}{y_M^{1-\alpha} - y_0^{1-\alpha}} D^{-\alpha}$$

Again, the maximum duration y_M was taken as the largest observed duration, while y_0 and αwere fitting parameters. The fitting process involved trying all exponents in the range from -1 to -4 with increments of 0.01, similar to previous work (Clauset et al., 2009). However, another important difference between our approach and previous work (Clauset et al., 2009) is that our fitting algorithm tried values of y_0 values increasing from 0, but only up to the point when the fitted power law matches the data well enough to have a Kolmogorov-Smirnov statistic $KS < 1/\sqrt{N_{samp}}$, where N_{samp} is the number of avalanches comprising the dataset. This prevents the algorithm from increasing the minimum size until most of the data are excluded from fitting. The threshold of $1/\sqrt{N_{samp}}$ is justified based on how KS variability is expected to vary with N_{samp} for surrogate datasets drawn from a true power law (Goldstein, Morris, & Yen, 2004) (Supplementary Figure 4.16).

For fitting model data size and duration distributions, we used the fitting function $f(S)$ above, because both size and duration are discrete variables for the model. Also, for the model data, x_M was used as a fitting parameter because there typically was a clear exponential cutoff in the model avalanche distributions.

After finding the best-fit power law, the next step was to assess goodness-of-fit q. For this, we again follow established methods (Clauset et al., 2009; Goldstein et al., 2004). We compared the experimental data to 1000 surrogate data sets drawn from the best-fit power law distribution. The surrogate data sets had the same number of samples as the experimental data set. In this way, the surrogate data sets are as close as possible to a power law, for a given finite sample size. The deviation between the surrogate data sets and a perfect power law was quantified with the KS statistic. The quality q of the power law fit was defined as the fraction of these surrogate KS statistics which were greater than the KS statistic for the experimental data. Thus, if the experimental data had a smaller KS statistic than at least 100 of the surrogate values, then $q>0.1$. We use a very conservative criterion, $q>0.1$, for judging the data to be power law distributed. This is demonstrated visually in Figure 4.1f,g and Figure 4.2e,f by plotting the experimental distribution over a gray band which delineates the 5-95 percentiles of the surrogate data sets. It should be noted that for a large number of samples, this goodness-of-fit test is very strict (i.e., more than about 200 avalanches (Clauset et al., 2009)). In our experiments, the number of avalanches during visual stimulation was 2467, on average (ranging from 415 to 13871).

Deviation between two distributions, δ.

Avalanches occurring during the transient period following stimulus onset were not power law distributed. Large avalanches occurred with high probability, often resulting in

bimodally distributed sizes and durations. To quantitatively measure how avalanche distributions from the transient periods deviate from the power laws observed during the visually-driven steady state periods, we used a measure δ, which is similar to measures developed in previous studies (W. L. Shew et al., 2009; Tetzlaff, Okujeni, Egert, Wörgötter, & Butz, 2010). To compute δ, we first constructed a cumulative distribution function (CDFs) for the test distribution (transient) and the reference distribution (visually-driven steady state). Then δ is the sum of 10 differences between the reference CDF and the test CDF (Supplementary Figure 4.17). The points, at which the 10 differences were taken, were equally spaced on a logarithmic scale between the minimum and maximum avalanche size. When $\delta > 0$, which typically was the case for avalanche distributions from the transient periods, this indicates that large events occurred more frequently than would be expected if they came from the same distribution as the visually-driven steady state periods (Supplementary Figure 4.17).

We also used δ to examine control distributions, in which avalanches were reanalyzed after randomly jittering the occurrence times of LFP peaks. For this, we added to each LFP peak time a random number drawn from a uniform distribution on $[-T_j,+T_j]$. Such jittering decreases spatiotemporal correlations and reduces the probability of large avalanches. In terms of δ, this results in $\delta < 0$. To quantify the effects of jittering, we determined how large the jitter time T_j must be to reach $\delta < -0.1$, a significant deviation. We found $T_j = 1.4 \pm 0.4$ (mean±SD) across all experiments (Supplementary Table 1).

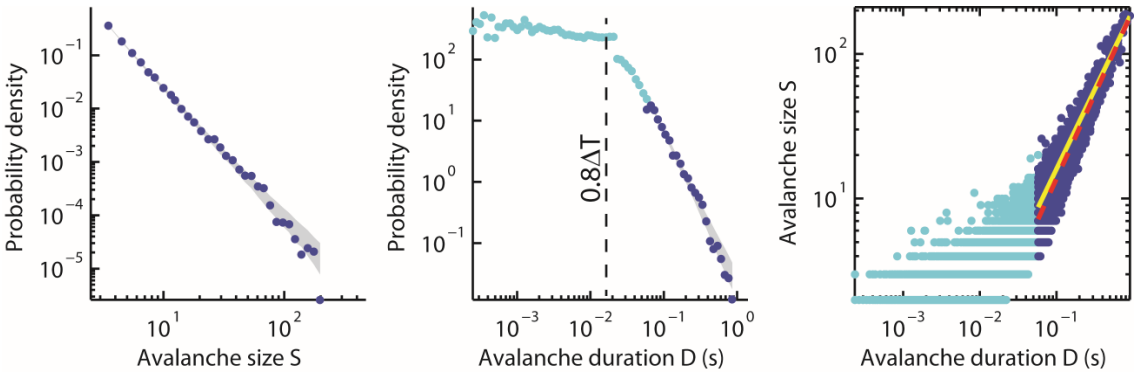

Supplementary Figure 4.15 Very short duration avalanches are distributed differently. The analysis of experimental data presented in the manuscript is based on analyzing only those avalanches with durations longer than 0.8 ΔT. The reason for this approach was that for very short duration avalanches, with D less than about ΔT, a different regime of avalanches is clear in the duration distribution (the flat region in the middle panel). The low D regime tends to have a nearly flat distribution of durations and scales differently with avalanche size (light blue points in right panel) This different regime may be due to influence of noise for small, short duration avalanches.

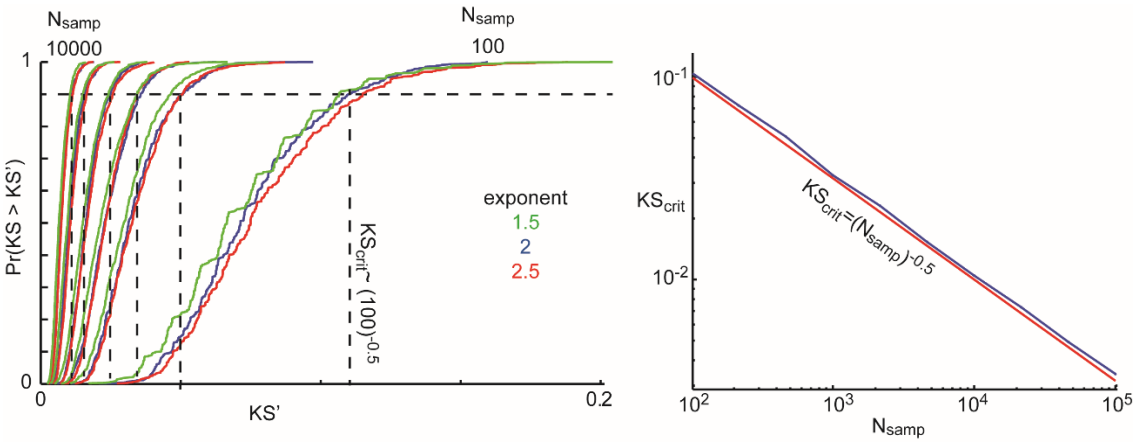

Supplementary Figure 4.16 Fitting the lower bound cutoff of power law regime depending on sample size. As discussed in methods, we used the KS statistic for fitting the lower cut off point x_0 in the power-law fitting process. We increased x_0 until a criterion level of KS was reached. The sensible choice for a criterion KS depends on the number of samples N. In this figure we describe numerical simulations used to determine the criterion KS. First, we computed the KS statistic for a perfect power-law reference CDF with exponent ε, compared to a surrogate data set with N samples drawn randomly from a power-law with exponent ε. We repeated this 1000 times. CDFs of these 1000 KS values are shown in the left panel above. Colors represent different exponentsε. Then we defined the criterion KS_{crit} to be the KS value below which 90% of the values lie (dashed line). We carried out this process for six different sample sizes N= 100, 500, 1000, 2000, 5000, and 10000. We found that KS_{crit} was very close to $1/\sqrt{N_{samp}}$ as shown in the right panel above (blue – data from left panel plot; red – exact $1/\sqrt{N_{samp}}$ function). This approach generalizes existing tabulated values for such fitting criteria (Goldstein et al., 2004).

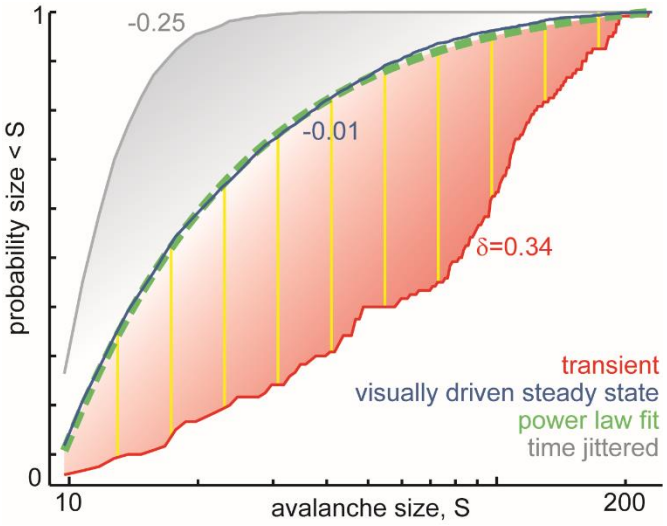

Supplementary Figure 4.17 Quantifying how avalanche distributions differ between transient periods, visually-driven steady state periods. The deviation δ is computed as the sum of 10 differences (e.g., yellow lines for transient avalanches) between a reference CDF (green) and the measured CDF (red). Here, the reference CDF is the best-fit power law for the visually-driven steady state (blue). If large avalanches are more or less prevalent in the measured CDF than in the reference CDF, then $\delta > 0$ or $\delta < 0$, respectively. Near zero deviation occurs when the measured CDF matches the reference CDF (e.g., blue). See Supplementary Figure 4.7 for similar CDF plots and δ values for avalanche size and duration distributions for all experiments.

4.6 References

4.6.1 Main Paper References

Bak, P., Tang, C., & Wiesenfeld, K. (1987). Self-organized criticality: An explanation of the 1/f noise. *Physical Review Letters*, *59*(4), 381–384.

Beggs, J. M. (2008). The criticality hypothesis: how local cortical networks might optimize information processing. *Philosophical Transactions. Series A, Mathematical, Physical, and Engineering Sciences*, *366*(1864), 329–43. doi:10.1098/rsta.2007.2092

Beggs, J. M., & Plenz, D. (2003). Neuronal avalanches in neocortical circuits. *The Journal of Neuroscience : The Official Journal of the Society for Neuroscience*, *23*(35), 11167–77. Retrieved from http://www.ncbi.nlm.nih.gov/pubmed/14657176

Beggs, J. M., & Timme, N. (2012). Being critical of criticality in the brain. *Frontiers in Physiology*, *3*, 163. doi:10.3389/fphys.2012.00163

Bialek, W. (2012). *Biophysics: Searching for Principles*. Princeton, NJ: Princeton University Press.

Bornholdt, S., & Röhl, T. (2003). Self-organized critical neural networks. *Physical Review E*, *67*(6), 1–5. doi:10.1103/PhysRevE.67.066118

Chung, S., Li, X., & Nelson, S. B. (2002). Short-term depression at thalamocortical synapses contributes to rapid adaptation of cortical sensory responses in vivo. *Neuron*, *34*(3), 437–46.

Clauset, A., Shalizi, C. R., & Newman, M. E. J. (2009). Power-Law Distributions in Empirical Data. *SIAM Review*, *51*(4), 661–703. doi:10.1137/070710111

Friedman, N., Ito, S., Brinkman, B., Shimono, M., DeVille, R., Dahmen, K., … Butler, T. (2012). Universal Critical Dynamics in High Resolution Neuronal Avalanche Data. *Physical Review Letters*, *108*(20), 1–5. doi:10.1103/PhysRevLett.108.208102

Gireesh, E., & Plenz, D. (2008). Neuronal avalanches organize as nested theta- and beta/gamma-oscillations during development of cortical layer 2/3. *Proceedings of the National Academy of Sciences of the United States of America*, *105*(21), 7576–81. doi:10.1073/pnas.0800537105

Haimovici, A., Tagliazucchi, E., Balenzuela, P., & Chialvo, D. R. (2013). Brain Organization into Resting State Networks Emerges at Criticality on a Model of the Human Connectome. *Physical Review Letters*, *110*(17), 178101. doi:10.1103/PhysRevLett.110.178101

Haldeman, C., & Beggs, J. M. (2005). Critical Branching Captures Activity in Living Neural Networks and Maximizes the Number of Metastable States. *Physical Review Letters*, *94*(5). doi:10.1103/PhysRevLett.94.058101

Kinouchi, O., & Copelli, M. (2006). Optimal dynamical range of excitable networks at criticality. *Nature Physics*, *2*(5), 348–351. doi:10.1038/nphys289

Klaus, A., Yu, S., & Plenz, D. (2011). Statistical analyses support power law distributions found in neuronal avalanches. *PloS One*, *6*(5), e19779. doi:10.1371/journal.pone.0019779

Kohn, A. (2007). Visual adaptation: physiology, mechanisms, and functional benefits. *Journal of Neurophysiology*, *97*(5), 3155–64. doi:10.1152/jn.00086.2007

Larremore, D. B., Shew, W. L., & Restrepo, J. G. (2011). Predicting Criticality and Dynamic Range in Complex Networks: Effects of Topology. *Physical Review Letters*, *106*(5), 1–4. doi:10.1103/PhysRevLett.106.058101

Levina, A., Herrmann, J., & Geisel, T. (2009). Phase Transitions towards Criticality in a Neural System with Adaptive Interactions. *Physical Review Letters*, *102*(11), 118110. doi:10.1103/PhysRevLett.102.118110

Levina, A., Herrmann, J. M., & Geisel, T. (2007). Dynamical synapses causing self-organized criticality in neural networks. *Nature Physics*, *3*(12), 857–860. doi:10.1038/nphys758

Meisel, C., & Gross, T. (2009). Adaptive self-organization in a realistic neural network model. *Physical Review E*, *80*(6), 1–6. doi:10.1103/PhysRevE.80.061917

Moretti, P., & Muñoz, M. a. (2013). Griffiths phases and the stretching of criticality in brain networks. *Nature Communications*, *4*, 2521. doi:10.1038/ncomms3521

Petermann, T., Thiagarajan, T. C., Lebedev, M. A., Nicolelis, M. A. L., Chialvo, D. R., & Plenz, D. (2009). Spontaneous cortical activity in awake monkeys composed of neuronal avalanches. *Proceedings of the National Academy of Sciences of the United States of America*, *106*(37), 15921–6. doi:10.1073/pnas.0904089106

Plenz, D., Niebur, E., & Schuster, H. G. (2014). *Criticality in Neural Systems*. (D. Plenz, E. Niebur, & H. G. Schuster, Eds.). Weinheim, Germany: Wiley.

Priesemann, V., Valderrama, M., Wibral, M., & Le Van Quyen, M. (2013). Neuronal Avalanches Differ from Wakefulness to Deep Sleep – Evidence from Intracranial Depth Recordings in Humans. *PLoS Computational Biology*, *9*(3), e1002985. doi:10.1371/journal.pcbi.1002985

Priesemann, V., Wibral, M., Valderrama, M., Pröpper, R., Le Van Quyen, M., Geisel, T., … Munk, M. H. J. (2014). Spike avalanches in vivo suggest a driven, slightly subcritical brain state. *Frontiers in Systems Neuroscience*, *8*(June), 108. doi:10.3389/fnsys.2014.00108

Ribeiro, T. L., Ribeiro, S., Belchior, H., Caixeta, F., & Copelli, M. (2014). Undersampled critical branching processes on small-world and random networks fail to reproduce the statistics of spike avalanches. *PloS One*, *9*(4), e94992. doi:10.1371/journal.pone.0094992

Saha, D., Morton, D., Ariel, M., & Wessel, R. (2011). Response properties of visual neurons in the turtle nucleus isthmi, 153–165. doi:10.1007/s00359-010-0596-3

Sethna, J. P., Dahmen, K. a, & Myers, C. R. (2001). Crackling noise. *Nature*, *410*(6825), 242–50. doi:10.1038/35065675

Shew, W. L., & Plenz, D. (2013). The functional benefits of criticality in the cortex. *The Neuroscientist : A Review Journal Bringing Neurobiology, Neurology and Psychiatry*, *19*(1), 88–100. doi:10.1177/1073858412445487

Shew, W. L., Yang, H., Petermann, T., Roy, R., & Plenz, D. (2009). Neuronal Avalanches Imply Maximum Dynamic Range in Cortical Networks at Criticality. *Journal of Neuroscience*, *29*(49), 15595–15600. doi:10.1523/JNEUROSCI.3864-09.2009

Shew, W. L., Yang, H., Yu, S., Roy, R., & Plenz, D. (2011). Information Capacity and Transmission Are Maximized in Balanced Cortical Networks with Neuronal Avalanches. *Journal of Neuroscience*, *31*(1), 55–63. doi:10.1523/JNEUROSCI.4637-10.2011

Sornette, D. (2006). *Critical Phenomena in Natural Sciences: Chaos, Fractals, Selforganization and Disorder: Concepts and Tools* (2nd ed.). Berlin: Springer-Verlag.

Stumpf, M. P. H., & Porter, M. A. (2012). Mathematics. Critical truths about power laws. *Science (New York, N.Y.)*, *335*(6069), 665–6. doi:10.1126/science.1216142

4.6.2 Supplementary Material References

Ariel, M., & Kogo, N. (2001). Direction tuning of inhibitory inputs to the turtle accessory optic system. *Journal of Neurophysiology*, *86*(6), 2919–30. Retrieved from http://www.ncbi.nlm.nih.gov/pubmed/11731548

Beggs, J. M., & Plenz, D. (2003). Neuronal avalanches in neocortical circuits. *The Journal of Neuroscience : The Official Journal of the Society for Neuroscience*, *23*(35), 11167–77. Retrieved from http://www.ncbi.nlm.nih.gov/pubmed/14657176

Betsch, B. Y., Einhäuser, W., Körding, K. P., & König, P. (2004). The world from a cat's perspective--statistics of natural videos. *Biological Cybernetics*, *90*(1), 41–50. doi:10.1007/s00422-003-0434-6

Clauset, A., Shalizi, C. R., & Newman, M. E. J. (2009). Power-Law Distributions in Empirical Data. *SIAM Review*, *51*(4), 661–703. doi:10.1137/070710111

Cosans, C. E., & Ulinski, P. S. (1990). Spatial organization of axons in turtle visual cortex: intralamellar and interlamellar projections. *Journal of Comparative Neurology*, *296*(4), 548–558. Retrieved from http://www.ncbi.nlm.nih.gov/pubmed/2358552

Goldstein, M. L., Morris, S. a., & Yen, G. G. (2004). Problems with fitting to the power-law distribution. *The European Physical Journal B*, *41*(2), 255–258. doi:10.1140/epjb/e2004-00316-5

Kinouchi, O., & Copelli, M. (2006). Optimal dynamical range of excitable networks at criticality. *Nature Physics*, *2*(5), 348–351. doi:10.1038/nphys289

Klaus, A., Yu, S., & Plenz, D. (2011). Statistical analyses support power law distributions found in neuronal avalanches. *PloS One*, *6*(5), e19779. doi:10.1371/journal.pone.0019779

Kriegstein, a R. (1987). Synaptic responses of cortical pyramidal neurons to light stimulation in the isolated turtle visual system. *The Journal of Neuroscience : The Official Journal of the Society for Neuroscience*, *7*(8), 2488–92. Retrieved from http://www.ncbi.nlm.nih.gov/pubmed/3612249

Langlois, D., Cousineau, D., & Thivierge, J. P. (2014). Maximum likelihood estimators for truncated and censored power-law distributions show how neuronal avalanches may be misevaluated. *Physical Review E*, *89*(1), 012709. doi:10.1103/PhysRevE.89.012709

Larremore, D. B., Shew, W. L., Ott, E., Sorrentino, F., & Restrepo, J. G. (2014). Inhibition Causes Ceaseless Dynamics in Networks of Excitable Nodes. *Physical Review Letters*, *112*(13), 138103. doi:10.1103/PhysRevLett.112.138103

Larremore, D. B., Shew, W. L., & Restrepo, J. G. (2011). Predicting Criticality and Dynamic Range in Complex Networks: Effects of Topology. *Physical Review Letters*, *106*(5), 1–4. doi:10.1103/PhysRevLett.106.058101

Levina, A., Herrmann, J., & Geisel, T. (2009). Phase Transitions towards Criticality in a Neural System with Adaptive Interactions. *Physical Review Letters*, *102*(11), 118110. doi:10.1103/PhysRevLett.102.118110

Levina, A., Herrmann, J. M., & Geisel, T. (2007). Dynamical synapses causing self-organized criticality in neural networks. *Nature Physics*, *3*(12), 857–860. doi:10.1038/nphys758

Mancilla, J. G., Fowler, M., & Ulinski, P. S. (1998). Responses of regular spiking and fast spiking cells in turtle visual cortex to light flashes. *Visual Neuroscience*, *15*(5), 979–93. Retrieved from http://www.ncbi.nlm.nih.gov/pubmed/9764539

Mante, V., Bonin, V., & Carandini, M. (2008). Functional mechanisms shaping lateral geniculate responses to artificial and natural stimuli. *Neuron*, *58*(4), 625–38. doi:10.1016/j.neuron.2008.03.011

Mulligan, K. a, & Ulinski, P. S. (1990). Organization of geniculocortical projections in turtles: isoazimuth lamellae in the visual cortex. *Journal of Comparative Neurology*, *296*(4), 531–547. Retrieved from http://www.ncbi.nlm.nih.gov/pubmed/2358551

Nishimoto, S., & Gallant, J. L. (2011). A three-dimensional spatiotemporal receptive field model explains responses of area MT neurons to naturalistic movies. *The Journal of Neuroscience : The Official Journal of the Society for Neuroscience*, *31*(41), 14551–64. doi:10.1523/JNEUROSCI.6801-10.2011

Northmore, D. P., & Granda, A. M. (1991). Ocular dimensions and schematic eyes of freshwater and sea turtles. *Visual Neuroscience*, *7*(6), 627–35.

Peirce, J. W. (2008). Generating Stimuli for Neuroscience Using PsychoPy. *Frontiers in Neuroinformatics*, *2*, 10. doi:10.3389/neuro.11.010.2008

Priesemann, V., Wibral, M., Valderrama, M., Pröpper, R., Le Van Quyen, M., Geisel, T., … Munk, M. H. J. (2014). Spike avalanches in vivo suggest a driven, slightly subcritical brain state. *Frontiers in Systems Neuroscience*, *8*(June), 108. doi:10.3389/fnsys.2014.00108

Ribeiro, T. L., Ribeiro, S., Belchior, H., Caixeta, F., & Copelli, M. (2014). Undersampled critical branching processes on small-world and random networks fail to reproduce the statistics of spike avalanches. *PloS One*, *9*(4), e94992. doi:10.1371/journal.pone.0094992

Saha, D., Morton, D., Ariel, M., & Wessel, R. (2011). Response properties of visual neurons in the turtle nucleus isthmi, 153–165. doi:10.1007/s00359-010-0596-3

Senseman, D. M. (1996). Correspondence between visually evoked voltage-sensitive dye signals and synaptic activity recorded in cortical pyramidal cells with intracellular

microelectrodes. *Visual Neuroscience*, *13*(5), 963–77. Retrieved from http://www.ncbi.nlm.nih.gov/pubmed/8903037

Shew, W. L., Yang, H., Petermann, T., Roy, R., & Plenz, D. (2009). Neuronal Avalanches Imply Maximum Dynamic Range in Cortical Networks at Criticality. *Journal of Neuroscience*, *29*(49), 15595–15600. doi:10.1523/JNEUROSCI.3864-09.2009

Shew, W. L., Yang, H., Petermann, T., Roy, R., & Plenz, D. (2009). Neuronal avalanches imply maximum dynamic range in cortical networks at criticality. *The Journal of Neuroscience : The Official Journal of the Society for Neuroscience*, *29*(49), 15595–600. doi:10.1523/JNEUROSCI.3864-09.2009

Tetzlaff, C., Okujeni, S., Egert, U., Wörgötter, F., & Butz, M. (2010). Self-Organized Criticality in Developing Neuronal Networks. *PLoS Computational Biology*, *6*(12), e1001013. doi:10.1371/journal.pcbi.1001013

Ulinski, P. (2007). *Evolution of Nervous Systems*. *Evolution of Nervous Systems* (pp. 195–203). Elsevier. doi:10.1016/B0-12-370878-8/00133-6

Wang, S.-J., Hilgetag, C. C., & Zhou, C. (2011). Sustained activity in hierarchical modular neural networks: self-organized criticality and oscillations. *Frontiers in Computational Neuroscience*, *5*(June), 30. doi:10.3389/fncom.2011.00030

Yang, H., Shew, W. L., Roy, R., & Plenz, D. (2014). Peak variability and optimal performance in cortical networks at criticality. In D. Plenz & E. Niebur (Eds.), *Criticality in Neural Systems* (pp. 335–346). Weinheim, Germany: Wiley.

Chapter 5: Spikepy, a Flexible Spike-sorting Application and Framework

The analysis of extracellular neural recordings usually begins with spike-sorting. There is an active discussion within the research community about how to best perform spike-sorting. Spikepy is a flexible spike-sorting application that serves to facilitate this discussion in two important ways. Firstly, it provides an extensible plugin-based framework that can be used as a test bed for new spike-sorting algorithms. And importantly, it is an easy-to-use application so the average electrophysiologist can have access to the latest spike-sorting advances.

5.1 Introduction

Recording the electrical potential from extracellular electrodes remains a popular technique in neuroscience. The extracellular signals recorded may include spikes (the remnants of neuronal action potentials) originating from multiple neurons. The category of analysis that involves both detecting these spikes and associating them with the correct source is called spike-sorting.

Spike-sorting research has been around for more than two decades and is still an active area of research (Einevoll, Franke, Hagen, Pouzat, & Harris, 2012; Lewicki, 1998). Much of the early tools developed required a great deal of manual control, but within the last ten years or so a

lot of effort has been spent to automate the spike-sorting process (Einevoll et al., 2012; Franke, Natora, Boucsein, Munk, & Obermayer, 2010; S. Kim & McNames, 2007; Pouzat, Mazor, & Laurent, 2002; Quiroga, Nadasdy, & Ben-Shaul, 2004). This is due in no small part to the growing popularity and shrinking cost of multielectrodes, which make manual sorting techniques unappealing.

The automation of spike-sorting processes should result in a lively discussion of the merits and costs of one algorithm over another, yet this is largely absent. The process of spike-sorting is complex, and often involves many steps to complete. Algorithm developers often focus on only one step in the process. When they then go to implement their new algorithm, they are forced to also implement the other steps, before they can evaluate the performance of the algorithm. As a result, the comparisons are not direct, since these other steps often influence performance in a significant way.

This paper introduces a framework that aims to address this by providing a standardized platform to perform spike-sorting. Spikepy is a plugin-based framework, where each step is a type of plugin, allowing algorithm developers to focus on just the step they are interested in. The framework takes care of creating both a graphical user interface as well as a full featured API. Additionally, the framework handles reading data in and exporting to various file formats via plugins. Many of the most popular algorithms are already written as plugins, making Spikepy a spike-sorting solution that is ready to be used without writing any code at all.

Spikepy is free and open-source software, released under the GPL version 3 software license. Spikepy will run in Windows, Mac osX and Linux. You can download Spikepy from

http://code.google.com/p/spikepy where there are installation instructions, sample data, as well as other documentation.

There is also a mailing list at http://groups.google.com/group/spikepy-users.

5.2 Methods

5.2.1 Plugin Framework

Spikepy is built around the plugin concept. Plugins are responsible for almost everything in Spikepy from loading data, to processing data, even visualizing results. Spikepy is responsible for coordinating these plugins and providing the user interface either through the GUI or as an API. This coordination is made possible through the use of Trial objects and their associated Resources.

Trial objects are a way of grouping data from various stages of processing together. The primary role of Trial objects is to provide access to their Resources which are where the data are stored. Resources store information about how the data were last altered and provide a mechanism to lock/unlock access to the data to facilitate multi-processing. Spikepy plugins require that some Resources are available in order to run and provide Resources as their outputs. (Figure 5.1)

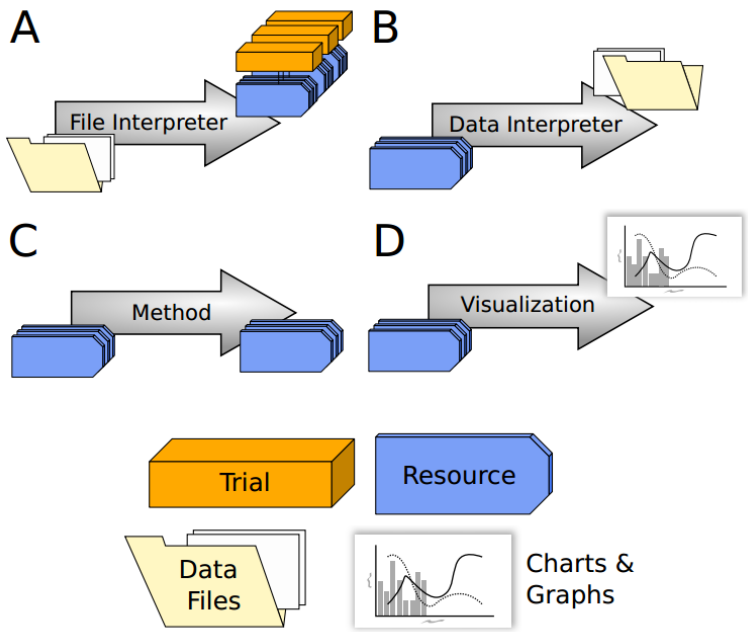

Figure 5.1 Spikepy plugin types. (**A)** FileInterpreters read in data files and create Trial objects. **(B)** DataInterpreters take Resources and produce data files. **(C)** Methods carry out the various spike-sorting processing stages. They require Resources as well as produce them. **(D)** Visualizations create charts and graphs from Resources.

5.2.2 Processing Stages

Spike-sorting is often carried out in four steps starting with filtering, spike-detection, feature-extraction, and then clustering. Spikepy generally follows this paradigm but allows for the possibility of different filtering to happen before spike-detection and feature-extraction. (Figure 5.2) This makes it possible to filter once to detect spikes, disregarding the spike-shape distortion associated with the filter. Another filtering stage before the extraction stage is performed when spike-shape is potentially more important. This process is further generalized to include any number of auxiliary steps that can occur before or after any of these required processing stages.

Each of the stages in Figure 5.2 corresponds to a method-plugin family, including the auxiliary stages. Spikepy determines the order in which processing will occur by attempting to solve the dependencies of a plugin (what Resources the plugin requires). This is possible since all plugins tell Spikepy what Resources they produce as well as what Resources they require. When it is possible multi-processing will occur, utilizing all available processors on the computer (settings allow you to limit the number of processes).

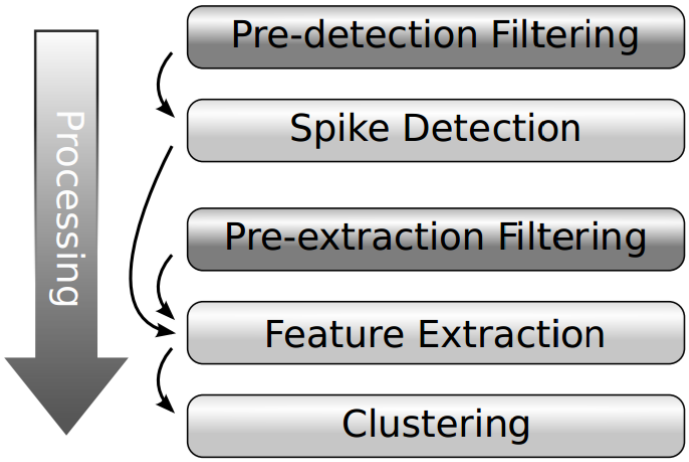

Figure 5.2 Spike-sorting processing stages. The five main processing stages are shown generally starting with filtering and ending with clustering. The two filtering stages are colored more darkly to indicate that they are entry-points to the spike-sorting process. AuxiliaryMethods can be run before or after any of the five required stages. Curved arrows indicate standard requirements (e.g., spike detection requires pre-detection filtering to have finished).

5.2.3 Extending Spikepy

Substantial effort has been made to ensure that writing plugins for Spikepy is simple and straightforward. Authors of new plugins do not have to know how the internals of Spikepy work. Figure 5.3 show the actual code that creates an auxiliary plugin that resamples a signal to a new

sampling frequency. The actual function that resamples the signal is not shown, only the source that is required to turn it into a plugin.

Plugins are Python classes that inherit from one of the base-classes corresponding to the four plugin types. (Figure 5.1) Plugins have class-variables that tell Spikepy how to handle the plugin. Obligatory class variables for SpikepyMethods include requires and provides which are lists of Resource names. There are also optional class-variables (described in the documentation) such as is stochastic that help Spikepy figure out when it is or is not necessary to run a SpikepyMethod plugin again with the same settings.

```
1  from spikepy.developer.methods import AuxiliaryMethod
2  from spikepy.common.valid_types import ValidInteger
3  from spikepy.utils.resample import resample
4
5  class ResampleAEF(AuxiliaryMethod):
6      name = 'Resample after Extraction Filter'
7      description = 'Resample the signal after running the Extraction Filter stage.'
8      runs_with_stage = 'extraction_filter'
9      requires = ['ef_traces', 'ef_sampling_freq']
10     provides = ['ef_traces', 'ef_sampling_freq']
11
12     # -- method parameters --  (become keyword arguments to run)
13     new_sampling_frequency = ValidInteger(10, 100000, default=30000)
14
15     def run(self, signal, sampling_freq, new_sampling_freq=30000):
16         return [resample(signal, sampling_freq, new_sampling_frequency),
17                 new_sampling_frequency]
```

Figure 5.3 Writing a Spikepy plugin. This code segment is all that is required to create a plugin that will resample the signal following the extraction-filtering stage. On lines 6 - 10 the class-variables tell Spikepy how to handle this plugin. Line 13 defines a plugin setting that allows the user to select the sampling frequency for the resampled signal. Spikepy will automatically build the GUI element for these settings. The run method on line 15 has positional arguments corresponding to the Resources that the plugin "requires", and keyword arguments that correspond to the plugin settings. Lines 16 - 17 return the data for the two Resources that this plugin "provides".

5.2.4 Strategies

One consequence of the flexibility that the plugin system provides is that the user makes many choices about how the data are processed. These decisions should be recorded in some way so that the research is reproducible and so that data can be batch processed. In Spikepy a strategy is an index of all the plugins used as well as all of the settings associated with those plugins. These strategies can be saved and shared easily, making it possible to communicate clearly how you analyzed your data.

5.2.5 Graphical Interface

Spikepy has an easy to use, cross-platform GUI that allows for a more interactive spike-sorting session (Figure 5.4). The interface lets the user choose plugins to use and enter processing settings and either run the entire strategy or just one stage of processing at a time. The GUI then generates all the relevant visualizations of the results of processing. Under the hood though, the GUI is accessing the exact same API that is available to anyone who wants to write Python scripts that use Spikepy.

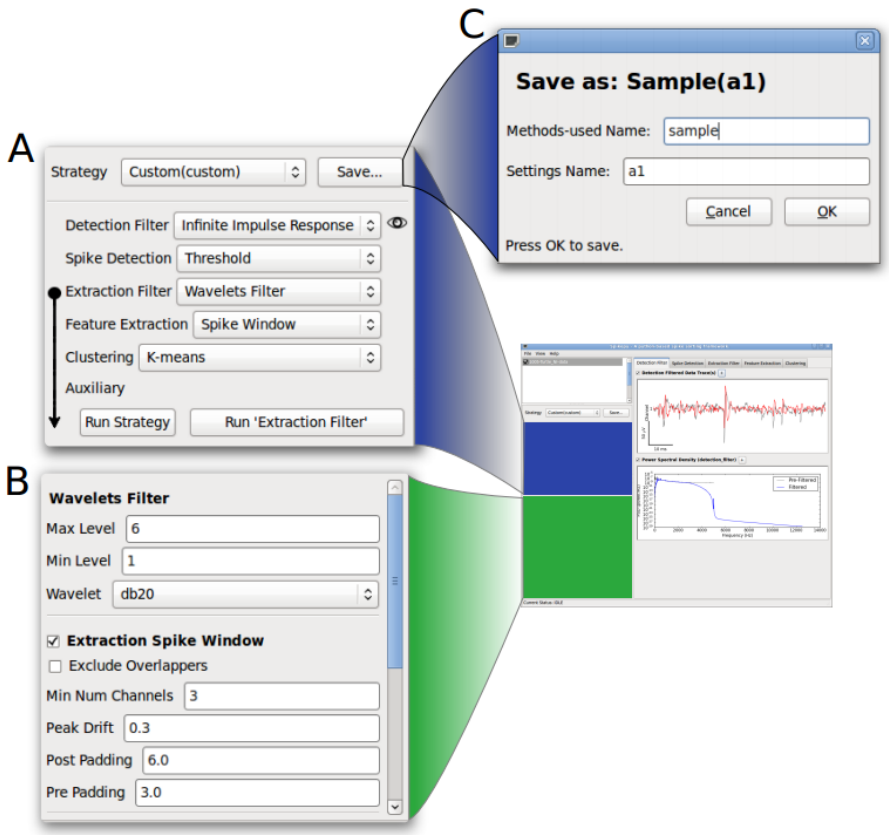

Figure 5.4 The Spikepy graphical user interface. In the background is a screen-capture of the main window in the Spikepy GUI. **(A)** A zoomed in view of the strategy panel where users can choose the method for each processing stage, choose previously saved strategies, and run stages or whole strategies. **(B)** A zoomed in view of the control panel for the Extraction Filter stage. The first section is for the currently selected method (Wavelets Filter) while the controls below this are for auxiliary methods that are associated with the Extraction Filter stage (not all are shown – notice the scrollbar). Note: all GUI control panels are automatically built by Spikepy, so plugin authors do not need to know how to program a GUI. **(C)** A view of the save strategy dialog. Users are prompted for a methods name and a settings name. All strategies using the exact same set of methods share a methods name making it easier to keep strategies organized.

5.2.6 Application Programming Interface

The Spikepy API turns Spikepy into a Python library that can be utilized in any Python program. The API is organized around the Session object. The Session object provides methods for opening files, creating and updating strategies, and all the other actions available through the

GUI. In addition to those methods, you can gain access to the underlying data in order to customize how the data are processed.

The arguments to many of the functions in the API are designed to make interactive programming (i.e., using iPython) easy. All arguments which are names, such as trial names, strategy names and plugin names will accept any unique substring instead of the entire name. For example, if the name of a plugin was Some Long Plugin Name, then the string Long would suffice as an argument, provided that there are no occurrences of Long in any other plugin names. That is, any unambiguous substring of a name can be used instead of the entire name.

5.3 Results

Spikepy is a plugin-based framework which means that it is easily extensible, in addition though, it comes prepackaged with a number of very useful plugins. In this section we will describe these builtin plugins, and compare and contrast them when appropriate. We will follow the standard processing order of stages as shown in Figure 5.2, and discuss auxiliary plugins throughout the section.

5.3.1 Filtering

There are two filtering stages in Spikepy, one that occurs just before the spike-detection stage, and one that occurs just before the feature-extraction stage. This means that a filter that is especially well suited to help with spike-detection can be used before the spike-detection stage and another filter that is more beneficial for feature-extraction can be used before that stage. From the standpoint of the plugin system, they are all simply filtering plugins.

There are three builtin filtering plugins as of Spikepy version 0.82, they are:

1. Infinite Impulse Response – IIR filters commonly referred to as Butterworth and Bessel type filters are so named because using them to filter an impulse (Dirac delta), the response will continue on infinitely in time.

2. Finite Impulse Response – FIR filters are also referred to as sinc type filters because they can be implemented by convolving a windowed sinc function with the signal. If you filter an impulse, the response will not continue on infinitely in time.

3. Wavelets – The signal is filtered by first decomposing the signal using wavelet decomposition, and then recomposing it using only some of the resulting wavelet coefficients, setting the others to zero.

These filters vary from one another in many ways. In terms of complexity the IIR filters are the least complex, followed by the FIR filters and finally the Wavelets filters. In terms of computation time required, the IIR filters are the fastest, followed by the Wavelets filters and finally the FIR filters. What is probably one of the most important qualities though is the ability of the filter to preserve spike shape while removing unwanted frequencies from the signal. In that regard, the FIR and Wavelets filters are about equally good, with the IIR filters distorting the waveform substantially more (Figure 5.5).

One drawback to using the Wavelets filter over the FIR filter, is that with the former you cannot specify the cutoff frequencies directly, instead you must specify the min-level and max-level. A simple formula relates these parameters to the cutoff frequencies:

$$\omega_{low} = \frac{\omega_s}{2^{L_{min}}}$$

$$\omega_{high} = \frac{\omega_s}{2^{(L_{max}+1)}}$$

where $\omega_{low}$is the lower cutoff frequency, $\omega_{high}$is the upper cutoff frequency, and ω_s is the sampling frequency of the signal. L_{min} and $L_{max}$are the min and max levels respectively. This means that the sampling frequencyof the signal essentially limits the choices of cutoff frequencies that the Wavelets filters can achieve. This limitation is absent in the FIR filters.

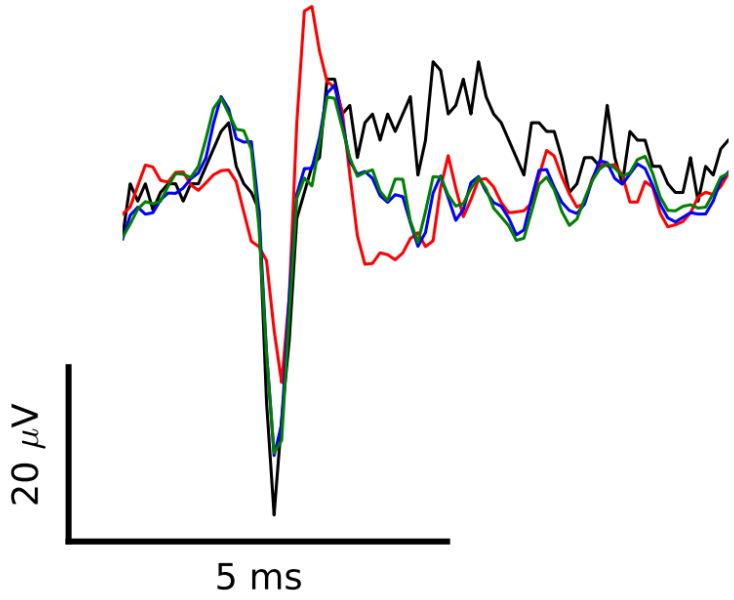

Figure 5.5 Comparing filter methods. (black) unfiltered (red) IIR filter: 3rd order Butterworth, band-pass (300-2,500 Hz) (blue) FIR filter: window=Hanning, taps=1001, band-pass (300-2,500 Hz) (green) Wavelets filter: wavelet=db20, min level=2, max level=4 (equivalent to band-pass (312-2,500 Hz) for this sampling frequency (10,000 Hz)).

5.3.2 Spike Detection

There is only one DetectionMethod plugin that comes with Spikepy and it offers threshold spike detection. Before we describe this plugin however, it should be noted that there are a couple of auxiliary plugins that are useful in conjunction with the spike-detection plugins. First, there is an auxiliary plugin that will resample the signal after filtering. This is usually used

to upsample the signal so that spikes are better aligned after detection. Also, there is an auxiliary plugin that implements the non-linear energy operator (Gibson, Judy, & Marković, 2010). This plugin accentuates the spikes relative to the noise (Figure 5.6), and may aide in spike-detection.

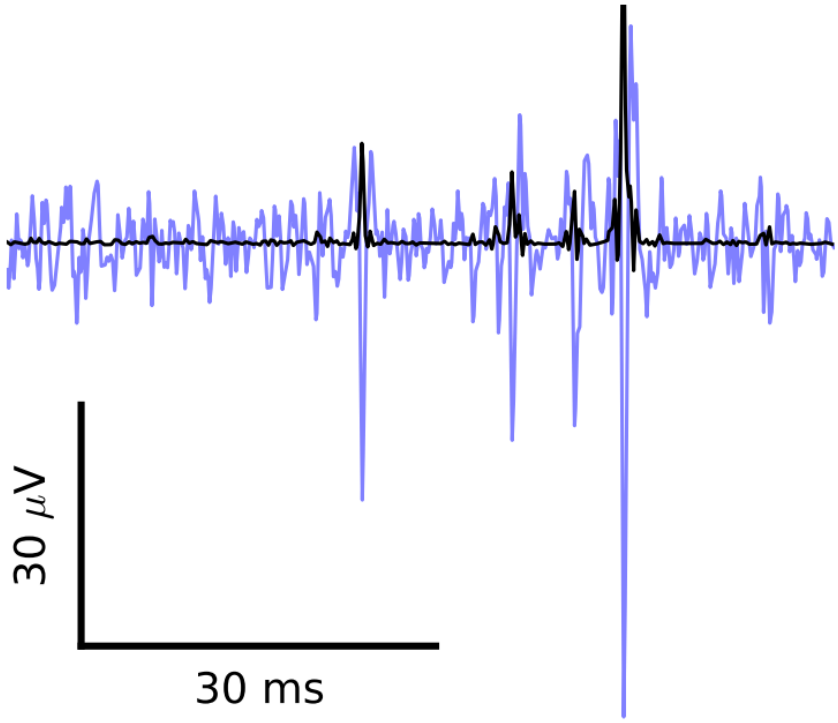

Figure 5.6 The non-linear energy operator auxiliary plugin. (light-blue) FIR filter: window=Hanning, taps=1001, band-pass (300-2,500 Hz) (black) Signal filtered in the same way, but applying the non-linear energy operator afterward. (result scaled by 30x).

The threshold spike-detection plugin that Spikepy comes with has a number of useful options. The plugin allows you to specify either one or two thresholds (see Figure 4.7). These thresholds can be specified in mV, or as a multiple of the standard deviation of the signal. Another possibility is to specify the threshold(s) as a multiple of the median value of the absolute value of the signal (calculated after removing the mean-value of the signal). In addition to the threshold(s), you can specify a max-spike-duration which will cause the algorithm to ignore spikes which are unphysiologically long (i.e., from recording artifacts or low frequency

oscillations). And finally, you can enforce a refractory period, causing the algorithm to remove spikes which occur too soon after previously detected spikes.

Looking forward, we would like to see additional spike-detection algorithms implemented. One promising method uses the Cepstrum of Bispectrum (Shahid & Smith, 2009; Shahid, Walker, & Smith, 2010). Another method involves using wavelets as spike templates (K. H. Kim & Kim, 2003). Yet another possibility is to threshold the temporal derivative(s) of the signal. This could be achieved by adding another auxiliary plugin similar to the nonlinear energy operator plugin.

5.3.3 Feature Extraction

Spikepy currently has two plugins to extract features from the signal given the spike times. The first is a simple spike-windowing plugin where a portion of the extraction-filtered signal is cut out surrounding each

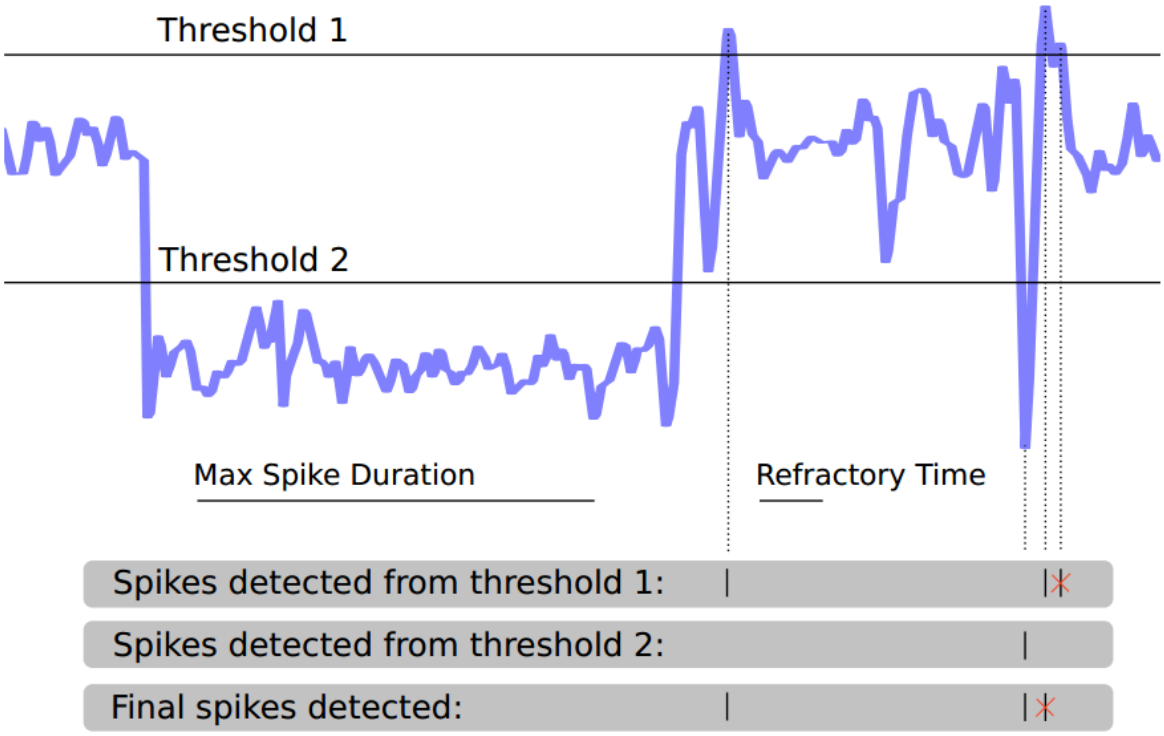

Figure 5.7 Threshold spike-detection plugin. You can specify up to two thresholds, a maximum spike duration, and a refractory time. The thresholds can be in various units such as mV, or standard deviations of the signal. The maximum spike duration and refractory time are in ms. Spikes that violate the maximum spike duration or refractory period are thrown out.

detected spike (Figure 5.8). Since the output of the detection stage is simply a list of spike times, one list per recording channel, this plugin must first determine if the spikes recorded on multiple channels are in fact the same event. The settings peak drift and min num channels specify how many channels must register a spike, and within what period of time for them to be grouped together as a single event.

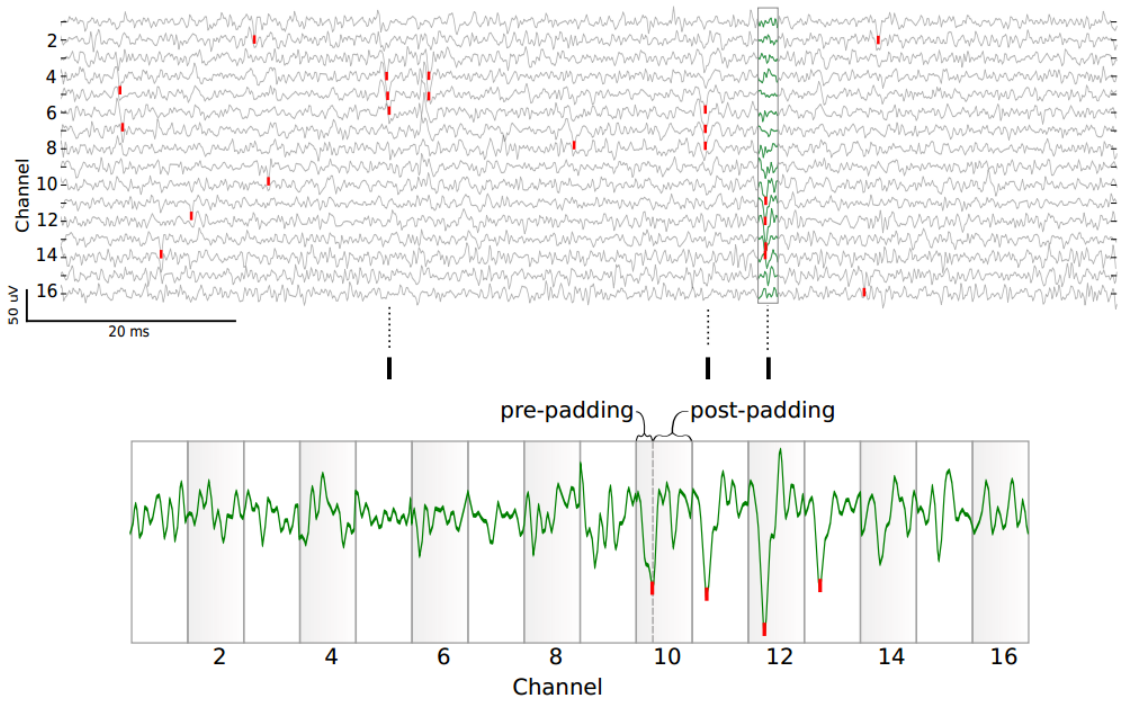

Figure 5.8 Spike window feature-extraction. **(top)** A short segment of a 16-channel extracellular recording showing spikes detected (red tick marks). **(middle)** A raster of spikes (in black) that meet the criteria of being on at least 3 channels within 0.3 ms of one another (peak drift=0.3 and min num channels=3). **(bottom)** The highlighted region in the top traces has been serialized to form a feature-vector. The parameters pre padding and post padding determine how much time before and after the spike to snip out of the traces.

The other feature-extraction plugin that comes with Spikepy is the method used in a paper by Rodrigo Quiroga et al. (Quiroga et al., 2004). This method uses the previous method as a starting point, then it utilizes wavelet decomposition to obtain wavelet coefficients. The distribution of these coefficients are then tested for normality and those coefficients with the lowest scores (largest difference from the normal distribution) are chosen. This results in a lowering of the dimensionality of the feature-vector, while maintaining or perhaps even enhancing the separation of events in feature-space. Many other feature-extraction methods exist, and are often called dimensionality-reduction techniques since they take the high-dimensional spike-window and return something with a much smaller feature-vector. Principal Component

Analysis, or PCA could be made into a feature-extraction plugin rather easily. Also easy to implement would be something as simple as spike-height and spike-width, or other scalar features of spikes such as spike-power.

5.3.4 Clustering

Spikepy has only one builtin clustering plugin as of version 0.82, the plugin implements the k-means clustering algorithm. There are a number of algorithms that we desire to have included in future releases of Spikepy. The super paramagnetic clustering algorithm that is used by WaveClus (Quiroga et al., 2004), a mixture-model algorithm (gaussians, student-t distributions, etc), and hierarchical clustering all seem interesting.

Spikepy has a number of clustering quality metrics implemented as an auxiliary plugin (Figure 5.9). These are the metrics described by Schmitzer-Torbert et al. (Schmitzer-Torbert, Jackson, Henze, Harris, & Redish, 2005), isolation distance, and L-ratio. The isolation distance is better if it is large, and the L-ratio is better if it is small. The actual magnitude of these metrics is dependent on the number of features that are being clustered, as well as the size of the feature vectors. They are therefore not useful for comparing the clustering quality achieved with other datasets unless they are of similar size. Additional clustering metrics should be made into auxiliary plugins such as those described in a recent paper by Hill et al. (Hill, Mehta, & Kleinfeld, 2011).

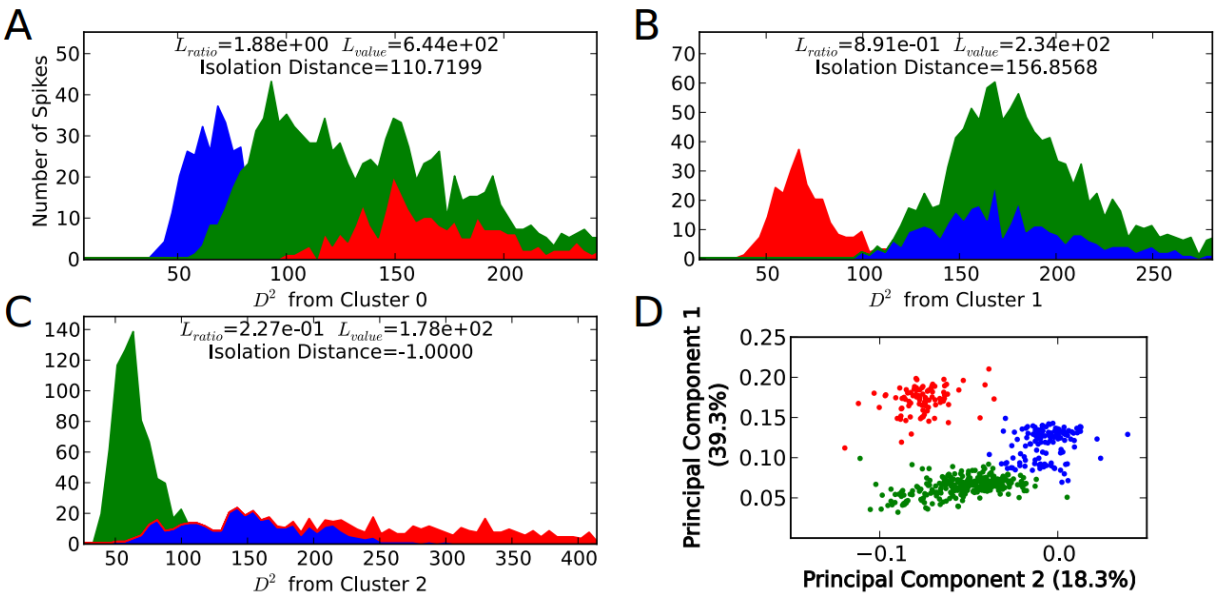

Figure 5.9 Clustering quality metrics. **(A-C)** A histogram of the squared Mahalanobis distance from the cluster center is shown for each of the three clusters. The histograms of the two 'other' clusters are drawn stacked on top of each other. The L-ratio, L-value, and isolation quality are also shown for each cluster. Notice in C) that the isolation distance is undefined, this is because this cluster contains more features than the other two clusters combined. **(D)** The data projected onto the first two principal components gives some idea of the clustering quality. The percentages shown indicate the amount of variance explained by the first two principal component vectors.

5.4 Discussion

Even as new high-tech imaging techniques that are capable of recording the spiking activity of neurons are gaining favor, recording with extracellular electrodes remains very popular. To get the most out of these recordings, reliable spike-sorting must be performed. Because of the trend towards more and more electrodes, as well as the numerous brain/computer interface applications, this process must become automated. A significant impediment to reliable and automated spike-sorting is the lack of a common framework that would allow easy comparisons between competing spike-sorting algorithms.

Existing spike-sorting solutions such as Spike2 or WaveClus are either proprietary software, or require proprietary software in order to run. In addition, they are not written with extensibility in mind, so new algorithms cannot be added easily. Notable exceptions to this include an open-source project called OpenElectrophy (Garcia & Fourcaud-Trocmé, 2009) and the cloud computing system called Carmen (L. S. Smith et al., 2007), although neither is designed specifically for spike-sorting and require you to commit your entire dataflow to use their system.

We have described the construction of both a flexible plugin-based framework to perform spike-sorting as well as a core set of plugins. It is cross-platform and entirely free open-source software meaning that it can be adopted in virtually any laboratory and will be maintained for as long as the community finds it useful. Those who need to perform spike-sorting in their workflow will find the combination of a user-friendly graphical user interface and a powerful application programming interface makes Spikepy very useful. Additionally, researchers who are developing new spike-sorting algorithms will want to take advantage of the plugin-based framework that allows for very quick prototyping (they won't have to write an entire spike-sorting application) and will give them the ability to easily compare the effectiveness of their algorithms to others. Moreover, it connects these two populations by getting the latest advancements into the hands of those who need to perform spike-sorting but who may not be experts in the specific sub-domains underlying such advancements.

5.5 References

Einevoll, G. T., Franke, F., Hagen, E., Pouzat, C., & Harris, K. D. (2012). Towards reliable spike-train recordings from thousands of neurons with multielectrodes. *Current Opinion in Neurobiology, 22*(1), 11–17. doi:10.1016/j.conb.2011.10.001

Franke, F., Natora, M., Boucsein, C., Munk, M. H. J., & Obermayer, K. (2010). An online spike detection and spike classification algorithm capable of instantaneous resolution of overlapping spikes. *Journal of Computational Neuroscience*, *29*, 127–148. doi:10.1007/s10827-009-0163-5

Garcia, S., & Fourcaud-Trocmé, N. (2009). OpenElectrophy: An Electrophysiological Data- and Analysis-Sharing Framework. *Frontiers in Neuroinformatics*, *3*(May), 14. doi:10.3389/neuro.11.014.2009

Gibson, S., Judy, J. W., & Marković, D. (2010). Technology-aware algorithm design for neural spike detection, feature extraction, and dimensionality reduction. *IEEE Transactions on Neural Systems and Rehabilitation Engineering : A Publication of the IEEE Engineering in Medicine and Biology Society*, *18*(5), 469–478. doi:10.1109/TNSRE.2010.2051683

Hill, D. N., Mehta, S. B., & Kleinfeld, D. (2011). Quality metrics to accompany spike sorting of extracellular signals. *The Journal of Neuroscience : The Official Journal of the Society for Neuroscience*, *31*(24), 8699–8705. doi:10.1523/JNEUROSCI.0971-11.2011

Kim, K. H., & Kim, S. J. (2003). A wavelet-based method for action potential detection from extracellular neural signal recording with low signal-to-noise ratio. *IEEE Transactions on Biomedical Engineering*, *50*(8), 999–1011. doi:10.1109/TBME.2003.814523

Kim, S., & McNames, J. (2007). Automatic spike detection based on adaptive template matching for extracellular neural recordings. *Journal of Neuroscience Methods*, *165*, 165–174. doi:10.1016/j.jneumeth.2007.05.033

Lewicki, M. S. (1998). A review of methods for spike sorting: the detection and classification of neural action potentials. *Network*, *9*(January), R53–R78. doi:10.1088/0954-898X/9/4/001

Pouzat, C., Mazor, O., & Laurent, G. (2002). Using noise signature to optimize spike-sorting and to assess neuronal classification quality. *Journal of Neuroscience Methods*, *122*, 43–57. doi:10.1016/S0165-0270(02)00276-5

Quiroga, R. Q., Nadasdy, Z., & Ben-Shaul, Y. (2004). Unsupervised spike detection and sorting with wavelets and superparamagnetic clustering. *Neural Computation*, *16*, 1661–1687. doi:10.1162/089976604774201631

Schmitzer-Torbert, N., Jackson, J., Henze, D., Harris, K., & Redish, a. D. (2005). Quantitative measures of cluster quality for use in extracellular recordings. *Neuroscience*, *131*, 1–11. doi:10.1016/j.neuroscience.2004.09.066

Shahid, S., & Smith, L. S. (2009). Cepstrum of bispectrum spike detection on extracellular signals with concurrent intracellular signals. *BMC Neuroscience*, *10*, P59. doi:10.1186/1471-2202-10-S1-P59

Shahid, S., Walker, J., & Smith, L. S. (2010). A new spike detection algorithm for extracellular neural recordings. *IEEE Transactions on Biomedical Engineering*, *57*(4), 853–866. doi:10.1109/TBME.2009.2026734

Smith, L. S., Austin, J., Baker, S., Borisyuk, R., Eglen, S., Feng, J., … Sernagor, E. (2007). The CARMEN e-Science pilot project : Neuroinformatics work packages . *PLoS Computational Biology*, (September), 591–598.

Chapter 6: Open Questions and Additional Topics

The art and science of asking questions if the source of all knowledge.

-Thomas Berger

6.1 Introduction

One of my greatest struggles writing this thesis (and more generally conducting the research represented herein) was and is being distracted by the multitude of opportunities for exploration that this system and data set provides.

I find it useful to think of scientific research as jigsaw puzzles that may never be finished. As you work on one, the hope is that you'll be able to connect enough pieces to eventually stand back, look at it, and say, "Neat. We can clearly see what this part of the picture is, and what it certainly is not. Now that there's some context for this region of the puzzle, hopefully others can add to it, fill in some missing pieces, or even fix misplaced pieces (if such a piece should be found out)".

As I dug through the pieces to put together whichever puzzle I happened to be working on, I constantly found pieces that belonged to other puzzles. Tossing those pieces aside would

certainly have expedited my progress on the original puzzle, but for better or worse, many of those pieces looked fascinating and held the promise of separate puzzles that might reveal awesome pictures. That fascination very often led to shifts in priorities, in which I would start looking for pieces to connect to my new piece in the new puzzle instead of the old puzzle. Often, this new puzzle would be abandoned for other new puzzles, but eventually I would return to a few puzzles that I had committed to bringing some clarity to (see above chapters and subchapters).

What's presented in this chapter is a collection of many of the other puzzles I have worked on. Some are mostly a pile of pieces, others are partially put together, and certainly, many of them will connect to each other and the above work. These are presented with the hope that others will pick them up and piece them together.

6.2 Changes in evoked responses and spontaneous activity during experiments

When we report our experimental findings, we are, with complete honesty, showing what the cortex is capable of and what patterns and variability exist with and without the presence of visual stimulation. What is not always explicitly stated, but is certainly implied, is that our results (to some extent) represent what is happening in the living, behaving animal in the wild.

Nearly all electrophysiology experiments seek to gain an understanding of what is happening in the normal living animal, and nearly all have experimental aspects that likely skew the data such that the recorded data is different than it might be in natural conditions (e.g., anesthetics, the stress of being in a lab or constrained, disrupted neural connections by intentional and unintentional acts of preparing the tissue, differences in nutrient availability when

ACSF is used,…). Many of these cannot be fully corrected for, and the expectation is that, even though there are unknown differences between experimentally observed neural activity and the neural activity under natural conditions, many of the features observed are still relevant.

While acknowledging that not all differences can be corrected for (or even known in many cases), it seems that we should do our best to understand those that can be studied. One such aspect in our experiments that stands out as an opportunity for further study is the change in neural activity over the course of several hour of the experiment.

I see three main reasons it might be valuable to study changes in neural activity over the course of an experiment: 1) to learn and correct for trends, 2) to establish what is usable and relevant data, and 3) possibly to learn about what mechanisms mediate certain types of activity.

If trends are found over the course of an experiment we tend to assume that t=0 is the most biologically relevant time, but it is worth considering whether the stress caused to the system may have transient effects that the brain recovers from, after which the brain is in a more biologically relevant state than it was for the intitial recordings

At some point it would be good to study in what area (or areas) of the brain the changes are taking place (e.g., retina, LGN, cortex,…).

An additional question to ask is, are the changes actually just adaptation? This could be tested if we consistently found that in the beginning of running a stimulus we saw response A, and then after 2 hours of running that stimulus we saw response B. To test this we would show the stimulus at the beginning of an experiment to confirm that we observe A. Then, instead of showing the stimulus repeatedly for 2 hours, we would either show a markedly different stimulus for 2 hours or show no stimulus at all for 2 hours. Following the 2 hours, we could then see if the

response to the original stimulus was closer to A (evidence for adaptation) or B (evidence for stimulus independent changes in activity).

This test has not been done, but anecdotally, the observation that, when the response to one stimulus decreases, the responses to other stimuli also decrease supports the hypothesis of stimulus independent changes in activity.

6.2.1 Visual Response Amplitude Diminishing

It is typical to have fairly reliable responses early in an experiment greatly diminished or completely absent responses late in an experiment as is shown in Figure 6.1, which shows responses to 6 early presentations of a complex movie followed by responses to 6 late presentations.

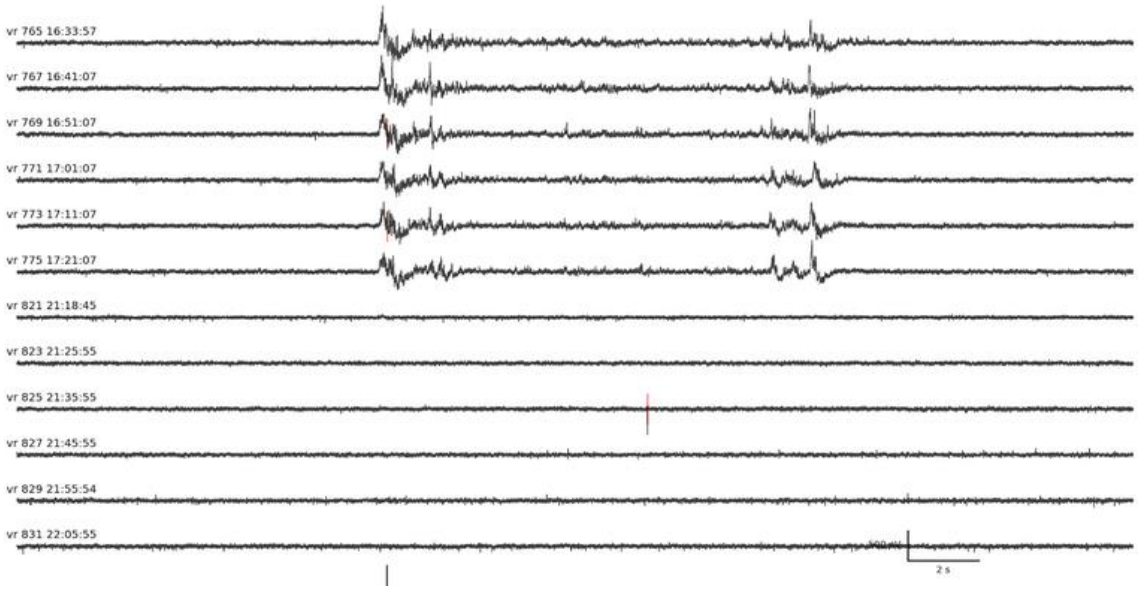

Figure 6.1 Experimental rundown. Responses to 12 repeated presentations of a complex movie. Data collected from Turtle 7.

6.2.2 Increased Spontaneous Activity over Time

Two features occasionally observed over the course of an experiment are gradually decreasing responses as well as increased spontaneous activity (Figure 6.2).

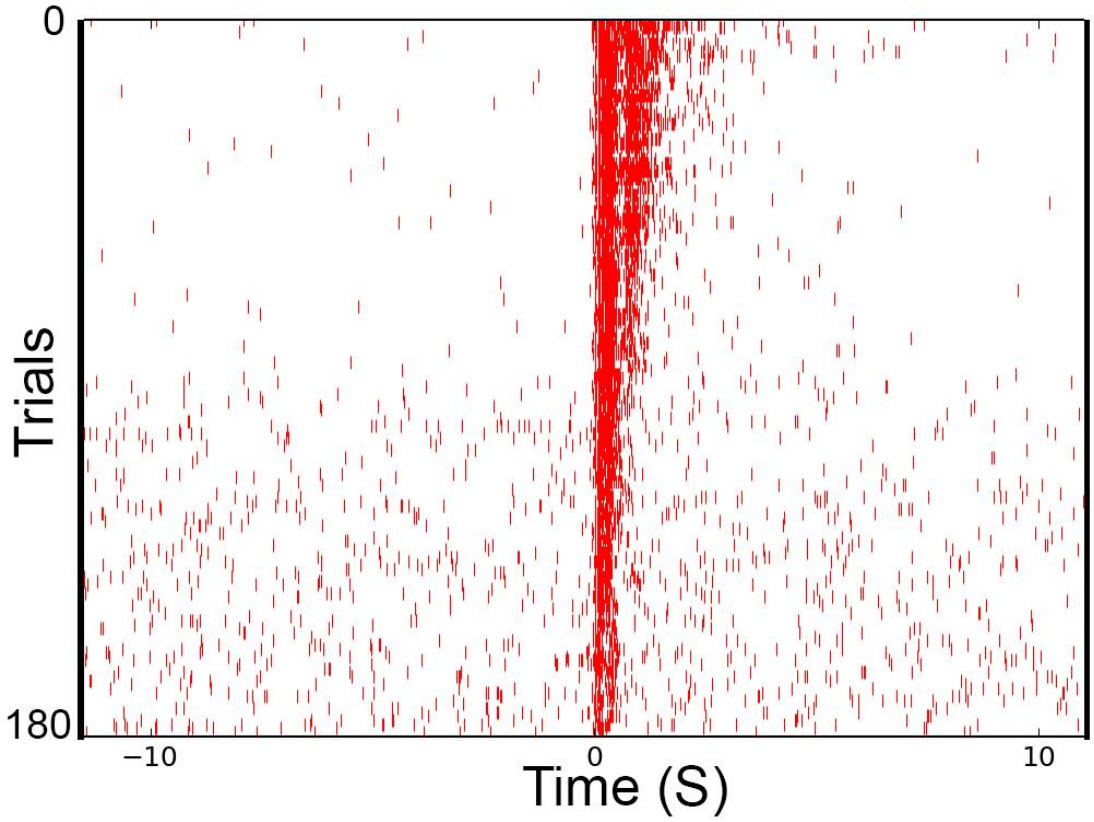

Figure 6.2 Rastergram of 180 LFP responses to LED Flashes. Data taken from Turtle 27, Electrode 95.

6.2.3 Changes in the Persistent Activity over the Course of an Experiment

The persistent activity of a response can change in ways different from how the initial response changes over the course of an experiment. Figure 6.3 show the persistent activity in response to LED flashes gradually shifting toward later and later responses during an experiment repeating this stimuli 120 times. Figure 6.4 shows persistent activity disappearing while the initial response remains.

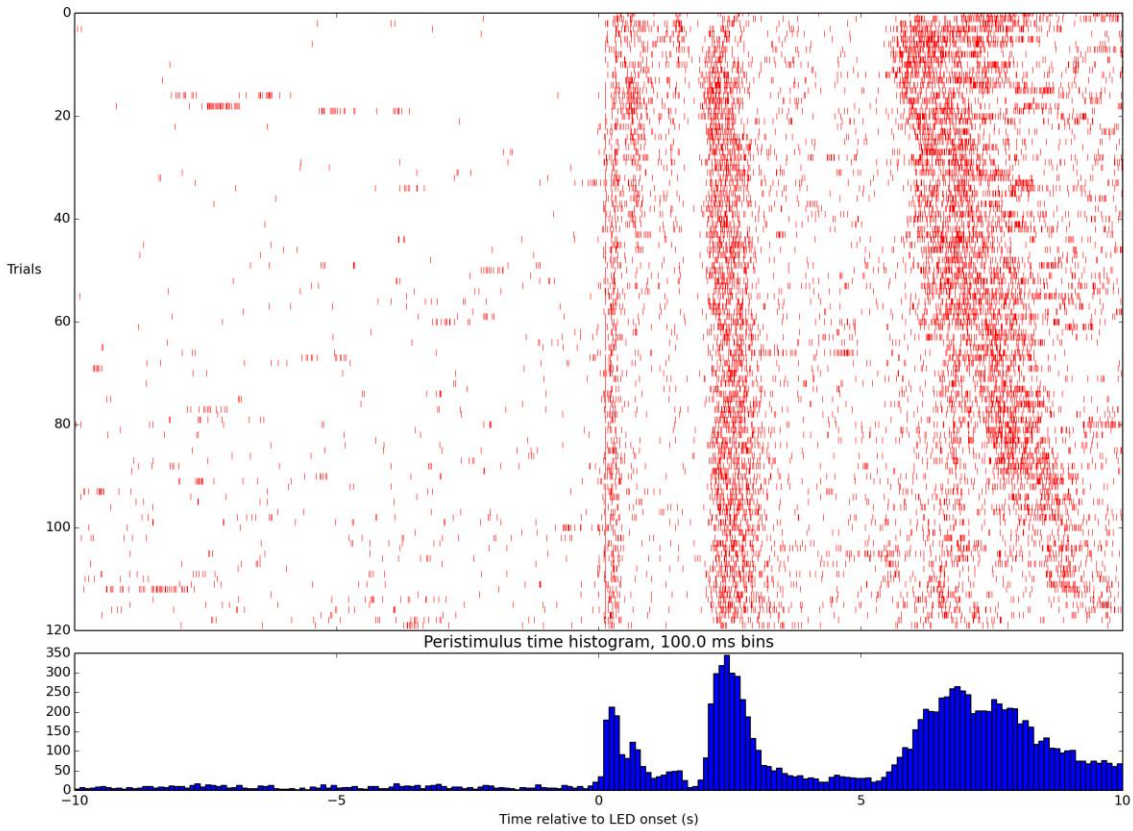

Figure 6.3 Persistent activity changing over the course of 120 trials. **(Top)** Rasters for LFP events in response to an LED flash at time 0 s**.(Bottom)** Peristimulus time histogram for all trials. Data from turtle 2, electrode 87.

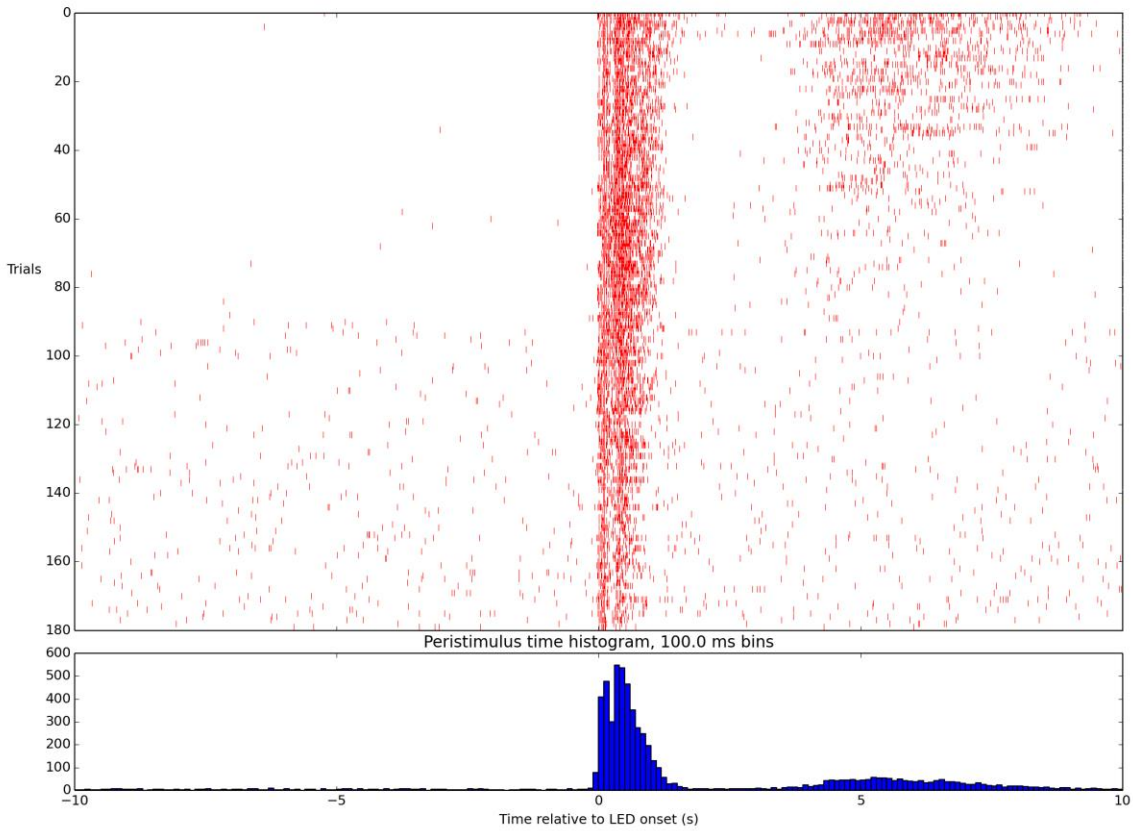

Figure 6.4 Persistent activity disappearing over the course of 120 trials. **(Top)** Rasters for LFP events in response to an LED flash at time 0 s**.(Bottom)** Peristimulus time histogram for all trials. Data from turtle 29, electrode 86.

6.2.4 Average LED Evoked LFP Shape over Time

In Chapter 1 we saw the average of LFP responses to LED flashes of different intensities. It is interesting to see how those change over time. Figure 6.5 shows precisely this. Interestingly, for the lowest LED intensity (blue), certain frequencies become more dominant throughout the course of the experiment (see the dark trace from 0 ms to 500 ms).

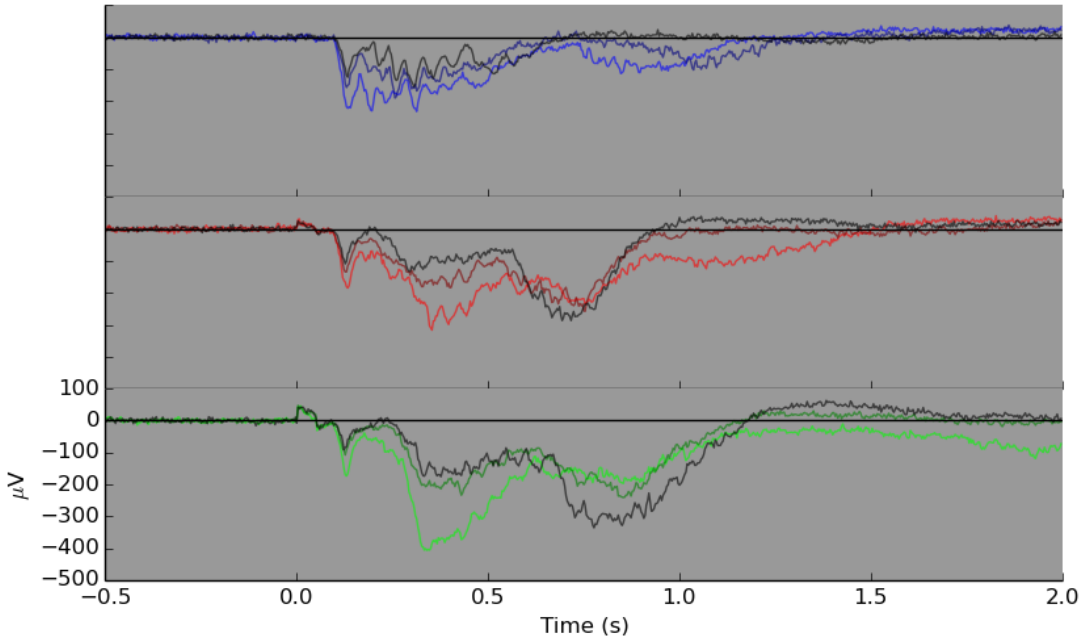

Figure 6.5 Changes in the average LFP response to LED flashes over time. Average response to low, medium, and high intensity LED flashes (blue, red, and green) are shown. The brightest colors are from the first 20 trial for each intensity, the medium brightness lines are for the second set of 20 trials for each intensity, and the darkest lines are from the last 20 trials for each intensity. Data from Turtle 32, electrode 22.

Another interesting observation concerns the changes in amplitude over time. Generally speaking, the amplitudes decrease over time, but for the responses to the high intensity flashes (green lines in Figure 6.5), the late response actually increases in amplitude over time.

6.2.5 Changes in LFP Burst Duration over Time

In Chapter 3 we investigated the distribution of the durations of LFP oscillations. These distributions change in a fairly reliable way over the course of the experiment. Figure 6.6 shows the over time we tend to have a higher percentage of shorter bursts.

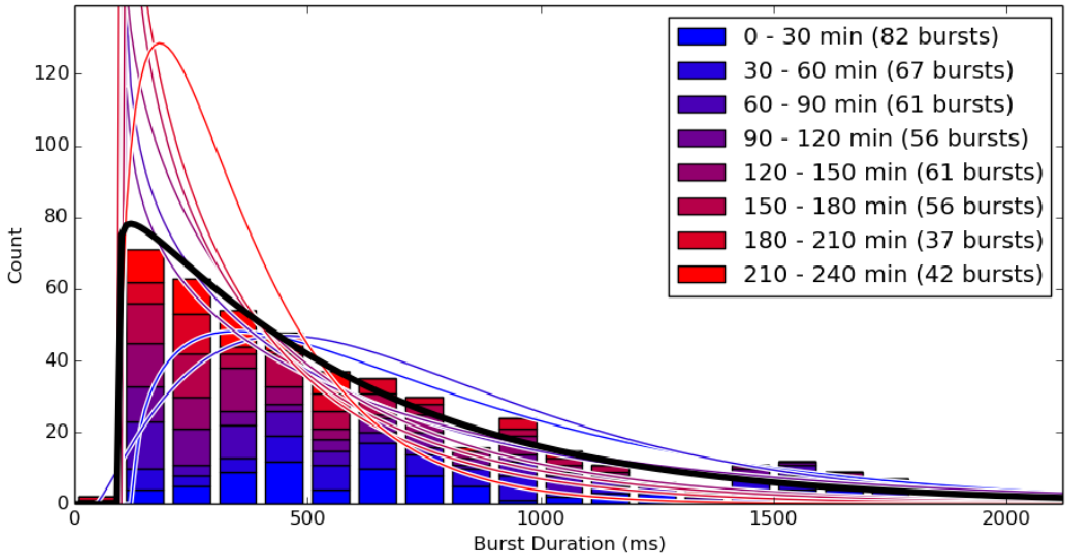

Figure 6.6 Burst duration distributions over time. The burst distributions from different periods of the experiment are shown together. The bluest distributions are the earliest periods, and the reddest distributions are the latest periods. Gamma fits have also been applied to each distribution as well as to the total (black line). The figure for Turtle 2 is shown above. The figures for Turtles 3, 23, 29, and 30 are shown below in that order.

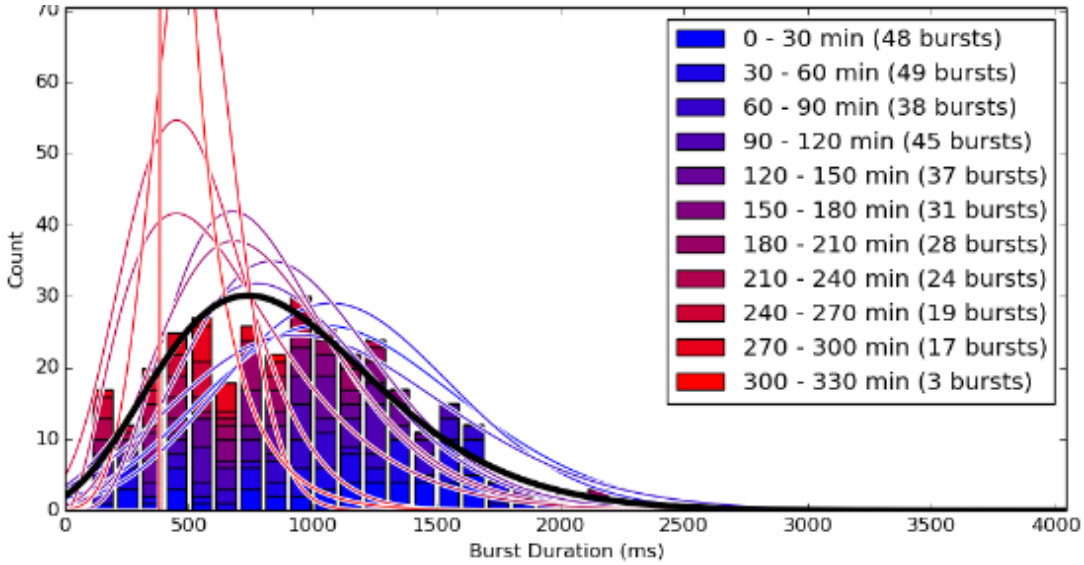
0 - 30 min (48 bursts)
30 - 60 min (49 bursts)
60 - 90 min (38 bursts)
90 - 120 min (45 bursts)
120 - 150 min (37 bursts)
150 - 180 min (31 bursts)
180 - 210 min (28 bursts)
210 - 240 min (24 bursts)
240 - 270 min (19 bursts)
270 - 300 min (17 bursts)
300 - 330 min (3 bursts)
Count
Burst Duration (ms)

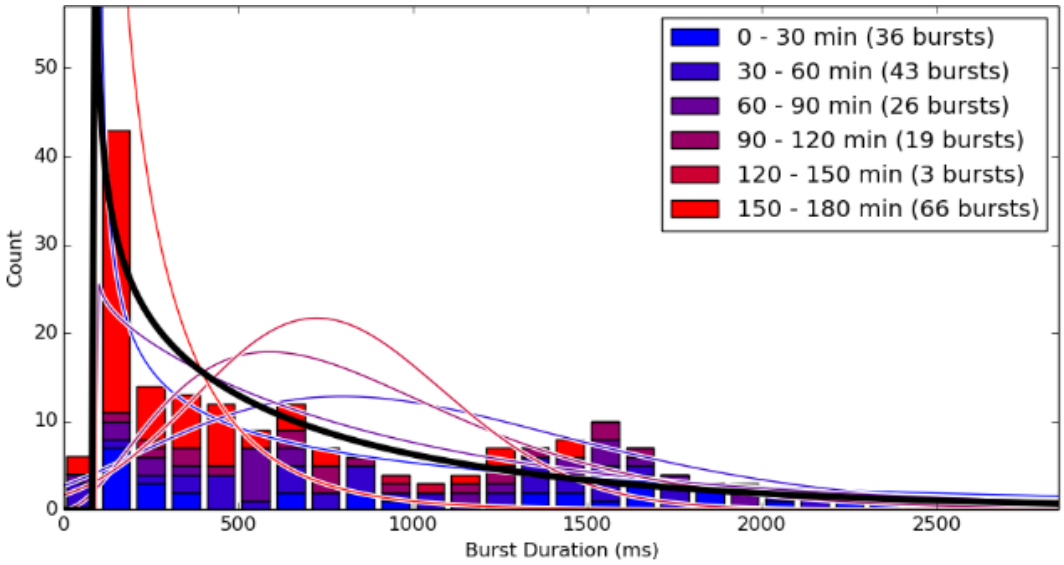
0 - 30 min (36 bursts)
30 - 60 min (43 bursts)
60 - 90 min (26 bursts)
90 - 120 min (19 bursts)
120 - 150 min (3 bursts)
150 - 180 min (66 bursts)
Count
Burst Duration (ms)

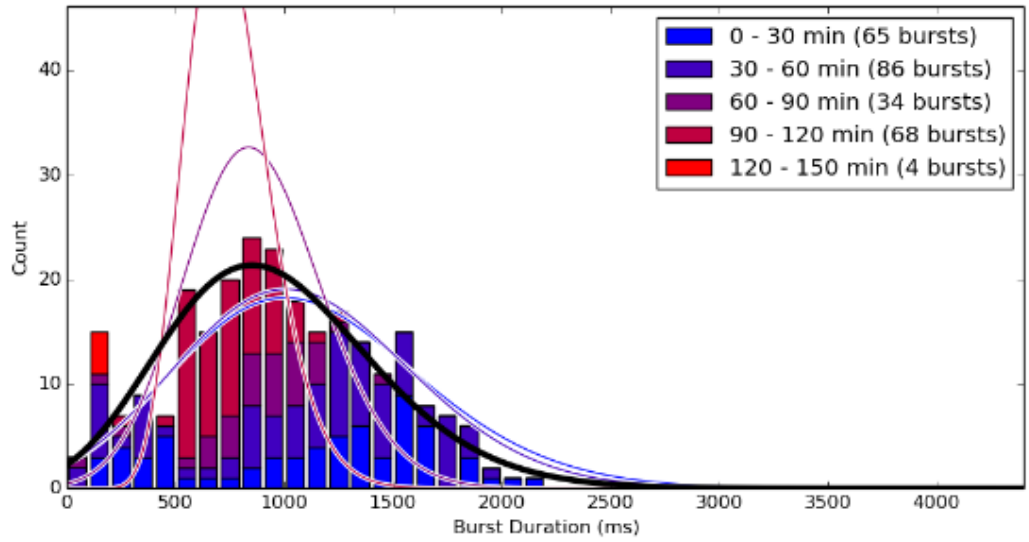

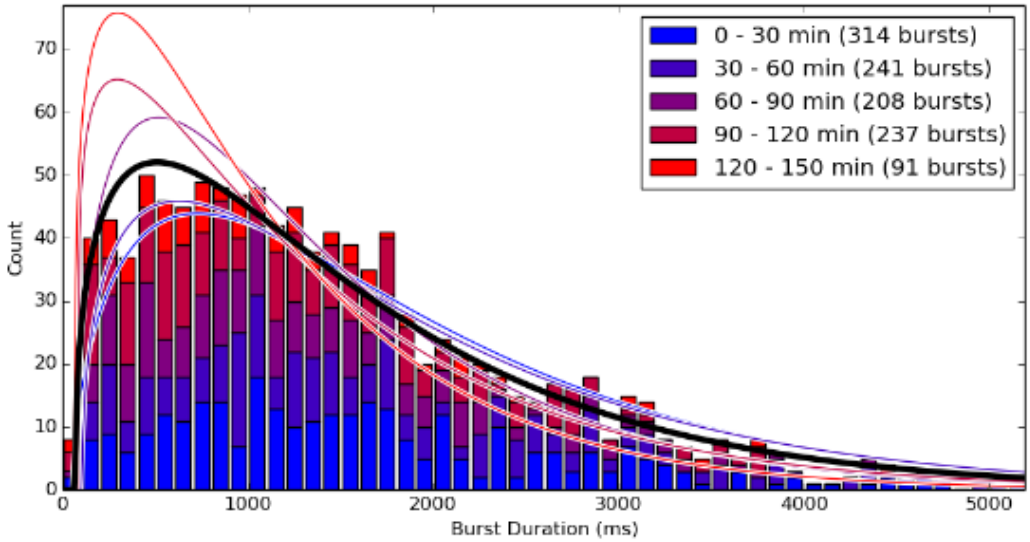

6.2.6 The 24 Hour Experiment

One of the tetrode experiments remained active for 24 hours. The turtle was anesthetized to begin the surgery at 12:PM. The first visually responsive recording was at 4:20 PM. The last visually responsive recording was at 12:46 AM.

Towards the end, there were plenty of spontaneous spikes without strong LFP bursts, but when there were strong LFP oscillations, there would be an increase in spikes for the duration of the oscillation and then the spontaneous spikes would cease for 5-20 seconds (Figure 6.7).

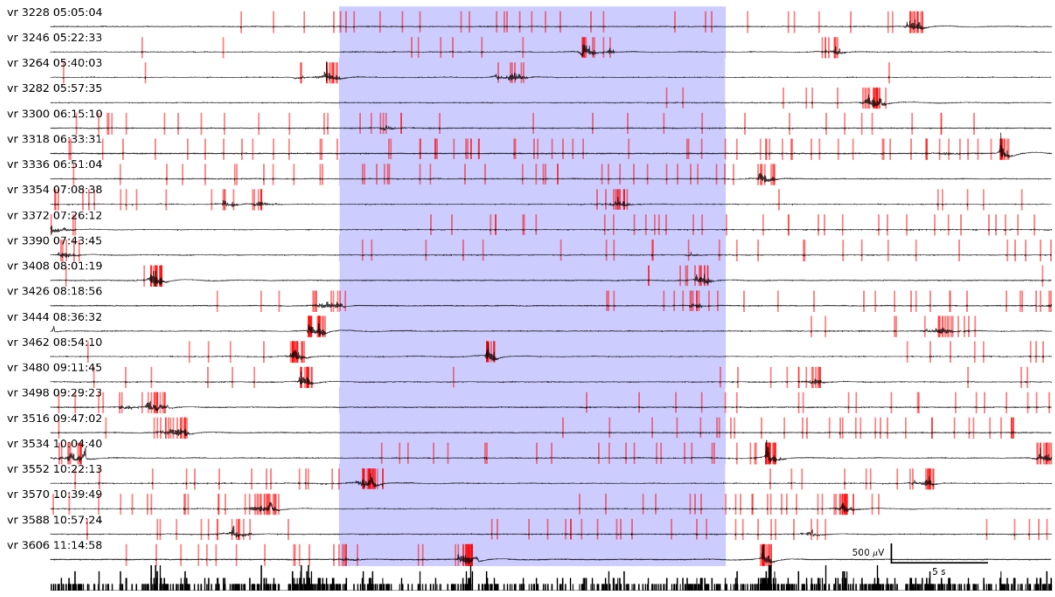

Figure 6.7 Activity recorded 24 hours into an experiment. Each row is a separate recording. The blue column indicates the timing of a diffuse visual stimulation. The LFP signal is shown in black, and spiking data are shown as red rasters with the peristimulus time histogram along the bottom.

6.2.7 Retinal Health

We take pictures of the retinal health at the beginning and the end of an experiment (See Section 6.25). Often those pictures are very different and it's clear that at the end, the retina is not healthy. It may be good to take pictures of the retina throughout the experiment to see at what point its health seems to degrade.

6.2.8 Physical Damage to the Cortex

For most of our experiments, we took pictures of the cortex at both the beginning and the end of the experiment. Some of our post experiment pictures show additional damage to the cortex. Figure 6.8 shows a tear in the cortex. If the tear was caused by over stretching the cortex with the pins used to secure the cortex, the damage associated with that tear likely extend beyond the short distance from the edge (that happens to be easily visible). It also may be the case that this damage takes time to take full effect, in which case some of the decrease in responsiveness could be due to physical damage.

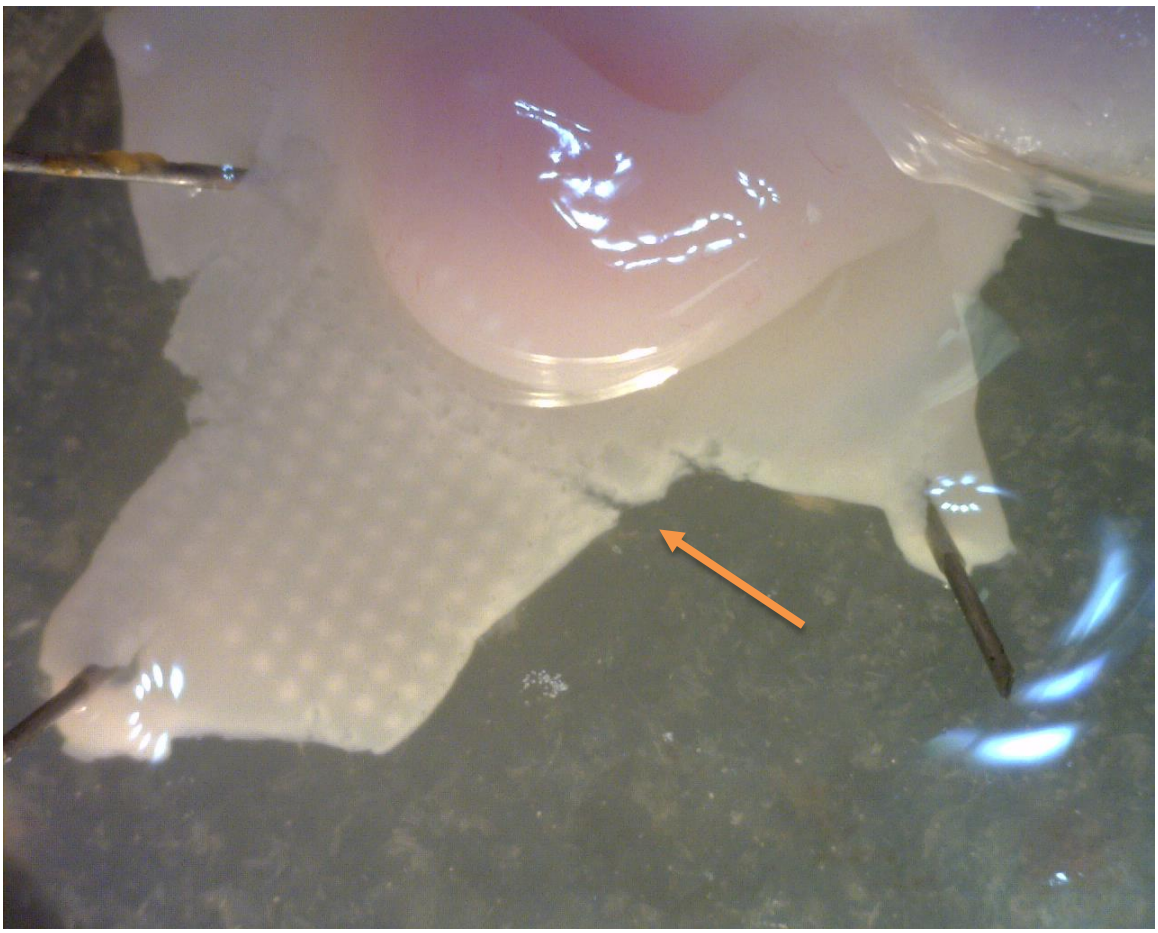

Figure 6.8 Picture of cortex with damage. Picture of the cortex in the recording chamber after an experiment. The 10x10 grid of light spots show where the MEA was placed. The arrow points to tearing in the cortex. Picture of turtle 7.

In addition to damage from tearing, there is also evidence for some experiments that the base of the MEA itself was pushing on the cortex (Figure 6.9). In addition to the two turtles shown, these visible impression are also found on at least turtles 4, 11, and 20. Each of these turtles had either no visual responses or only weak visual responses. With that in mind it's probably less likely in *these* cases that this damage prevented activity, and more likely that inactivity caused this damage (in the sense that after doing the normal search for visual responses without success, the experimenters may have become more aggressive with the MEA placement).

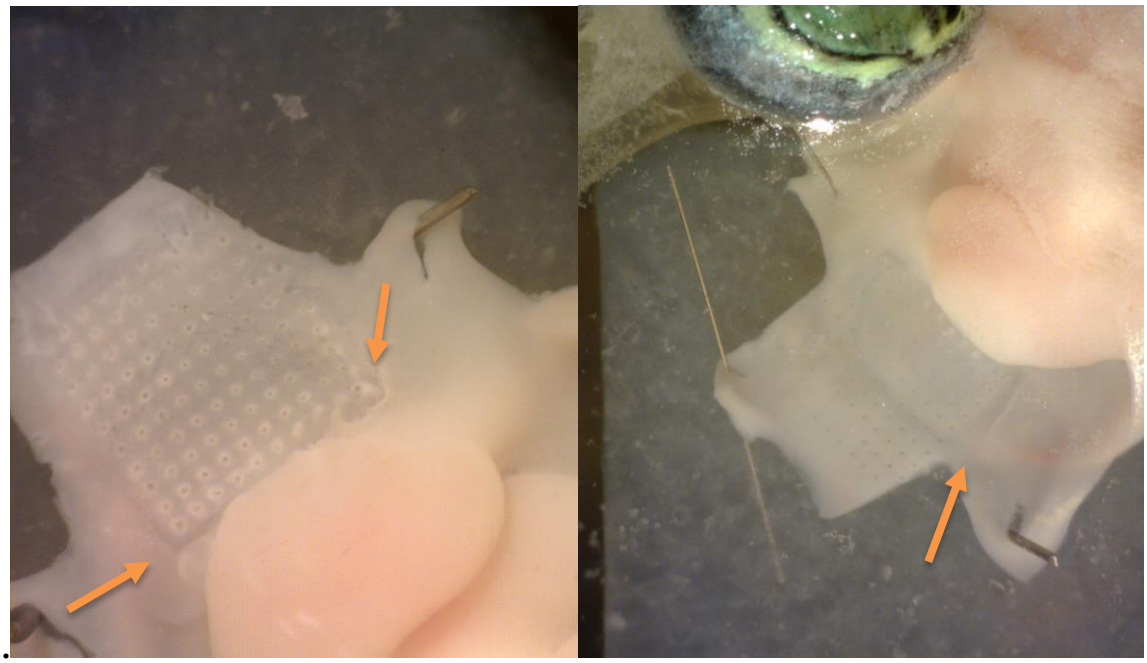

Figure 6.9 Pictures of cortex with impressions from the MEA. Picture of the cortex in the recording chamber after an experiment. The 10x10 grid of spots show where the MEA was placed. The arrows points to depressions left in the cortex by the base of the MEA. Pictures of turtle 32 **(Left)** and turtle 39 **(Right)**.

6.2.9 Anoxia Induced Increase in Extracellular GABA Levels

Even though turtles are resistant to the effects of anoxia (Hounsgaard & Nicholson, 1990), we still hope that, by circulating of oxygenated ACSF (artificial cerebral spinal fluid), we keep the brain in a nearly normoxic state.

One pattern that we've noticed regarding experimental rundown of activity, is that we seem to maintain strong visual responsiveness for longer periods of time in our experiments using single electrodes/tetrodes than in our experiments using MEAs. One possible explanation for this is that the tissue is getting less oxygen in the MEA experiments.

There are two reasons this might be the case. First, the MEA itself inhibits the flow of ACSF in the area we're recording from. The Utah array we've used is a 10x10 array with 400 µm spacing, and there is less than 1 mm between the surface of the cortex and the solid base that the electrodes secure to. In this 4x4 mm area, it is very likely that there is reduced ACSF flow.

The second reason we may have less ACSF flow in the MEA experiments, is that the surface of the recording chamber that the brain sits against is different. In single electrode and tetrode experiments, we have a layer of nylon mesh sitting on the surface of the recording chamber precisely for the reason of allowing increase ACSF flow. For our MEA experiments, we've replace the nylon mesh layer with a layer of agar. We do this to protect the MEA. If the MEA were to go all the way through the cortex and hit nylon, it would almost certainly break, costing thousands of dollars. On the other hand, if it goes through the cortex and hits agar, it will be just fine. Unfortunately, the agar layer almost certainly prevents the flow of ACSF beneath the brain.

Suspecting that the flow of oxygenated ACSF is decreased in our MEA experiments, we should consider what effects that might have. It has been shown in turtle that the extracellular level of the inhibitory neurotransmitter GABA can increase drastically during sustained anoxia, reaching 90 times the normoxic level after 240 min (Nilsson & Lutz, 1991). Though the extent to which our tissue may be oxygen deprived is certainly less than severe than what was used for that study, it may be the case that the level of deprivation was still enough to substantially increase GABA levels. In any case 240 min is the correct order of magnitude for when we typically saw a decrease in visual responsiveness, and an increase in inhibitory neurotransmitter levels seems like a very reasonable explanation for a decrease in neural activity.

6.3 Correlated Activity at Distant Electrodes or Incorrect Electrode Map

When plotting LFP receptive field similarity versus distance (see Chapter 3), we typically see a negative slope (i.e., nearby electrodes tend to have more similar LFP receptive fields than distal electrodes). By decreasing the threshold we use for characterizing electrodes as visually responsive, we can include additional electrodes in our analysis. For turtle 7 this means including electrode 83 (among others).

When we plot the RF similarity versus distance for electrode 83 with all other visually responsive electrodes (Figure 6.10), in contrast to the typical result, the data is actually better described by a positive slope. Additionally if we look at the RF similarity versus distance plots for all the other electrodes we see that they now have a point that doesn't seem consistent with the general trend of all the other points. If we highlight the points in these graphs that represent

an electrode pair involving electrode 83 (Figure 6.10, points colored orange), we see that those strange points are those involving electrode 83.

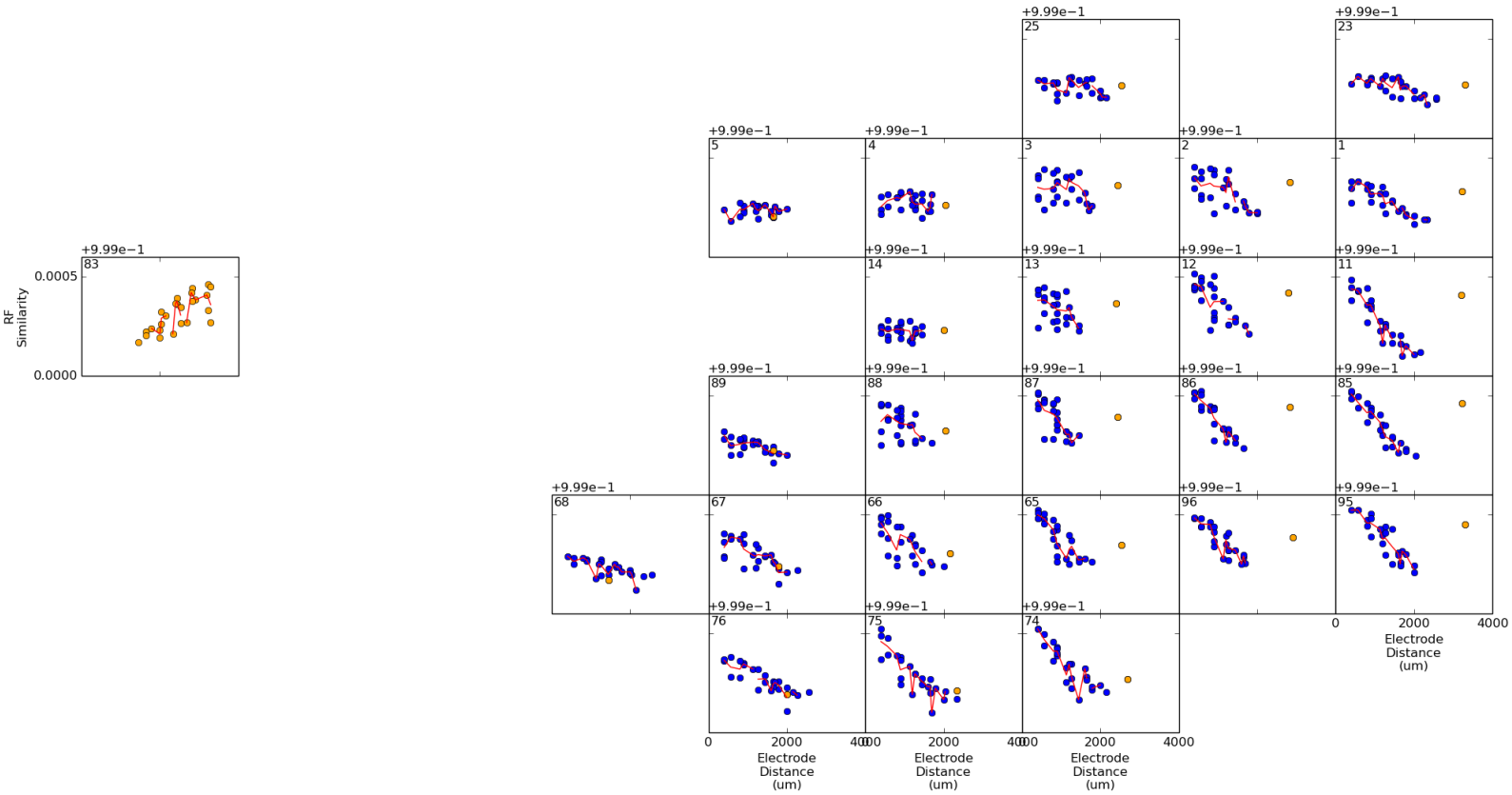

Figure 6.10 Turtle 7 receptive field similarity with electrode 83 highlighted.

One possible explanation to this odd observation is that the supposed electrode map (the spatial location on the MEA corresponding to each signal, which is just identified by some electrode number of the computer) is actually incorrect. Further investigation into this hypothesis, reveals a consistent finding.

If we modify our electrode map such that electrode 83 is moved to location that is normally reserved for electrode 85 (and simply exclude the data from electrode 85), we end up with a set of RF similarity plots in which data points for electrode pairs including electrode 83 are consistent with the general trends established by the rest of the data (Figure 6.11).

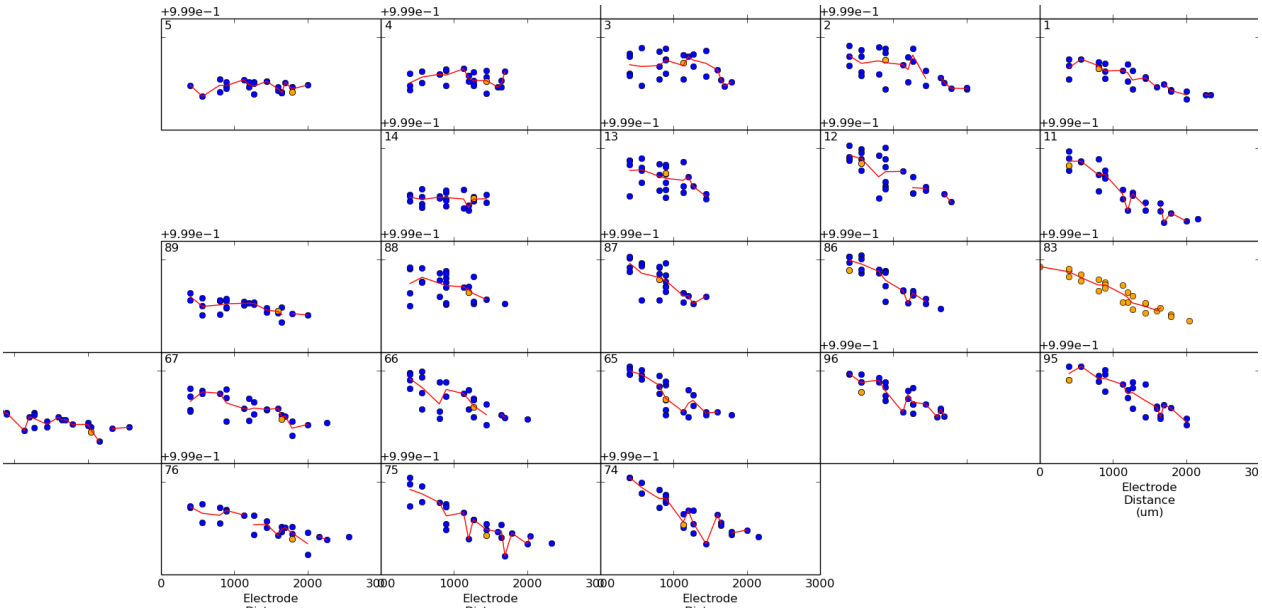

Figure 6.11 Turtle 7 receptive field similarity with electrode 83 and 85 swapped.

To further test this hypothesis, we can see if this manipulation ‘fixes’ the trends of RF similarity plots for other turtles.

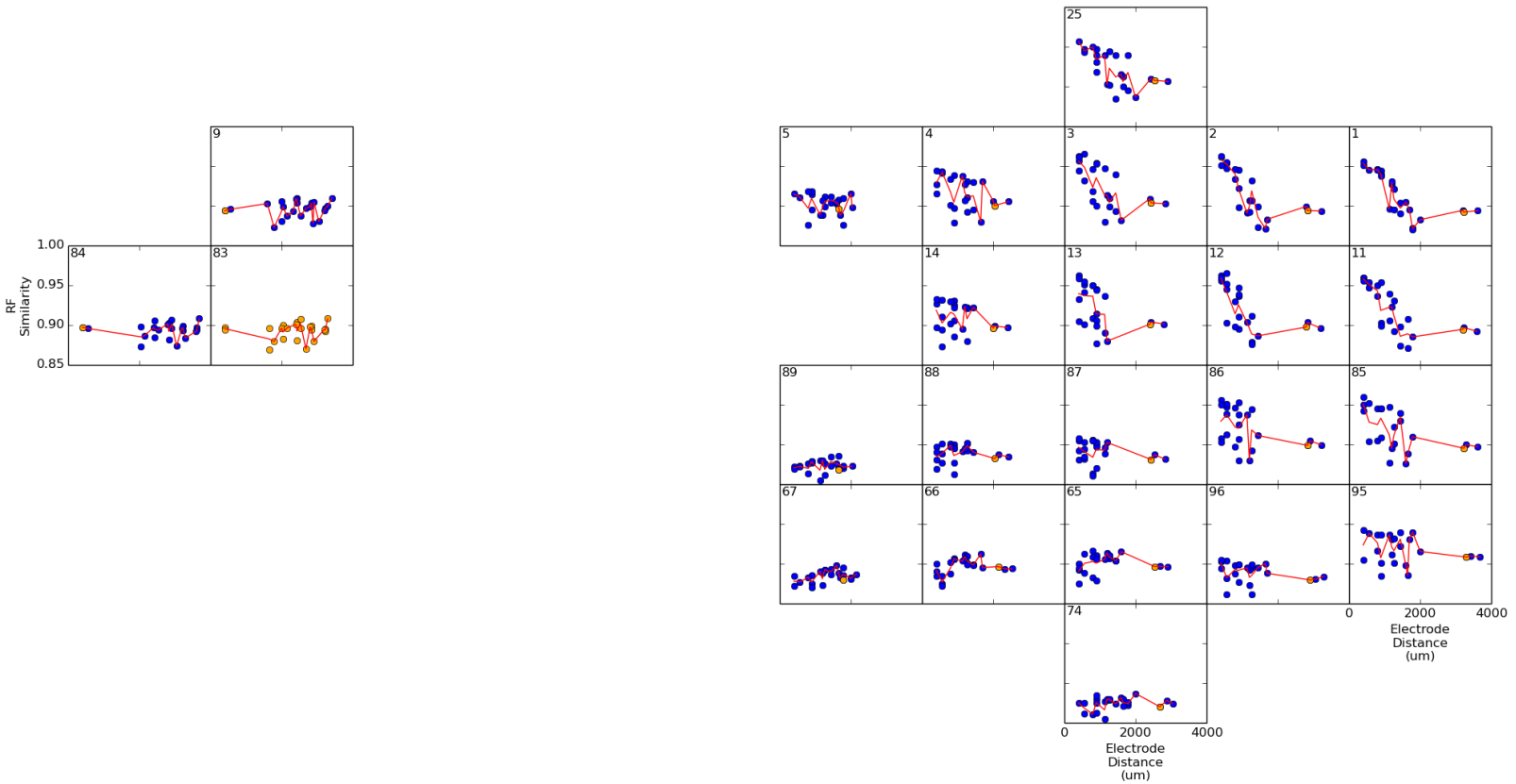

Figure 6.12 Turtle 6 receptive field similarity with electrode 83 highlighted.

6.4 Visually evoked and ongoing electrode groups

There is some evidence that, at times, one set of electrodes will be active together for spontaneous activity and a different set of electrodes will be active together for visually evoked activity (Figure 6.13). It would be interesting to see if these groups are completely disjoint and if they are consistent over the course of an experiment.

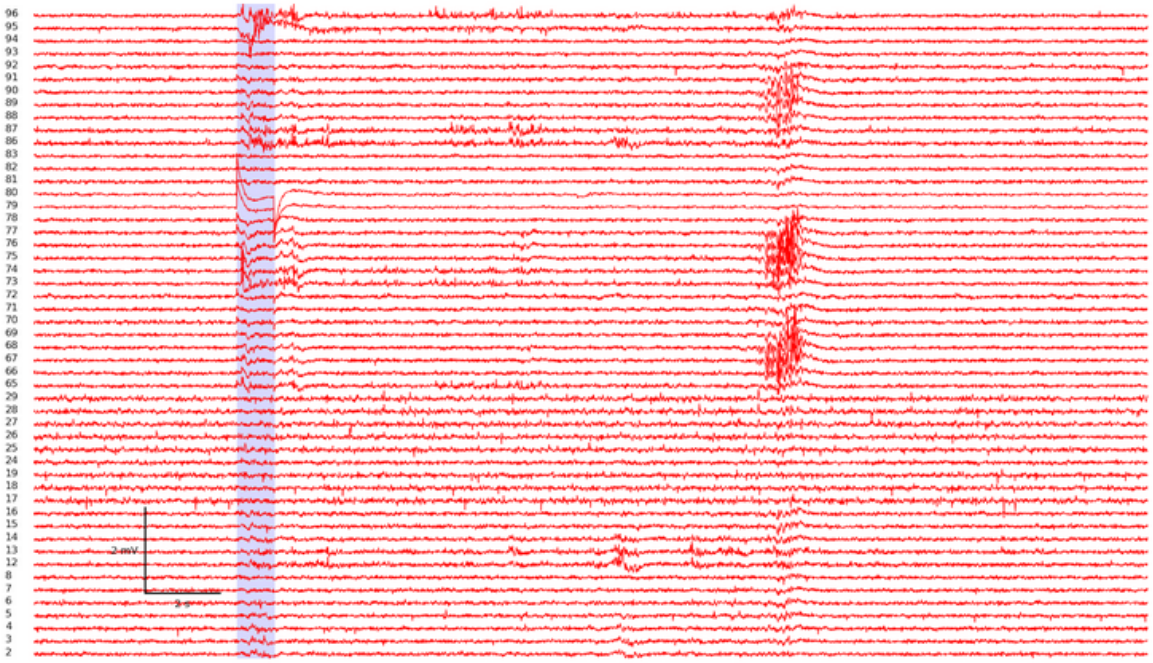

Figure 6.13 Distinct groups of electrodes sharing LFP bursts. Each row shows the raw data of a different electrode. Data from Turtle 2, recording vis001, 240 sec into the file.

6.5 Strange Fluctuations

Fairly often, we recorded many strange large fluctuations in the extracellular voltage that we have no explanation for (Figures 6.14-17). Our typical response is along the lines of, “That’s weird, I guess we can’t use that data.”, and then we move along. These never get very much of

our attention, but maybe they should get some. After all, they *are* generated by the circuitry of the cortex, so at the very least they tell us that the cortical circuitry is capable of producing these signals. It would be interesting to take an inventory of strange fluctuations and see if certain features show up again and again in multiple turtles.

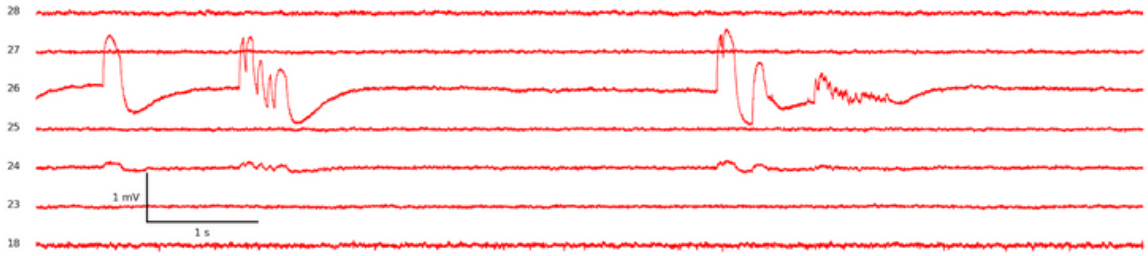

Figure 6.14 Strange fluctuations in Turtle 7.Each row shows the data from a separate electrode. Raw data 894 seconds into file 001.

Figure 6.15 Strange fluctuations in Turtle 6. Each row shows the data from a separate electrode. Raw data 120 seconds into file 001.

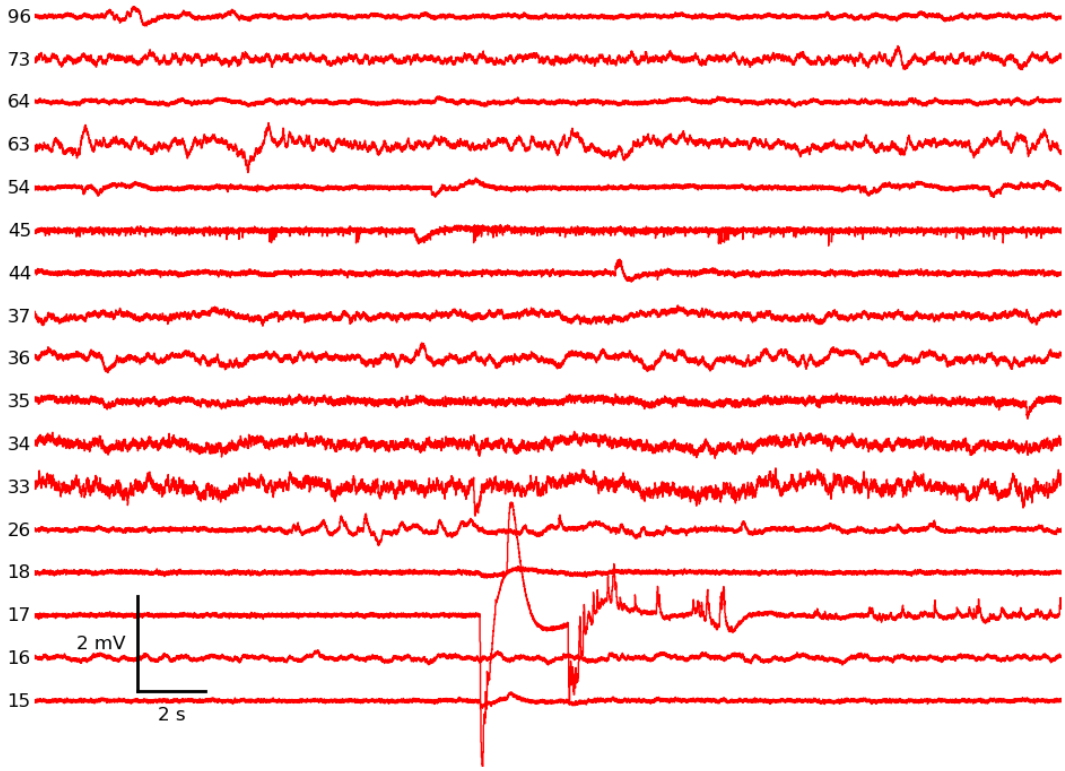

Figure 6.16 More strange fluctuations in Turtle 6. Each row shows the data from a separate electrode. Raw data 710 seconds into spontaneous recording001.

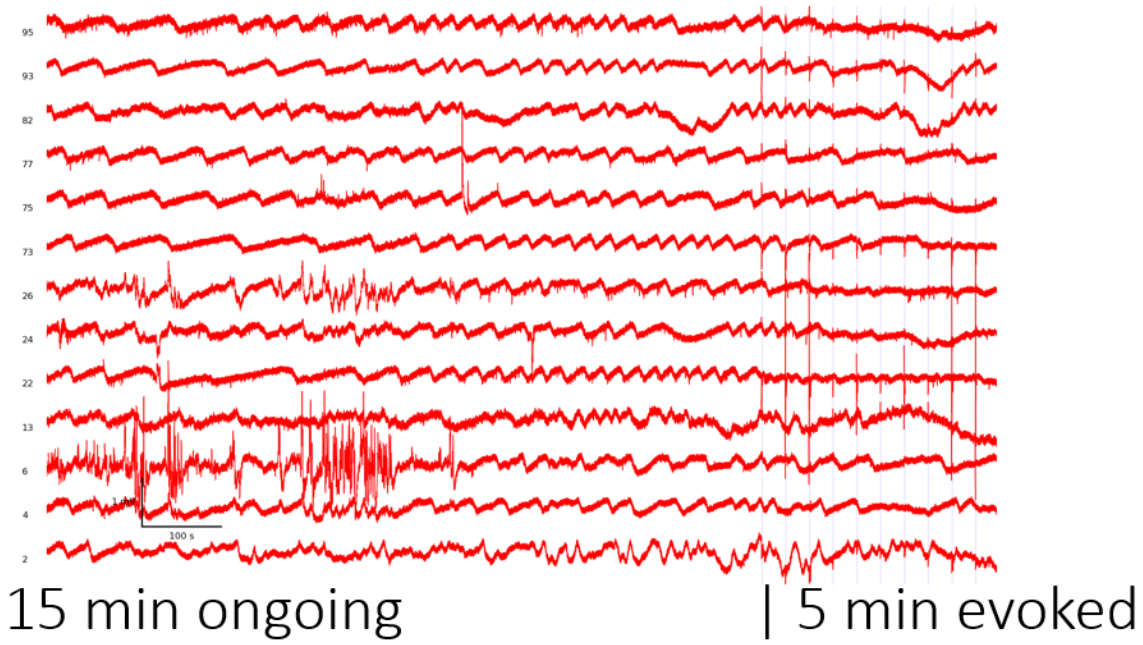

Figure 6.17 Strange fluctuations in Turtle 32. Each row shows the data from a separate electrode. Raw data in at the beginning of recording LED001.

6.6 Direction Dependent Response Variability

Usually when we look for direction sensitivity, we look for difference in the strength of the response, but it may actually be useful to look for differences in other aspects of the response as well. For instance in Figure 6.18, the average strength of responses to dots moving in opposite directions are roughly similar, but the reliability of those responses are vastly different.

Figure 6.18 Direction dependent response variability. Each row is a separate trial. The LFP signal is shown in black. Action potentials are shown as red rasters. Each colored column indicates the timing of a black dot moving across a white screen.

6.7 Long Term Adaptation (30 s – 60 s)

In the experiment done on 3/15/2012 we observed reliable on and off responses to a screen alternating between a white and green screen every 60 s, but when the time between switching the screen color was 20 s (or less) the responses were very rare (Figure 6.19).

Recognizing that full recovery from adaptation can take between 20 and 60 s is important for designing future experiments.

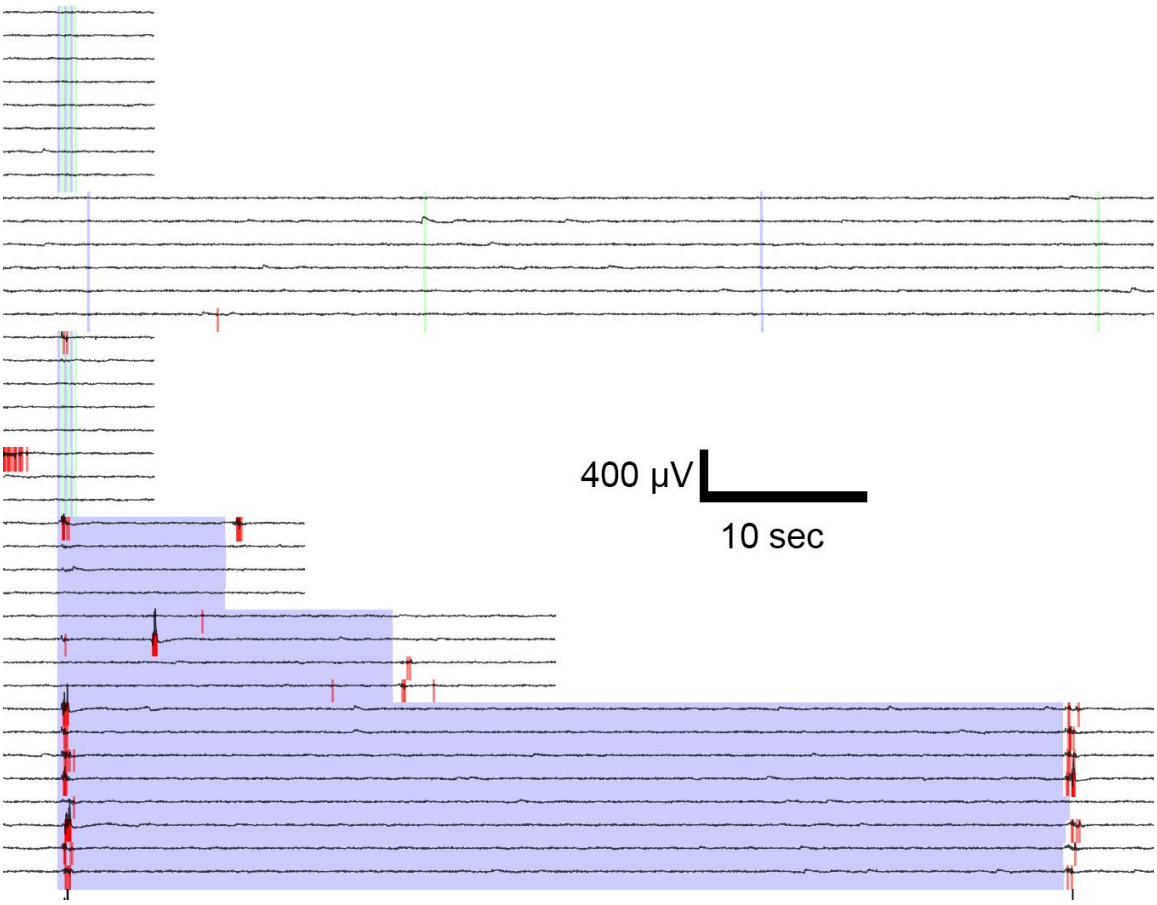

Figure 6.19 Long term adaptation. Each row is a different trial. Each colored area indicates the timing of a full screen color change. There were 10 s, 20 s, and 60 s durations of color change (bottom three modes) as well as faster flashes of color changes (top three modes). LFP (black) and action potentials (red) are shown.

6.8 Precisely timed coordinated activity in specific frequency ranges in multiple electrodes

6.8.1 Introduction to shared bouts of activity

For some of our experiments, we filtered the recorded extracellular voltage in several narrow-pass-bands and plotted all filtered signals using Butterworth filters as was done in

(Rutishauser et al., 2013). This was often done for many of the electrodes from the MEA. For any one of those sets of plots, the filtered signals we plotted had many bouts of increased activity. When flipping through many of these figures made for different electrodes, we noticed that some of the bouts of activity seen in one figure would be present in in the next figure (i.e., from another electrode) with almost exactly the same timing, while others would be present for only one of the two electrodes (See Supplementary Figure 2.17). There are many interesting questions to answer regarding these shared bouts of activity.

One possibility for the detection of bouts of activity is to use the same technique as was used for LFP burst detection in Chapter 3, with threshold values changed appropriately.

After detecting the bout times for all frequency bands on all electrodes, we could define coincident bouts on two electrodes, A and B, as shared if at least 80 % (or some other appropriate value) of the duration of the bout on electrode A overlapped with the duration of the bout on electrode B (and vice versa).

This may be well visualized by plotting the Hilbert transforms of the narrow frequency bands from the two electrodes on top of each in different colors other with alpha 50% and the plots filled to the x axis.

For a more detailed study of shared bouts, one could go beyond simply labeling bouts as shared or not shared. This may be done by considering the relative amplitude of the coincident bouts. If the amplitude of the bout on electrode A is very strong (either absolutely or with respect to the typical level of activity on electrode A) and the amplitude of the bout on electrode B is very weak, the bout would be weakly shared.

Many questions come to mind regarding shared bouts:

Q1: What percentage of bouts are shared?

Q2: Are there certain groups of electrodes that tend to share bouts together?

Q3: Are shared bouts stimulus specific?

If there are groups of electrodes that tend to share bouts together, does the shared visually evoked activity of these groups provide more stimulus specificity than any of the individual electrodes taken alone?

Q4: Are unshared bouts stimulus specific?

Instead of (or in addition to) the hypothesis underlying Q3, one could look at the stimulus specificity of unshared bouts of activity.

Q4: Are shared bouts frequency dependent?

If a pair (or group) of electrodes shares bouts of activity in one frequency range, do they also share bouts for other frequency ranges?

Q5: What's the spatial arrangement of groups of electrodes that share bouts?

When a group of electrodes does share bouts of activity, is there a pattern to how those electrodes are distributed around the MEA? Are they neighboring electrodes or scattered? Do they lie along a rostral-caudal line? Do the lie along a dorsal medial line? Is the spatial arrangement different for groups that are defined by sharing different frequency bands? For these questions, we may get a clearer picture using the more involved quantification of shared bouts that includes the strength with which they are shared.

6.8.2 Discrete LFP generators

If we find that certain bouts are shared only by neighboring electrodes, and that the relative amplitude of the bouts on those electrodes (relative to the amplitude on the other

electrodes), then we may actually by looking at LFP signals that sample overlapping volumes. If this is the case we would learn that 1) there are discrete LFP generators, 2) the locations of these generators, and 3) the spatial extent of our LFP recording volume.

The recording volume of the LFP has often been thought to be within roughly 150-400 μm of the electrode (Katzner et al., 2009; Dajun Xing et al., 2009), but others have suggested in may be as large as several millimeters at times (Kajikawa & Schroeder, 2011). With this in mind, it may be plausible that multiple electrodes record activity from a single location.

If we find what appear to be discrete generators, we may have a new potentially awesome signal to analyze. This could move us from hearing the muddled noise of the crowd to hearing the details of individual components within the crowd, which may have more stimulus specificity or reveal clearer patterns between different aspects of cortical activity. It would be good revisit many of our previous studies in the context of generators and repeat studies using generator-specific signals.

6.8.3 Time Delays and Signal Propagation

It could reasonably be suspected that when several electrodes share a bout, it is because the cells near the electrodes share common inputs. If these electrodes are different distances from the common input cells, we might expect slight differences in the onset time of the bouts. This could also reveal something resembling propagating waves as have been discussed in several studies (Du, Ghosh, & Ulinski, 2005; Du, Ghosht, & Ulinski, 2003; J C Prechtl et al., 1997; David M Senseman & Robbins, 2002).What follows is a plan to investigate this.

When a group of electrodes shares bouts, for each bout, take the average time of bout onset (averaged over all electrodes in the sharing group). Then for each of those electrodes, look at the difference between its bout onset time and the average onset time. We'll call this time difference the bout onset delay. Finally, for each electrode in the sharing group, plot the distribution of bout onset delays. If the distributions for some of the electrodes are significantly different from other electrodes, this may suggest something about signal propagation.

6.9 Clarifying the Spatial Features of the Receptive Field with Stationary Stimuli

With very few exceptions, we probed the receptive field by presenting a black dot moving across a white background. In only a couple experiments did we present stationary black dots at different locations in the visual field. Then, the RF from this stimuli could be compared with that from the moving dots. This stimuli would offer the advantage of not requiring a latency/delay to determine what part of the visual field actually elicited the activity recorded. An additional advantage of this stimuli over moving dots, is that we wouldn't need to worry about response to one area of the visual field being inhibited by adaptation to motion in another area (or conversely mistakenly interpreting persistent activity elicited by motion in one area as a response to motion in a different area of the visual field stimulated slightly later). This experiment was done on 4/05/2012, but this was late in the experiments and visual responses were less reliable.

6.10 Extending Receptive Field Similarity Analysis

For the moving dot experiments, we were able to plot LFP receptive field versus electrode pair distance across the array. The results from these experiments are interesting, but we didn't consider response similarity for other stimuli or similarity between pairs of spiking units. There may be more to learn by extending our analyses to include these

6.10.1 Defining Response Similarity for Diffuse Flash and Complex Movie Stimuli

For the moving dot experiments, the LFP event times were converted to locations along paths in the visual field, the paths were then binned, and the event counts in those bins were used to compare pairs of electrodes and calculate a similarity. A very similar technique could be used to calculate response similarity for experiments using LED flashes and complex movie presentations. For these stimuli, instead of binning over paths in the visual field, we could simple bin time starting with the stimulus onset (or possibly slightly after stimulus onset to avoid artifacts) and ending with the end of the response (or slightly after since including additional time of inactivity won't affect the results). After make that change, the remaining analysis would proceed exactly as with the moving dots.

For the LED experiments, this may produce a much richer set of results than what we've already seen from the moving dot analysis. It would be interesting to test if the similarity results produced by moving dot data would be reproduced by other stimuli.

A More Complete Picture of the Visual Cortex

In addition to verifying or comparing with previous results from the moving dot data, the LED experiment also give us an opportunity to get a more complete picture of visual cortex

because those experiments often had more visually responsive electrodes than the 4 moving dot experiments had.

6.10.2 RF Similarity versus Distance for Action Potential Data

In Chapter 2, for moving dot data, we showed that action potential receptive fields tend to be significantly similar to LFP receptive fields and that for LFP receptive fields from different electrodes there is a trend (at least in the rostral visual cortex) of nearby electrode pairs having more receptive field similarity than distant electrode pairs. Connecting these two results together, we might expect that we would see the same trend if we compare action potential receptive fields from different electrodes with each other.

On the other hand, the receptive fields found with spike data are at times smaller than those found using the LFP. Action potential-action potential RF similarity has not been considered yet. It would be interesting to repeat these analyses for spike data to see if the same (or other trends emerge).

6.11 Adaptation for Complex Movies

Often, when showing a complex video, there is a strong response to the onset and offset of the video, which may likely be due to a change in luminance/contrast. Later in the complex video there may be other activity that is reliably evoked across trials. It's difficult to tell if the timing of the later activity aligns with interesting (activity-evoking) happening within the stimulus OR if the timing of this activity is actually delayed activity from the video onset (we've seen responses to LEDs that have an initial response ~1s and then a second response after ~9s), OR if the lack of activity before the later activity is the result of adaptation from the video onset

and the later activity happens after that adaptation dies off. To distinguish between these possibilities, one could show the videos many times with different sections of the beginning of the video removed.

6.12 Checking Orientation Tuning Decoupled from Spatial Tuning

Our main tool for looking at direction tuning has been moving dots. While it is true that the moving dots are moving in a specific direction, it is also true that the dots (as they move) occupy a broad range of locations in the visual field. Consequently, when we record a strong response to a dot moving across the top of the screen, we can't actually say if the response is caused by the dot occupying that area of the visual field, or by the dot moving with a certain direction (or if the combination of direction and location is important).

There is some evidence that the location is more important: 1) opposite angles along the same path tend to have the same response, and 2) every time a pair of opposite angles (e.g., 0 and 180 degrees) have a strong response for paths only along the bottom half of the visual field, the responses to the perpendicular directions are also primarily in the bottom half of the visual field.

Despite evidence that the direction of motion may have little impact on response strength, it would be nice to test for orientation with a more targeted and controlled experiment. One way of doing this would be to used small windows (maybe 10 visual degrees) in which a sine grating moves. In this way, orientation tuning could be tested in localized areas of the visual field. By doing this at many locations throughout the visual field we could also test spatial tuning as a whole, and whether orientation varies throughout the visual field.

6.13 Electrical Stimulation

When doing single electrode experiments, there was a concern that we were biasing our selection of cells to record from by stopping our search for a cell when we found an actively spiking cell. This could mean that we record primarily from a subset of cells that are spontaneously active, while there could be other sets of cells with other visual response properties that we overlooked. To prevent this bias, we attempted to find cells by electrical stimulation during six experiments. The first two (7/12/11 and 7/14/11) were dedicated to determining the best conditions/settings/locations for recording and stimulating. During these experiments, electrical stimulation was provided using patch electrodes with broken tips. Two sites within the cortex (Figure 6.20) and one site in the lateral forebrain bundle were stimulated while recording with a ½ megaohm tungsten electrode.

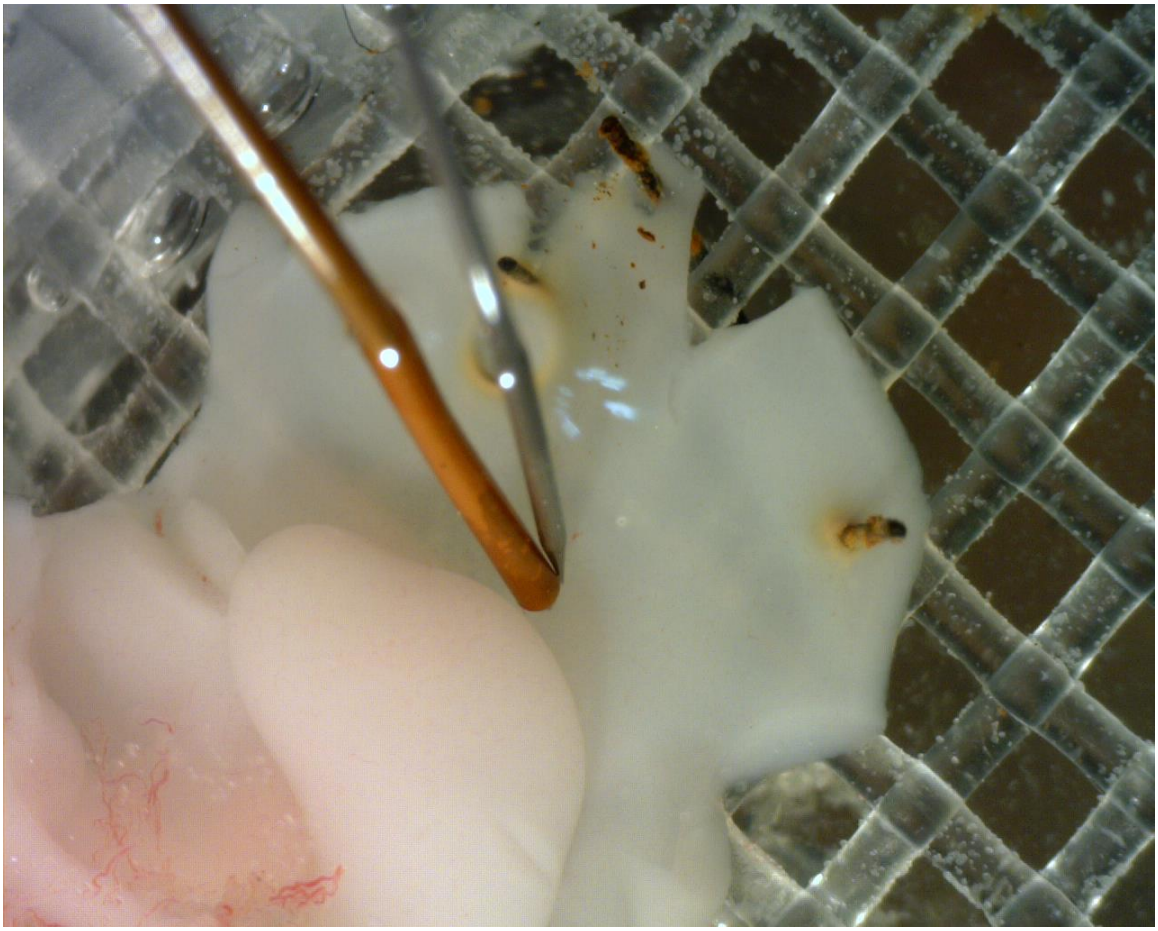

Figure 6.20 Stimulating electrode place in the cortex. Picture of the cortex with a stimulating electrode (thick) and a recording electrode (thin).

6.13.1 Antidromic Stimulation

Over many stimulating/recording configurations I saw no clear evidence of antidromic stimulation even when I recorded near spiking cells. On 8/03/2011 there were responses that may or may not have been antidromic spikes (Figure 6.21), but the cell was not visually responsive.

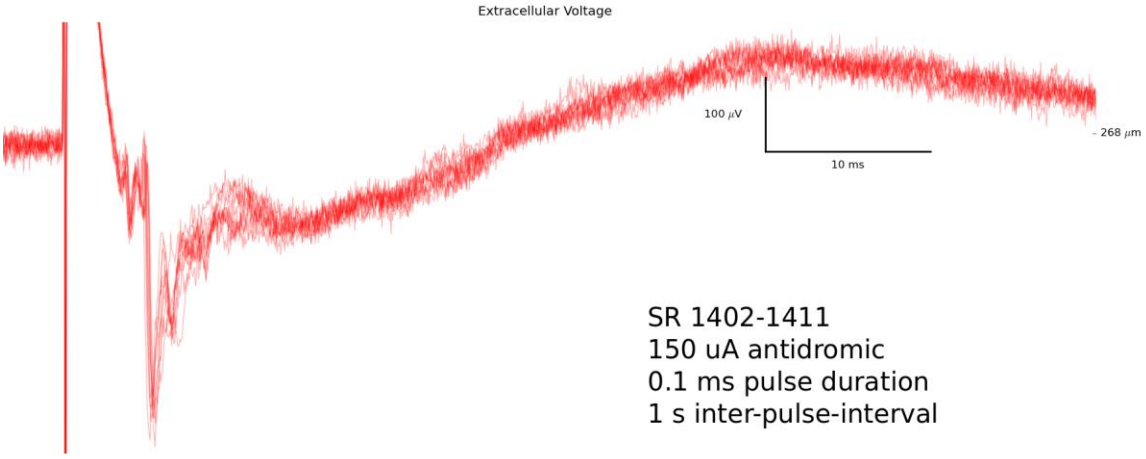

Figure 6.21 Possible antridromic stimulation. Several trials overlaid on top of each other. The negative deflection with a width of a few milliseconds may have been from an antidromically stimulated cell.

6.13.2 Recording Depth Dependent Results

On 7/12 changing recording depths (from 0 um to 250 um) changed only the scale of the response to electrical stimulation

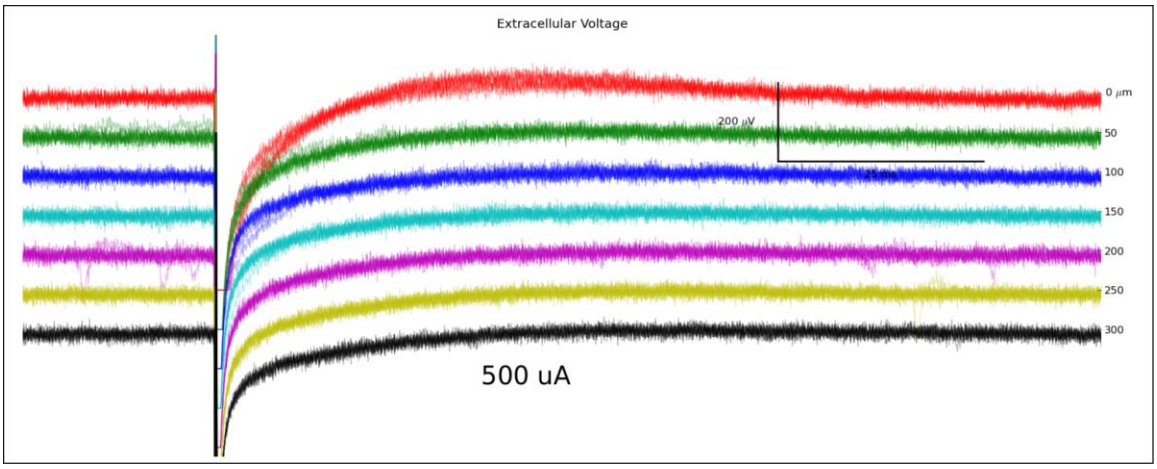

Figure 6.22 Changes in amplitude of response to electrical stimulation at different recording depths. Recordings taken from 6 different depths.

On 7/14 the same depth changes resulted in a continuous change to the structure of the response to electrical stimulation

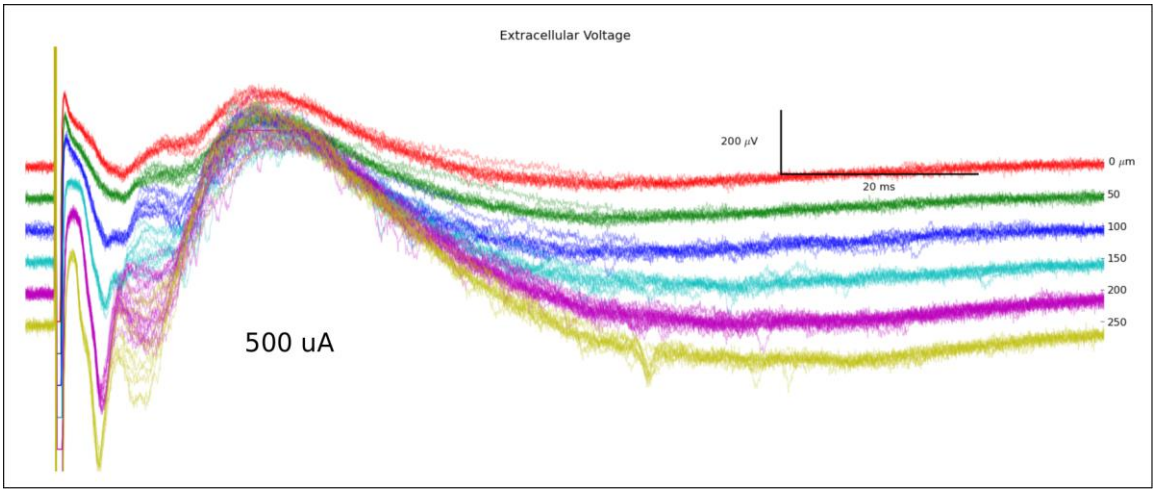

Figure 6.23 Changes in shape of response to electrical stimulation at different recording depths. Recordings taken from 6 different depths.

6.14 Stimulus Specificity of Spectrogram Structures

Likely as a result of smoothing, the spectrograms of responses to moving dot stimuli do not clearly reveal narrow frequency bands of increased activity, but in this smoother picture, repeatability in response is more evident than when looking with the finer spectral resolution and coarser temporal resolution of the PSD's and relative powers. The spectrograms are suggestive of spatial stimulus specificity in the response amplitude, directional stimulus specificity in the response time course, and averages that clearly seem representative of individual trials.

Looking at the spectrogram of recorded signals reveals consistent differences between stimuli. Figure 6.24 shows the spectrograms for electrode 85, turtle 7. If we compare the spectrograms for the responses to a dot moving at 0 degrees to those for the responses to a dot

moving at 180 deg, we can see clear differences. The 0 degree spectrograms show a very sharp onset across a broad range of frequencies (0-60 Hz) with the higher frequencies dying off more quickly than the lower frequencies. In contrast, the 180 degree spectrograms show a blurrier/smoother onset (of the same frequency range) with all frequencies dying off with the roughly the same time course.

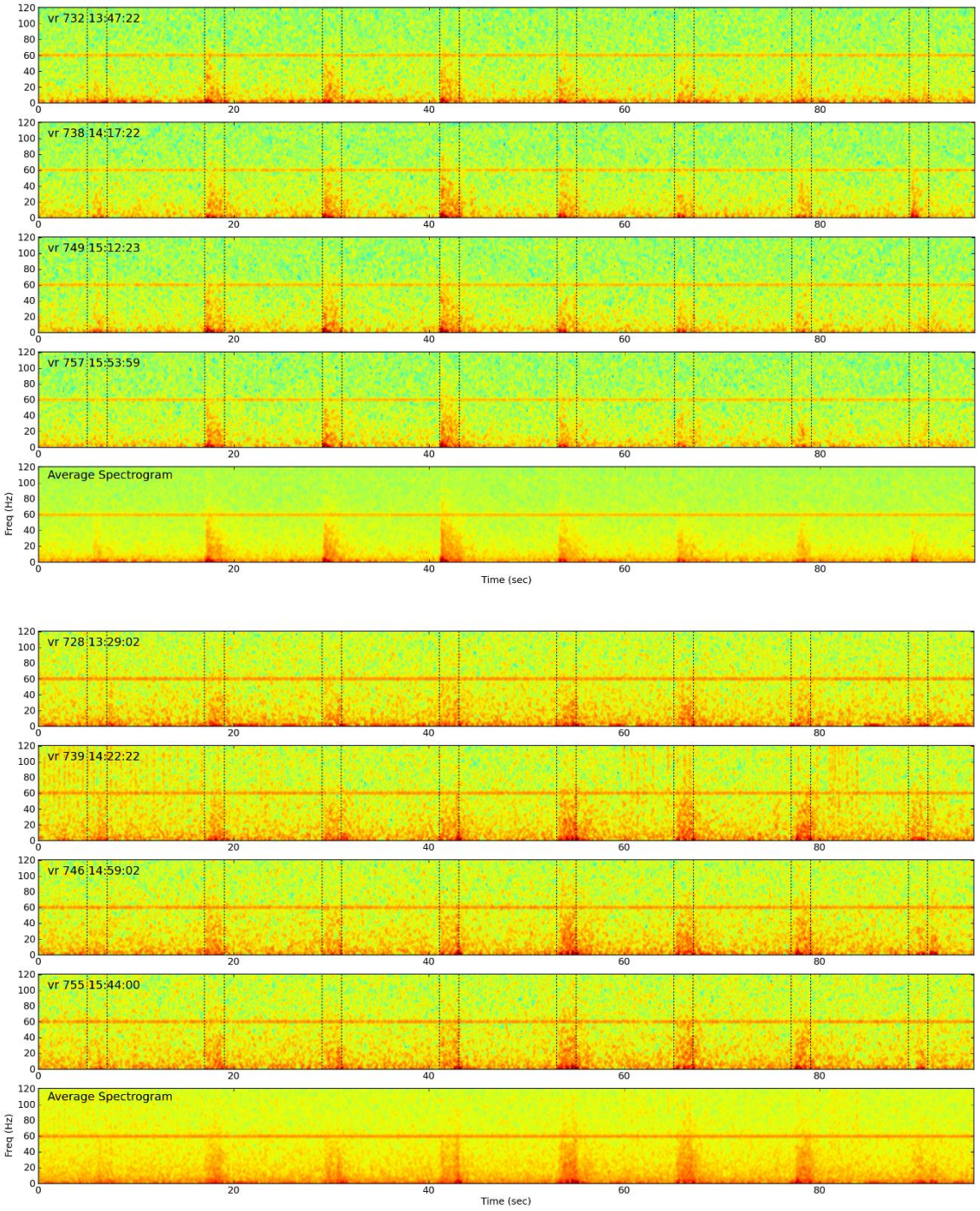

Figure 6.24 Spectrogram responses to dots moving in opposite directions. Responses to dots moving along 8 paths. **(Top Half)** Responses to 4 trials of motion at 0 degrees with the average beneath. **(Bottom Half)** Responses to 4 trials of motion at 180 degrees with the average beneath.

6.15 Possible Responses to Absent Stimuli

The experiment performed on 9/28/2011 had its strongest and most reliable response 1 s after the last bar Figure 6.25. For these trials, there was 1 second between bars. Therefore, this response could be a response to an ‘absent’ stimuli. In other words, the turtle may have expected a stimulus after 1 s of no stimulation, because most moving bar presentations were followed by another moving bar 1 s later. Then the absence of such a subsequent moving bar could have been detected as a deviation from expectations, and that deviation may have evoked a response.

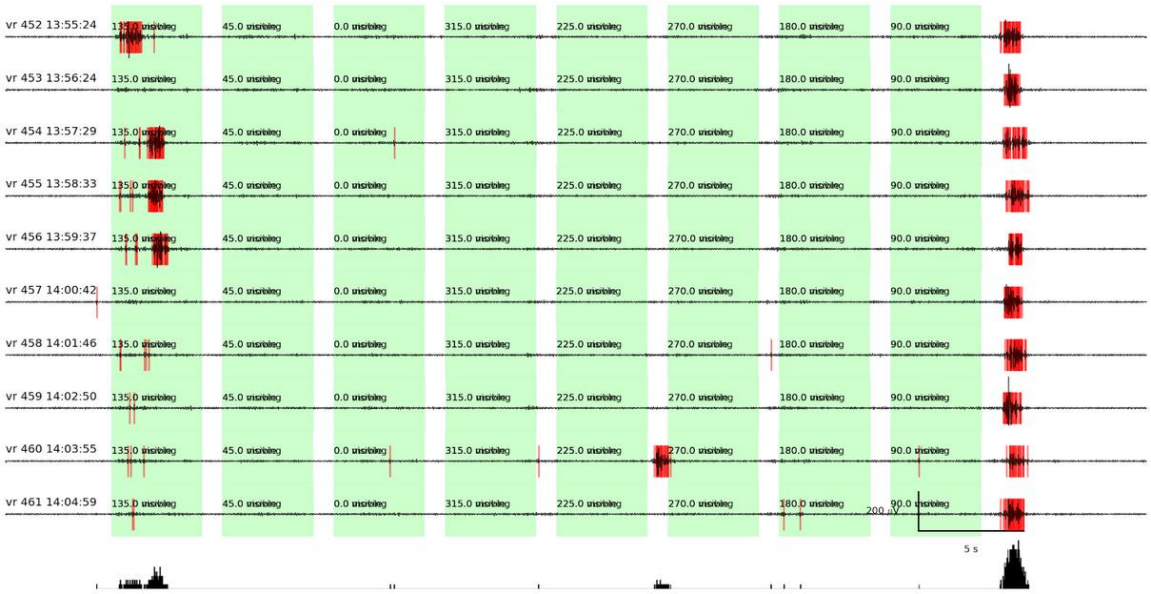

Figure 6.25 Possible Response to Missing Stimuli. LFP responses (black signal) and spike responses (red rasters) to ten presentations of a black bar moving across a white screen in eight different directions. Bottom: A peristimulus time histogram of the spiking responses.

Responses to missing expected stimuli have also been recorded in humans with scalp EEG recordings of responses to auditory stimulation, (McCallum, 1980), and even in the LFP of turtle visual cortex, dorsal ventricular ridge, and optic tectum (J. C. Prechtl & Bullock, 1994; James C. Prechtl & Bullock, 1993).

6.16 LFP Burst Refractory Period

In Chapter 3 we demonstrated the effects of adaptation to both spontaneous and visually evoked activity. In that study, the activity we were quantifying was LFP events, which primarily happened to manifest within LFP bursts. If we step back and look at the bursts as our activity of interest (instead of individual LFP events), we may gain further insight into adaptation. By detecting LFP burst (using the same methods used in Chapter 4) times and plotting the distributions of interburst interval times, we may discover an LFP burst refractory period, and learn a bit more about the timescale of adaptation.

6.17 A Clearer Picture of V1 in the Cortex

Use the pictures taken after the experiments were finished to see where the electrodes were. Indicate on the cortex which were visually responsive (and maybe the strength with which they responded). Do this for many experiments (not only on their own cortical map, but also together on one picture of a cortex), and see if a clearer picture emerges regarding where the visually responsive region of the cortex is.

In most of our experiments the dorsal rostral corner of the MEA was visually responsive. Unless, by chance, we happened to place our electrodes right at a strong border across which visual responses stopped, this suggests that we were usually missing out on some visually responsive region of the cortex. It may be useful to place the MEA more dorsally and rostrally (to the extent that the practical experimental limitations allow) to get a clearer picture of what the dorsal and rostral borders of the visual cortex look like. An added benefit of this, of course, is simply having more visually evoked data.

When performing studies it may be important to probe the system with many different stimuli, and a sufficient number of times to account for the variability of responsiveness of different areas to different stimuli. One study shows substantial overlap of effective and ineffective recording sites for a particular stimulus (Figure 6.26) (J. C. Prechtl & Bullock, 1994).

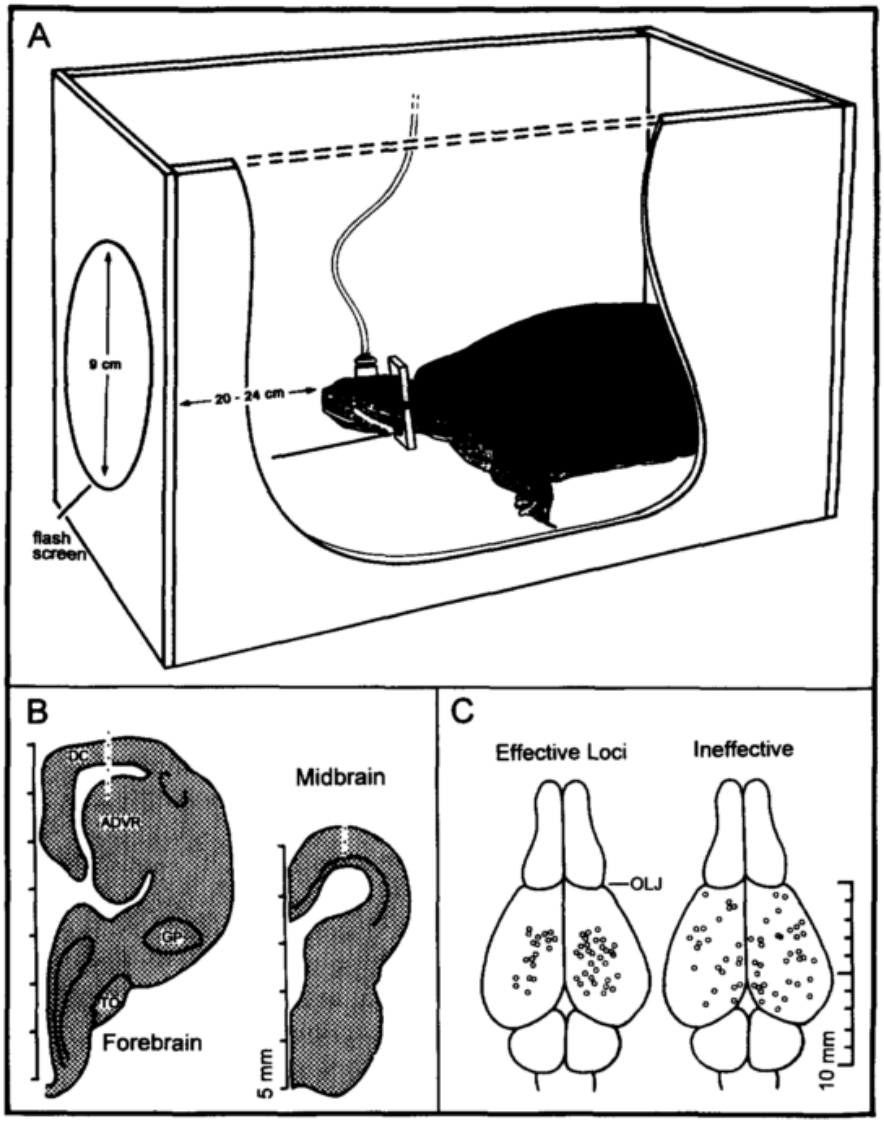

Figure 6.26 Overlap of effective and ineffective recording sites in turtle cortex. **(A)** Experimental design. **(B)** Placement of shank array in dorsal cortex. **(C)** Recording sites that were effective and ineffective at eliciting responses from omitted stimuli. Figure taken from (J. C. Prechtl & Bullock, 1994).

6.18 Sparsely Spiking Cells

It may be that we're near more visually responsive spiking cells than we realize, but we haven't noticed them because they spike so sparsely. For instance the spiking cell recorded from electrode 42 from turtle 77, had only 6 spikes during 512 presentations of a dot moving along a path across the visual field, but it is almost certain that those 6 spike were visually evoked (as opposed to random) (see discussion in Chapter 2.12.3).

We have many additional examples of sparsely spiking cells that may be visually responsive (Figrue 6.27). There are many stimulus specificities that we have yet to see in LFP responses or in responses of cells that spike abundantly. It would be good to give more attention to sparsely spiking cells to see if they have different response properties.

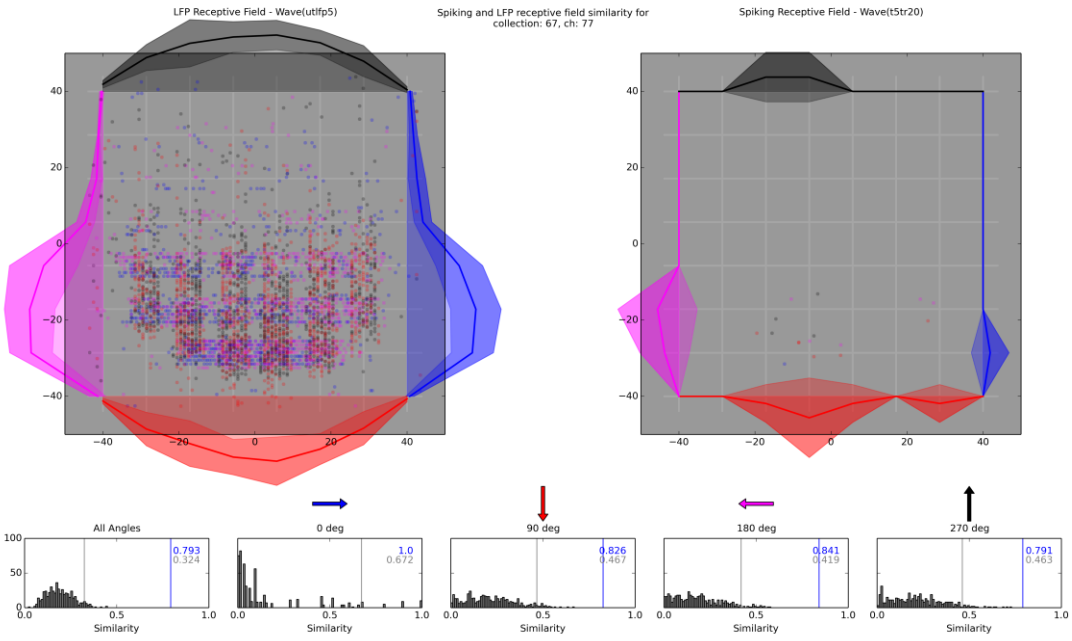

Figure 6.27 Receptive field of a sparsely spiking cell. **(Right)** Receptive field of a spiking cell. **(Left)** Receptive field of the LFP picked up by the same electrode. **(Bottom)** An indication of the similarity between the two receptive fields showing a comparison with shuffled data. The following figures follow the same format.

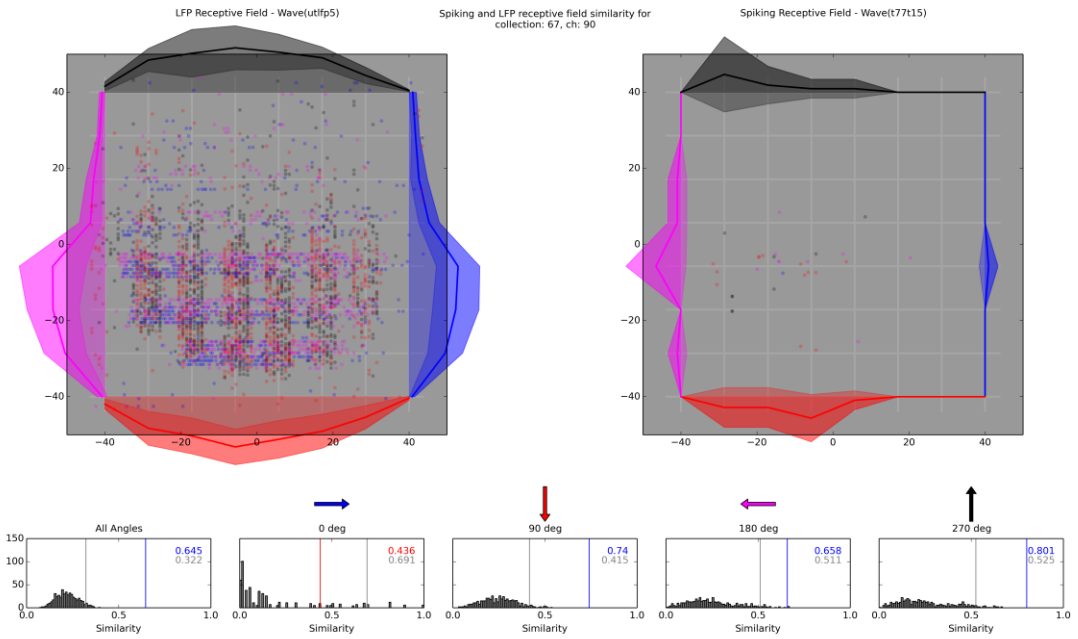
LFP Receptive Field - Wave(utlfp5)
Spiking and LFP receptive field similarity for collection: 67, ch: 90
Spiking Receptive Field - Wave(t77t15)
All Angles
0.645
0.322
0 deg
0.436
0.691
90 deg
0.74
0.415
180 deg
0.658
0.511
270 deg
0.801
0.525
Similarity

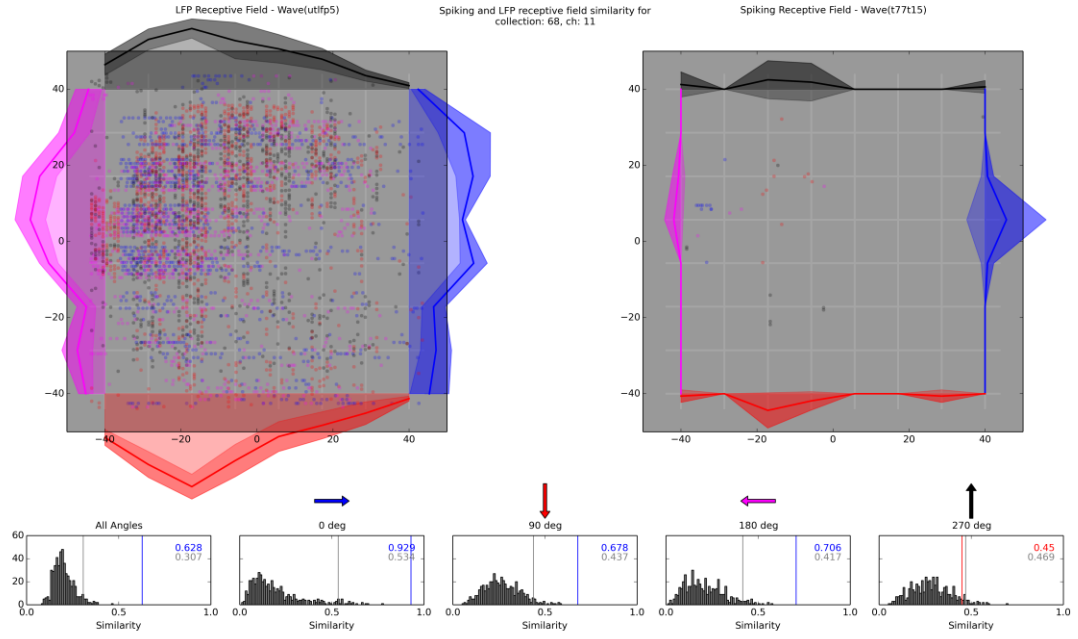
LFP Receptive Field - Wave(utlfp5)
Spiking and LFP receptive field similarity for collection: 68, ch: 11
Spiking Receptive Field - Wave(t77t15)
All Angles
0.628
0.307
0 deg
0.929
0.538
90 deg
0.678
0.437
180 deg
0.706
0.417
270 deg
0.45
0.469
Similarity

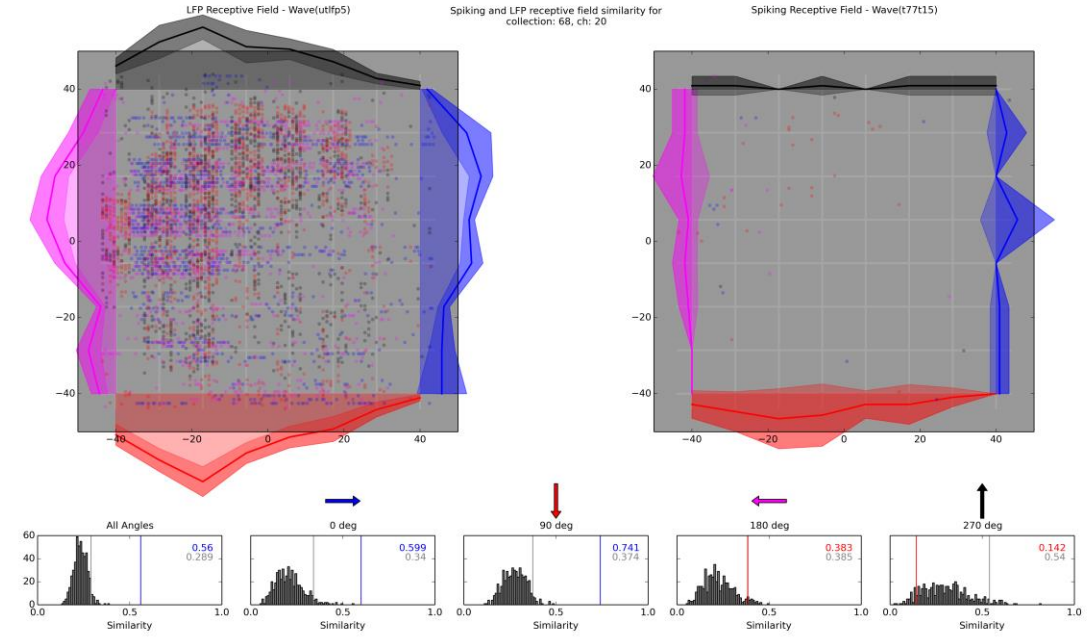
LFP Receptive Field - Wave(utlfp5)
Spiking and LFP receptive field similarity for collection: 68, ch: 20
Spiking Receptive Field - Wave(t77t15)
All Angles
0.56
0.289
0 deg
0.599
0.34
90 deg
0.741
0.374
180 deg
0.383
0.385
270 deg
0.142
0.54
Similarity

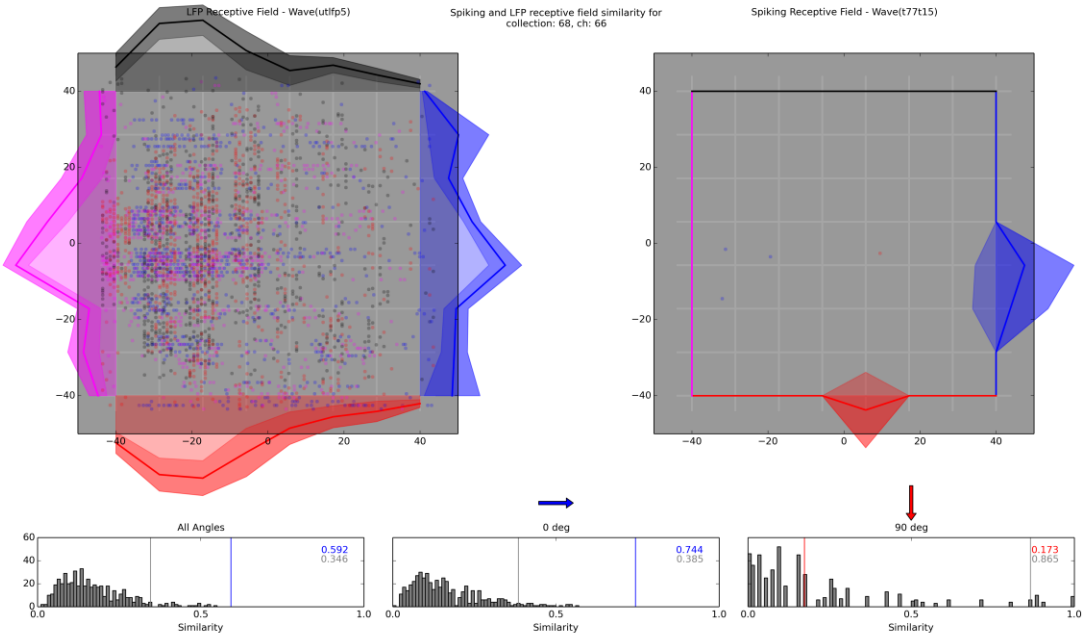
LFP Receptive Field - Wave(utlfp5)
Spiking and LFP receptive field similarity for collection: 68, ch: 66
Spiking Receptive Field - Wave(t77t15)
All Angles
0.592
0.346
0 deg
0.744
0.385
90 deg
0.173
0.865
Similarity

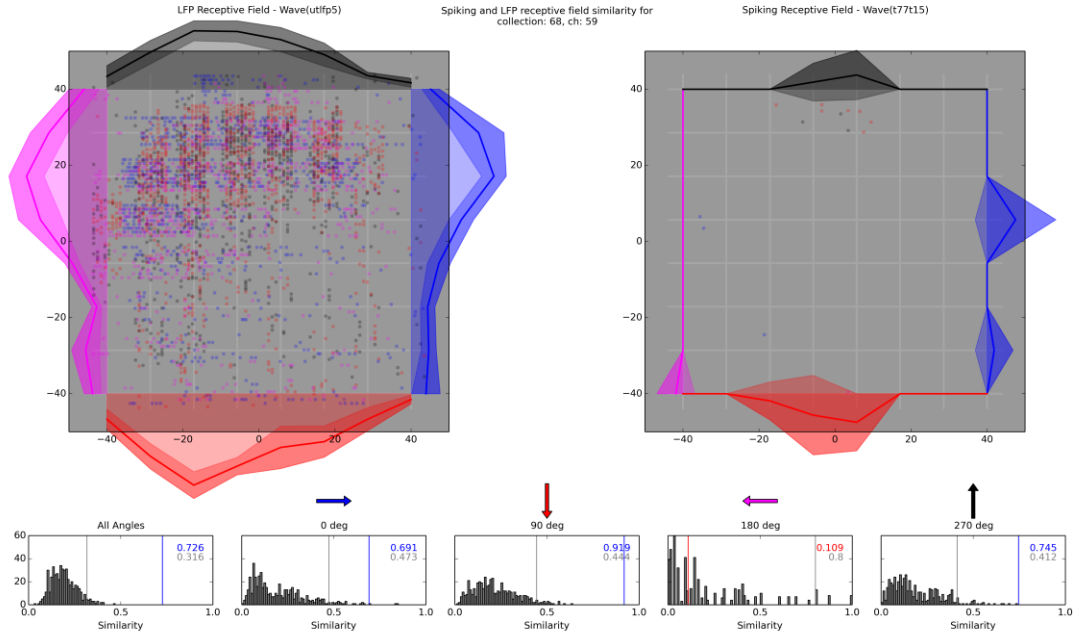
LFP Receptive Field - Wave(utlfp5)
Spiking and LFP receptive field similarity for collection: 68, ch: 59
Spiking Receptive Field - Wave(t77t15)
All Angles
0.726
0.316
0 deg
0.691
0.473
90 deg
0.919
0.444
180 deg
0.109
0.8
270 deg
0.745
0.412
Similarity

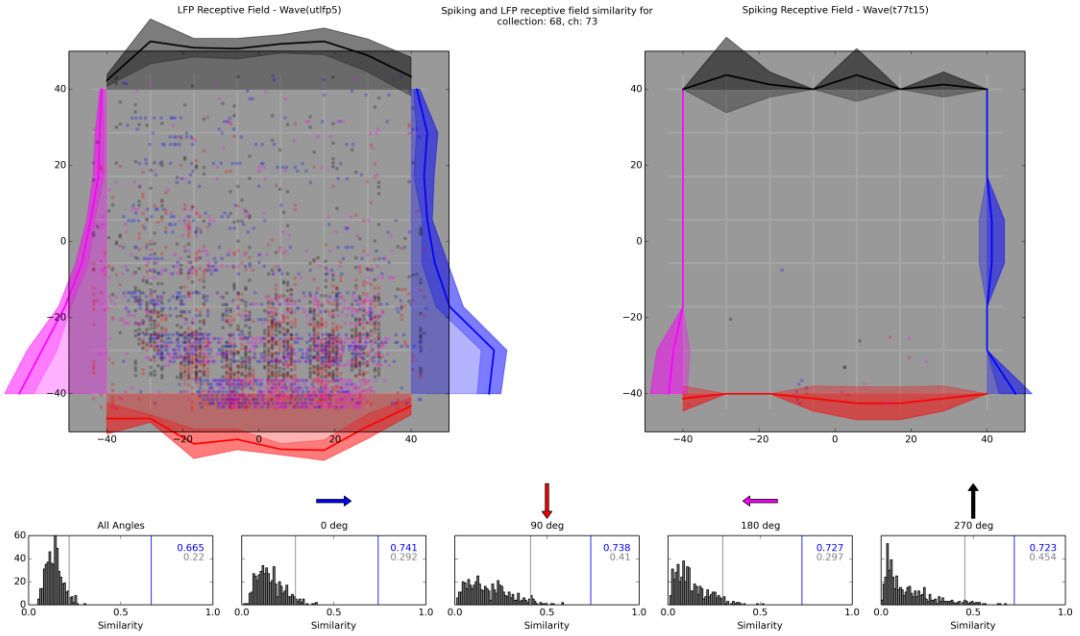
LFP Receptive Field - Wave(utlfp5)
Spiking and LFP receptive field similarity for collection: 68, ch: 73
Spiking Receptive Field - Wave(t77t15)
All Angles
0.665
0.22
0 deg
0.741
0.292
90 deg
0.738
0.41
180 deg
0.727
0.297
270 deg
0.723
0.454
Similarity

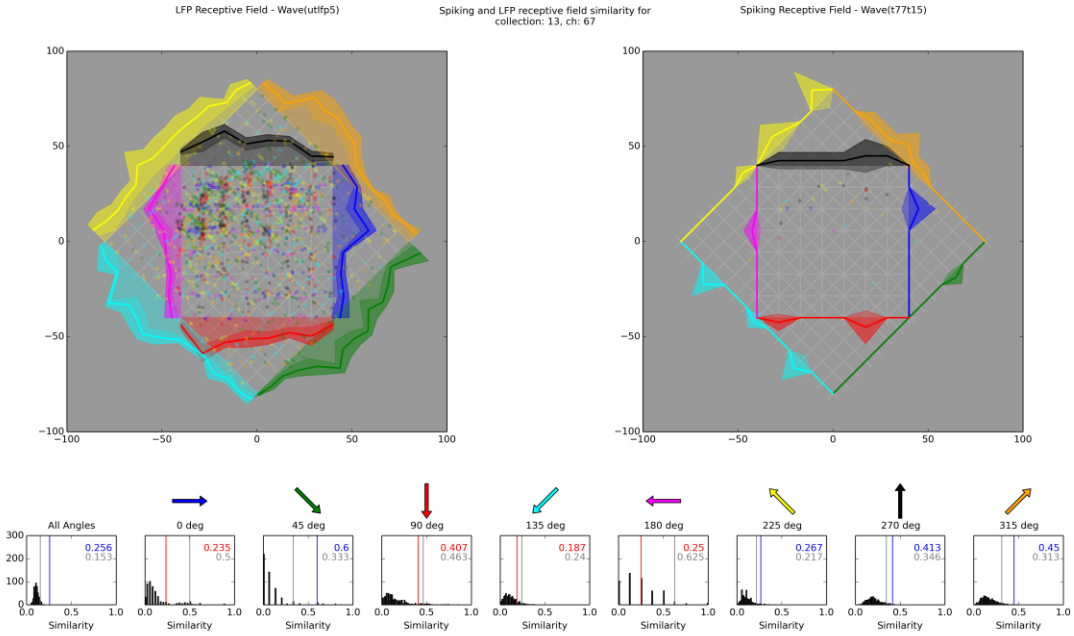
LFP Receptive Field - Wave(utlfp5)
Spiking and LFP receptive field similarity for collection: 13, ch: 67
Spiking Receptive Field - Wave(t77t15)
All Angles
0 deg
45 deg
90 deg
135 deg
180 deg
225 deg
270 deg
315 deg
0.256
0.153
0.235
0.5
0.6
0.333
0.407
0.463
0.187
0.24
0.25
0.625
0.267
0.217
0.413
0.346
0.45
0.313
Similarity

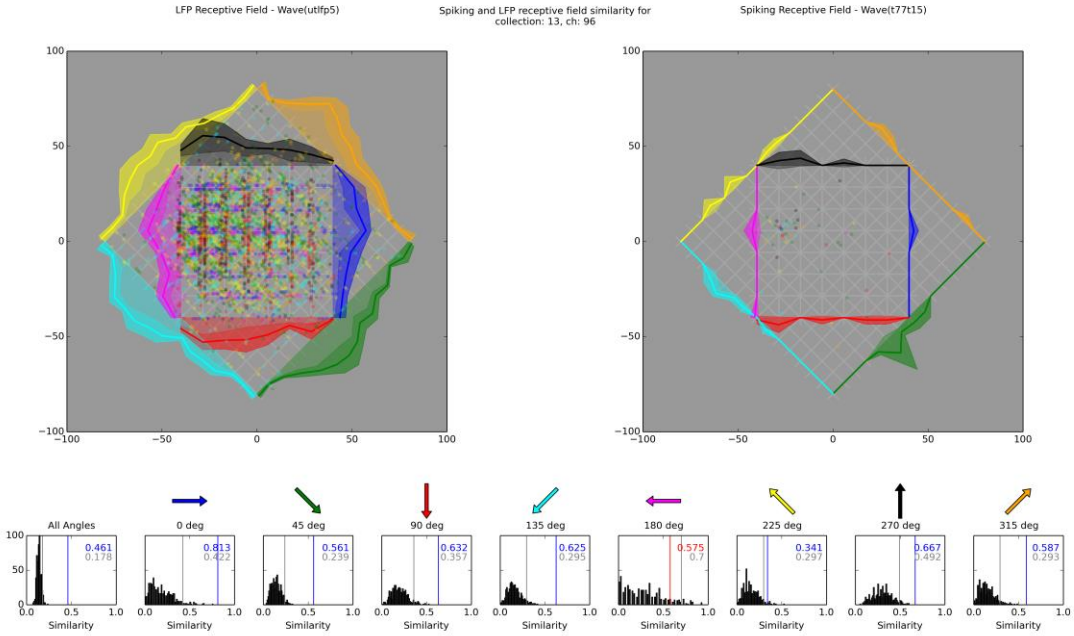
LFP Receptive Field - Wave(utlfp5)
Spiking and LFP receptive field similarity for collection: 13, ch: 96
Spiking Receptive Field - Wave(t77t15)
All Angles
0 deg
45 deg
90 deg
135 deg
180 deg
225 deg
270 deg
315 deg
0.461
0.178
0.813
0.422
0.561
0.239
0.632
0.357
0.625
0.295
0.575
0.7
0.341
0.297
0.667
0.492
0.587
0.293
Similarity

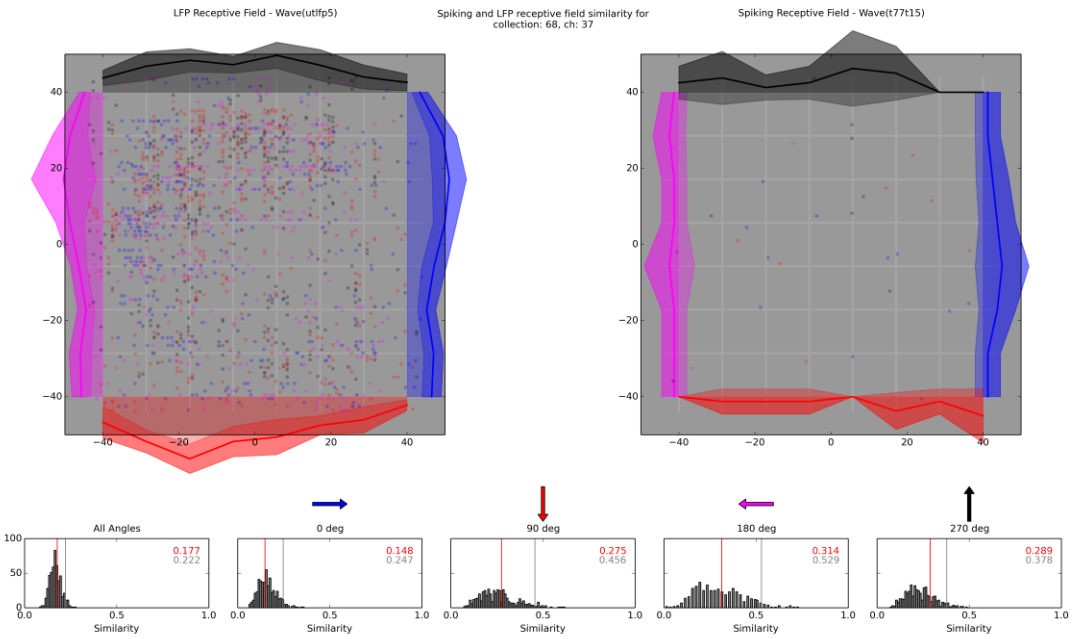

6.19 MEA Spike Response Latencies

6.19.1 Overview

So far only a cursory glance has been given to the spike response latencies from the MEA data. We've quickly flipped through the data and picked out 41 electrodes across 13 turtles that appeared to have large spikes in response to the few trials we looked at.

To do a more thorough study, a standard spike detection should be done for all electrodes, and those detected spikes should be used to determine visual responsive cells using the same algorithm used to establish visual responsive electrodes with LFP events in Chapter 2.

6.19.2 First, Second, and Third Spike Latencies

When looking at the distributions of first spike latencies, for some cells (e.g., the cells recorded by electrodes 5 and 9 for turtle 68 and less clearly the cell recorded by electrode 50 for turtle 71), there is a clear early first spike latency that occurs very often and a later first spike latency that also occurs often, without many occurrences of first spike latencies in between (Figure 6.28).

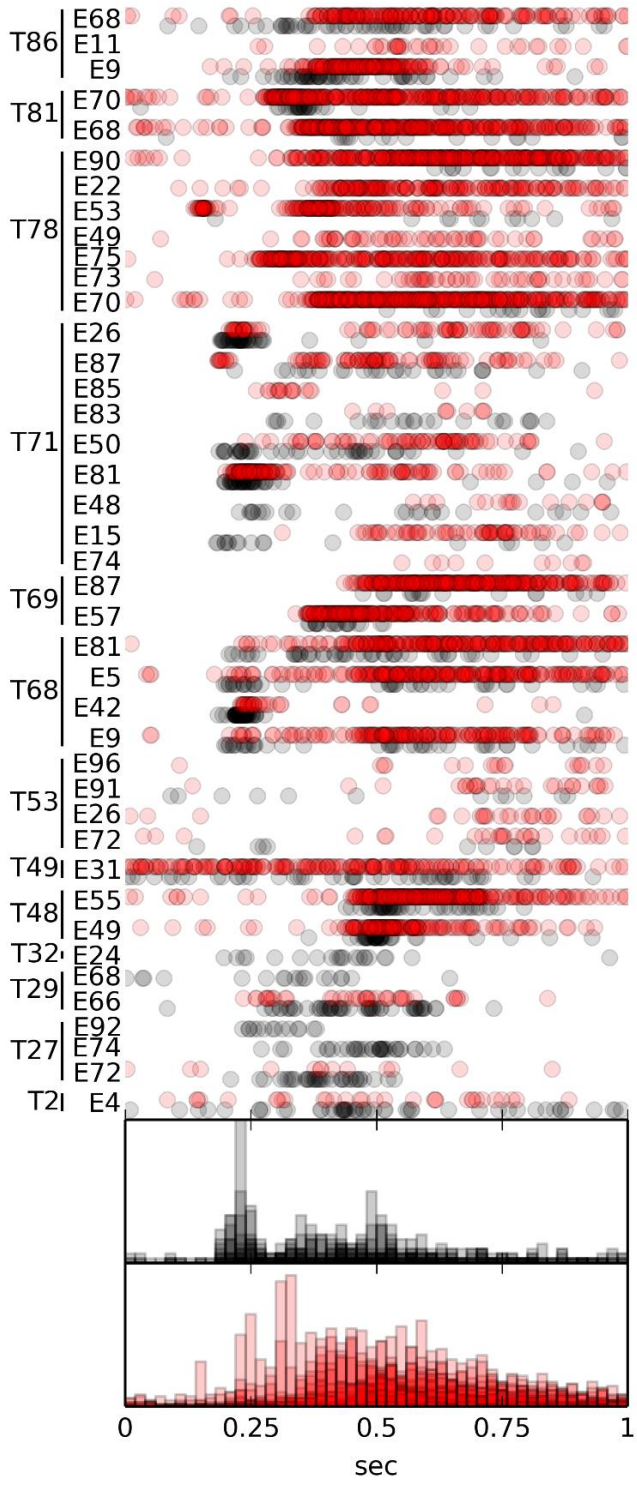

Figure 6.28 Early and late first spike latencies. **(Top)** The timing of the first spikes following either the onset of a red LED flash (turtles 2 -32) or the transition from a blank screen to the beginning of a complex movie (turtles 48-86). **(Bottom)** Summary histogram of all data. Early responses (from the first 60 trials) are shown in red. Late responses (to later trials) are shown in black.

One possible explanation for this, may be that there the full spiking response (beyond the first spike) is a series of somewhat precisely timed spikes and that the probability of one of the spikes in the series occurring does not depend on whether the previous spike occurred

6.19.3 Variability from Turtle to Turtle

The variability in first spike latency for electrode to electrode tends to be much less than the variability from turtle to turtle. In Figure 6.28 you can that all four electrodes shown for turtle 68 have a first spike latency of ~200-250 ms quite often. The electrodes from turtles 53 and 48 seem to be similarly grouped.

6.19.4 Establishing First Spike Latency Lower Bounds with Extended Recordings

Section 6.2 describes how visual responses can change and diminish over the course of a few hours. Because of this, for many of our analyses, we use only the early portion of our recordings, with the assumption that they more accurately represent the activity of the turtle in nature.

While the additional data may obscure an otherwise clear result for most analyses, it may be provide a cleaner result if we are interested establishing a lower bound for first spike latencies for individual cells. When we limit our study to just the first 60 trials, there are some cells that fire sparsely enough that we don't have good enough statistics to clearly identify a reliable first spike latency (e.g., the cells recorded by electrodes 57 and 87 for turtle 69, Figure 6.28). If, instead, we include data from hundreds of trials, we can end up having enough data for an obvious minimum value for spike latency.

As is the case with many of the features we analyze, we can see clear changes in the distributions of first spike latencies from the beginning of the experiment to the end, but it seems that one import feature of the distributions may be preserved throughout the experiment: the timing of the earliest first spikes. One could argue that it might be reasonable to expect this. After all, if the latency of the earliest first spikes is primarily dependent on the time it takes for excitatory signals to propagate along the pathway to the cell, then slower signal propagation increasing the latency seems much more likely than faster signal propagation existing to decrease the latency (but these assumptions may be too lofty).

If we want to lend support to the claim that the earliest first spike latencies are preserved over time without using such lofty and simplistic assumptions, we can instead look to the data. Though the motivation to use the extended data set was that some channels had very few data, other channels had plenty data that show an obvious earliest first spike latency (electrode 42 from turtle 68, electrode 70 from turtle 81, and electrode 49 from turtle 48, Figure 6.28). If we compare the earliest first spike latencies found using only the first 60 trials with the earliest first spike latencies found using all trials, we see that they agree very well. The fact that the cells that we can test provide reliable first spike latencies over long periods of time suggests that those that we can't test also might.

6.19.5 Trends Relating to Cortical Location and Visual Field Location

Mazurskaya reported that the latency to first spike to stimuli in the nasal visual field and stimuli in the temporal visual field differed by 100 ms (P. Mazurskaya, 1973). This would be something to check with stationary dots. In addition to checking this for individual neurons it

would also be good to see if the region of the visual field that evoked the earlier first spike latency varied across the electrode array.

6.20 Big Picture Turtle Clustering

A recurring theme in this research has been variability. There's variability at all levels (e.g., trial to trial, cell to cell, recording site to recording site). At maybe the coarsest level, turtle to turtle, we may be able to better understand our prep with a more deliberate look at this variability.

There are dozens of parameters that can be used to describe each experiment with a single turtle as a whole: the number of days since the turtle was fed, the time of day the surgery began, the person performing the surgery, the estimated locations and lengths of the cuts to the cortex, the location of the electrodes, the amount of time between anesthetization and the first occurrences of visual responses, the amount of time that visual responses continued, the number of spiking cells, the number of LFP visually responsive electrodes, the quality of the cut through the retina, the presence of persistent LFP activity in response to LED flashes, the presence (or amount of) ongoing LFP bursts (or spiking activity), and high level summary values for any other feature that has been studied.

We could looking for patterns and correlations among these parameters in a few ways. The simplest would be to simply look at two or three parameters at a time by plotting one parameter versus another with a point for each turtle. This process could easily automated to be done for all pairs of parameters. Alternatively, we could look at all parameters at once using a clustering algorithm.

If trends are found linking a methodological parameter to a parameter of neurological activity, this may inform/affect our methods. If trends are found linking two parameters of neurological activity, this may provide clues to the underlying mechanisms.

6.21 Recording Multiple Areas with Multiple Arrays of Shanks

In nearly all of our experiments, we have only placed electrodes in the cortex. We know that most of the inputs to cortical cells come from other cells within in the cortex, but to better understand the nature of the different contributions to cortical activity, it would be nice to record simultaneously from the cortex and the LGN.

6.21.1 Identifying LGN and Cortically Driven Cortical Activity

The relative timing of LGN and cortical activity may help us understand what activity is driven directly by LGN inputs as opposed to being a secondary effect of additional processing in the cortex. This is more likely to be relevant for action potential data since the time differences between different stages of processing may be too short to discern with the limited temporal precision of the LFP signal.

One topic for which the LFP signal may be quite useful is spontaneous activity. For some turtles, we see spontaneous LFP oscillations. We think that these occur independently of LGN activity. In an experiment on 3/15/2012, recording with a single extracellular electrode in a cortical slab (a cortex disconnected from the rest of the brain), we observed bursts of LFP oscillations. This tells us that bursts of LFP oscillations *can* occur without any LGN input, but

that doesn't preclude the possibility that, in a normally connected brain, the spontaneous LFP bursts are actually triggered by some activity in the LGN.

6.21.2 Existing Data and Future Experiments

For two experiments (turtles 15 and 16), we attempted experiments using multiple arrays of shank electrodes: one in the cortex and one in the LGN (Figure 6.29). Unfortunately, the electrodes were long enough and flimsy enough that the surface tension of the ACSF that they were partially submerged in caused the electrodes to bend towards each other. This can be seen in Figure 6.29. This made it difficult to cleanly insert the electrodes into the tissue. For this reason, in future experiments shorter electrodes should be used or the arrays should be modified (maybe with glue or Sylgard) so that the electrodes are rigidly spaced sufficiently close to the end of the electrodes that the glue/Sylgard support (and the portions of the electrodes beyond the support) are completely submerged in the ACSF.

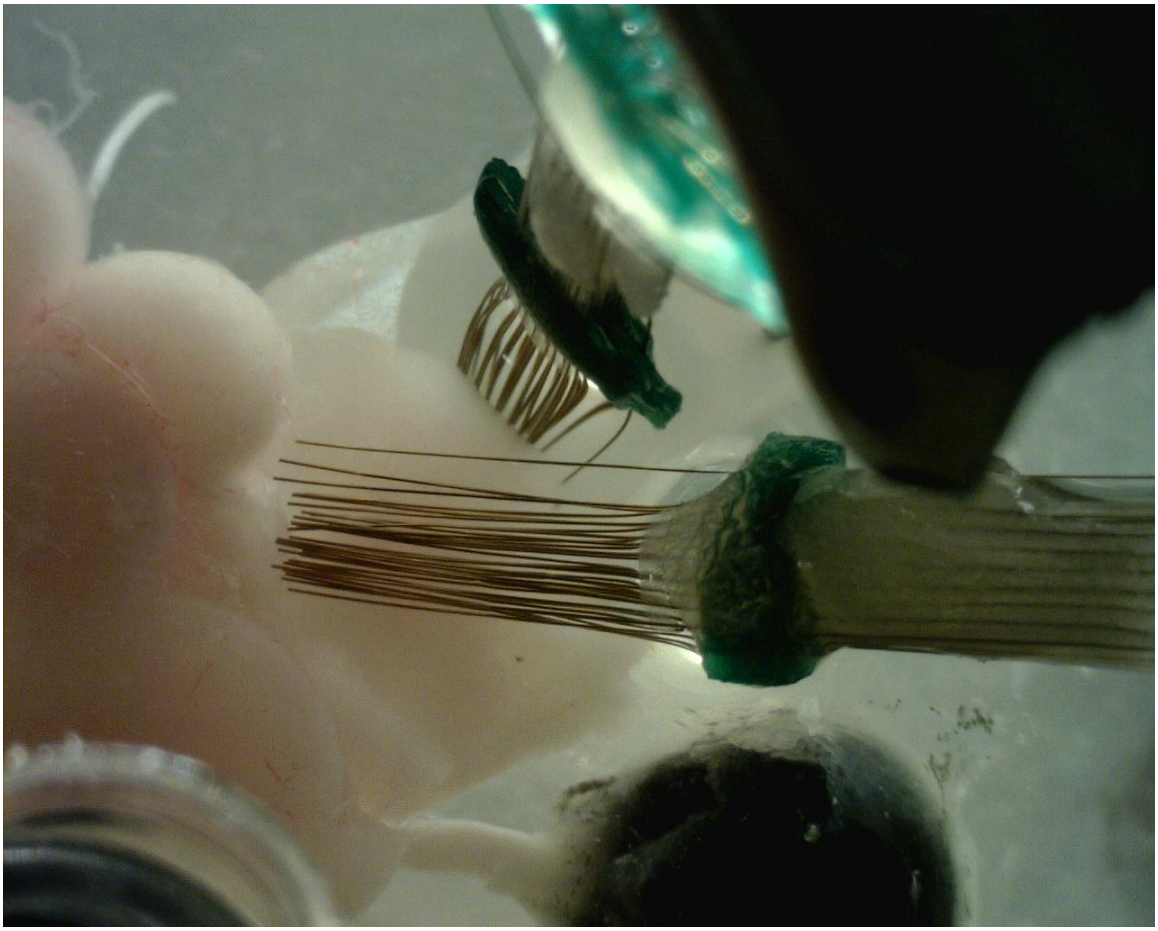

Figure 6.29 Multiple MEAs to simultaneously record cortical activity and thalamic input.

6.22 Relevance of the Ipsilateral Eye

Our standard procedure is to remove the eye (by cutting the optic nerve) that is ipsilateral from the cortex we're recording from. From a practical standpoint, it would extremely difficult to project the same image with the same orientation to both eyes. We know that the LGN projects to the ipsilateral cortex, and Nautiyal and Ulinski reported that while all the retinal lesions they made produced degenerated axons in the contralateral cortex, only some of the retinal lesions produced degeneration in the ipsilateral LGN (P S Ulinski & Nautiyal, 1988). With that in mind, if we are going to present stimuli to only one eye, the contralateral eye is the obvious choice.

The fact that most of the sensory input comes from the contralateral eye does not imply that the input from the ipsilateral eye is irrelevant or has no effect on the signal recorded on the retina (in fact, it would be absolutely surprising if the LGN received input from the ipsilateral retina, and this didn't affect the activity in the cortex). There are two experiments that might help us better understand the relevance of the ipsilateral eye.

6.22.1 Matching Stimuli

I started this section by mentioning that matching the orientation of a stimulus presented to both eyes is likely a practical limitation. This is certainly true if we're using stimuli with much spatial structure, but it's much less of an issue if we use diffuse flashes. The experiment is simple. Record the response to a diffuse flash presented to both eyes and then compare the results to those when the flash in presented to only one eye. Of course the interpretation of the analysis would need to consider how relevant the responses to a diffuse flash are to other stimuli.

6.22.2 Disconnecting Versus Covering the Eye

Close one eye and look at the world. Now sever one optic nerve and look at the world. We know that our visual perception is hardly affected by having one eye closed or covered, but we don't have an intuitive sense of how our perception is changed when an optic nerve is cut and the severed axons are left in ACSF.

Again, this is a simple thing to test. We could leave the contralateral eye attached but covered by an opaque screen and collect a data set (ongoing data and responses to flashes, moving dots, and complex movies). Then we would snip the optic nerve and collect another data set to compare.

These two experiments could be done in the same turtle and then the turtle could continue to be used by the researcher for whatever other experiments were planned.

6.23 Further Study of LED Flash LFP Responses

When averaging over the responses of 180 presentations of LED flashes, we find remarkable phase coherent responses and reproducibility at several different frequencies. Furthermore, if we present LED flashes of three different amplitudes, we get three different average that clearly share many features, but vary in their overall time courses, the prominence of certain features, and in other ways that aren't so simply described. While some of the changes as we increase stimulus intensity seem clear (e.g., the overall time course of the response increases with LED intensity), others are less obvious (e.g., the changes of amplitudes of specific cycles of the oscillatory responses or the superpositions of very low and medium frequencies and precisely what those frequencies are). To more fully understand flash intensity dependence, it would be good to repeat these experiments at several other intensities (including lower intensities) to see how we get from one response to another and how this develops from responses to very weak intensities.

6.24 The Effects of Surgical Cuts into the Cortex

Out of necessity, we make cuts into the cortex before recording any data. The cuts allow us to flatten the cortex so that we have a clear target for an array of electrodes to be inserted. Each cut severs a myriad of cortical connections. We assume that these lost connections don't have a significant effect on the visual responses we record (after all, we do still see strong responses), but we haven't conducted any experiments to explicitly test this. The closest thing

we've done is retrospectively look at the cuts we've made after conducting an experiment with little or no visual responsiveness to check if they are noticeably different from experiments that had strong visual responses. One conclusion we arrived at through this type of thinking was that removing the entire olfactory bulb may affect visual responses, and, consequently, our new policy is only to cut off the tip of the olfactory bulb.

Of course we only assume a strong response is a good thing (i.e., that a very strong response is what we would also find in the animal behaving in the wild, if we had access to those neural signals). It may be that when we're rejoicing in the lab over the most magnificently strong LFP response seen on almost every electrode, what's actually happening is that some regulatory mechanism that's required to suppress/inhibitactivity to a biologically useful level, has been disabled/diminished and we're recording from a malfunctioning brain.

Even if this isn't the case (and we certainly hope it's not), it would still be good to understand better what (if any) effects our cortical cuts have on visual responses. It may be possible to test this experimentally. We could do an experiment in which we make no cortical before placing the brain in the recording chamber. We could then insert a single electrode (or maybe a shank electrode if it weren't prohibitively large) into the visual cortex through the DVR, around the DVR, or even through the pial surface, without make any cuts (or with only minimal cuts if the visual cortex can't be accessed with no cuts).

After finding a site with evoked LFP activity (and hopefully spikes as well), we could then record a baseline activity set (e.g., ongoing activity, responses to flashes, and responses to moving dots). Then we would cut off the end of the olfactory bulb and record another activity set. This could be repeated for the rostral-caudal cortical cut, and the two medial-dorsal cortical

cuts. For each cut we could even record an activity set first after making a partial cut and then again after making a deeper cut.

If any differences are observed after any of the cuts, this could 1) further our understanding of the visual pathways and connectivity and 2) motivate changes to our experiments in the hope of recording more biologically relevant activity.

An additional feature to look for before making cuts is the extent of the visual cortex. Though it's difficult to compare rostral-caudal locations without very precise landmarks, it seems that at least one study has recorded visual responses in more caudal regions than we have (P. Mazurskaya, 1973), and it's not the case that we haven't seen it because we haven't looked for it. Consistently, when our MEAs extend into these regions, the LFPs and unit activity is not visually responsive. That we should expect visual responses in the more caudal areas of the cortex is also supported less directly by HRP stains, that suggest that the caudal cortex receives input from visually responsive thalamic regions (Mulligan & Ulinski, 1990).

With these reports in mind, it might be worth checking whether the discrepancy with what we've observed could be explained by the cuts we make to the tissue. To test this we could quite simply carry out the experiment described above, while being sure to search for visually responsive areas in this caudal region before making any cuts.

6.25 A Second Look at Retinal Health

Not only is this section itself a second look at retinal health (another section involved retinal health in a different context), but also, this section really is about taking a second look at retinal health while performing each experiment.

To clarify, every experiment, we take a first look at retinal health immediately after hemisecting the eye. At this point we can tell if we accidentally caused some undue damage to the retina by not getting a very clean cut. Signs of undue damage include visibly obvious tears and retinal peeling.

The limited consideration we've given to the effects that retinal health have had on our recorded activity has typically just involved this first look, but in addition to this first look, for most experiments, we have also taken and saved a second look. That is to say that when the experiment is finished we take an additional picture of the retinal.

The picture of health of the retinal at the end of the experiment (actually, the morning following the experiment is when the picture is usually taken) tends to be drastically different than the picture taken before the experiment, and as a whole is not representative of the retina for to early recordings, but certain aspects of the retinal picture taken the next morning may highlight damage to the retina that was likely to be present for the entire experiment (albeit easy to overlook in the pre experiment pictures). It seems that as the general health of the retina degrades over time, certain defects are emphasized.

In Figure 6.30 we compare the retinas of two turtles both before and after an experiment. In the before pictures, we can see that turtle 10 seems to have a cleaner cut and less retinal peeling than turtle 8. The after pictures are consistent with those observations, but additionally they show extensive retinal tearing in turtle 8. After starting an experiment, there are no external forces applied to the retina (with the exception of gravity and the very gentle flow of ACSF into the eyecup). With that in mind, it is most likely that the tearing damage we see in the post experiment picture for turtle 8 represents damage that was present the entire experiment (because

there is no event mid experiment that would cause tearing), but only manifests so clearly after the experiment. For this reason, when considering the effects of retinal health on recorded activity, it's advisable to look at both the pre experiment and post experiment pictures.

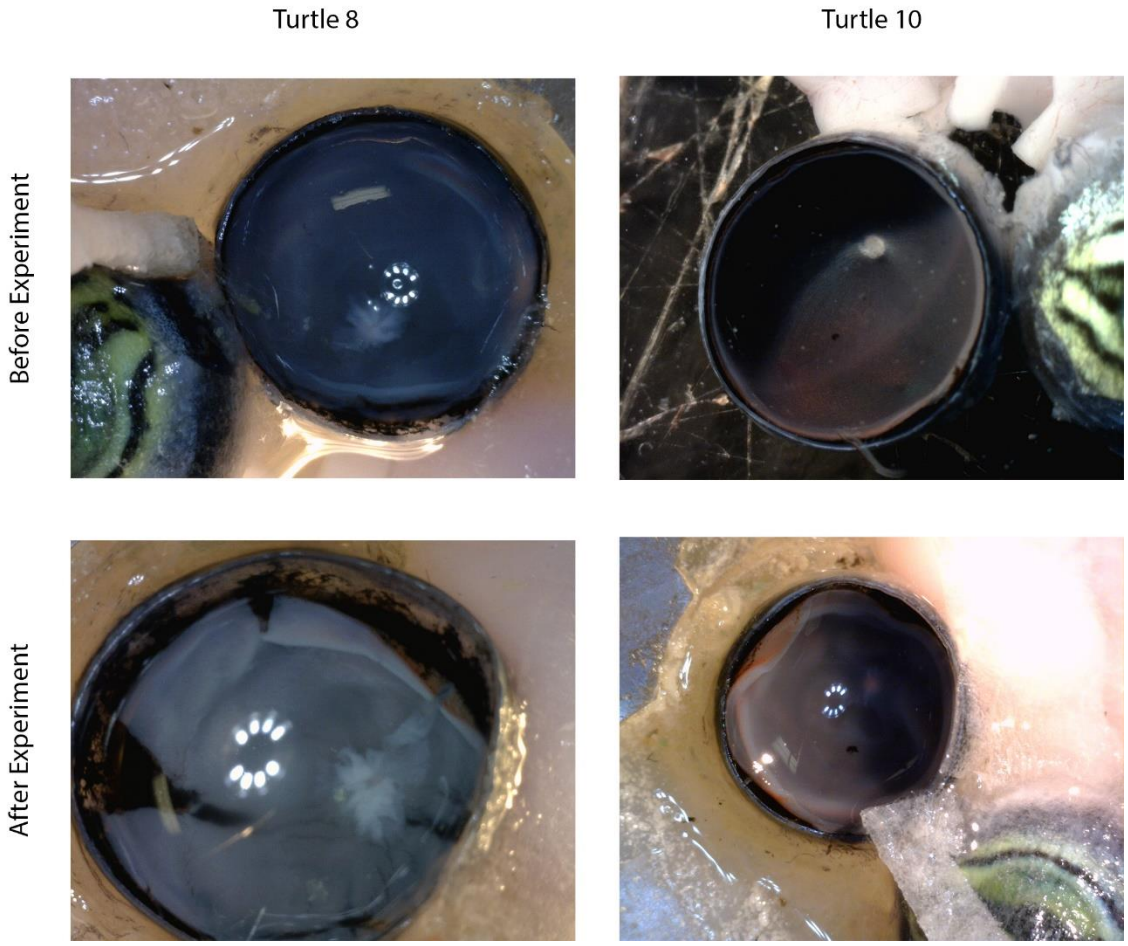

Figure 6.30 Retinal health before and after experiments. Pictures of two retinas taken at the beginning of an experiment and the taken again the following morning.

6.26 Frequency Dependent Receptive Field Similarity

In rat hippocampus it appears that theta band activity may be more similar over long ranges than gamma activity is (Figure 6.31).

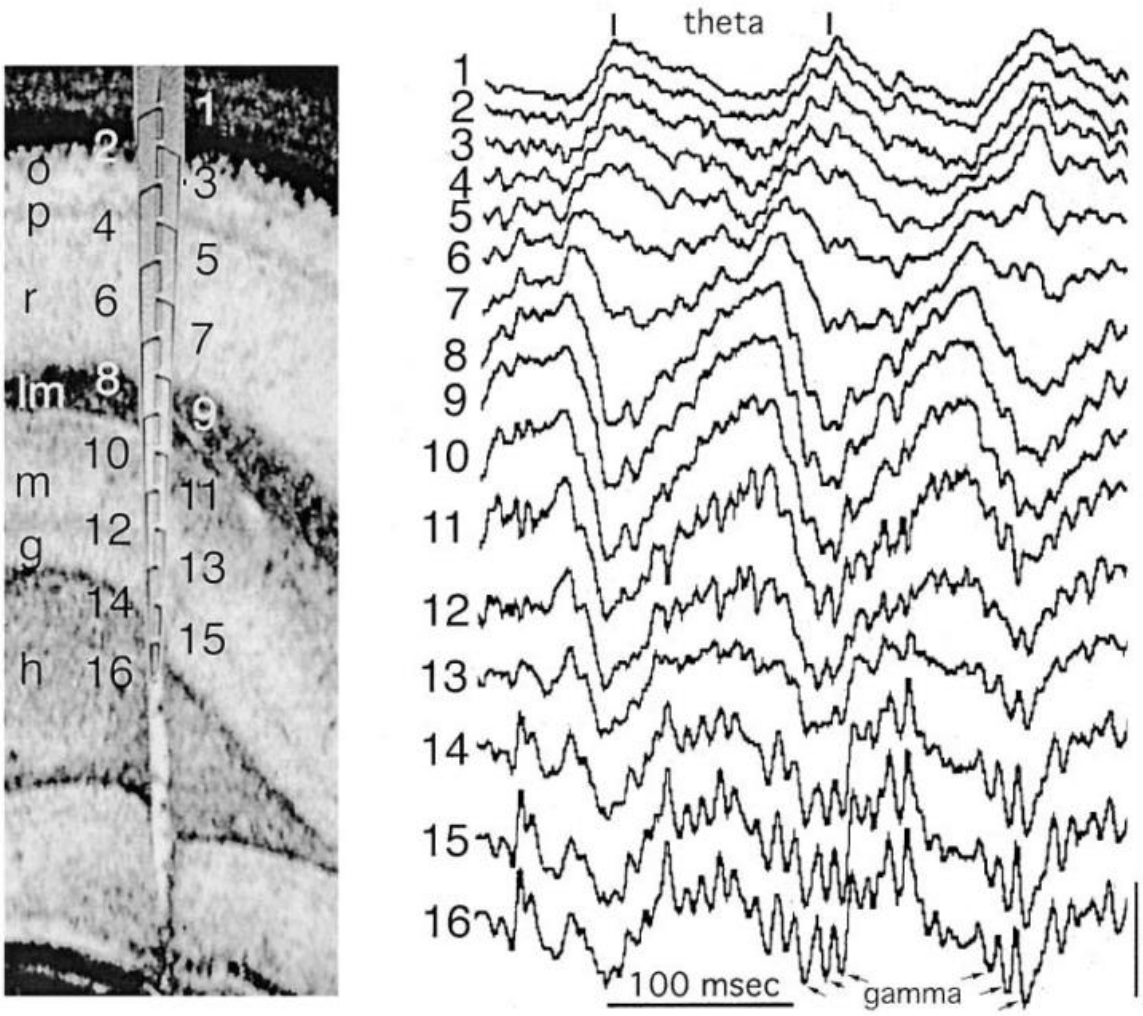

Figure 6.31 Theta and gamma band frequencies in rat hippocampus**.** Figure taken from (Buzsáki, 2002)

It would be interesting to repeat the receptive field similarity studies (see Chapter 3) using different frequency ranges. As the study was first done it used a 7 Hz – 59 Hz passband filter. Alternatively, we could recreated the figures several times using several smaller passband filters from 0 Hz – 100 Hz, and compare the resulting RF similarity versus electrode distance plots. A hypothesis might be that passbands with higher frequencies have steeper similarity versus distance slopes (to the extent that the frequency bands have enough activity to reveal any trends).

6.27 Detailed Experimental Methods

6.27.1 Hemisecting the Eye

To make it easier to get a clean cut through the eye without causing excessive damage to the retina or optic nerve, we use modified ring forceps. We took a pair of ring forceps and cut out a section of one of the rings large enough for an optic nerve to fit through (Figure 6.32). This allows us to hold the eye with the optic nerve roughly in the center of the open ring. In so doing, we can securely hold the eye with the plane through which we want to make our cut in the center of and parallel to the forceps (so that the forceps are not in the way of the cut we want to make) without squeezing the optic nerve against the eye. After securing the eye, we make the cut using platinum chrome double edge razor blades.

Figure 6.32 Modified ring forceps. Ring forceps with a hole ground out of one of the rings.

6.27.2 Perfusion Details

To perfuse the eye without obstructing the image we project onto the retina, a small wick was made from a Kimwipe (Figure 6.33). The wick connected an ACSF feed located ~1 cm above and to the side of the eye to the inside edge of the hemisected eye. If any brain tissue were large enough to extend above the surface of the ACSF (e.g., the right cortex or the optic tecta), it would be cover with a small piece of Kimwipe so that it would also stay in contact with ACSF (Figure 6.33).

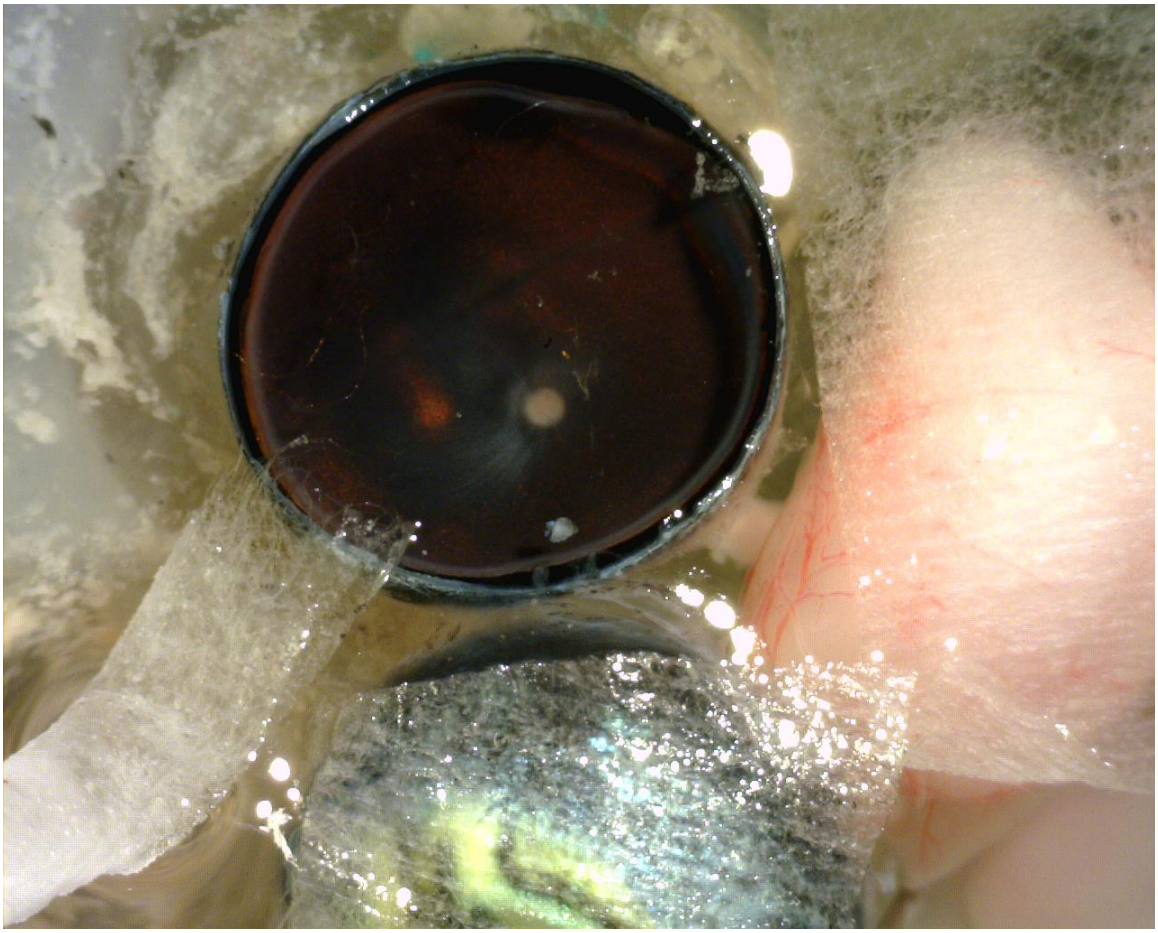

Figure 6.33 Wick for retinal perfusion and keeping tissue wet. A thin strip of Kimwipe leads from a perfusion dripper into the eyecup. Other pieces of Kimwipe cover tissue that would not be submerged in ACSF. Picture from turtle 14.

6.27.3 Finding a Visually Responsive Recording Site

After positioning the brain in the recording chamber, we need to place our electrode(s) appropriately to record the signals we're interested in. Over the course of a few years, we used a few different methods used to find recording.

Establishing a Zero Depth

The first step was always to establish a zero point (specifically a zero depth). Two techniques were used to do this: visual inspection and signal monitoring.

First, we would simply look through the microscope as we lowered the electrode(s) toward the tissue and look for either a dimple in the tissue or for the tip of the electrode to disappear into the tissue. Dimples were difficult to see because our electrodes typically entered the tissue without causing much disturbance. Looking for the electrode tip to disappear behind tissue provided results with mixed confidence. Often, the tip didn't actually disappear after entering tissue, but instead you could see the inserted tip through the translucent tissue. The point at which this started was sometimes clear, and sometimes not. The variability was likely do to lighting differences from experiment to experiment, as we didn't use lights with a fixed position (they moved around throughout the experiments to light different areas). Both of these visual cues were made more difficult to find by the distortion from the meniscus that the ACSF would form with the electrode.

In addition to looking for visual indications, we also watched the signal coming in from the electrode. If we observed neural activity, this served to tell us that we were definitely in tissue, but didn't tell us how deep we were. We didn't find a clear and reliable marker that we made first contact with the tissue.

Eventually, we found that all of these techniques were more effective if we first got the electrode very near the tissue, momentarily drained the ACSF from the chamber, and then proceeded to look for these indications. This eliminated the distorting meniscus, and changed the electrical signal from the difference between ACSF and tissue to the difference between air and tissue, which was a much clearer difference.

Finding Visual Responses

For our single electrode and tetrode experiments, the search for a visually responsive recording site was done by presenting a search stimuli to the retina while slowly lowering the

electrode into the cortex. The most common search stimulus used was a collection of dots of different sizes bouncing around the visual field at different speeds.

While the stimulus was presented we lowered the electrode into the tissue at 1-5$\mu m/s$, and look for neural activity in the live signal from the electrode. If we didn't find a visually responsive region after getting sufficiently deep (~500 μm), we would lift the electrode from the tissue, move laterally 100 μm and try again.

Depending on the resolution used to monitor the live signal, it could be difficult to distinguish between activity at different frequencies (e.g., a spike versus slower fluctuation). To make this easier, we added an audio monitor to the search procedure. The greater resolution of the

It should be noted that we were specifically looking for visually responsive areas. Therefore, if there were cells with high stimulus specificity that weren't responsive to our search stimuli, our experiments would be unlikely to reveal those.

6.28 Moving Dot Figures with Perpendicular Projections

Instead of adding a curve for each angle indicating the number of events for each path, add a histogram for each angle, summing over all paths counting the number of events at each location along the path (Figure 6.34). It will be interesting to answer the following questions: Do the histograms showing responses at different locations along the path agree with their opposite angles? Do they agree with the average path responses for perpendicular angles? This may provide additional insights regarding the durations of responses and the latency of responses.

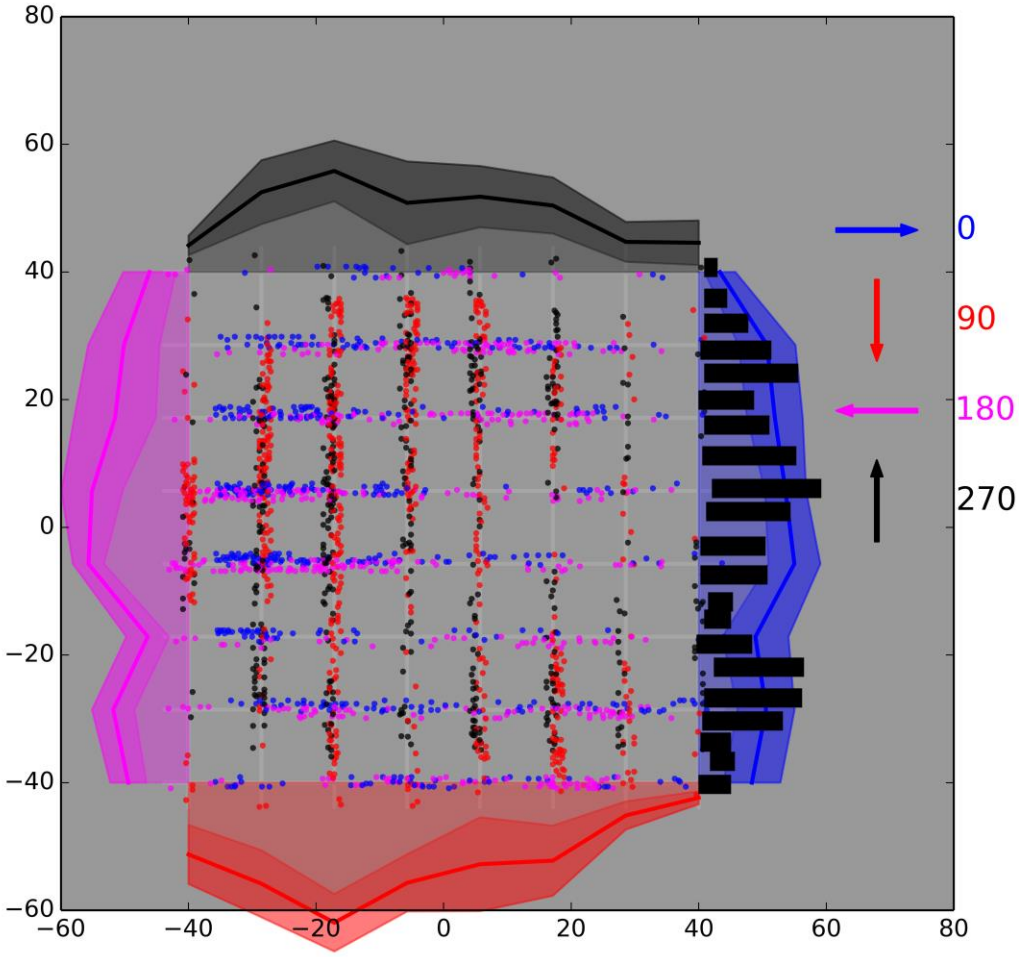

Figure 6.34 Moving dot receptive perpendicular projections (concept). Black bars show where the histogram for the black 270 degree data would logically go.

6.29 References

Buzsáki, G. (2002). Theta oscillations in the hippocampus. *Neuron*, *33*, 325–340. doi:10.1016/S0896-6273(02)00586-X

Du, X., Ghosh, B. K., & Ulinski, P. (2005). Encoding and decoding target locations with waves in the turtle visual cortex. *IEEE Transactions on Bio-Medical Engineering*, *52*(4), 566–77. doi:10.1109/TBME.2004.841262

Du, X., Ghosht, B. K., & Ulinski, P. (2003). Decoding the Position of a Visual Stimulus from the Cortical Waves of Turtles, 2–7.

Hounsgaard, J., & Nicholson, C. (1990). The isolated turtle brain and the physiology of neuronal circuits. *Preparations of Vertebrate Central Nervous System In Vitro*, *6*, 155–181.

Kajikawa, Y., & Schroeder, C. E. (2011). How local is the local field potential? *Neuron*, *72*(5), 847–858. doi:10.1016/j.neuron.2011.09.029

Katzner, S., Nauhaus, I., Benucci, A., Bonin, V., Ringach, D. L., & Carandini, M. (2009). Local origin of field potentials in visual cortex. *Neuron*, *61*(1), 35–41. doi:10.1016/j.neuron.2008.11.016

Mazurskaya, P. (1973). Retinal projection in the forebrain ofEmys orbicularis. *Neuroscience and Behavioral Physiology*. Retrieved from http://link.springer.com/article/10.1007/BF01186006

McCallum, W. C. (1980). Brain slow potential changes elicited by missing stimuli and by externally paced voluntary responses. *Biological Psychology*, *11*(1980), 7–19. doi:10.1016/0301-0511(80)90022-8

Mulligan, K. A., & Ulinski, P. S. (1990). Organization of geniculocortical projections in turtles: isoazimuth lamellae in the visual cortex. *Journal of Comparative Neurology*, *296*(4), 531–547. Retrieved from http://www.ncbi.nlm.nih.gov/pubmed/2358551

Nilsson, G. E., & Lutz, P. L. (1991). Release of inhibitory neurotransmitters in response to anoxia in turtle brain. *The American Journal of Physiology*, *261*, R32–R37.

Prechtl, J. C., & Bullock, T. H. (1993). Plurality of Viual Mismatch Potentials in a Reptile. *Journal of Cognitive Neuroscience*, *5*, 177–187. doi:10.1162/jocn.1993.5.2.177

Prechtl, J. C., & Bullock, T. H. (1994). Event-related potentials to omitted visual stimuli in a reptile. *Electroencephalography and Clinical Neurophysiology*, *91*, 54–66. doi:10.1016/0013-4694(94)90018-3

Prechtl, J. C., Cohen, L. B., Pesaran, B., Mitra, P. P., & Kleinfeld, D. (1997). Visual stimuli induce waves of electrical activity in turtle cortex. *Proceedings of the National Academy of Sciences of the United States of America*, *94*(14), 7621–6. Retrieved from http://www.pubmedcentral.nih.gov/articlerender.fcgi?artid=23872&tool=pmcentrez&rendertype=abstract

Rutishauser, U., Kotowicz, A., & Laurent, G. (2013). A method for closed-loop presentation of sensory stimuli conditional on the internal brain-state of awake animals. *Journal of Neuroscience Methods*, *215*(1), 139–55. doi:10.1016/j.jneumeth.2013.02.020

Senseman, D. M., & Robbins, K. a. (2002). High-speed VSD imaging of visually evoked cortical waves: decomposition into intra- and intercortical wave motions. *Journal of*

Neurophysiology, *87*(3), 1499–514. Retrieved from http://www.ncbi.nlm.nih.gov/pubmed/11877522

Ulinski, P. S., & Nautiyal, J. (1988). Organization of retinogeniculate projections in turtles of the genera Pseudemys and Chrysemys. *The Journal of Comparative Neurology*, *276*(1), 92–112. doi:10.1002/cne.902760107

Xing, D., Yeh, C.-I., & Shapley, R. M. (2009). Spatial spread of the local field potential and its laminar variation in visual cortex. *The Journal of Neuroscience : The Official Journal of the Society for Neuroscience*, *29*(37), 11540–9. doi:10.1523/JNEUROSCI.2573-09.2009